

Nonlinear Beam-Based Vibration Energy Harvesters and Load Cells

by

Jocelyn Maxine Kluger

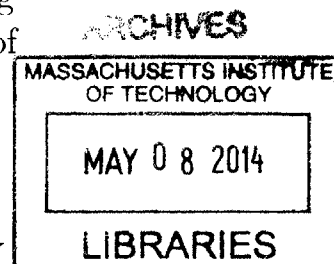
Submitted to the Department of Mechanical Engineering
in partial fulfillment of the requirements for the degree of

Master of Science in Mechanical Engineering

at the

MASSACHUSETTS INSTITUTE OF TECHNOLOGY

February 2014



© Massachusetts Institute of Technology 2014. All rights reserved.

Author
..... Department of Mechanical Engineering
January 31, 2014

Certified by
..... Alexander H. Slocum
Professor of Mechanical Engineering
Thesis Supervisor

Certified by ..
..... Themistoklis P. Sapsis
Assistant Professor of Mechanical Engineering
Thesis Supervisor

Accepted by
..... David E. Hardt
Chairman, Department Committee on Graduate Theses

Nonlinear Beam-Based Vibration Energy Harvesters and Load Cells

by

Jocelyn Maxine Kluger

Submitted to the Department of Mechanical Engineering
on January 31, 2014, in partial fulfillment of the
requirements for the degree of
Master of Science in Mechanical Engineering

Abstract

This thesis studies a novel nonlinear spring mechanism that is comprised of a cantilever wrapping around a curved surface as it deflects. Static force versus displacement tests and dynamic "initial displacement" tests verified the spring theory for a large range of oscillator parameters. Various human motion energy harvester configurations that use the nonlinear spring were numerically optimized for power, robustness, and adaptivity. Based on the optimization results, both the nonlinear and linear devices studied in this thesis generate more power per volume and per mass when excited at one's hip while walking than current commercial energy harvesters. The two degree-of-freedom (2DOF) nonlinear oscillator is more adaptive to different excitation signals and resistant to power decay when parasitic damping is present than the 1DOF and 2DOF linear systems. These significant advantages are caused by the 2DOF nonlinear system harvesting its optimal power at large electromagnetic damping coefficients, whereas the optimal power generation for the linear systems occurs at low electromagnetic damping coefficients. This thesis also examined what electromagnetic damping coefficients can be generated by magnet-and-coil geometries that satisfy the energy harvester constraints. The final chapter of this thesis investigates a load cell that uses the stiffening spring to maintain high resolution over a large range of forces and prevent large forces from damaging the load cell. Future work will include testing a full energy harvester prototype and exploring other applications of the nonlinear spring.

Thesis Supervisor: Alexander H. Slocum
Title: Professor of Mechanical Engineering

Thesis Supervisor: Themistoklis P. Sapsis
Title: Assistant Professor of Mechanical Engineering

Acknowledgments

I am very grateful to my advisors, Professor Alex Slocum and Professor Themis Sapsis for their support, guidance, and patience.

This project would not have been possible without the generous financial support of the Martin family (the Martin Fellowship in Design), Mr. A. Neil Pappalardo, the Tata Center, the Naval Engineering Education Center, and the National Science Foundation. Thank you! (NSF would like you to know: This material is based upon work supported by a National Science Foundation Graduate Research Fellowship. Any opinion, findings, and conclusions or recommendations expressed in this material are those of the author and do not necessarily reflect the views of the National Science Foundation.)

Additionally, I am very thankful for the assistance of the MIT Hobby Shop staff. Ken Stone and Hayami Arakawa patiently walked me through how to use the CNC and waterjet machines step-by-step countless times. Thank you to the Edgerton Machine Shop, especially Mark Belanger, for sharing his machining expertise and preventing the destruction of several important parts. A very big thank you to the Pappalardo Machine Shop, especially to Jim Dudley for dedicating hours of his time to run the tilted-head waterjet, even machining the load cells last-minute on the day before Christmas Eve.

Thank you Dr. Barbara Hughey for introducing me to and lending me the accelerometers and high speed camera.

Thank you to my PERG and SAND labmates for all of their advice. This project couldn't have been possible without all their help in designing and machining. Thank you Deborah Alibrandi for all of the administrative help.

Finally, thank you to my wonderful parents for their encouragement, to my brother and sister for occasionally checking in to make sure I was all right, and to all of my other family members for their loving support. Thank you to all my friends for their assistance in helping me occasionally take my mind off the project. Thank you to Sam for the moral support, vegetables, and hot meals I otherwise would not have had.

Contents

- 1 Introduction 13**
 - 1.1 System Requirements and Constraints 14
 - 1.2 Current Energy Harvesters 15
 - 1.3 Current Nonlinear Springs 18

- 2 Nonlinear Spring Theory 22**
 - 2.1 Determination of the contact point 25
 - 2.2 Force versus deflection for quadratic and general surfaces 27
 - 2.3 Safety factor against yield 30

- 3 Experimental Verification 34**
 - 3.1 Force versus Displacement Test 36
 - 3.2 Initial Displacement Test 40
 - 3.3 Single Base Drop Test 49
 - 3.4 Multiple Base Drop Test 54

- 4 Numerical Optimization and Comparison of Linear and Nonlinear Energy Harvesters Excited by Human Motion 58**
 - 4.1 Excitation Signals 62
 - 4.2 Comparison of 1DOF Systems Excited by Foot Motion 66
 - 4.2.1 Cubic Nonlinear Spring Summary 67
 - 4.2.2 Walking 70
 - 4.2.3 Running 73

4.2.4	Comparison of Robustness and Adaptivity	75
4.3	Comparison of 1DOF Systems Excited by Hip Motion	78
4.3.1	Walking	79
4.3.2	Running	81
4.3.3	Comparison of Robustness and Adaptivity	83
4.4	Comparison of 2DOF Systems Excited by Hip Motion While Walking	85
4.4.1	Nonlinear	88
4.4.2	Linear	97
4.5	Energy Harvester Performance Summary	104
4.5.1	Adaptivity to different excitation signals	108
4.5.2	Robustness to an excitation signal's small frequency variations	110
4.5.3	Power per Volume	111
4.5.4	Power versus parasitic damping	113
4.5.5	Power versus signal noise	115
5	Electromagnetic Theory	117
5.1	Theory	118
5.1.1	Calculate the magnetic field	118
5.1.2	Calculate the flux through each coil	124
5.1.3	Calculate the flux gradient through each coil	124
5.1.4	Calculate the electromagnetically-induced damping and Power to Load	124
5.2	Parameter Constraints	128
5.3	Optimization	128
6	Energy Harvester Conclusions	132
7	Nonlinear Load Cell	135
7.1	Introduction	135
7.2	Theory	137
7.2.1	Load Cell for Cantilevers With Rigid Connections	144
7.2.2	Load Cell for Cantilevers With Rotational Spring Connections	147

7.3	Experimental Verification	152
7.3.1	Fabrication	152
7.3.2	Experimental procedure	154
7.3.3	Results	155
7.4	Spring Steel Load Cells Simulated Performance	156
7.4.1	Load Cell with Rigid Connections	157
7.4.2	Cantilevers with Rotational Spring Connection	161
7.5	Conclusions and Future Work	165
A	Matlab Codes	167
A.1	Nonlinear spring force versus displacement	167
A.2	Load cell force versus displacement	170
A.3	Track objects in a video	180
A.4	Energy harvester simulation	185
A.5	Electromagnetic Damping	203

List of Figures

2-1	Novel nonlinear spring	23
2-2	Tip force versus contact point	30
2-3	Contact point versus tip displacement	31
2-4	Spring force versus displacement	31
2-5	Spring force versus stiffness	32
2-6	Stress in spring along cantilever length	33
3-1	Dynamic test set-up	35
3-2	Force versus displacement test set-up	36
3-3	Force versus displacement test for surface with $n = 2$	38
3-4	Force versus displacement test for surface with $n = 3$	39
3-5	Force versus displacement test for surface with $n = 5$	40
3-6	Initial displacement test- oscillator 1, time series	43
3-7	Initial displacement test- oscillator 1, wavelet transform	44
3-8	Initial displacement test- oscillator 2, time series	45
3-9	Initial displacement test- oscillator 2, wavelet transform	46
3-10	Initial displacement test- oscillator 3, set-up	47
3-11	Initial displacement test- oscillator 3, time series	48
3-12	Initial displacement test- oscillator 3, wavelet transform	49
3-13	Single base drop test- base time series	51
3-14	Single base drop test- oscillator 2, time series	52
3-15	Single base drop test- oscillator 2, wavelet	53
3-16	Multiple base drop test- base time series	55

3-17	Multiple base drop test- oscillator 2, time series	56
3-18	Multiple base drop test- oscillator 2, wavelet	57
4-1	Experimental Set-up for collecting foot acceleration data	63
4-2	Foot motion data	64
4-3	Hip motion data	65
4-4	1DOF nonlinear system CAD rendering and component diagram	67
4-5	Power optimization surface for 1DOF cubic system excited by walking foot .	68
4-6	Power optimization surface for 1DOF cubic system excited by running foot .	69
4-7	Power optimization surface for 1DOF nonlinear system excited by walking foot	71
4-8	Time series of optimal 1DOF nonlinear system excited by walking foot . . .	72
4-9	Power optimization surface for 1DOF nonlinear system excited by running foot	73
4-10	Time series of optimal 1DOF nonlinear system excited by running foot . . .	74
4-11	Adaptivity of 1DOF harvesters for time-rescaled foot walking signal	76
4-12	Adaptivity of 1DOF harvesters for time-rescaled foot running signal	76
4-13	Robustness of 1DOF harvesters for different foot motions	77
4-14	Power optimization for 1DOF nonlinear, linear systems excited by walking hip	79
4-15	Time series of optimal 1DOF nonlinear, linear systems excited by walking hip	80
4-16	Power optimization for 1DOF nonlinear, linear systems excited by running hip	81
4-17	Time series of optimal 1DOF nonlinear, linear systems excited by running hip	82
4-18	Adaptivity of 1DOF harvesters for time-rescaled hip walking signal	84
4-19	Adaptivity of 1DOF harvesters for time-rescaled hip running signal	84
4-20	Robustness of 1DOF harvesters for different hip motions	85
4-21	General 2DOF system component diagram	86
4-22	Nonlinear 2DOF Type1: Moderate EM damping system CAD rendering and component diagram	89
4-23	Power optimization for 1DOF linear "half" system: $\pm 1.7cm$ displacement constraints, 30g mass. Excited by walking hip	90
4-24	Power optimization for 1DOF nonlinear "half" system: $\pm 1.7cm$ displacement constraints, 30 g mass. Excited by walking hip	90

4-25	Power optimization for the 2DOF nonlinear type 1 system (moderate damping) excited by walking hip	91
4-26	Time series of the 2DOF nonlinear type 1 system(moderate damping) excited by walking hip	92
4-27	Nonlinear 2DOF Type1: Moderate EM damping system CAD rendering and component diagram	94
4-28	Power optimization for the first 2DOF nonlinear linear system excited by walking hip	95
4-29	Modified force versus displacement	96
4-30	Time series of optimal 2DOF nonlinear system excited by walking hip	97
4-31	Linear 2DOF system, version 2 CAD rendering and component diagram . . .	98
4-32	Time series of optimal 2DOF linear system excited by walking hip, low damping	100
4-33	Power optimization for 2DOF linear system, with moderate electromagnetic damping, excited by walking hip	101
4-34	Time series of optimal 2DOF linear system, with moderate damping, excited by walking hip	102
4-35	Power optimization for 2DOF linear system, with large electromagnetic damping, excited by walking hip	103
4-36	Time series of optimal 2DOF linear system, with moderate damping, excited by walking hip	104
4-37	Adaptivity of energy harvesters for different hip motions	109
4-38	Adaptivity of 2DOF energy harvesters to time-rescaled hip walking signal . .	110
4-39	All harvesters optimized power per volume when excited by hip walking . . .	112
4-40	Effect of parasitic damping on optimal power harvested	114
4-41	Optimized power (normalized by signal power) versus signal noise	116
5-1	Magnet-over-Coil schematic	118
5-2	Magnetic charge density along the magnet-air interface	121
5-3	Magnetic potential	122
5-4	Magnetic field at the coil-steel backing interface	123

5-5	Equivalent circuit	125
5-6	Magnetic flux, flux gradient, electromagnetically-induced damping, and power versus magnet position	127
5-7	Optimization of Electromagnetic Damping- Trial 1	130
5-8	Optimization of Electromagnetic Damping- Trial 2	130
5-9	Optimization of Electromagnetic Damping- Trial 3	131
5-10	Optimization of Electromagnetic Damping- Trial 4	131
7-1	Load Cell Problem Set-Up	139
7-2	Load Cell Free Body Diagram	139
7-3	Free Body Diagram Segments.	140
7-4	Load cell with rigid connections, deflection along cantilever length	144
7-5	Load cell with rigid connections, force versus deflection	145
7-6	Load cell with rigid connections, stiffness versus force	145
7-7	Load cell with rigid connections, cantilever/surface contact point versus force	146
7-8	Load cell with rigid connections, stress versus force	146
7-9	Load cell with rotational spring connections, deflection along cantilever length	147
7-10	Load cell with rotational spring connections, force versus deflection	148
7-11	Load cell with rotational spring connections, stiffness versus force	148
7-12	Load cell with rotational spring connections, contact point versus force . . .	149
7-13	Load cell with rotational spring connections, stress versus force	149
7-14	Load cell with rotational spring connections, stress along curved segment . .	150
7-15	Load cell with rotational spring connections, bending moment versus force .	150
7-16	Load cell with rotational spring connections, cantilever tip angle versus force	151
7-17	Load cell with rotational spring connections, effective rotational spring stiff- ness versus force	151
7-18	Load cell CAD	153
7-19	Fabricated load cells	153
7-20	Load cell force versus displacement test set-up	154
7-21	Load cell with rigid connections, force versus displacement test	155

7-22	Load cell with rotational spring connections, force versus displacement test .	156
7-23	Load cell with rigid connections: stiffness at $F= 0.17\text{N}$	157
7-24	Load cell with rigid connections: stiffness at $F= 100\text{N}$	158
7-25	Load cell with rigid connections: maximum cantilever stress at $F= 100\text{N}$. .	158
7-26	Load cell with rigid connections: force versus deflection versus D	159
7-27	Load cell with rigid connections: stiffness versus force versus D	159
7-28	Load cell with rigid connections: stress versus force versus D	160
7-29	Load cell with rigid connections: contact point versus force versus D	160
7-30	Load cell with rotational springs: stiffness at $F= 0\text{N}$	161
7-31	Load cell with rotational springs: stiffness at $F= 800\text{N}$	162
7-32	Load cell with rotational springs: maximum cantilever stress at $F= 800\text{N}$. .	162
7-33	Load cell with rotational springs: force versus deflection versus R	163
7-34	Load cell with rotational springs: stiffness versus force versus R	163
7-35	Load cell with rotational springs: stress versus force versus R	164
7-36	Load cell with rotational springs: contact point versus force versus R	164

List of Tables

1.1	General Commercial Energy Harvesters	16
1.2	Passive Human Motion Harvesters	17
4.1	Summary of Experimentally Recorded Foot and Hip Motions	63
4.2	Simulated 1DOF Cubic Oscillator Performance	70
4.3	Summary of human motion nonlinear energy harvesters studied in thesis . .	107
5.1	Electromagnetic System Parameters	128

Chapter 1

Introduction

Several technological processes; such as energy harvesting from ambient vibrations, shock absorption from external loads, and passive control or suppression of mechanical instabilities; involve targeted energy transfer from one component of a structure to another. In particular, energy harvesting is the process of using ambient energy sources to generate useful forms of energy such as electricity. The energy in these ambient sources is usually spread over a range of frequencies. Applications of energy harvesting range from MEMs sensors implanted in the human body to monitor biological signs [27] to small electronics such as wireless sensors in remote locations [16]. Shock absorption is the process of protecting a primary structure from an ambient force or external pressure load. Shock absorption applications include passive protection of buildings from earthquake excitations, offshore platforms from water wave impacts, or delicate instruments from external loads [9] [25]. Passive control of mechanical instabilities is another important area that has recently emerged in the context of targeted energy transfer. Examples include the suppression of aeroelastic instabilities on wings due to fluttering [7] and the elimination of aeroelastic instabilities in suspension bridges [26].

This thesis focuses on energy harvesting from human motion vibrations for powering macro-scale personal devices such as cell phones. This energy harvester should satisfy power requirements and parameter constraints, and it should be competitive with currently available commercial energy harvesters. As discussed in Section 1.3, one way to increase the energy harvester's efficiency is to use a nonlinear spring. Many different nonlinear springs

have been studied, and each has different advantages and disadvantages.

1.1 System Requirements and Constraints

The ultimate goal of this project is to fully power cell phones by walking or running. 2.5G smartphones consume about 70 mW when in suspension mode (i.e. when the only power consumed by the phone is checking for incoming signals). They consume about 800 mW during a phone call. A typical cell phone's fully-charged battery stores 16 kJ; or, enough power for 5.5 hours talk time or browsing time on a 3G network, 10 hours browsing time on Wi-Fi, 40 hours of audio listening, or 225 hours standby. [1]. To make a cell phone self-sustaining, an ambulatory energy harvester must convert at least 70-800 mW of the power in human motion into electricity.

During motion, different parts of the body exert different amounts of power. An average 80 Kg male's center of mass exerts 0.5 J/step; the hip, 20 J/step; the knee, 25 J/step; and the heel, 2 J/step. Some of this power is available for electricity without hindering human motion; especially when the exerted power is "negative work" (i.e., the joint muscle absorbs energy and converts it to heat) [14]. Zarrugh et al. [13] measured actual adult strides to range from 1 step/sec (for an extremely slow walk velocity of 0.4 m/s) to 2 steps/sec (for a brisk walk velocity of 1.6 m/s). According to the New York Times Health and Wellness blog, the average American takes 5,000 steps per day, which equates to traveling about 2.5 miles or 4 Km [17]. If every step provides about 0.1 J of electricity, then up to 500 J may be available for powering a cell phone, enough energy for a 10 minute phone call.

This thesis will assume that the energy exerted by a person to excite the oscillator is significantly less than the energy normally exerted by the person to walk. Therefore, the person's walking will not be affected by the energy harvester that he/she is carrying.

In addition to the human power available and phone power required, further design considerations are ensuring that the device is not overly burdensome to carry around. That is, one must limit the device's mass and volume. An oscillator's dissipated power tends to be proportional to the proof mass and displacement amplitude. Therefore, the longest and heaviest device that is not burdensome should be designed. As a general rule-of-thumb, it

seems reasonable to think that the largest device people are willing to carry around is the size and mass of a cell phone because many people already carry one in their pocket all day. As a baseline, the largest cell phone found via an internet search was the Samsung Galaxy S II. This device has the dimensions: 2.5 x 6.6 x 0.85 cm. It has a mass of 133 g. Thus, the energy harvester should be constrained to a mass of about 133 g and total oscillator displacement of 7 cm.

1.2 Current Energy Harvesters

Many low-frequency energy harvesting devices are already in existence, but they could be greatly improved in terms of how convenient they are for the user or how much power they generate. Most low-frequency commercial energy harvesters that are already on the market use power inputs that are non-human, such as sunlight or spinning bicycle wheels; or require the user's active motion; such as operating a manual crank, pull-cord, or shaker. Information on these harvesters is shown in Table 1.1. Several commercial energy harvesters that use passive human motion as their power source are: Seiko watches, the nPower Personal Energy Generator, and the Bionic power knee-brace-like "PowerWalk". Some of these passive human motion harvesters are listed in Table 1.2.

Table 1.1: General Commercial Energy Harvesters

Name	Location	Mechanism Description	Power Output (W)	Volume, cm^3 (in^3)	Mass, g	Cost, \$	Source
Voltaic Solar Charger	laptop bag	PV panel	Two 2.0 Watt solar panels charge a battery. 4.5 hours in the sun will fully charge a cell phone.	106 (5)	590	129	¹
K3 Wind and Solar Charger	anywhere outside	impeller and PV panel	1 hour of sun and wind provides 30 minutes talk time	1472 (86)	300	100	²
Nokia Bike-Powered Phone Charger	bicycle wheel spoke	dynamo	Pedaling at 6mph for 10 minutes results in 30 minutes talk time or 37 hours standby (phone power not specified)	50 (3)	50	18	^{3, 4}
Shake Flashlight	hand	magnet through coil	30 seconds of shaking provides up to 15 minutes of green light (the LED's consume 0.1 W)	490 (30)	308	30	⁵
Crank Flashlight	hand	dynamo	2 minutes of cranking provides 15 minutes of light (the LED's consume 1 W)	680 (41)	425	30	⁶

¹<http://www.voltaisystems.com/>

²<http://www.kinesisindustries.com/products>

³<http://www.wired.com/gadgetlab/2010/06/nokia-announces-bike-powered-phone-charger/>

⁴<http://press.nokia.com/wp-content/uploads/mediaplugin/doc/nokia-bicycle-charger-kit-datasheet.pdf>

⁵<http://www.appliedinnotech.com/product/nightstar-green-led-flashlight/>

⁶<http://www.redflarekits.com/crank-lite?gclid>

Table 1.2: Passive Human Motion Harvesters

Name	Location	Mechanism Description	Power Output (W)	Volume, cm^3 (in^3)	Mass, g	$\frac{Power}{Volume}$, W/cm^3	$\frac{Power}{Mass}$, W/Kg	Cost, \$	Source
Seiko Kinetic Watch	wrist	asymmetric rotating proof mass with electromagnetic generator	5e-6	16 (1)	150	3.1e-7	3.3e-8	300	[15], 7
nPower PEG	near hip	magnet inside coil	3e-2	490 (33)	396	6.1e-5	7.6e-5	150	8, 9,
Instep Nano Power	foot	reverse electrowetting (conductive liquid deforms)	2	101 (6.2)	—	2e-2	—	—	10
Back-pack	back	bag contents load frame via spring and drive pinion gear on generator	7.4	24e3 (1440)	38e3	3.1e-4	1.9e-4	—	11
Bionic Power	knee	high torque knee joint performing negative work drives generator	12	—	750	—	1.6e-2	1000	12

⁷<http://www.seikousa.com/gallery/index.php>

⁸<http://www.gizmag.com/npower-peg-charger-for-hand-held-electronics/14957/>

⁹<http://www.pcworld.com/product/651107/tremont-electric-npower-peg.html>

¹⁰<http://www.designboom.com/technology/motion-powered-energy-harvester-fits-in-shoe/>

¹¹<https://www.sciencemag.org/content/309/5741/1725.short>

¹²<http://www.bionic-power.com/index.htm>

1.3 Current Nonlinear Springs

For all energy harvester designs, one aims to design elements that are capable of transferring the input energy irreversibly and efficiently. In typical energy harvesting applications, the ambient vibration can be described as a stochastic, multi-frequency signal that is often characterized by time-varying features [20].

However, traditional single degree of freedom linear vibration harvesters are efficient only close to their design point; that is, when the excitation frequency matches the harvester's natural frequency. Therefore, linear harvesters respond inefficiently to ambient vibrations [21]. In order to absorb ambient vibrations effectively, it is essential for an energy harvester to be characterized by adaptivity (i.e. the ability to adjust its resonance frequency/ies depending on the input spectrum) and robustness (i.e. the ability to maintain its energy harvesting performance even if the excitation varies significantly).

Methods for overcoming this mistuning problem include: designing systems that do not use a spring, control theory of linear spring systems, 2 degree-of-freedom linear systems, continuous linear systems, and nonlinear springs. Below, we give a critical overview of these techniques, focusing on their different advantages and disadvantages.

Mitcheson et al [12] describe a micro-scale coulomb-force parametric generator (CFPG) that absorbs ambient energy without using a spring. Instead, the CFPG uses a charged capacitor plate that snaps away from a counter-electrode when excited by large accelerations. Since the CFPG does not have a spring, it does not have a resonant frequency and responds similarly to acceleration signals that have the same magnitude but different frequencies. The CFPG, however, only functions well when the excitation displacement greatly exceeds the allowable travel length of its sliding plate. Another shock absorption device that functions without a spring is the MEMS-fabricated hydraulic valve that fits inside a shoe, as described in [28]. A controller allows hydraulic fluid flowing in between two chambers to pulse on a piezoelectric element. Resulting strain in the piezoelectric element converts the mechanical energy into electric energy. Additionally, [16] discusses a device small enough to fit in a shoe that consists of a clamshell made from two piezoelectric elements. The device flattens with each heel-strike and toe-off. [16] also reviews other energy harvesting devices that absorb

ambient energy without vibrating.

The performance of energy harvesters with linear springs can be improved by using control strategies to alter the oscillator's resonance frequency [21] or creating linear devices with two or more degrees of freedom so that the system has multiple resonant frequencies [24]. [21] and [24] present devices with better performance than traditional single linear springs. However, the controlled devices consume some of the collected power, and the multiple degree of freedom systems are bulky and have limited robustness.

Another approach is to use a nonlinear spring. Essentially nonlinear springs- that is nonlinear springs without linear stiffness components- do not have preferential linear frequencies. Therefore, they are more robust to variations in the external excitation and preserve their good performance level for a wide range of conditions [6], [18], [25], . The simplest form of an essentially nonlinear spring is a cubic one. It may be implemented by linear springs supporting the proof mass at nonperpendicular angles. For example, MacFarland et al. [11] investigate the dynamics of a nonlinear oscillator realized by a thin elastic rod (piano wire) clamped at its ends without pretension that performs transverse vibrations at its center. To leading order approximation, the stretching wire produces a cubic stiffness nonlinearity. Despite its success in various applications, this design can suffer from significant frictional losses, especially in small scale applications, due to the guided motion of the moving mass [25]. In addition, there are limitations related to the spring breaking or yielding when the external forces become too large.

A different class of nonlinear springs are those with negative linear stiffnesses, which are usually characterized by a bi-stable configuration. Cottone et al [2] describe a nonlinear spring implemented by an inverted pendulum with a tip magnet that faces an opposing static magnet. For a small enough gap between the magnets, the cantilever has two equilibriums. For small base input accelerations, the tip magnet oscillates linearly about one of the equilibriums. For large enough accelerations, the tip magnet cycles between the two equilibriums. Thus, if the ambient accelerations are sufficiently large, the device can resonate in the presence of noise.

As described in [3], nonlinear springs may be physically implemented by helical springs with thickening coil wires or changing overall diameters. Another way to achieve nonlinear

behavior is by employing multiple linear components that interact more strongly the further they deflect. For example, in the leaf springs of automobile suspensions, several layers of arc-shaped spring steel are clamped together. As the center of the upper arc deflects, it contacts the arc below it, and both springs further deflect in contact. As more and more arcs deflect, the spring effectively stiffens. However, the many arcs of the leaf spring result in a lot of friction [3].

Mann and Sims [10] describe an oscillator that is implemented by a magnet sliding in a tube with two opposing magnets as the end caps. This configuration causes the stiffness to be the summation of a linear and cubic component. Altering the magnet spacing affects the linear term but not the nonlinear term. Consequently, while the ratio of the nonlinear stiffness to linear stiffness can be adjusted, the linear stiffness cannot be completely removed. Another disadvantage of this device is that it loses energy to friction as the center magnet slides along the tube.

In [4], an ultra-wide bandwidth resonator is made out of a doubly-clamped piezoelectric beam. The double-clamps cause the cantilever to stretch as it bends, resulting in a nonlinear stiffness. However, the beams also have a linear stiffness. The linear stiffness is negligible compared to the nonlinear stiffness when the beam's residual stiffness is minimized. Thus, the linear stiffness component can never completely be removed, and efforts to minimize the linear stiffness component hinder the system optimization.

In all of the the aforementioned devices there are important limitations having to do with factors such as large friction, large volume, many parts which reduce the overall lifetime, or important linear stiffness components that cannot be removed. The goal of this thesis is the theoretical and experimental study of a new nonlinear spring design for the purposes of energy harvesting that overcomes these limitations. Using a cantilever beam that oscillates between two contact surfaces with carefully selected curvature, this thesis illustrates numerically and experimentally that i) the resulting nonlinear spring has a negligible linearized component, ii) the order of its nonlinearity does not remain constant but increases as the amplitude gets larger, and iii) the spring achieves a theoretically infinite force for a finite displacement. The last property is of crucial importance since it allows the device to act as a typical spring with polynomial nonlinearity for moderate vibration amplitudes and to effectively behave as

a vibro-impact spring for larger amplitudes. Additionally, the spring is designed so that it does not break under large forces- an important feature for applications involving multi-scale load cells.

Chapter 2

Nonlinear Spring Theory

The new nonlinear element is based on a cantilever beam that oscillates between two surfaces of given geometry (i.e. curvature). In particular, it is a modification of Timoshenko's design [22] that consists of a cantilever that wraps along a surface as it bends (Figure 2-1). Timoshenko investigates a spring for which the surface has a constant radius of curvature (i.e. a quadratic shape). In this case the cantilever-quadratic surface spring behaves linearly until a critical force is applied (see below for details). Above the critical force, the cantilever-quadratic surface spring behaves nonlinearly. However, during the initial regime (whose extent cannot be reduced), the spring resonates primarily with a single dominant frequency and therefore suffers from the lack of robustness that characterizes linear systems.

This project employs a contact surface with variable curvature along its length and demonstrates that this modification can substantially change the behavior of the nonlinear element. It is well known that the behavior of a free cantilever tip is linear for small displacements or forces, and the cantilever radius of curvature is smallest at the root and infinite (straight beam) at the tip. For this reason, the surface radius of curvature was made infinite at the cantilever's root and decreasing along its length. That is, the second derivative of the surface spatial function equals zero at the root and grows larger along the length. Accordingly, contact between the beam and the surface begins immediately after the application of even a very small force. As proven in this chapter, this choice in surface curvature eliminates the linear regime that characterizes the original Timoshenko design and leads to essentially nonlinear behavior of the element.

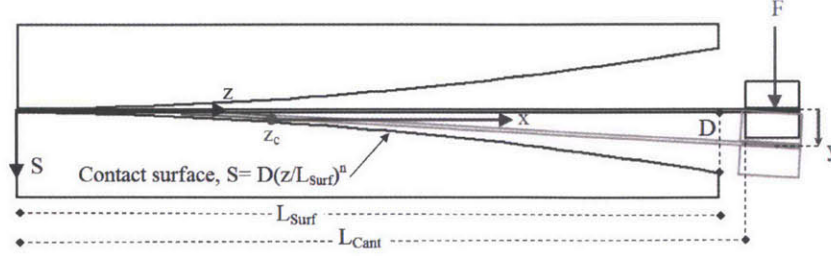


Figure 2-1: Nonlinear spring implemented by a cantilever beam that vibrates between two curved surfaces. The cantilever has length L_{Cant} , second moment of area I , and elastic modulus E . The surface curve has the form $S = D(z/L_{Surf})^n$, where D is the gap between the surface end and undeflected cantilever, and n is an arbitrary power greater than 1. The axial coordinate z is measured from the surface root. The axial coordinate x is measured from the contact point, z_c .

The force versus deflection of both the original design and the proposed one follow the same general derivation, given below. The schematic for both nonlinear springs is shown in Figure 2-1. In the original Timoshenko design for a surface of constant radius, the surface shape has the form:

$$S = D \left(\frac{z}{L} \right)^2 = \frac{z^2}{2R} \quad (2.1)$$

where $D = L^2/2R$ is the gap between the surface and undeflected cantilever at the end of the surface ($z = L$). L is the surface length, R is the surface constant radius of curvature ($1/R = d^2S/dz^2$), and z is the coordinate in the axial direction along the surface. To achieve the desired infinite-valued curvature at the root of the beam, the surface shape is given the form:

$$S = D \left(\frac{z}{L} \right)^n \quad (2.2)$$

where D , L , and z are defined in the same way as in eq. 2.1. n is an arbitrary power greater than 2. As described below, this constraint on n ensures that the surface radius of curvature is infinite at $z = 0$ and decreases along its length, which is required to make the spring essentially nonlinear.

The deflection of the cantilever tip, y can be approximated as the sum of three components:

$$y = \delta_1 + \delta_2 + \delta_3 \quad (2.3)$$

The first component, δ_1 , is the beam displacement of the "free" part of the cantilever, i.e. the part of the cantilever that is not in contact with a surface. The tip displacement of this beam segment is found using the Euler-Bernoulli equation:

$$EI \frac{d^4 w}{dz^4} = -q(z) \quad (2.4)$$

where $q(z) = 0$ is the applied load along the beam length, E is the beam elastic modulus, and I is the beam moment of inertia. Integrating eq. 2.4 results in the beam deflection equation:

$$EIw = -\frac{q}{24}x^4 + \frac{c_1}{6}x^3 + \frac{c_2}{2}x^2 + c_3x + c_4 \quad (2.5)$$

where c_i are the constants of integration, and x is measured from the contact point, as shown in Figure 2-1. The boundary conditions for the free cantilever are: clamped at $z = z_c$, so at $x = 0$, the beam has zero displacement and slope: $w(0) = 0$ and $\frac{dw(0)}{dx} = 0$ (the displacement and slope of the surface are not considered in this component of the displacement). The boundary conditions at the tip of the beam are a point force F and zero-moment: $\frac{d^3 w(L_{free})}{dx^3} = -F/EI$ and $\frac{d^2 w(L_{free})}{dz^2} = 0$. Substituting these boundary conditions into eq. 2.5 results in the following values for the constants of integration:

$$c_1 = -F; \quad c_2 = FL_{free}; \quad c_3 = c_4 = 0 \quad (2.6)$$

Therefore, the resulting deflection component at the tip is:

$$\delta_1 = \frac{FL_{free}^3}{3EI} \quad (2.7)$$

For the cantilever/surface spring, the free length is given by

$$L_{free} = L - l(S(z_c)) \quad (2.8)$$

where z_c is the contact point of the cantilever with the surface, S is the spatial function of the surface curve, and l is the arc length of the surface from $z = 0$ to $z = z_c$. In Section 2.1 below, we describe in detail the determination of the contact point z_c and arc length of

beam in contact with the surface, $l(S(z_c))$.

The second component of the cantilever tip deflection is due to the cantilever slope at the contact point. Because the cantilever is tangent to the surface while they are in contact, the cantilever slope equals the surface slope at the contact point. This angle at the contact point causes the added deflection δ_2 at the cantilever tip:

$$\delta_2 = \frac{dS}{dz} \Big|_{z=z_c} L_{free} \quad (2.9)$$

The third component of the cantilever tip deflection is due to the surface position at the contact point:

$$\delta_3 = S(z_c) \quad (2.10)$$

Combining δ_1 , δ_2 , and δ_3 , the tip deflection due to force F is:

$$y = \frac{FL_{free}^3}{3EI} + \frac{dS}{dz} \Big|_{z=z_c} L_{free} + S(z_c) \quad (2.11)$$

Alternatively, the total deflection, y , can be determined by solving the beam deflection equation eq. 2.5 for the boundary conditions $w(x=0) = S(z_c)$, $\frac{dw(0)}{dx} = S'(z_c)$, $\frac{dw^2(x=L_{free})}{dx^2} = 0$, and $\frac{dw^3(x=L_{free})}{dx^3} = -F/EI$. For these boundary conditions, the integration constants affected by the tip boundaries, c_1 and c_2 remain equal to those given in eq. 2.6. The other constants become $c_3 = \frac{dS}{dz} \Big|_{z=z_c}$ and $c_4 = S(z_c)$.

2.1 Determination of the contact point

The location of the contact point, z_c , along the surface is the point at which the cantilever curvature equals the surface curvature (surface contact condition):

$$\frac{d^2S}{dz^2} \Big|_{z=z_c} = \frac{d^2w}{dz^2} \Big|_{z=z_c} \quad (2.12)$$

where z is the axial coordinate along the surface.

This is the case because the curvature of a free cantilever decreases (i.e. the cantilever gets flatter) along its length, while the surface curvature increases along its length (i.e. the

surface gets rounder). z_c is the point where the surface would no longer prevent the natural deflection of the free cantilever. Alternatively, at z_c , the curvature at the root of a free cantilever of length L_{free} subject to force F equals the surface curvature to which it is tangent. The boundary condition defined by eq. 2.12 is required because the cantilever is tangent to the surface at the contact point. Also, for static equilibrium, the beam curvature equals the surface curvature (beam curvature is continuous) because no external moment is applied.

The curvature at the root of a free cantilever is:

$$\frac{d^2w}{dz^2} = \frac{F}{EI}L_{free} \quad (2.13)$$

where L_{free} is the free cantilever length. Substituting eq.s 2.2 and 2.13 into eq. 2.12:

$$n(n-1)D\left(\frac{z_c}{L}\right)^{n-2} = \frac{F}{EI}L_{free} \quad (2.14)$$

The free cantilever length is defined as: $L_{Free} = L_{Cant} - l(S(z_c))$, where L_{Cant} is the entire cantilever length and $l(S(z_c))$ is the arc length of the cantilever segment in contact with the surface. This assumes that the cantilever segment in contact with the surface follows the surface curve exactly and does not detach from the surface. Therefore, the length of cantilever in contact with the surface is equal to the arc length of the surface. The arc length of the surface from $z = 0$ to z_c is:

$$l(S(z_c)) = \int_0^{z_c} \sqrt{1 + \left(\frac{dS}{dz}\right)^2} dz. \quad (2.15)$$

For small deflections, one can assume that $(dS/dz)^2 \ll 1$. Then, $l(S(z_c)) = z_c$ and $L_{Free} = L - z_c$. In this context, eq. 2.14 takes the form

$$n(n-1)D\left(\frac{z_c}{L}\right)^{n-2} = \frac{F}{EI}(L - z_c) \quad (2.16)$$

For $n = 2$ Timoshenko's original design is recovered (see next subsection) while for larger values of n the contact point has a different behavior.

2.2 Force versus deflection for quadratic and general surfaces

If the spring uses Timoshenko's quadratic surface ($n = 2$) with the spatial equation given by eq. 2.1 and the deflections are small, then eq. 2.16 can be explicitly solved for the contact point z_c :

$$z_c = L - \frac{2DEI}{L^2F} = L - \frac{EI}{RF} \quad (2.17)$$

where the constant radius of curvature $R = L^2/2D$ and the variables are defined as in eq. 2.1. Then, eqs 2.3-2.12 can be combined to find the tip deflection, y , as a function of F :

$$y = \begin{cases} \frac{2}{3\sqrt{3}\alpha\beta}F & \text{if } 0 \leq F \leq \sqrt{3}\alpha \\ \frac{1}{\beta} - \frac{\alpha^2}{\beta F^2} & \text{if } F > \sqrt{3}\alpha \end{cases} \quad (2.18)$$

where $\alpha = EI/\sqrt{3}RL$ and $\beta = 2R/L^2 = 1/D$. The nonlinearity threshold force $F_{crit} = \sqrt{3}\alpha$ was determined by solving eq. 2.13 when $L_{free} = L$ since the cantilever will first begin to wrap around the surface at their root. Solving eq. 2.13 with $L_{free} = L$ shows that $F_{crit} = EI/LR = \sqrt{3}\alpha$. Before contact ($F < F_{crit}$ or $y < 2D/3$), this spring deflects in the same way as a linear cantilever beam. Eq. 2.18 also shows that $y \rightarrow \frac{1}{\beta} = D$ as $F \rightarrow \infty$, which agrees with what is expected to physically happen.

For $n \geq 3$ the cantilever begins to wrap around the surface for any small, non-zero force, a property that causes essentially nonlinear spring behavior. Figure 2-2 shows the contact point variation as a function of the load force for various orders of surface nonlinearity n .

Figure 2-4a shows the force-displacement curve for various orders of contact surface nonlinearity, n . In all cases, the force reaches unbounded values as the critical deflection value D is approached- a property of particular importance for design of nonlinear elements that can withstand extreme loads (e.g. load cells). The surface curvature defines the smoothness of the transition to very large force values. Specifically, for small values of n , the spring force suddenly blows up very close to the critical value of deflection, D . For larger values of n , there is a smooth transition to the blow-up regime that is also associated with negligible linear stiffness for very weak forces.

Figure 2-4b shows the spring force versus deflection with a logarithmic force scale. For a typical essentially nonlinear spring with polynomial nonlinearity, the slope of the log of the reaction force is constant. In the proposed design, the slope of the log of the reaction force increases, signifying that the order of the nonlinearity increases continuously with increasing deflection. This feature of variable order of nonlinearity is inherently connected with the theoretical blow-up of the reaction force for finite-displacement. This feature allows the proposed nonlinear element to behave as an essentially nonlinear spring for moderate excitation forces and as a vibro-impact element for very large excitation forces. The physical reason for this blow-up is that at large enough forces, the cantilever fully wraps around the surface, and the tip cannot deflect any further.

The stiffness of the spring at a given force is closely related to the contact point between the cantilever and surface at that force. As shown in Figure 2-3, all of the springs have contact point $z_c/L_{Surf} = 0$ when deflection $y/D = 0$, and $z_c/L_{Surf} = 1$ when deflection $y/D = 1$. The figure also shows that for larger n , the value of the contact point in between $y/D = 0$ and $y/D = 1$ is larger than the contact point of a smaller n surface at the same y/D value. For the z_c/L_{Surf} versus y/D curves to have these three qualities, the slope of the curve for a larger- n -surface must be larger for small y/D values and smaller for large y/D values. This makes sense because the interference of the surface with the cantilever's deflection depends on the surface curvature. As n increases, the shape of the surface (with all other parameters equal) is flatter near the root and rounder near the tip. Where the surface is flatter (large n , near root), the contact point increases more for a given increase in tip deflection. Where the surface is rounder (small n , near the tip), the contact point increases less for the same increase in tip deflection.

One can think of the spring stiffness as the stiffness of the free cantilever length. Regardless of the surface n value, all cantilevers have the stiffness of a full-length free cantilever when $F = y = z_c = 0$ because the cantilever is unaffected by the surface. All cantilevers approach infinite stiffness for large forces ($F \rightarrow \infty$ when $y/D \rightarrow 1$ and $z_c/L_{Surf} \rightarrow 1$) because the cantilever fully wraps around the surface: the free cantilever length is zero. As described in the paragraph above; for in-between force values, the free cantilever length shortens at varying rates for different n .

For larger n surfaces and small deflections, y/D ; the rate of change in the contact point, z_c/L , for increasing y/D is larger than that of a smaller n surface. This means that at a given [small] y/D value, a larger n spring has a shorter free cantilever length and is stiffer—so at a given [small] force F , the larger n spring has deflected by a smaller amount. For larger n surfaces and large deflections, y/D ; the opposite is true: the rate of change in the contact point, z_c , (i.e. rate of change in free cantilever length) for increasing y/D is smaller than that of a smaller n surface. This means that at a given [large] force F , as the cantilever deflects, the stiffness of a larger n spring does not increase as much as a smaller n spring.

In summary, for larger n surfaces: the spring is stiffer than smaller n surfaces for small applied forces. The spring is weaker than smaller n surfaces for large applied forces. The spring stiffnesses always blow up to infinity for very large forces. The rate of blow up is slower for larger n surfaces at those large forces.

The relationship of the contact point, deflection, and spring stiffness for varying n described above is in agreement with Figures 2-2 to 2-5.

Apart from dependence on the contact surface nonlinearity, n , the resulting force versus deflection curve also depends on several adjustable parameters: cantilever length, L , cantilever rigidity EI , and surface maximum deflection D . This dependence is briefly explained below: As shown in Figure 2-3, the relationship between contact point/surface length and displacement/maximum surface gap is independent of L , EI , and D .

When a given displacement/surface gap results in a specific contact point/surface length, the resulting free cantilever length is $L_{Free} = L(1 - z_c/L)$, where it is assumed that $L = L_{Cant} = L_{Surf}$. While the fraction L_{Free}/L_{Total} remains the same for a given deflection, y/D ; the effective cantilever has a longer dimensionalized length and is therefore a weaker spring. Consequently, a longer cantilever length results in a weaker spring for all force values. Similarly, the resulting free cantilever is more rigid when EI is larger, so a cantilever with a larger EI results in a spring that is stiffer for all force values.

For larger maximum surface gap D values, a cantilever can deflect to a larger value, y before the surface interferes with its deflection. Thus, a spring with a larger maximum surface gap, D , is weaker.

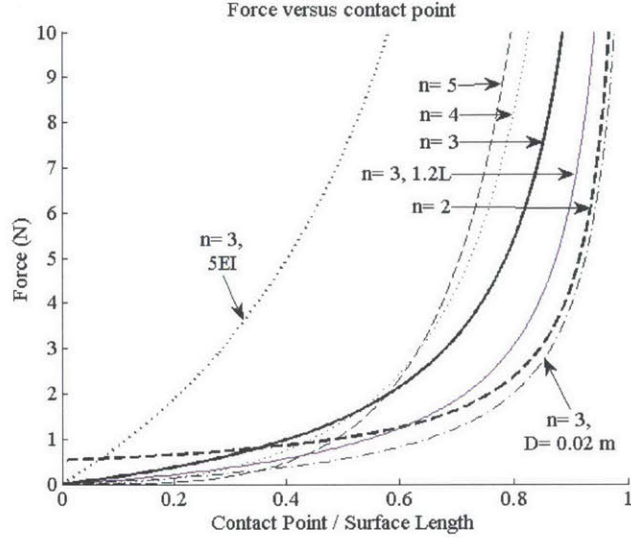


Figure 2-2: Tip force versus contact point (normalized by surface length) for varied spring parameters. These plots are for a spring with the following constant parameters: cantilever height $h = 0.032in$, cantilever base $b = 0.1875in$, cantilever length $L = 15.7cm$, elastic modulus $E = 160.6MPa$, maximum surface gap $D = 3cm$. The surface curvature is varied by changing the value of n in the surface spatial function $S = D(x/L)^n$. The circle in the $n = 2$ curve is when contact between the cantilever and surface begins.

2.3 Safety factor against yield

For the spring to have a long life, it needs a sufficient safety factor against yield, $SF = \sigma_{max}/\sigma_{yield}$, where σ_{max} is the maximum stress in the spring's cantilever and σ_{yield} is the cantilever material's yield stress. In vibration applications, for example, a safety factor against yield of 2 allows the oscillator to have a near-infinite fatigue life. The stress in a cantilever in pure bending is:

$$\sigma = -Ec \frac{d^2y}{dz^2} \quad (2.19)$$

That is, stress in the cantilever is proportional to its curvature. As described in section 2.1, for a given applied tip force, the maximum cantilever curvature occurs at the contact point, and at this point, the cantilever curvature, $\frac{d^2w}{dz^2}$, equals the surface curvature, $\frac{d^2S}{dz^2}$. The surface curvature, $\frac{d^2S}{dz^2}$, increases along the surface length. Also described in section 2.1, the value of the contact point, z_c , increases with larger applied tip force. Therefore, when larger forces are applied, the maximum curvature (and normal stress) in the cantilever is both larger and occurs at larger z values.

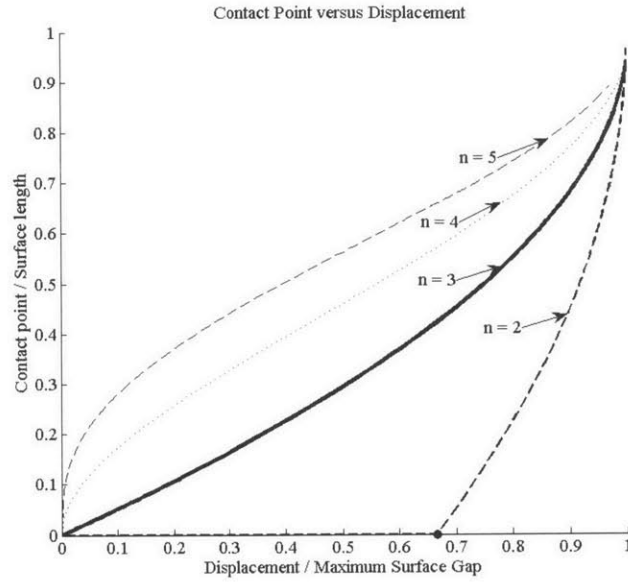
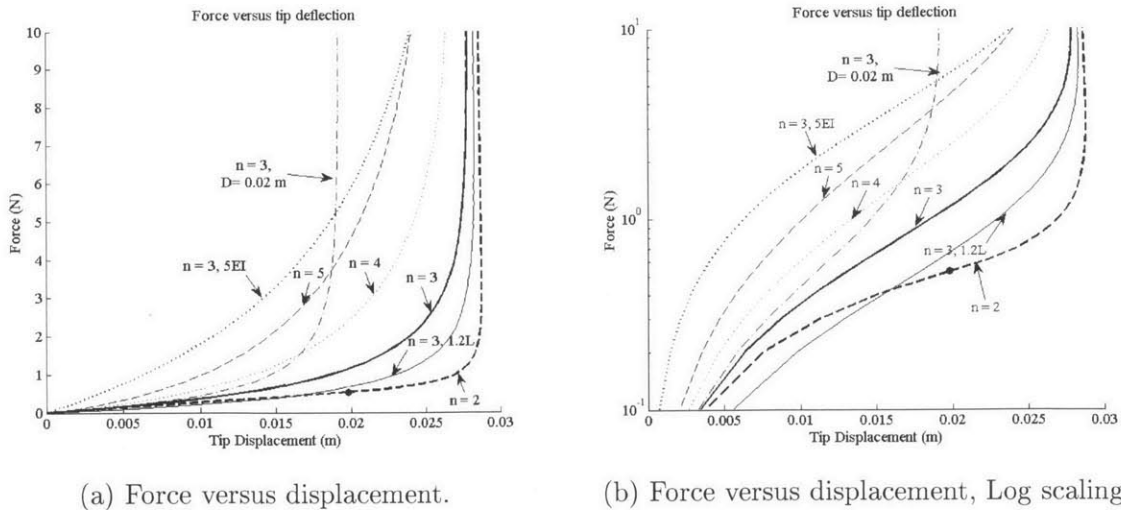


Figure 2-3: Contact point (normalized by surface length) versus tip displacement (normalized by maximum surface gap, D) for varied spring parameters. The surface curvature is varied by changing the value of n in the surface spatial function $S = D(x/L)^n$. The circle in the $n = 2$ curve is when contact between the cantilever and surface begins. These curves are independent of the cantilever length, cross-section and elastic modulus, and the surface length and maximum surface gap, D . These curves assume that the maximum surface gap is small (they do not account for arc length) and $L_{Surf} = L_{Cant}$.



(a) Force versus displacement.

(b) Force versus displacement, Log scaling.

Figure 2-4: These plots are for a spring with the following parameters: cantilever height $h = 0.032in$, cantilever base $b = 0.1875in$, cantilever length $L = 15.7cm$, elastic modulus $E = 160.6MPa$, maximum surface gap $D = 3cm$. The surface curvature is varied by changing the value of n in the surface spatial function $S = D(x/L)^n$. The circle in the $n = 2$ curve is when contact between the cantilever and surface begins.

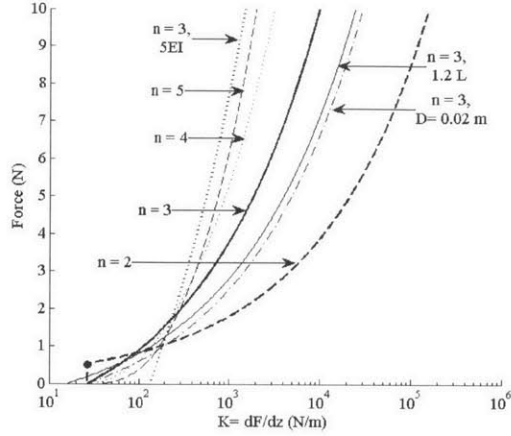
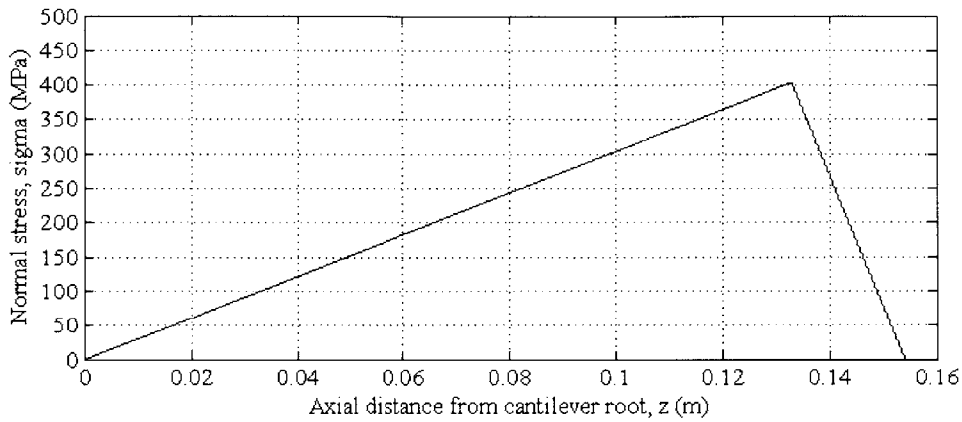


Figure 2-5: Tip force versus spring stiffness for varied spring parameters. These plots are for a spring with the following constant parameters: cantilever height $h = 0.032in$, cantilever base $b = 0.1875in$, cantilever length $L = 15cm$, elastic modulus $E = 160.6MPa$, maximum surface gap $D = 3cm$. The surface curvature is varied by changing the value of n in the surface spatial function $S = D(x/L)^n$. The circle in the $n = 2$ curve is when contact between the cantilever and surface begins.

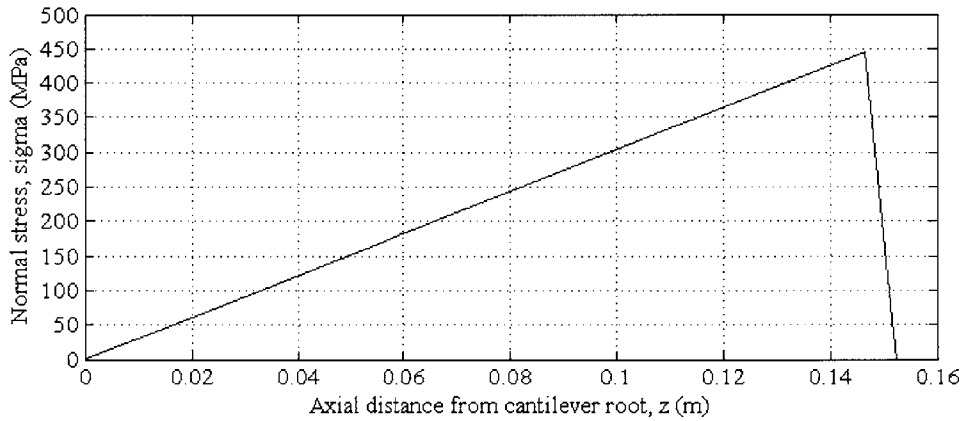
This relationship between contact point location, stress, and applied tip force is illustrated in Figure 2-6.

The largest stress in the cantilever occurs when the contact point is at the surface end, $z_c = l_{surf}$; that is, when the cantilever tip is deflected to the maximum value, D (assuming that the fully-deflected cantilever does not overhang the surface).

Since the largest stress in the cantilever for any applied force is proportional to the maximum surface curvature, one can design the spring to meet a safety factor against yield by setting the maximum surface curvature, $\left. \frac{d^2S}{dz^2} \right|_{z=L_{Surf}}$ below a certain value.



(a) Normal stress along cantilever. Force applied, $F = 10N$



(b) Normal stress along cantilever. Force applied, $F = 40N$

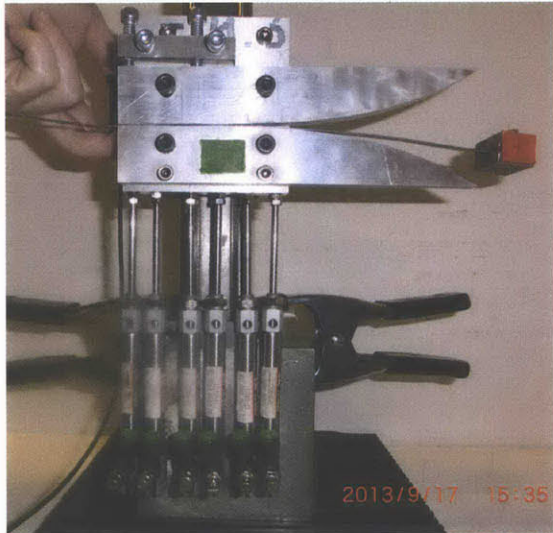
Figure 2-6: Simulated normal stress along the cantilever for different applied forces. The spring had parameters: $L_{cant} = 15.7cm$, elastic modulus $E = 160.6e9Pa$, cantilever base dimension $b = 0.187inches$, cantilever height $h = 0.032inches$, surface length $L_{surf} = 15cm$, surface gap at surface end $D = 3cm$, and surface curve power $n = 3$. The peak in the stress curves occurs at the contact point.

Chapter 3

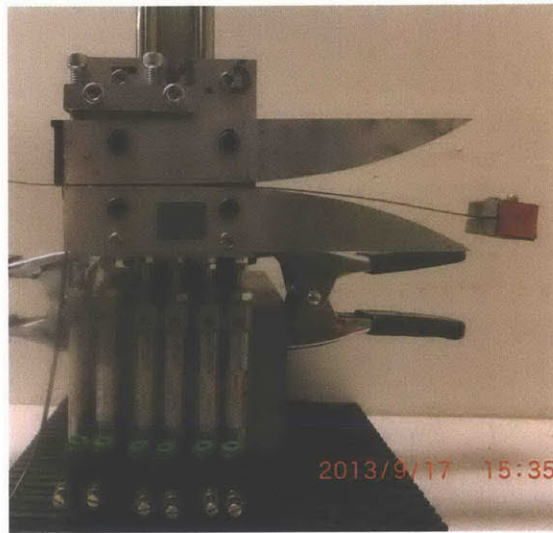
Experimental Verification

The theory was verified by performing static "Force versus Displacement Tests" and dynamic "Initial Displacement Tests". In the initial displacement test, the end-mass attached to the cantilever was given an initial displacement, and the resulting oscillation was video-recorded. Other tests that can be used to verify the energy harvesting theory are the "Single Base Drop Test" and the "Multiple Base Drop Test," for which the entire spring is raised and dropped on a vertical rail one or multiple times, respectively, and the oscillator motion is video-recorded. Exciting the spring in this way simulates real-life energy harvester excitation by human motion (such as the foot or hip rising and falling during walking). The base drop tests were not extensively studied for this thesis, and therefore cannot strongly prove or disprove the theory. However, this section includes these test results to-date to demonstrate the viability of the test set-up for simulating human motion excitation of the energy harvester.

All of the tests were performed on nonlinear springs configured as shown in Figure 3-1. The tests used various cantilevers with lengths ranging from 8.7 cm to 16 cm, heights of 0.4-0.8 mm, and widths of 4.7 to 12.7 mm. The maximum gap between the cantilever and surface ranged from 1 cm to 4.7 cm, and the cantilever overhang from the surface edge ranged from 0-10% the surface length. The end-mass on the cantilever ranged from 25 to 120 g.



(a) Raised set-up for "Base Drop" test



(b) Lowered set-up

Figure 3-1: Dynamic test set-up. For the base drop tests, the entire oscillator slides along the rail. The pneumatic cylinders reduce the table-top impact acceleration. For the initial displacement test, the base cart is clamped to the steel block. Shown here is an oscillator with cantilever length, 15.7 cm; width, 4.8 mm; height, 0.81 mm; spring steel cantilever elastic modulus 160.6 GPa; The contact surface follows the curve $S = D(x/L_{surf})^n$. It has length, $L_{surf} = 15cm$; maximum gap, $D = 3cm$, and curvature power, $n = 3$. The steel end-mass is 60 g.

3.1 Force versus Displacement Test

The force versus displacement experiments were compared to the theoretical force versus displacement curves described in Section 2.2. For springs with small deflections, the tip force versus deflection was measured by using an Admet force tester with a 10 N load cell in compression mode, with a rigid probe applied to the cantilever tip. For springs with large deflections, the Admet force tester was used in tension mode with the 10 N load cell. The cantilever/surface spring was clamped to a horizontal sliding rail, which was clamped to the table. The force was applied using a 10-cm wire with two loops at its ends. One wire end was looped around a nut adhered to the cantilever tip. The other was looped around a hook bolted to the load cell. This configuration was chosen over a traditional rigid force probe so that only a vertical force was applied and measured at the cantilever tip. The tension-mode test set-up is shown in Figure 3-2.

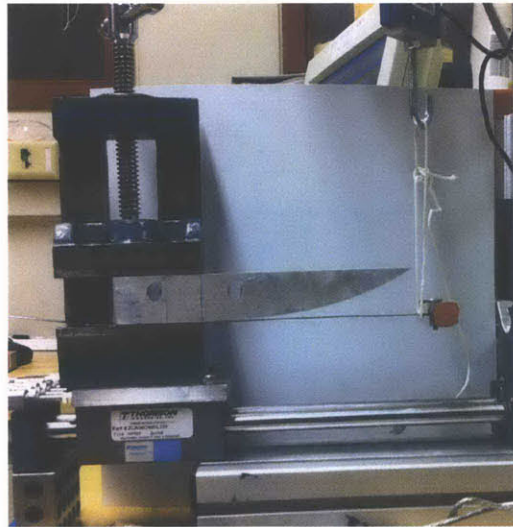


Figure 3-2: Experimental set up of Force versus Displacement test in tension mode. In later versions of the experiment, the string was replaced with a wire.

Figures 3-3 to 3-5 show the test results for springs with surface curve powers $n = 2$, $n = 3$, and $n = 5$. Other spring parameters are listed in the captions. These results verify the theory and are repeatable for a large range of spring parameters.

Some of tests were performed after spreading thin layers of Elmer's Slide-All or Moly-Lithium Grease over the surfaces, which reduce friction between the cantilever and surface.

This was done in order to investigate how friction affects the experimental force versus displacement curves. Additionally, for an energy harvester, it is desirable to minimize friction in order to minimize parasitic losses. Figures 3-4 and 3-5 show that the lubricants had little effect on the force versus displacement curves compared to the tests without the lubricants. For the same reasons, Figure 3-5 shows the test results of surfaces with small sinewave teeth cut along the edge. Figure 3-5 shows that the sinewave teeth did reduce the force required to displace the tip.

For the $n = 3$, $D = 3cm$, $EI = .0341Nm^2$ spring shown in Figure 3-4, the largest error between the experiment and theory occurs for mid-range applied forces. At this force, the experimental displacement exceeds the theoretical displacement by 4.5%. This error, which can be seen in the other springs as well, may be caused by the cantilever slightly lifting off of the surface in between the cantilever root and the contact point (which causes the curvature at the contact point cantilever to be less than theoretically predicted, and therefore less force is required for a given displacement).

These experimental results highlight the singular property of this nonlinear spring: there is a maximum tip displacement for which the force theoretically approaches infinity.

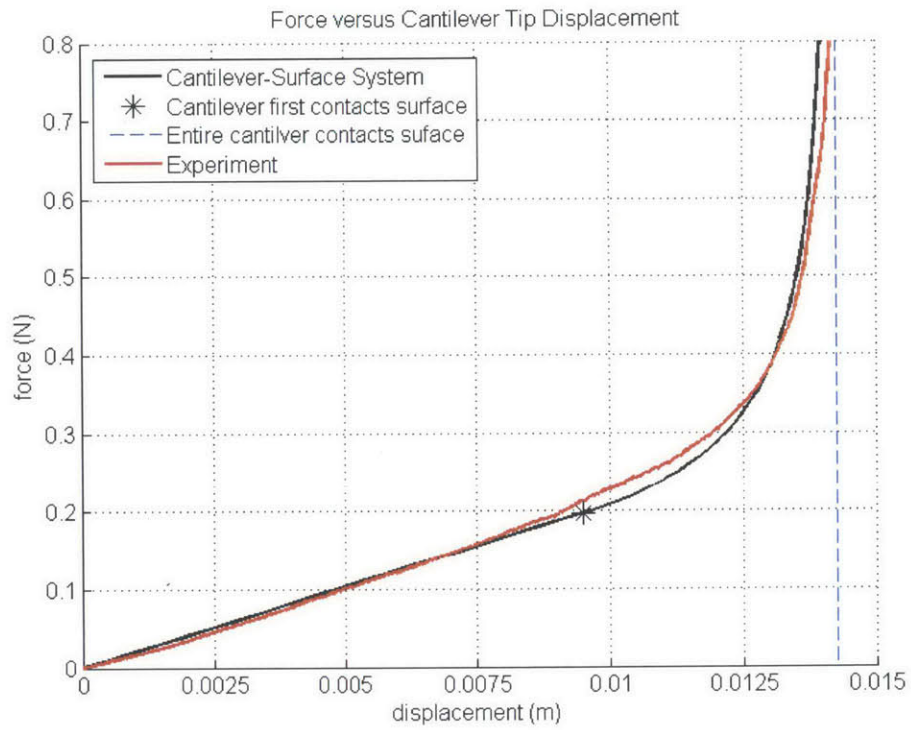


Figure 3-3: Force versus displacement test results for a surface with $n = 2$. Other parameters are cantilever length $L_{Cant} = 17cm$, height $h = 0.8mm$, width $w = 4.7mm$, elastic modulus $E = 190GPa$, surface length $L_{Surf} = 17cm$, surface radius $R = 1m$, maximum surface gap $D = L_{Surf}^2/2R = 1.42cm$.

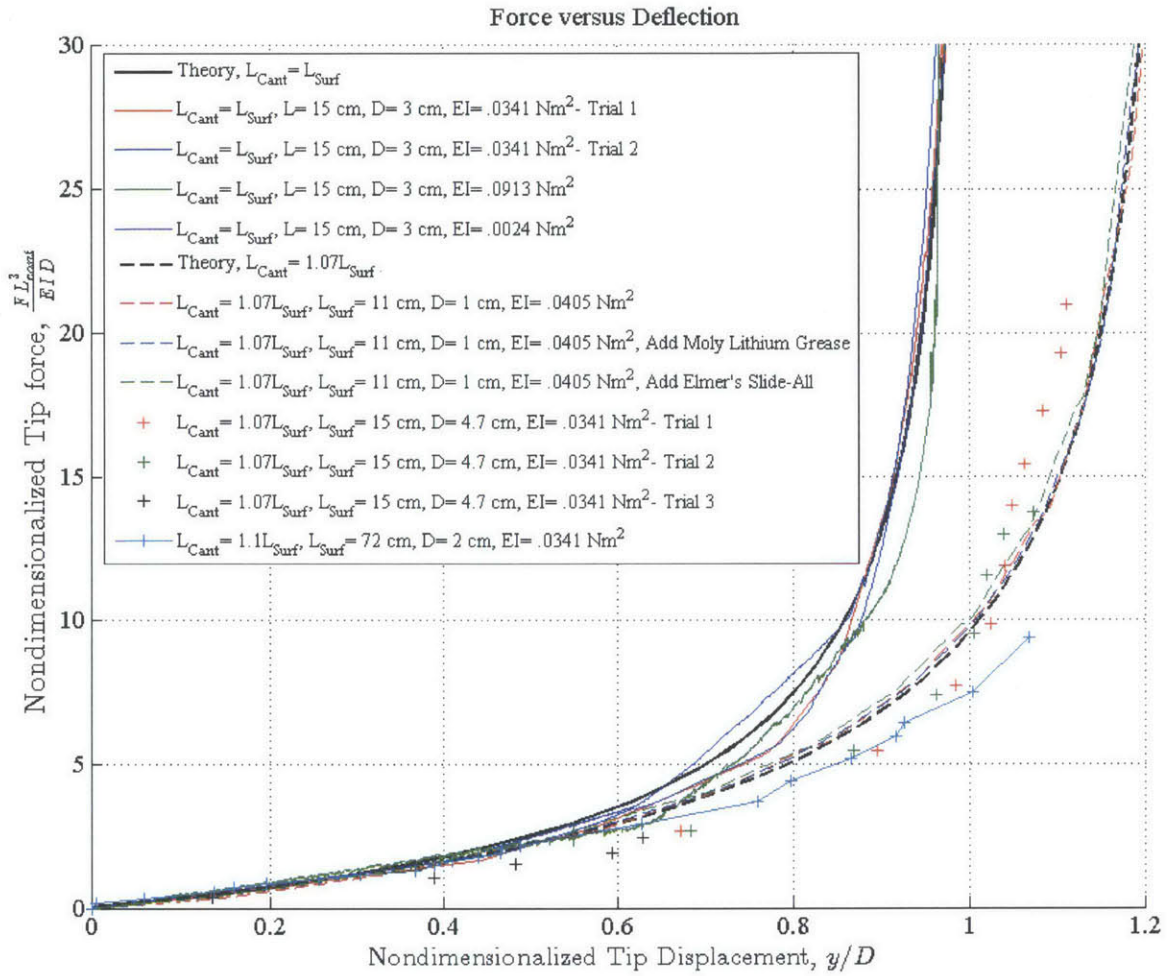


Figure 3-4: Force versus displacement test results for surfaces with $n = 3$.

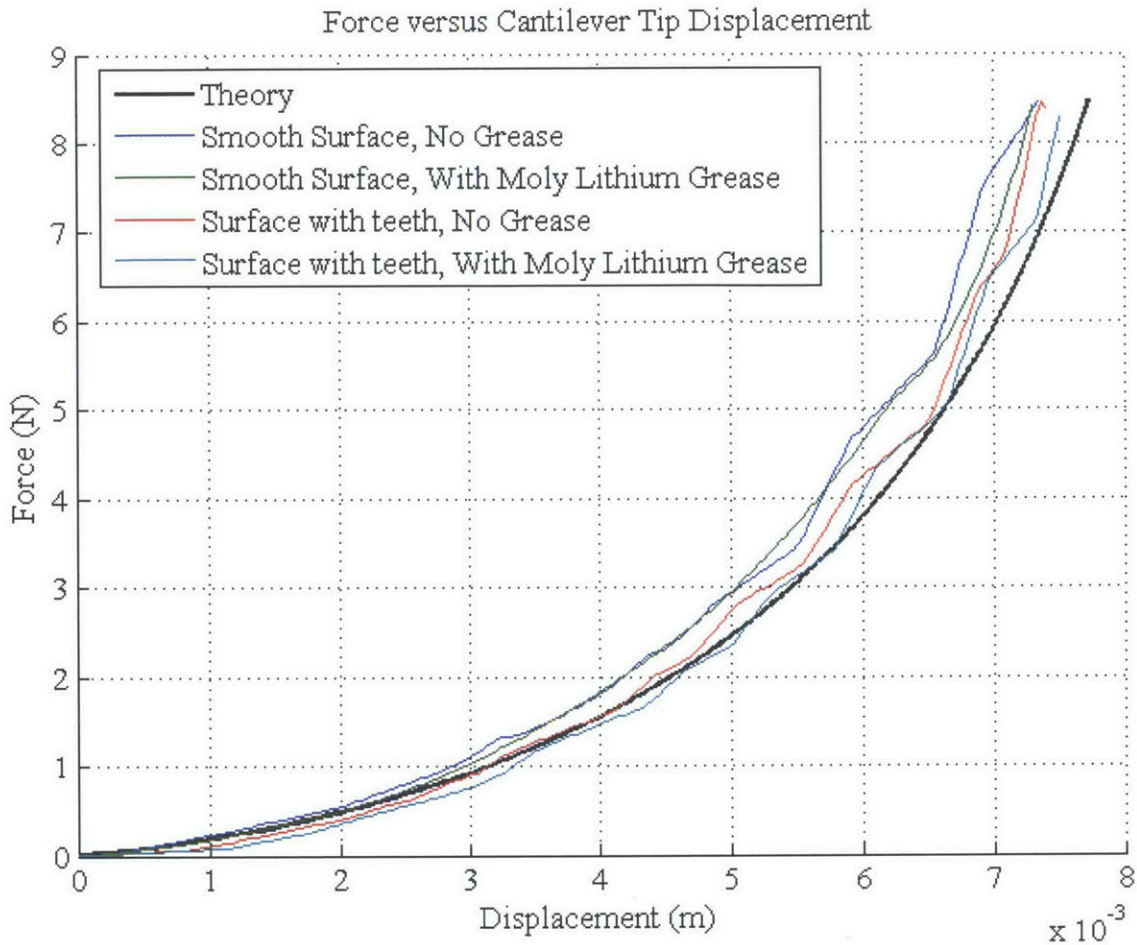


Figure 3-5: Force versus displacement test results for surfaces with $n = 5$. Parameters are cantilever length $L_{Cant} = 11cm$, height $h = 0.8mm$, width $w = 4.7mm$, elastic modulus $E = 190GPa$, surface length $L_{Surf} = 11cm$, maximum surface gap $D = 1cm$. The "surfaces with teeth" labeled in the legend refer to surfaces with 3mm-radius sinewave teeth cut along the edge, which were tested to see if they reduced friction.

3.2 Initial Displacement Test

For these tests, a mass was attached to the nonlinear spring and released from an initial displacement at $t = 0$ seconds. The mass was colored red and its motion was recorded at 480 frames per second with a Samsung TL30 camera. A Matlab program tracked the red object's position in each video frame (the code is given in the Appendix). The damping coefficient was determined by curve-fitting the oscillation amplitude envelope using Matlab

cftool. The mass velocity and acceleration were calculated by numerically differentiating the displacement time series in Matlab. Figures 3-6 to 3-12 show comparisons of the experimental time series and wavelet transforms to the theoretical predictions for three different oscillators. The qualitative trends in the experimental dynamics over time agree well with the theory for the first two tests. The third test does not agree well with the theory, and it is included in this section as an example of the limitations to the theory: that is, too heavy an end mass causes higher modes in the cantilever, which are not accounted for in the theory. These higher modes are not picked up by the camera because even though the end-mass wobbles, the location of center of mass tracked by the camera does not significantly wobble.

The simulation assumes that the cantilever oscillates in its first mode only, so the higher mode frequencies shown in Figure 3-7 reflect the nonlinear effect of the surfaces, rather than the cantilever's higher vibration frequencies. The experimental frequencies are slightly lower than the theoretical frequencies, and this might be a result of the experimental stiffness being slightly lower than the theoretical stiffness for mid-range displacements (see the force versus displacement test results in Figure 3-4).

The simulation models a point mass that equals the end-mass of the experimental oscillator, with linear damping equal to the experimentally-determined damping. The simulation uses the nonlinear spring stiffness predicted in Chapter 2, with a modification so that the deflection of the center of the end-mass is calculated instead of the cantilever tip deflection. This modification is described below.

For a given force, the end-mass deflection is calculated by multiplying half the mass length by the cantilever tip slope. The cantilever tip slope equals the slope of the free cantilever if its root had 0-slope plus the slope at the roots (i.e. the contact point):

$$\frac{dy}{dz} = \frac{FL_{free}^2}{2EI} + \left. \frac{dS}{dz} \right|_{z=z_c}. \quad (3.1)$$

Then, the mass deflection is defined as:

$$y_{mass} = y + \frac{dy}{dz} \frac{L_{mass}}{2}, \quad (3.2)$$

where y is the cantilever tip deflection and L_{mass} is the mass length in the axial direction.

The first system test results are shown in Figures 3-6 and 3-7. This test used the nonlinear oscillator shown in Figure 3-1, and the mass was released from an initial displacement of 3.4 cm. Figure 3-7 includes the constant frequency of a linear oscillator with the same mass and initial energy as the nonlinear spring in the initial displacement experiment.

The initial energy in the nonlinear spring was found by integrating the product of the incremental spring force and tip deflection. That is, the energy in the spring is defined as:

$$E = \int_0^y F(Y) dY \quad (3.3)$$

where Y is a dummy variable, F is the spring force at end-mass displacement Y , and y is the final end-mass displacement.

Using equations 3.1 to 3.3 for the nonlinear spring shown in Figure 3-1 with an end-mass displacement of 3.4 cm, the initial energy in the tested spring was 0.033 J. A linear oscillator with this same displacement and initial energy has a stiffness of $K = 57N/m$. If this linear oscillator had the same mass as the nonlinear oscillator (60 g), then the linear oscillator's natural frequency would be 4.9 Hz. Figure 3-7 shows that the nonlinear spring oscillates with multiple frequencies that exceed that of the linear spring's constant 4.9 Hz.

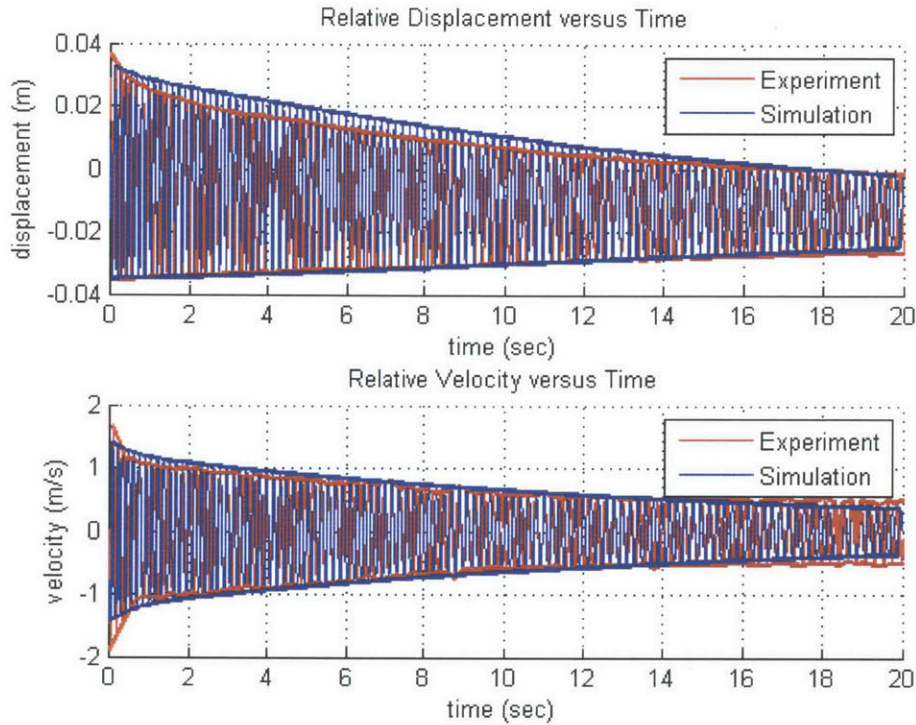


Figure 3-6: Initial displacement test for the first nonlinear oscillator. The system had parameters: $mass = 60g$, $L_{cant} = 15.7cm$, elastic modulus $E = 160.6e9Pa$, cantilever base dimension $b = 0.187inches$, cantilever height $h = 0.032inches$, surface length $L_{surf} = 15cm$, surface gap at surface end $D = 3cm$, and surface curve power $n = 3$. The damping envelope indicated that the viscous damping in the system is 0.007 Ns/m . A photograph of the system is shown in Figure 3-1.

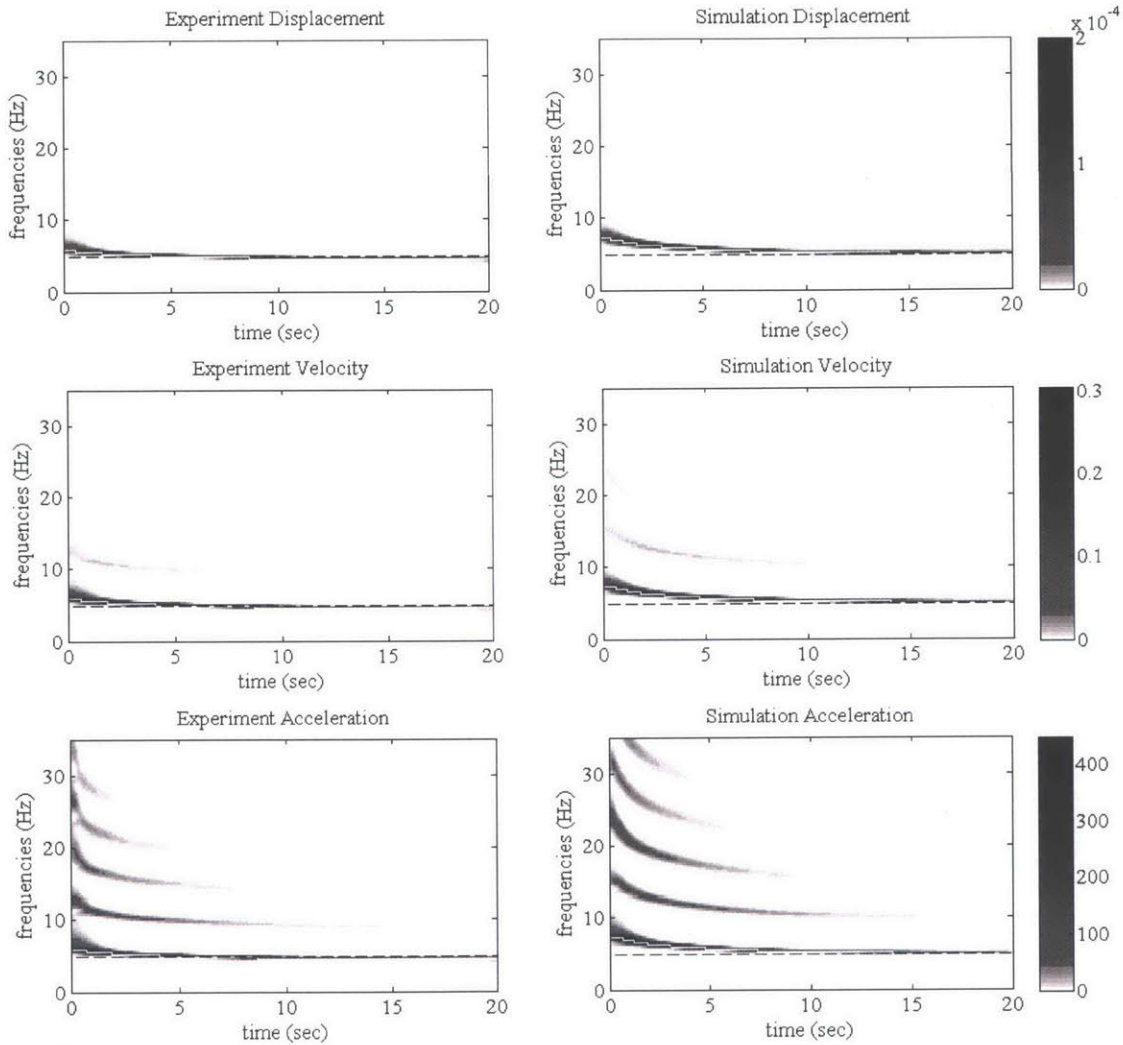


Figure 3-7: Wavelet transforms for the initial displacement test for the first nonlinear oscillator. Left: experiment results. Right: simulation results. The dashed line at $f = 4.9\text{Hz}$ represents the frequency of a linear mass-spring system for which the mass, initial energy, and initial displacement equals that of the cantilever/surface spring system. The cantilever/surface spring system had parameters: $mass = 60\text{g}$, $L_{cant} = 15.7\text{cm}$, elastic modulus $E = 160.6\text{e}9\text{Pa}$, cantilever base dimension $b = 0.187\text{inches}$, cantilever height $h = 0.032\text{inches}$, surface length $L_{surf} = 15\text{cm}$, surface gap at surface end $D = 3\text{cm}$, and surface curve power $n = 3$. The damping envelope indicated that the viscous damping in the system is 0.007Ns/m . A photograph of the system is shown in Figure 3-1.

The initial displacement test was also performed on a system with a shorter cantilever and lighter mass. A photograph of the system [with a mass 5 times heavier than what was used in this test] is shown in Figure 3-10. The test results are shown in Figures 3-8 and 3-9.

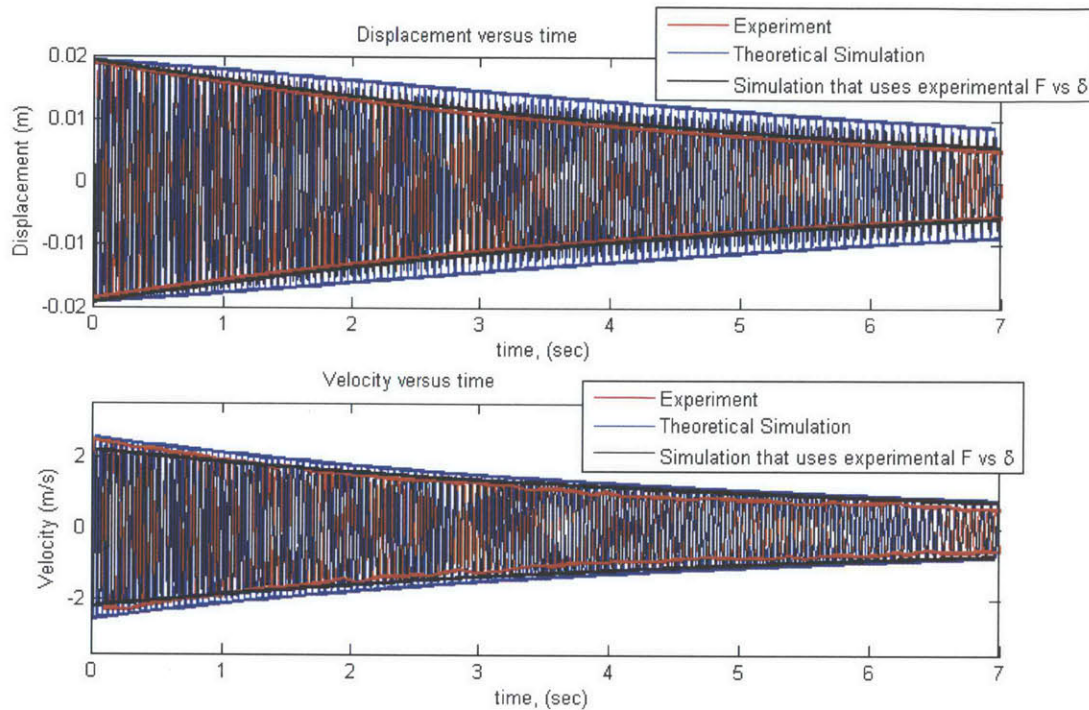


Figure 3-8: Initial displacement test for the second nonlinear oscillator. The system had parameters: $mass = 25g$, $L_{cant} = 8.7cm$, elastic modulus $E = 160.6e9Pa$, cantilever base dimension $b = 0.187inches$, cantilever height $h = 0.032inches$, surface length $L_{surf} = 7.2cm$, surface gap at surface end (if $L_{Surf} = L_{Cant}$) $D = 2cm$, and surface curve power $n = 3$. The damping envelope indicated that the viscous damping in the system is $0.02 Ns/m$. A photograph of the system [with a heavier mass] is shown in Figure 3-10.

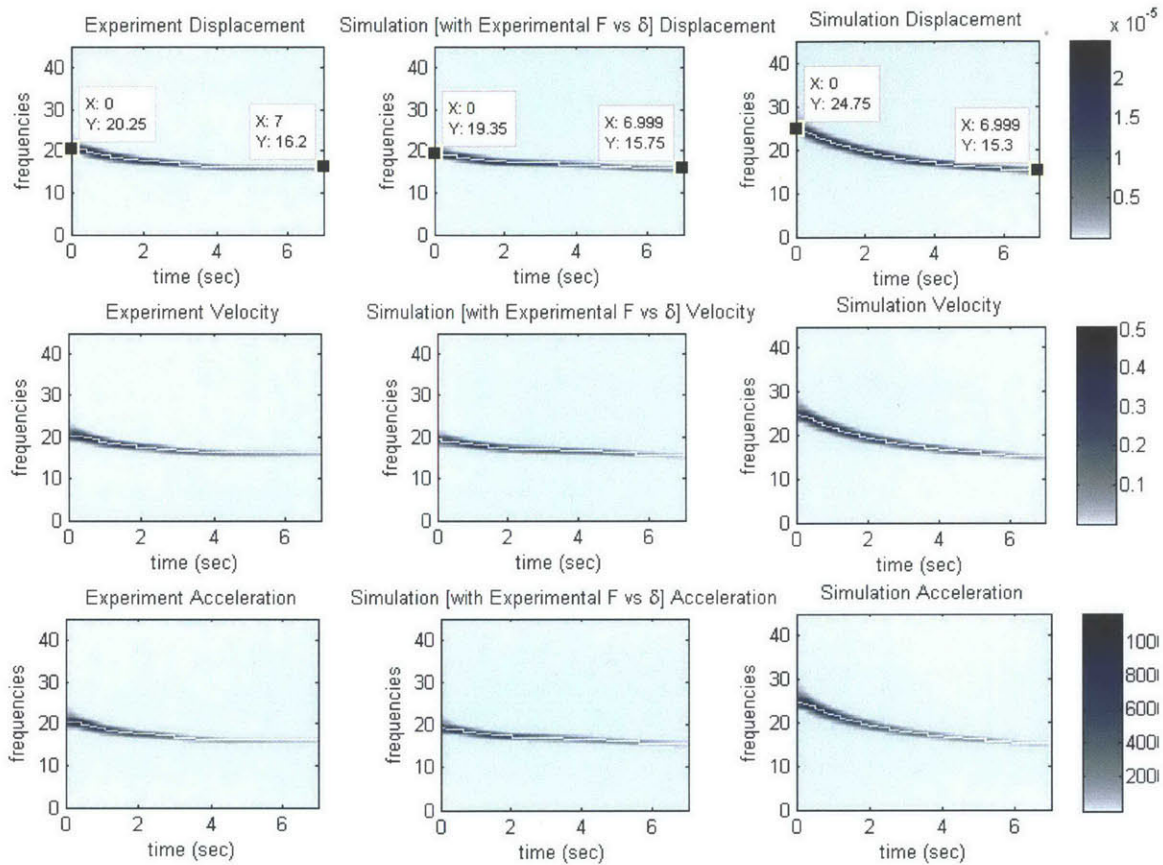


Figure 3-9: Wavelet transforms for the initial displacement test for the second nonlinear oscillator. The system had parameters: $mass = 25g$, $L_{cant} = 8.7cm$, elastic modulus $E = 160.6e9Pa$, cantilever base dimension $b = 0.187inches$, cantilever height $h = 0.032inches$, surface length $L_{surf} = 7.2cm$, surface gap at surface end (if $L_{Surf} = L_{Cant}$) $D = 2cm$, and surface curve power $n = 3$. The damping envelope indicated that the viscous damping in the system is $0.02 Ns/m$. A photograph of the system [with a heavier mass] is shown in Figure 3-10.

The third system tested did not agree with the theory. This system has the same parameters as the system of Figures 3-8 and 3-9, but instead of a 25 g end-mass, it had a 125 g end-mass. The oscillator is shown in Figure 3-10. The results are shown in Figures 3-11 and 3-12.

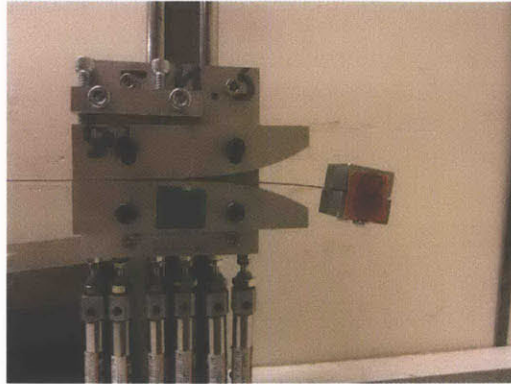


Figure 3-10: Experimental set-up for the initial displacement test of oscillator 3. The spring had parameters: $mass = 120g$, $L_{cant} = 8.7cm$, elastic modulus $E = 160.6e9Pa$, cantilever base dimension $b = 0.187inches$, cantilever height $h = 0.032inches$, surface length $L_{surf} = 7.2cm$, surface gap at surface end (if $L_{Surf} = L_{Cant}$) $D = 2cm$, and surface curve power $n = 3$. The damping envelope indicated that the viscous damping in the system is 0.012 Ns/m.

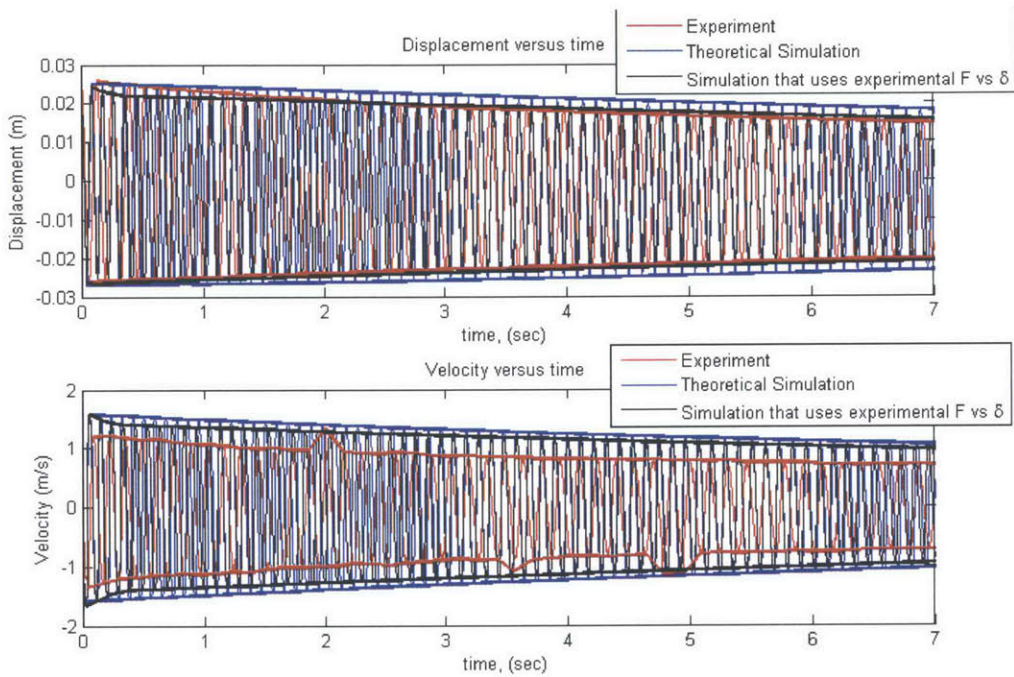


Figure 3-11: Initial displacement test for the third nonlinear oscillator. The system had parameters: $mass = 125g$, $L_{cant} = 8.7cm$, elastic modulus $E = 160.6e9Pa$, cantilever base dimension $b = 0.187inches$, cantilever height $h = 0.032inches$, surface length $L_{surf} = 7.2cm$, surface gap at surface end (if $L_{Surf} = L_{Cant}$) $D = 2cm$, and surface curve power $n = 3$. The damping envelope indicated that the viscous damping in the system is $0.012 Ns/m$. A photograph of the system is shown in Figure 3-10.

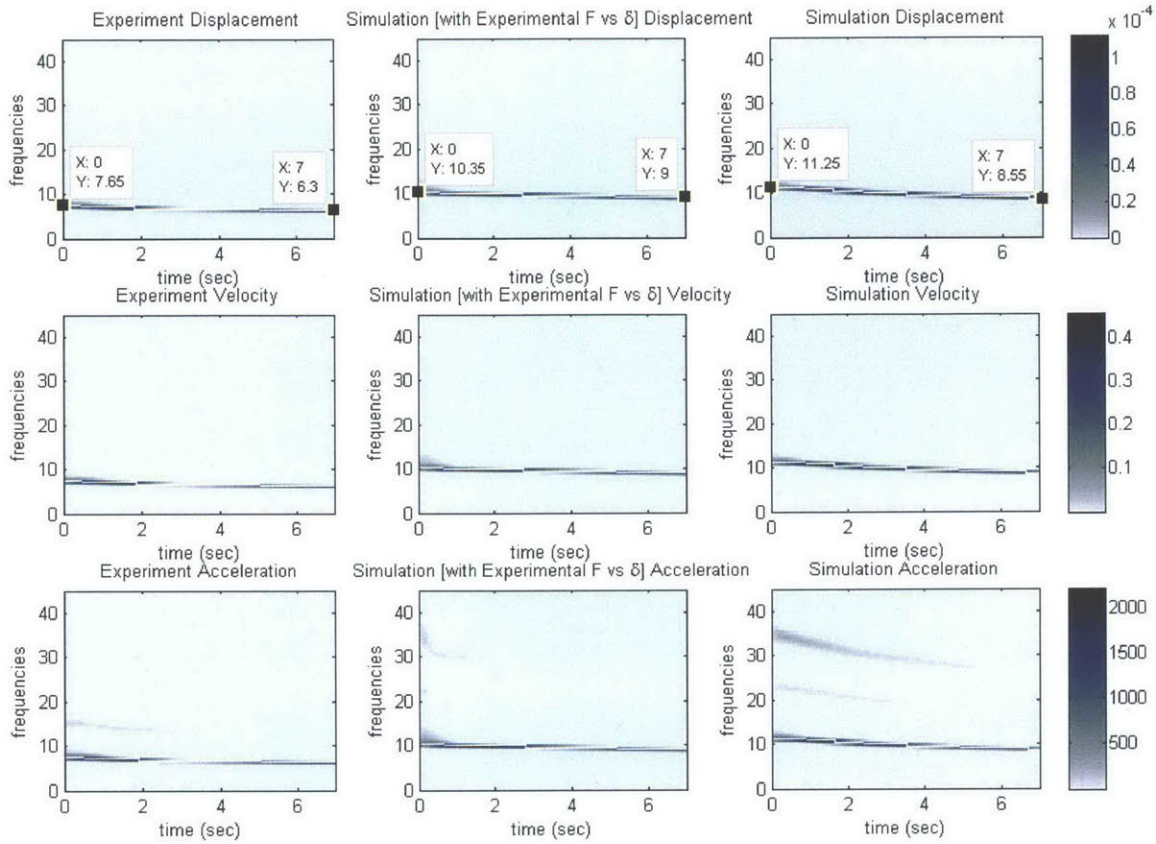


Figure 3-12: Wavelet transforms for the initial displacement test for the third nonlinear oscillator. The system had parameters: $mass = 125g$, $L_{cant} = 8.7cm$, elastic modulus $E = 160.6e9Pa$, cantilever base dimension $b = 0.187inches$, cantilever height $h = 0.032inches$, surface length $L_{surf} = 7.2cm$, surface gap at surface end (if $L_{Surf} = L_{Cant}$) $D = 2cm$, and surface curve power $n = 3$. The damping envelope indicated that the viscous damping in the system is 0.012 Ns/m . A photograph of the system is shown in Figure 3-10.

3.3 Single Base Drop Test

The Base Drop test simulates the vertical motion of a single foot step. The experiment does this by bolting the nonlinear spring surfaces to a cart (the "base") that slides along a near-frictionless vertical rail, as shown in Figure 3-1. The time series of a foot's vertical motion while walking is shown in Figure 3-16. The foot motion was recorded by attaching a Vernier 5-g accelerometer to a person's while she walked, as shown in Figure 4-1. During walking, the foot has a vertical displacement range of 38 cm, maximum velocity of $-1.4m/s$ (right

before ground impact), and maximum acceleration of $-40m/s^2$ (also right before ground impact). A more in-depth description of the human motion dynamics is given in Section 4.1. In the base drop test, the foot's maximum velocity was generated by dropping the oscillator from a height of 10 cm (using kinematics, this is the height required for an object in free-fall to reach a velocity of $-1.4m/s$). The foot's maximum acceleration was generated by engaging pneumatic cylinders at the oscillator's impact. The pneumatic cylinders decrease the oscillator's deceleration (as opposed to rigidly hitting the table-top). The rate of deceleration can be adjusted by changing the size of the air nozzle in the cylinders.

As was done for the initial displacement test, the experiment was recorded at 480 frames per second with a Samsung TL30 camera. The mass was colored red, and the base was colored green. A Matlab program (given in the appendix) tracked the red and green objects' positions in each video frame. The damping coefficient was determined by curve-fitting the oscillation amplitude envelope from an initial displacement test using Matlab cftool. The mass velocity and acceleration were calculated by numerically differentiating the displacement time series in Matlab. The base acceleration was recorded using a Vernier 25-g accelerometer. In order to minimize noise, the base motion plots show the base acceleration directly recorded by the accelerometer, base velocity calculated by numerically integrating the acceleration, and base displacement that was directly recorded by the camera.

The experimental time series and wavelet transforms are shown in Figures 3-13 to 3-15. The experiment and theory somewhat agree.

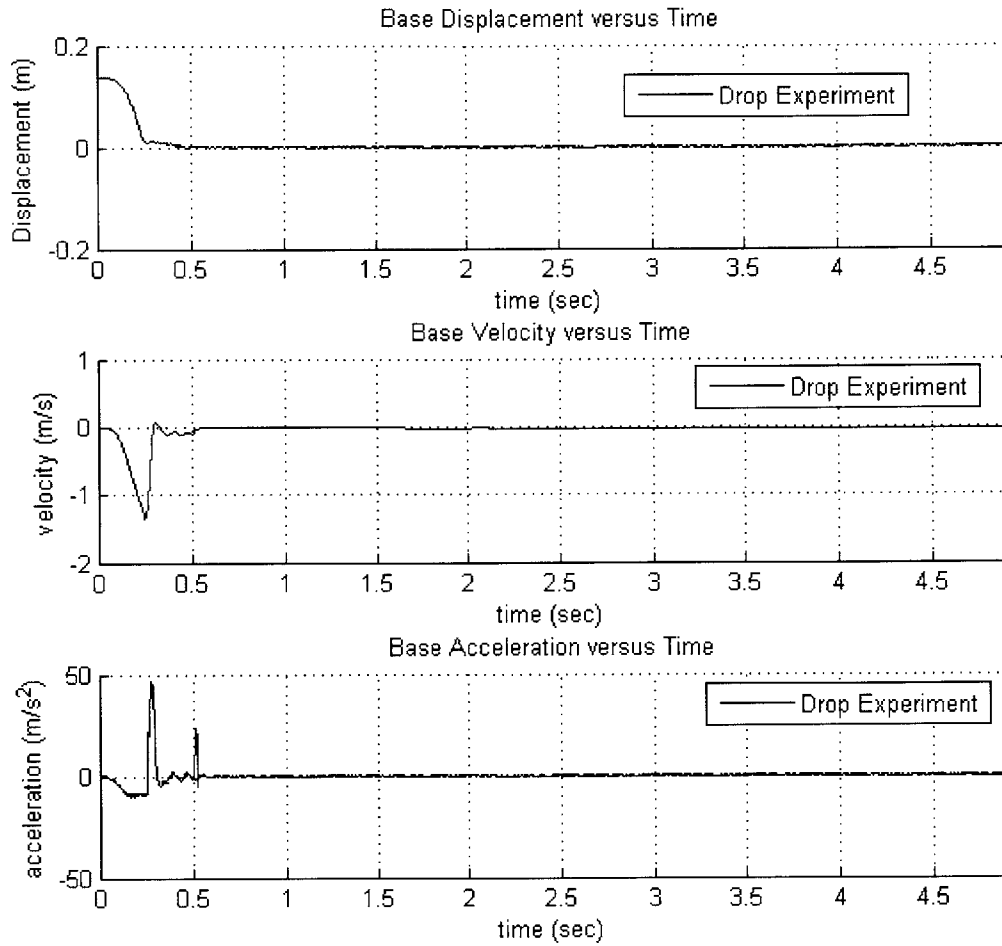


Figure 3-13: Base motion time series for base drop test. The base was raised to a height of 10 cm and dropped so that the pneumatic cylinders compressed upon contact with the table. The experimental set-up (for a nonlinear spring with different parameters) is shown in Figure 3-1.

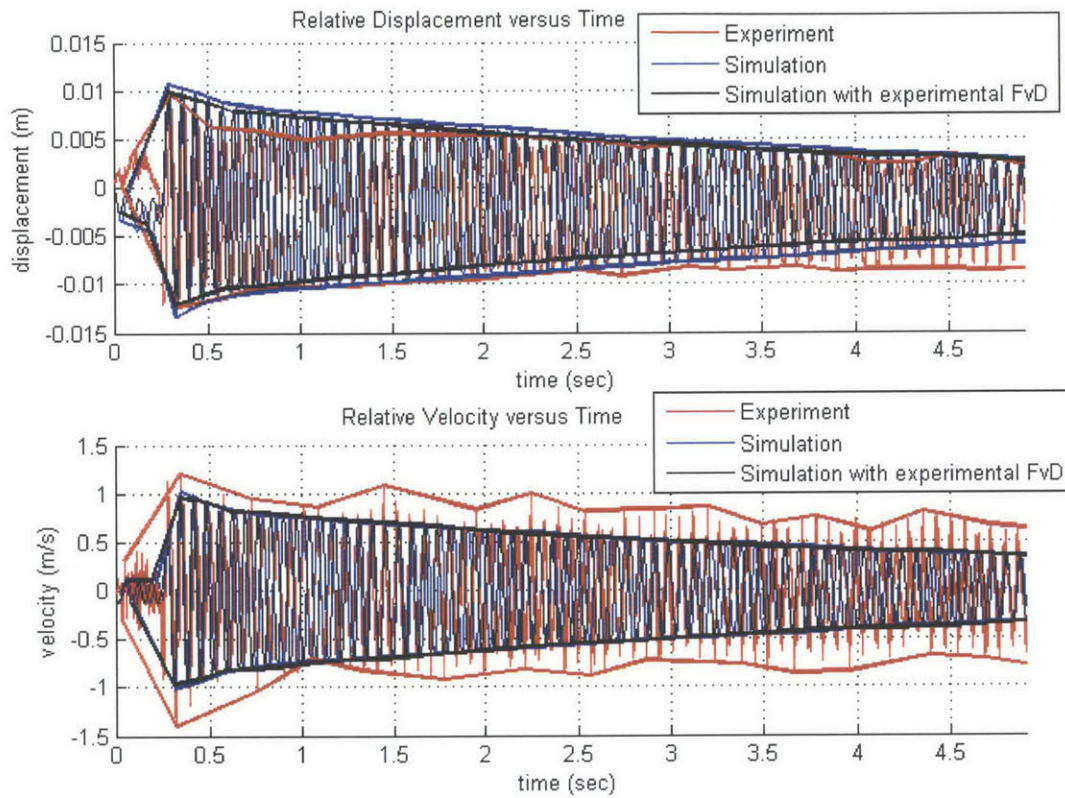


Figure 3-14: Mass motion time series for the base drop test, oscillator 2. The system had parameters: $mass = 25g$, $L_{cant} = 8.7cm$, elastic modulus $E = 160.6e9Pa$, cantilever base dimension $b = 0.187inches$, cantilever height $h = 0.032inches$, surface length $L_{surf} = 7.2cm$, surface gap at surface end (if $L_{Surf} = L_{Cant}$) $D = 2cm$, and surface curve power $n = 3$. The damping envelope indicated that the viscous damping in the system is $0.02 Ns/m$. A photograph of the system [with a heavier mass] is shown in Figure 3-10.

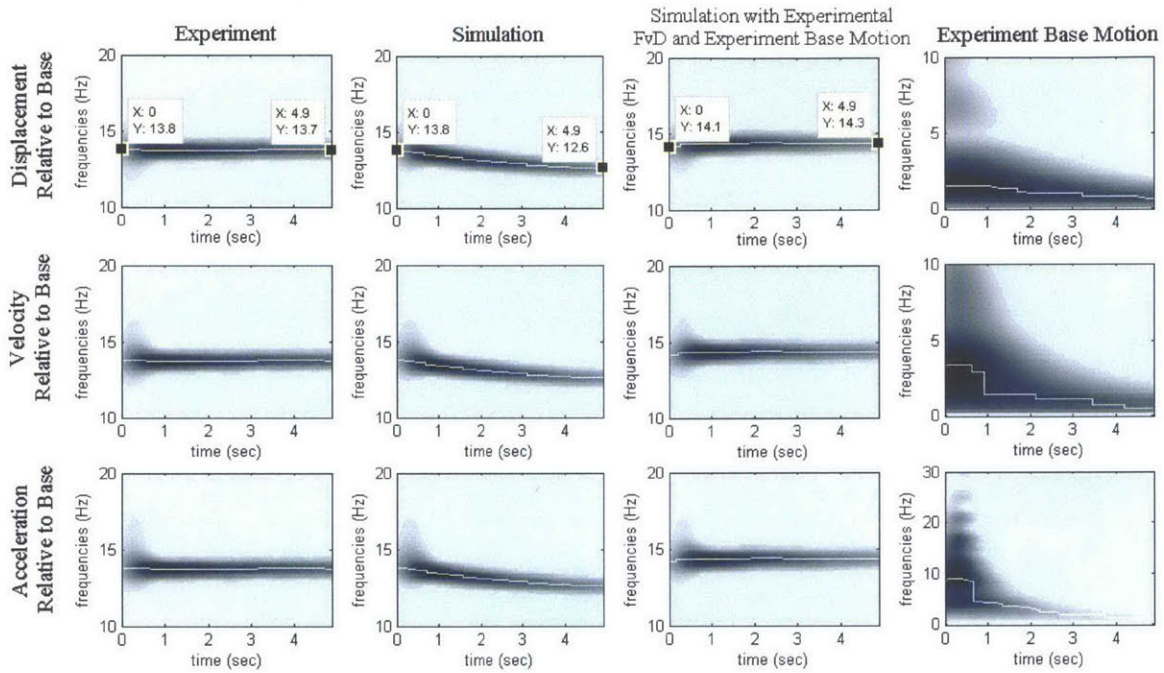


Figure 3-15: Wavelet transforms for the base drop test, oscillator 2. The system had parameters: $mass = 25g$, $L_{cant} = 8.7cm$, elastic modulus $E = 160.6e9Pa$, cantilever base dimension $b = 0.187inches$, cantilever height $h = 0.032inches$, surface length $L_{surf} = 7.2cm$, surface gap at surface end (if $L_{Surf} = L_{Cant}$) $D = 2cm$, and surface curve power $n = 3$. The damping envelope indicated that the viscous damping in the system is $0.02 Ns/m$. A photograph of the system [with a heavier mass] is shown in Figure 3-10.

3.4 Multiple Base Drop Test

The "Multiple Base Drop Test" was performed in the same way as the "Single Base Drop Test" (see Section 3.3 for a description of the experimental procedure and Figure 3-1 for a picture of the set-up). For this experiment, instead of manually lifting and dropping the oscillator once, it was manually lifted and dropped multiple times at a rate of roughly one drop per second, which matches the frequency of one foot while walking. The experimenter quickly raised the oscillator to the peak height by aligning the top of the cart to a marker line on the rail with one hand and extending the pneumatic cylinders with the other hand. Although manually lifting and dropping the oscillator is not a precise technique, the non-uniformity of the excitation signal is similar to the non-uniformity of actual human motion. The experiment does not require high precision and accuracy in the excitation signal.

Figure 3-16 shows that the cart's experimental peak velocity and acceleration agree well with the foot's actual walking peak acceleration and velocity. Figures 3-17 and 3-18 show the experimental mass time series and wavelet transform. The experimental oscillator relative motion does not agree well with the simulated oscillator motion (the simulation used the experimental base acceleration). The reason for this discrepancy might be errors in the experimentally-measured damping, spring stiffness (e.g. the elastic modulus), and mass (e.g. a scale with low precision).

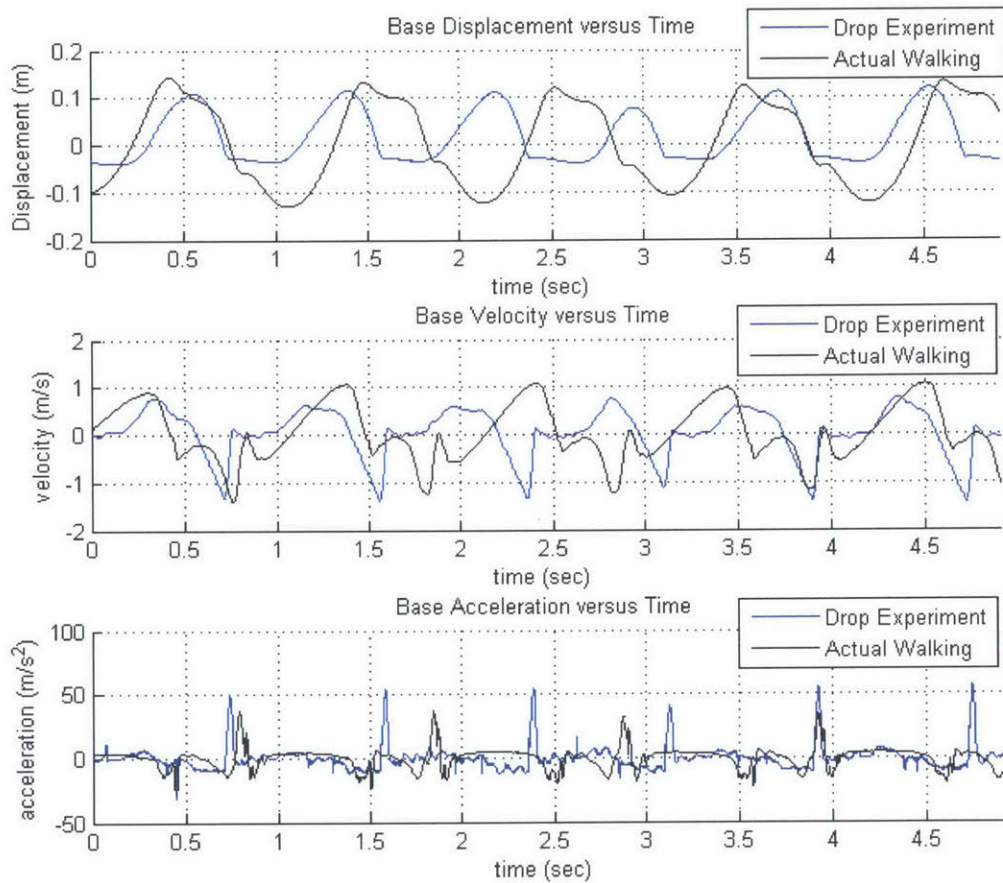


Figure 3-16: Base motion time series for the multiple base drop experiment. The base was repeatedly raised to a height of 10 cm and dropped so that the pneumatic cylinders compressed upon contact with the table. The motion is compared to the actual foot motion while walking.

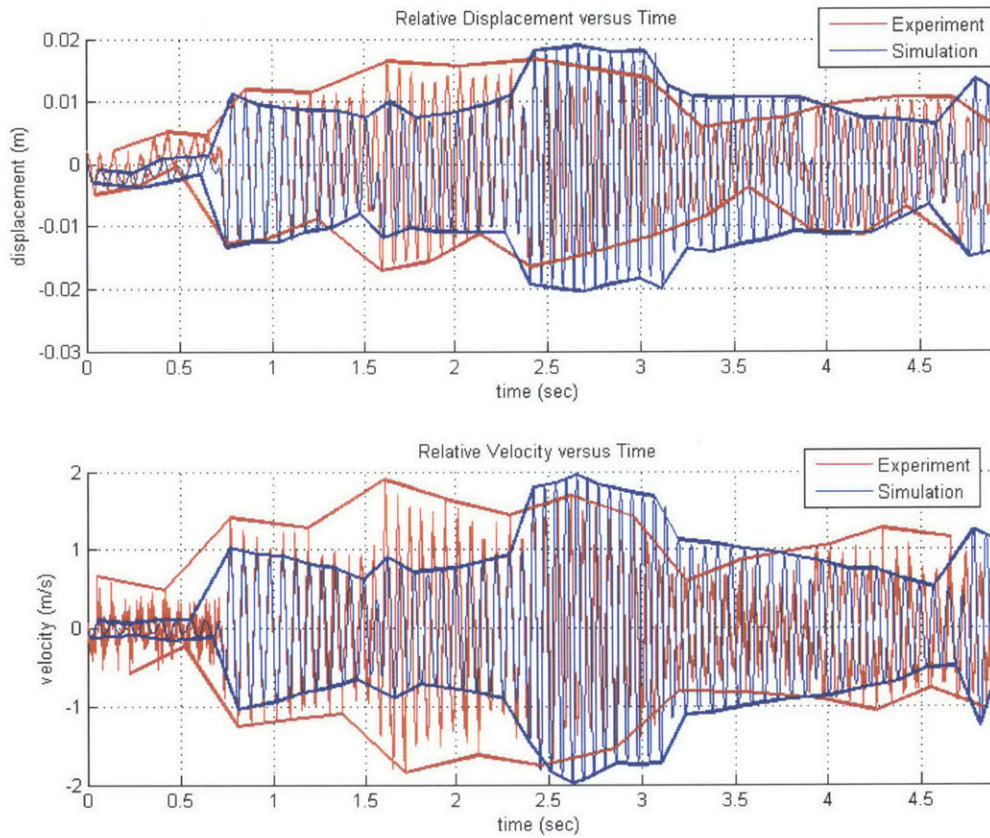


Figure 3-17: Mass motion time series for the multiple base drop test, oscillator 2. The system had parameters: $mass = 25g$, $L_{cant} = 8.7cm$, elastic modulus $E = 160.6e9Pa$, cantilever base dimension $b = 0.187inches$, cantilever height $h = 0.032inches$, surface length $L_{surf} = 7.2cm$, surface gap at surface end (if $L_{surf} = L_{cant}$) $D = 2cm$, and surface curve power $n = 3$. The damping envelope indicated that the viscous damping in the system is 0.02 Ns/m . A photograph of the system [with a heavier mass] is shown in Figure 3-10.

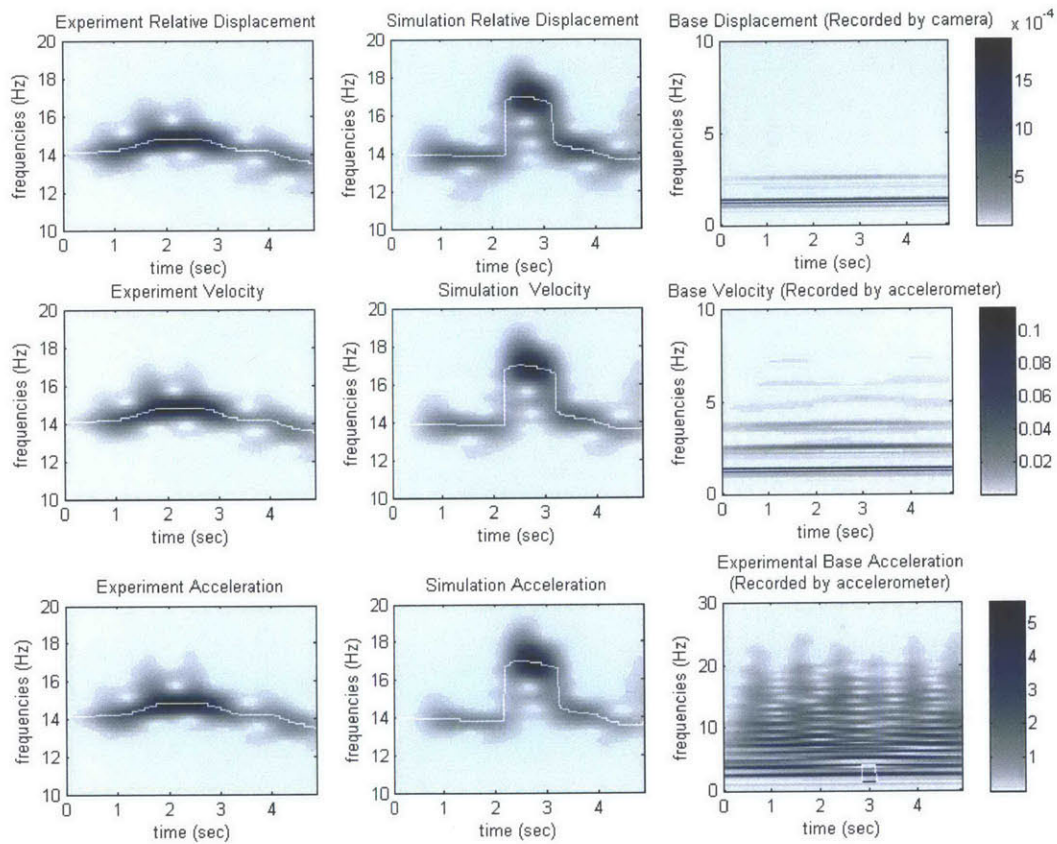


Figure 3-18: Wavelet transforms for the multiple drop test, oscillator 2. The system had parameters: $mass = 25g$, $L_{cant} = 8.7cm$, elastic modulus $E = 160.6e9Pa$, cantilever base dimension $b = 0.187inches$, cantilever height $h = 0.032inches$, surface length $L_{surf} = 7.2cm$, surface gap at surface end (if $L_{surf} = L_{cant}$) $D = 2cm$, and surface curve power $n = 3$. The damping envelope indicated that the viscous damping in the system is $0.02 Ns/m$. A photograph of the system [with a heavier mass] is shown in Figure 3-10.

Chapter 4

Numerical Optimization and Comparison of Linear and Nonlinear Energy Harvesters Excited by Human Motion

The goal of this thesis is to design an energy harvester that maximizes the electric power generated by human motion, a noisy signal. An optimized energy harvester will produce the most power for a specific excitation signal. Additionally, the energy harvester should be robust: the amount of power should not significantly decrease when the excitation frequency slightly varies, such as when a person walks at a different pace. Furthermore, the energy harvester should be adaptive: the power should not plummet when different people use the same harvester or the same person runs instead of walks. Finally, the energy harvester should have an electromagnetically-induced damping coefficient that greatly exceeds the mechanical damping coefficient so that most of the dissipated energy is harvested instead of removed from the system.

This thesis considers several energy harvester configurations and types of motion excitation. All of the energy harvesters consist of magnets attached to springs that move through or over coils. The total allowable peak-peak amplitude of the mass or masses with respect to the base is 6.8 cm (that is a 1DOF mass can travel 6.8 cm pk-pk. Each mass of the 2DOF harvester can travel 3.4 cm pk-pk). The amplitude constraints represent the harvester casing. When the mass travels the maximum distance, it elastically collides with the

outer casing. The model for these collisions is described several paragraphs below. Please note that the "linear" device is not actually a traditional linear oscillator because of the amplitude constraints.

The springs may be linear (such as a helical coil or free cantilever) or nonlinear (such as the spring described in Chapter 2). The energy harvester may be configured to have one moving mass (one degree-of-freedom, or 1DOF) or two moving masses (two degrees-of-freedom, or 2DOF). The base of the energy harvester is excited by the foot's motion while walking or running; or by the hip's motion while walking, walking quickly, running, or biking.

The energy harvester performance is predicted using a simulation that numerically solves the energy harvester's equation of motion when the base is excited by the human motion acceleration. The equation of motion consists of terms for the proof masses, electromagnetic damping, and spring forces. All masses except the proof masses are considered negligible. This assumption is valid because the spring steel cantilevers weigh only a few grams while the proof masses weigh 60 or more grams. The oscillating magnets and nonlinear spring contact surfaces are the proof masses. The simulations only consider the total energy dissipated: the power optimization plots do not distinguish between energy dissipated by mechanical damping and energy dissipated by electromagnetic damping. Experiments showed that the mechanical damping from ranged from 0.007 to 0.02 Ns/m (see Chapter 3). The smallest electromagnetic damping value considered in the simulations is 0.05 Ns/m, for which 0.007 Ns/m parasitic damping equates to a 14% power loss and 0.02 Ns/m parasitic damping equates to a 40% power loss. The effect of different amounts of parasitic damping on the optimized systems' harvested power is illustrated in Figure 4-40 in Section 4.5.4. If the spring is linear, then the spring force is found according $F = kx$, where k is the spring coefficient and x is the mass displacement from equilibrium. If the spring is nonlinear, then the spring force is numerically solved according to the theory in Chapter 2, with a modification to account for the end-mass deflection as described in Section 3.2. Additionally, the spring forces at large deflections are modified to account for the harvester's outer casing constraints. The simulation assumes that the cantilever of the nonlinear spring oscillates only in its first mode. This assumption is verified (with limitations) in Section 3.2.

The final simulation uses Matlab's built-in function `ode113` to numerically solve the dif-

ferential equations of motion. Initially, we tried using the classical Runge-Kutta method (RK4) to numerically solve the equations. RK4 was used instead of Matlab's built-in differential equation solvers so that elastic collisions between the masses and the base could be simulated. During a collision, the proof mass acceleration is temporarily undefined, so the equation of motion cannot be used to determine the new acceleration, and then the corresponding displacement and velocity. Our RK4 routine found the new mass velocities and displacements after a collision by using the conservation of momentum and conservation of energy principles. The RK4 routine produced consistent results for the 1DOF simulated systems. However, it did not produce consistent, reliable results for the the 2DOF systems, for which the collisions occur more frequently and over smaller distances (the dynamics did not converge for smaller simulated time steps). Switching to ode113, which is a good solver for "nonstiff systems" and has "low to high accuracy," corrected these inconsistency issues.

1

To simulate elastic collisions using ode113, the spring forces were modified so that they approached infinity for deflection values, x , near and exceeding the displacement constraints between the masses and base, x_{crit} . The modified spring force was defined as:

$$F_{Simulated} = \begin{cases} F_{Theoretical} + \frac{\epsilon}{x-x_{crit}} & \text{if } x < x_{crit} \\ \max\left(F_{Theoretical} + \frac{\epsilon}{x-x_{crit}}\right) + \frac{1}{\epsilon} \left(\frac{x}{x_{crit}}\right)^5 & \text{if } x \geq x_{crit} \end{cases} \quad (4.1)$$

where ϵ is a sensitivity parameter that was set to $1e - 5Nm^2$. See Figure 4-29 for a sample modified force versus displacement curve.

This chapter first describes the human motion excitation signals used in the simulations. Then, it compares the harvested power, robustness, and adaptivity of 1DOF systems excited by foot motion in Section 4.2. Section 4.2 shows that the 1DOF linear system excited by foot motion actually outperforms the nonlinear system in terms of peak power output, robustness, and adaptivity. The good performance of the linear system agrees with the performance of coulomb-force parametric generator (CFPG) described in [12]. The CFPG is a device for which the proof mass oscillates between its constraints without a spring. Since the CFPG

¹<http://www.mathworks.com/help/matlab/ref/ode113.html>

does not have a spring, it does not have a resonant frequency and responds similarly to acceleration signals that have the same magnitude but different frequencies. The CFPG, however, only functions well when the excitation displacement greatly exceeds the allowable travel length of its sliding plate.

This suggests that our linear 1DOF harvester might have outperformed the nonlinear 1DOF harvester because the foot displacement amplitude (30 cm pk-pk. See Section 4.1) greatly exceeds the proof mass amplitude relative to the casing (6.8 cm pk-pk). For this reason, the next step in this project was to investigate the energy harvester performance for smaller excitation displacements, such as the hip motion (while walking, the hip has 4 cm pk-pk amplitude. See Section 4.1). Although the hip motion has less available power than the foot motion, being able to carry the energy harvester in a pocket or backpack might be more practical or convenient than carrying it in the shoe. Furthermore, the higher efficiency of a nonlinear device over a linear device is more important when the power source is less powerful. Thus, the hip motion seemed like a promising new niche for our nonlinear energy harvester.

However, as shown in Section 4.3, even when excited by hip motion, the 1DOF linear system outperformed the 1DOF nonlinear system, and neither of them showed very good adaptivity or robustness. A new approach for finding a powerful, adaptive, robust system that used the nonlinear spring was to investigate the 2-degree-of-freedom systems. As described in [25], the 2DOF nonlinear energy harvester can have higher peak power, robustness, and adaptivity than the 1DOF linear, 1DOF nonlinear, and 2DOF linear harvesters.

Section 4.4 describes the 2DOF linear and nonlinear systems. This thesis examines 2DOF nonlinear systems with a moderate (0.4 Ns/m) and large (1.6 Ns/m) amount of electromagnetic damping in between the masses. For comparison, this thesis also examines the 2DOF linear systems with low damping (0.05 Ns/m for each mass relative to the base; no damping in between the masses), and with the same moderate (0.4 Ns/m) and large (1.6 Ns/m) electromagnetic damping as the 2DOF nonlinear systems. While more damping tends to decrease the system's optimized power for the walking hip motion, it tends to make the harvester less susceptible to harvested power losses when parasitic damping is present.

All of the energy harvester results are summarized in Section 4.5.

4.1 Excitation Signals

The energy harvester simulations used experimentally collected human motion acceleration as the base input. A Vernier accelerometer was mounted to a person's foot while walking and running, as shown in Figure 4-1. The walking data used an accelerometer that could measure up to 5 gravity. The running data used a 25-g accelerometer. The hip motion data was collected by putting the 25-g accelerometer in a person's pocket, a similar acceleration to what a cell phone would experience. The accelerometer was connected to a laptop via a Vernier LabQuest Mini sensor-computer interface. Vernier Logger Lite software recorded the acceleration data at 1,000 Hz.

In Matlab, the acceleration data was truncated to one (for the hip) or two (for the foot) periods. The acceleration at the first index of the truncated signal was added to the end of the truncated signal to ensure that it was periodic. The acceleration data was transformed to the frequency domain by taking the fast Fourier transform (FFT). The FFT components were used to obtain the velocity and displacement time series. The inverse-FFT signals were sequentially repeated in time to simulate a longer signal.

Figures 4-2 and 4-3 show the collected data on the foot and hip motions. The foot maximum velocities occur right before ground impact, and the maximum accelerations occur at impact (as impulses). The running foot dominant frequency is roughly twice the walking foot dominant frequency because the raised foot accelerates when the opposite foot lands. Similarly, the walking hip dominant frequency is roughly twice the walking foot dominant frequency because the right hip accelerates when the left foot lands. The hip dominant frequency slightly increasing as the travel speed increases agrees with the observations of [13]. Figures 4-2 and 4-3 also show that the distribution of power among different frequencies has a longer tail for the foot motion than for the hip motion.

Table 4.1 summarizes each motions' vertical displacement range, maximum velocity, maximum acceleration, dominant frequency (based on the velocity FFT), average velocity time signal squared, and ratio of power in the dominant frequency to total power. This table includes the mean square of each velocity signal based on the velocity time series because the signal's power is proportional to this value ($Velocity_{MS} = mean[Velocity^2(t)]/2$). The

velocity signal mean squares can be used to compare the relative power in the motion. For example, the running foot motion has about fifteen times the power of the walking foot motion. This table also includes the velocity FFT's largest modulation squared divided by the velocity time signal's mean square. This ratio represents the fraction of signal power contained in the dominant frequency. For example, the last column of Table 4.1 shows that the running foot and hip walking quickly motions have the least power concentrated in the dominant frequency, while the hip running motion has the most concentration (least noise).

Table 4.1: Summary of Experimentally Recorded Foot and Hip Motions

Motion	Displacement range (cm)	Maximum velocity (m/s)	Maximum acceleration (m/s^2)	Dominant Velocity Frequency (Hz)	Mean square velocity ($(m/s)^2$)	(Power at Dominant Frequency) / (Signal Power)
Foot Walk	27	-1.3	37	0.95	0.047	0.36
Foot Run	37	-1.7	170	1.5	0.71	0.35
Hip Walk	4.0	-0.38	9	1.9	0.012	0.36
Hip Walk Quickly	6.3	-0.72	29	2.3	0.043	0.35
Hip Run	9.5	-1.07	28	2.9	0.17	0.48
Hip Bike	2	$\pm .21$	-5	2.2	0.0065	0.40



Figure 4-1: Experimental Set-up for collecting foot acceleration data

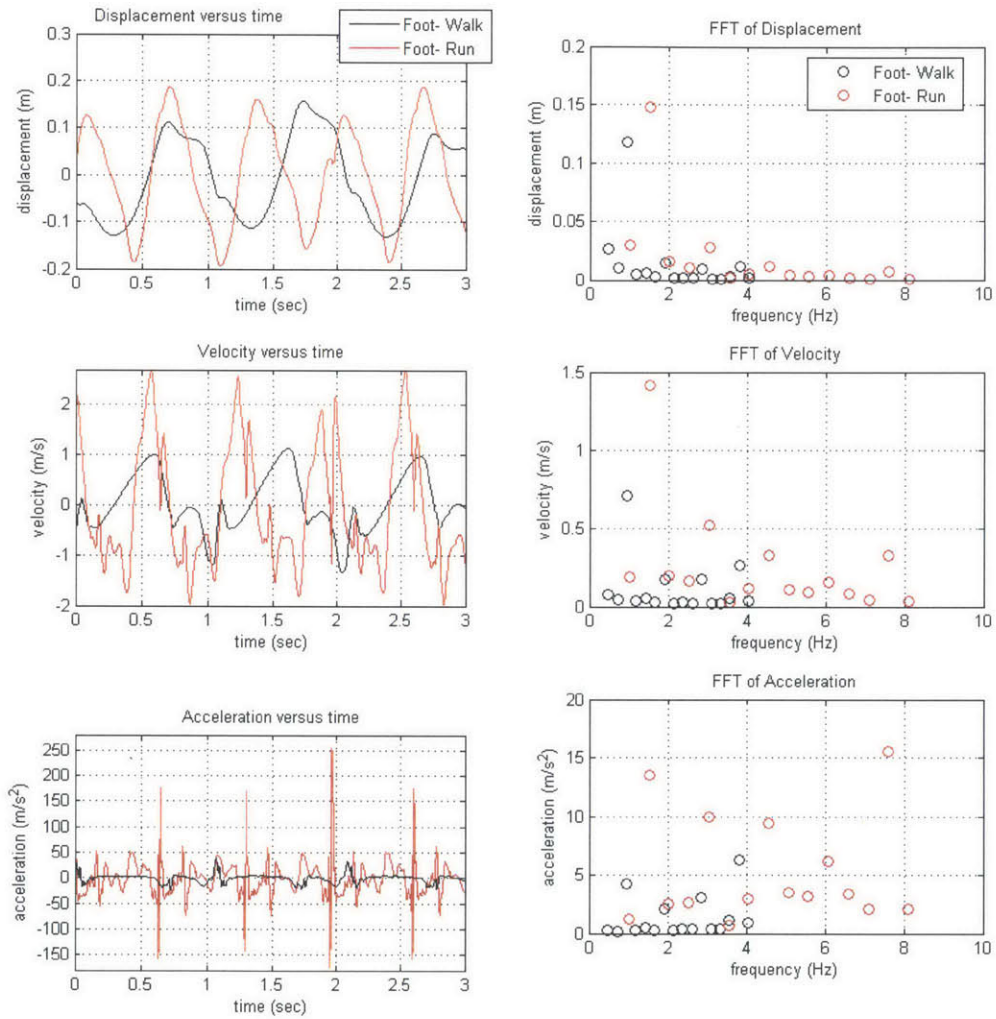


Figure 4-2: Foot motion data. Here, the signal of several periods was repeated. The FFT show the frequency components that sum to 90% the power in the motion, where power in the motion is defined as $mean[Velocity^2(t)]/2$, the mean square of the velocity signal.

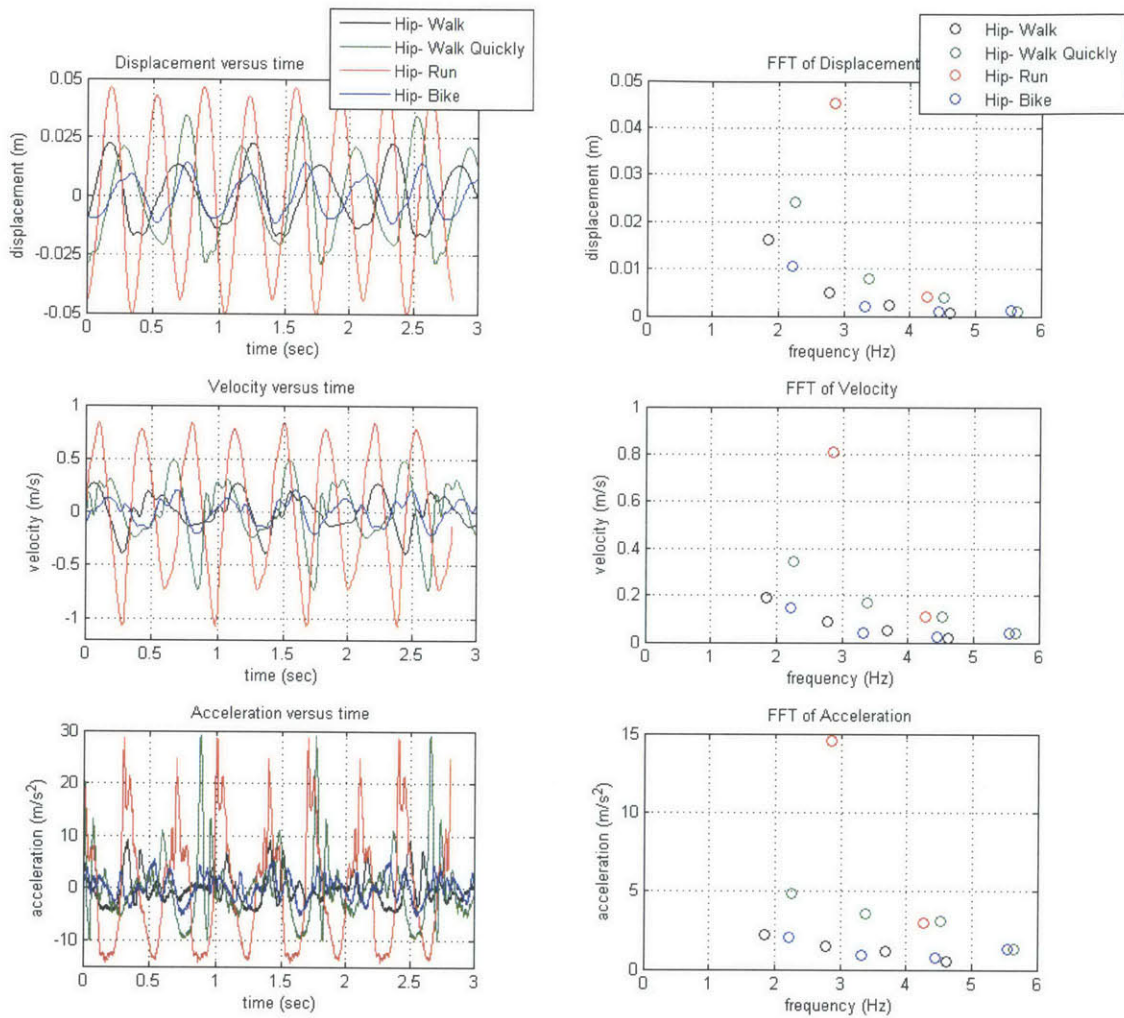


Figure 4-3: Hip motion data. Here, the signal of a signal period was repeated. The FFT show the frequency components that sum to 90% the power in the motion, where power in the motion is defined as $mean[Velocity^2(t)]/2$, the mean square of the velocity signal.

4.2 Comparison of 1DOF Systems Excited by Foot Motion

This section studies the performance of 1DOF energy harvesters with a linear spring, cubic nonlinear spring, or cantilever-surface nonlinear spring. We hypothesized that an optimized harvester with a cantilever-surface spring would harvest the same or more power than the harvester with the cubic spring due to the similar force versus displacement curve shape for small displacements and the blow-up of the force for large displacements [25]. The 1DOF energy harvester consists of a magnet with mass m attached to an outer casing (i.e. "base") by a linear or nonlinear spring. The magnet motion is electromagnetically damped by a coil that is rigidly attached to the outer casing. The base is excited by the human motion signal, h . A CAD rendering and component diagram of the 1DOF energy harvester are shown in Figure 4-4.

The cubic spring oscillator was simulated with a mass of 125 g, the estimated maximum mass that a person would not mind carrying around. The other two oscillators were simulated with masses of 60 g. This lighter mass was used in the simulations because experiments with the heavier mass showed higher modes and did not agree with the theory (See Chapter 2. However, the power results of all three springs can be compared by considering "doubled" versions of the energy harvesters with the cantilever-surface and linear spring. That is, if the left-hand and right-hand sides of the equation of motion (Equation 4.2) are multiplied by 2, then the numerically simulated dynamics for the "single" EOM still hold. The "doubled" system has twice the mass, twice the spring stiffness, twice the electromagnetic damping, and twice the power as the "single" system. The parameters of the doubled system can be physically implemented by doubling the magnet and cantilever width. Increasing the width in this way should prevent the higher modes of the cantilever because the magnet mass will remain centered on the cantilever.

The equation of motion for this system is:

$$m\ddot{X} = -F(X) - \lambda\dot{X} - m\ddot{h} - mg \quad (4.2)$$

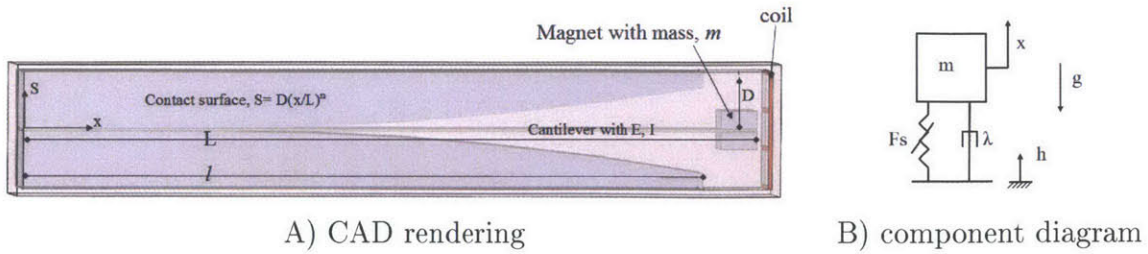
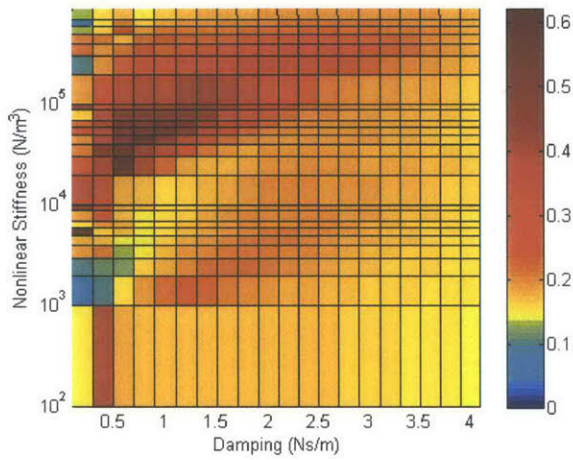


Figure 4-4: 1DOF nonlinear system CAD rendering and component diagram

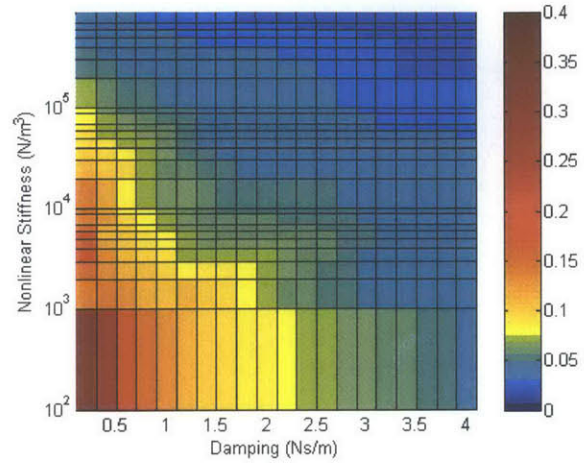
where m is the magnet mass, X is the magnet displacement with respect to the base, F is the force exerted by the spring, λ is the electromagnetic damping coefficient, and g is the downwards acceleration due to gravity. For the linear spring, $F = kX$, where k is the spring coefficient and X is the mass displacement relative to the base. For a cubic nonlinear spring, $F = kX^3$. For the nonlinear spring studied in this thesis, F is a function of X and is determined using the theory described in Chapter 2. Collisions of the mass with the base (which occur whenever the displacement of the mass wrt the base exceeds ± 3.4 cm) are simulated by modifying the theoretical $F(X)$ to approach infinity for relative mass displacements near and exceeding ± 3.4 cm, as shown in Equation 4.1.

4.2.1 Cubic Nonlinear Spring Summary

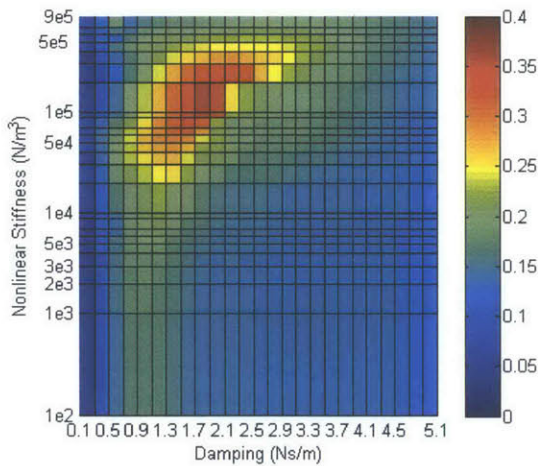
The cubic 1DOF oscillator was simulated for the walking and running foot motion for varied parameters. The relative displacement constraints between the mass and base were varied among no constraint, 3 cm, and 2 cm. All of the oscillators had a mass of 125 g. The power optimization surfaces for walking and running are shown in Figures 4-5 and 4-6, respectively. The optimal parameters are summarized in Table 4.2. These figures show the steady state relative displacement of the oscillators without constraints. For the oscillators with constraints, all of the optimal oscillators had maximum relative displacements equal to the constraints.



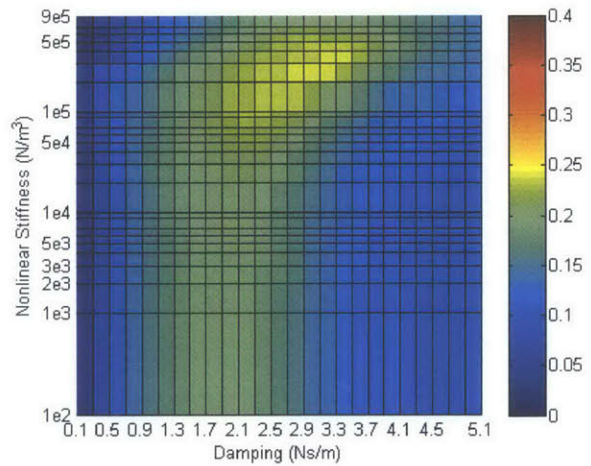
(a) Power, no Displacement constraints (W)



(b) Steady state relative displacement amplitude (m)

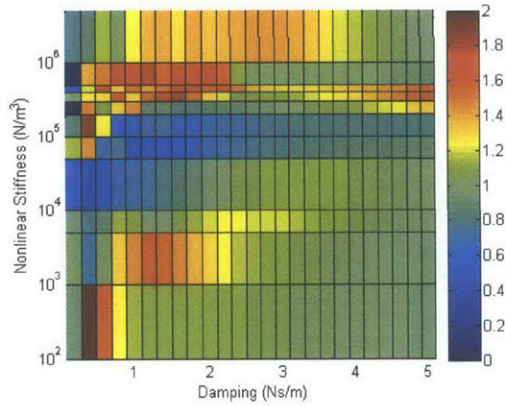


(c) Power, 3 cm Displacement constraints (W)

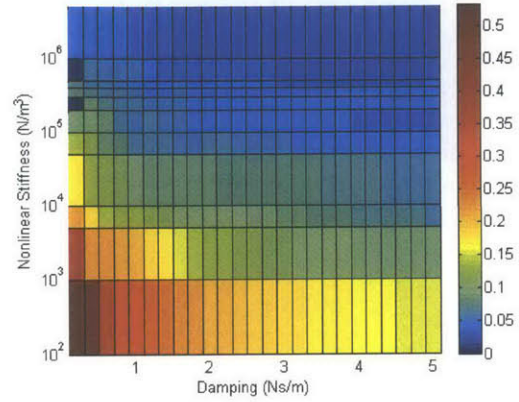


(d) Power, 2 cm Displacement constraints (W)

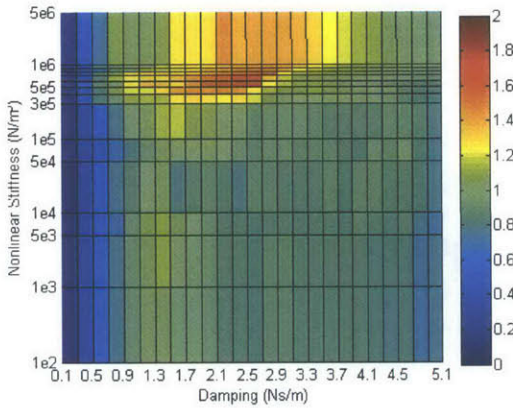
Figure 4-5: Power Harvested by 1DOF cubic system excited at foot while walking for $m = 125g$. Please note that the mass in this simulation is twice the total mass of the other systems described in this thesis.



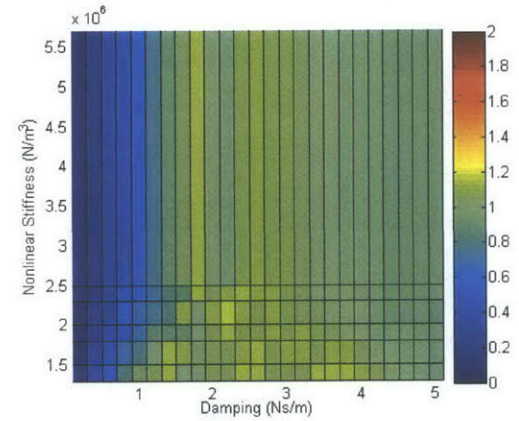
(a) Power, no Displacement constraints (W)



(b) Steady state relative displacement amplitude (m)



(c) Power, 3 cm Displacement constraints (W)



(d) Power, 2 cm Displacement constraints (W)

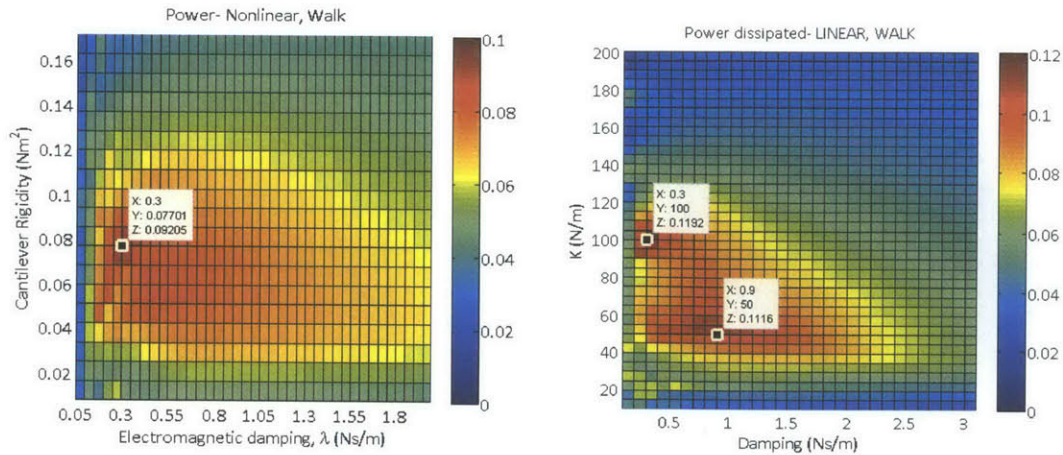
Figure 4-6: Power Harvested by 1DOF cubic system excited by foot while running for $m = 125g$. Please note that the mass in this simulation is twice the total mass of the other systems described in this thesis.

Table 4.2: Simulated 1DOF Cubic Oscillator Performance for $m = 125g$. Please note that these simulations used a total mass of 125g, while all of the other simulations in this thesis used a total mass of 60g.

Motion	Displacement constraints (m)	Spring Stiffness, C (N/m^3)	Damping Coefficient, λ (Ns/m)	Maximum Relative Displacement (m)	Average Power Dissipated (W)
Walk	none	$5e4$	0.8	0.06	0.48
Walk	0.03	$1e5$	1.7	0.03	0.36
Walk	0.02	$2e5$	2.9	0.02	0.24
Run	none	$1e5$	0.3	0.10	1.85
Run	0.03	$5e5$	2.3	0.03	1.7
Run	0.02	$1e6$	3.3	0.02	1.2

4.2.2 Walking

Figure 4-7 shows the power harvested by the 1DOF linear oscillator and by the 1DOF nonlinear cantilever-surface oscillator when excited by the foot while walking. Figure 4-8 shows the time series of the linear and nonlinear energy harvesters that harvest the most power for the foot walking excitation signal.



(a) Nonlinear harvester that uses the cantilever-surface nonlinear spring. The electromagnetic damping and cantilever rigidity are varied. Constant parameters are $L_{cant} = 15.7\text{cm}$, surface length $L_{surf} = 15\text{cm}$, surface gap at surface end $D = 3\text{cm}$, and surface curve power $n = 3$.

(b) Linear harvester

Figure 4-7: Power Harvested by 1DOF systems excited by the foot while walking. The base of the system is excited by the walking foot acceleration shown in Figure 4-2. Both systems have $mass = 60\text{g}$, and the displacement of the mass relative to the surfaces is constrained to $\pm 3.4\text{cm}$.

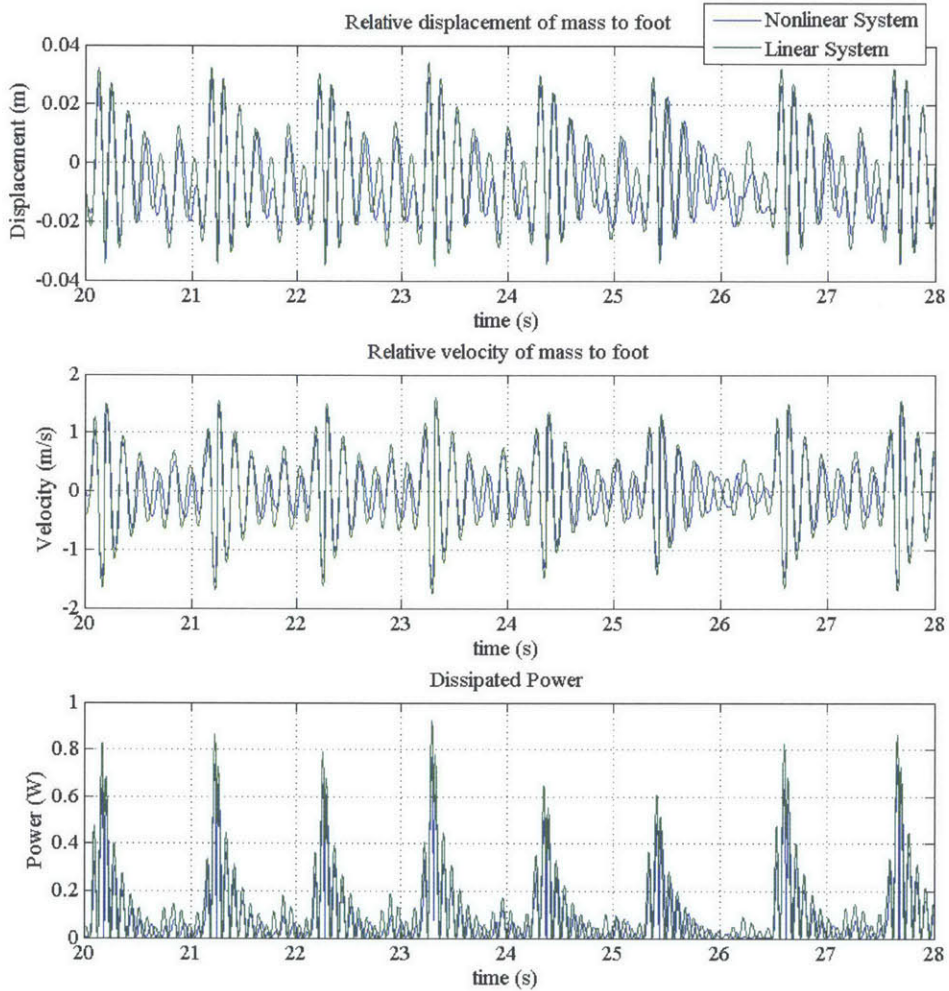
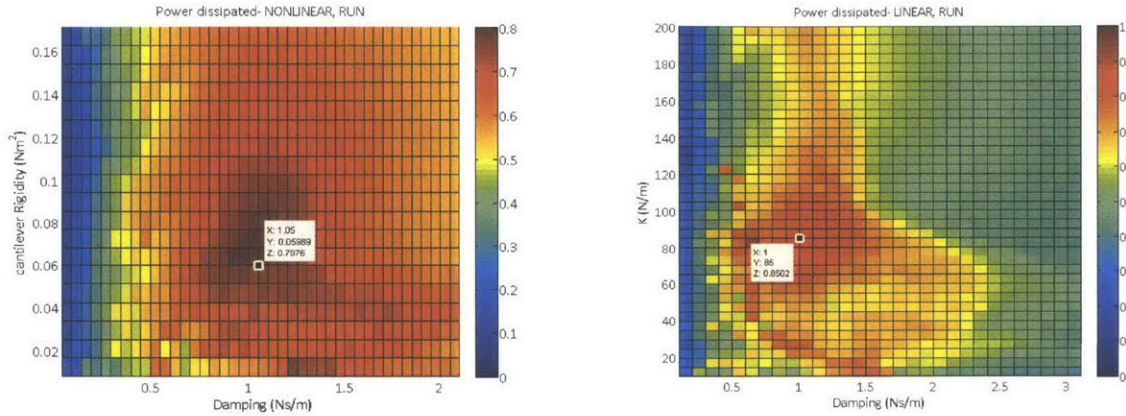


Figure 4-8: Dynamics of linear and nonlinear 1DOF systems when excited by WALKING. Nonlinear system has parameters: $EI = 0.06845Nm^2$, electromagnetic damping $\lambda = 0.3Ns/m$, $mass = 60g$, $L_{cant} = 15.7cm$, surface length $L_{surf} = 15cm$, surface gap at surface end $D = 3cm$, and surface curve power $n = 3$. The linear system has parameters: $mass = 60g$, linear spring stiffness $K = 100N/m$, and damping coefficient $\lambda = 0.3Ns/m$. Both systems have a maximum displacement of the mass relative to the surface/base of $\pm 3.4cm$. The nonlinear system harvests 0.0904 W. The linear system harvests 0.119 W.

4.2.3 Running

Figure 4-9 shows the power harvested by the 1DOF linear and nonlinear cantilever-surface oscillators when excited by the foot while running. Figure 4-10 shows the time series of the linear and nonlinear energy harvesters that harvest the most power for the foot running excitation signal.



(a) Nonlinear harvester that uses the cantilever-surface nonlinear spring. The electromagnetic damping and cantilever rigidity are varied. Constant parameters are $L_{cant} = 15.7cm$, surface length $L_{surf} = 15cm$, surface gap at surface end $D = 3cm$, and surface curve power $n = 3$. (b) Linear harvester

Figure 4-9: Power Harvested by 1DOF systems excited by the foot while Running. The base of the system is excited by the running foot acceleration shown in Figure 4-2. Both systems have $mass = 60g$, and the displacement of the mass relative to the surfaces is constrained to $\pm 3.4cm$.

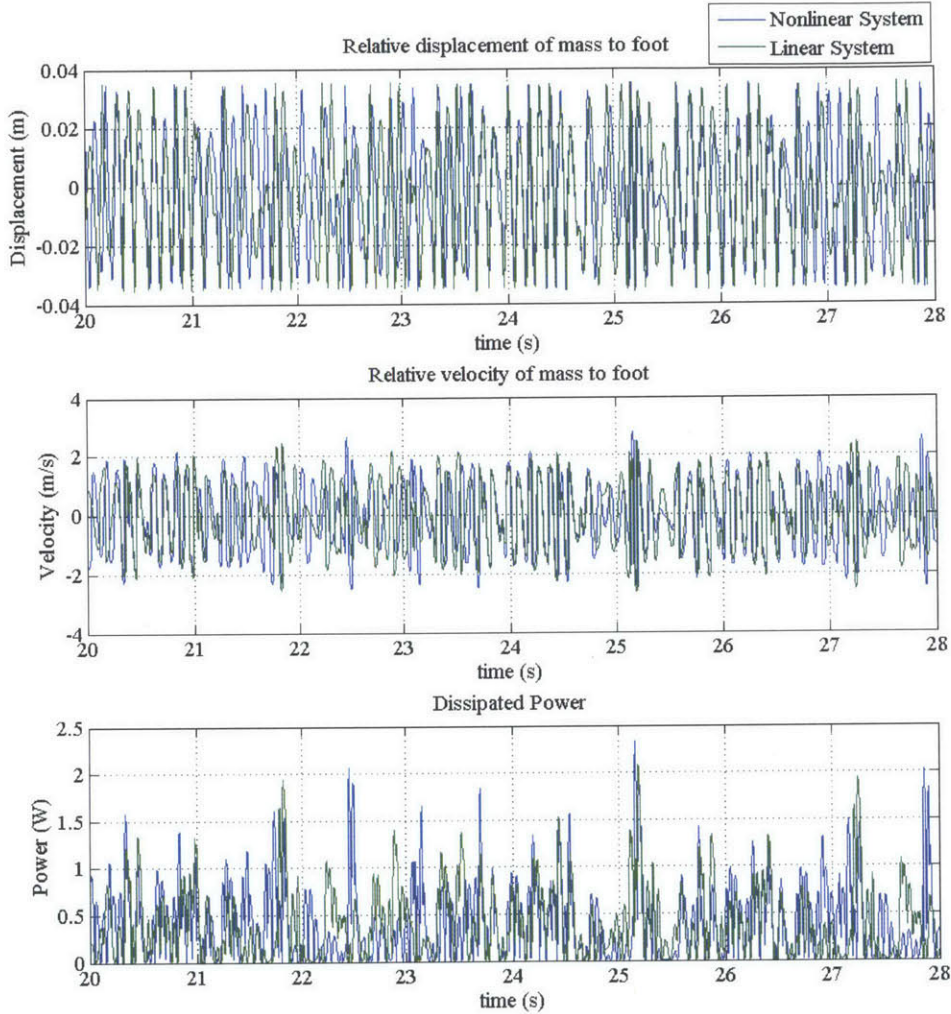


Figure 4-10: Dynamics of linear and nonlinear 1DOF systems when excited by RUNNING. Nonlinear system has parameters: $EI = 0.06845Nm^2$, electromagnetic damping $\lambda = 0.3Ns/m$, $mass = 60g$, $L_{cant} = 15.7cm$, surface length $L_{surf} = 15cm$, surface gap at surface end $D = 3cm$, and surface curve power $n = 3$. The linear system has parameters: $mass = 60g$, linear spring stiffness $K = 100N/m$, and damping coefficient $\lambda = 0.3Ns/m$. Both systems have a maximum displacement of the mass relative to the surface/base of $\pm 3.4cm$. The nonlinear system harvests 0.452 W. The linear system harvests 0.439 W.

4.2.4 Comparison of Robustness and Adaptivity

Sections 4.2.2 and 4.2.3 numerically determined the nonlinear cantilever-surface and linear harvesters that harvested the most power when excited by the foot motion while walking and running, respectively. Here, those optimal systems are compared for robustness and adaptivity.

Figures 4-11 and 4-12 illustrate the harvesters' robustness to small changes in the excitation signal by showing the power harvested by each system when excited by a motion with a rescaled time signal. The rescaled time range of 0.5-2 represents the range of human walking frequencies described in [14]. Figure 4-13 illustrates the harvesters' adaptivity by showing the numerically simulated power harvested by each system when excited by different experimentally recorded foot accelerations.

Figure 4-11 shows that the linear systems harvest more power than the nonlinear systems for time rescaling 1-2 of the foot walking signal. The nonlinear systems harvest more power than the linear for time rescaling 0.5. Figure 4-12 shows that the linear and nonlinear systems harvest roughly the same power for time rescaling of the foot running signal, with the linear system harvesting slightly more power. Figure 4-13 shows that the linear and nonlinear systems harvest roughly the same power for different motion excitation signals.

Figure 4-13 also shows the power harvested by a linear harvester with the same parameters as the linear optimal walking parameters but without the displacement constraints. Without the displacement constraints, the power harvested by the linear system while running greatly decreases. This demonstrates the role that the displacement constraints play in changing the dynamics of the linear harvester. As suggested by [12], the large ratio of foot displacement to mass-base relative motion might cause the linear system to outperform the nonlinear system. For this reason, Section 4.3 investigates the power harvested by the 1DOF systems when excited by the hip motion, which has a smaller displacement.

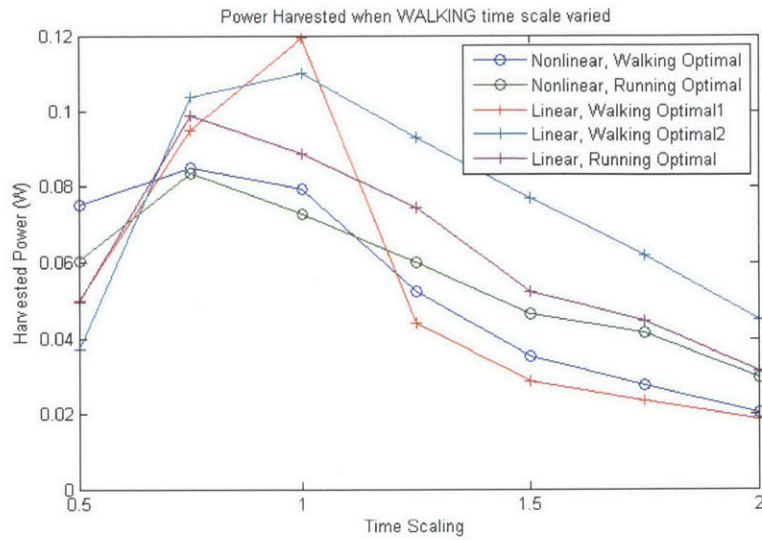


Figure 4-11: Power harvested by the optimal 1DOF springs when the time scale of the walking foot excitation signal is rescaled (e.g. when the "Time Scale" equals 2, the steps occur twice as fast).

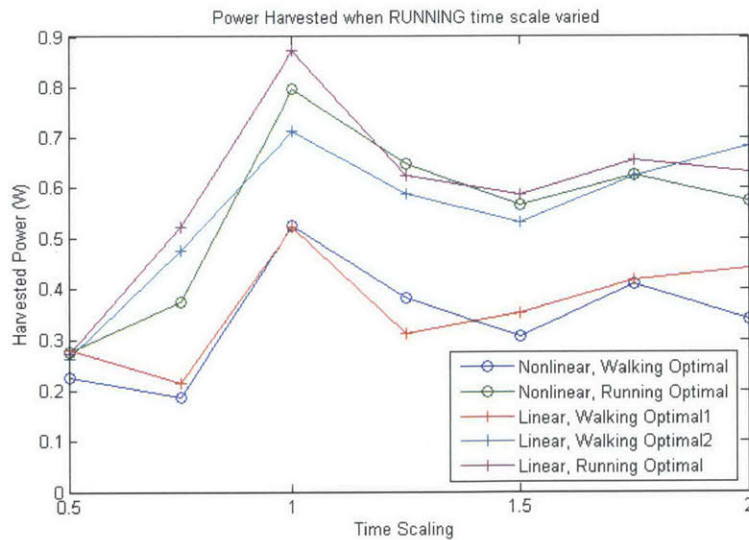


Figure 4-12: Power harvested by the optimal 1DOF springs when the time scale of the running foot excitation signal is rescaled (e.g. when the "Time Scale" equals 2, the steps occur twice as fast).

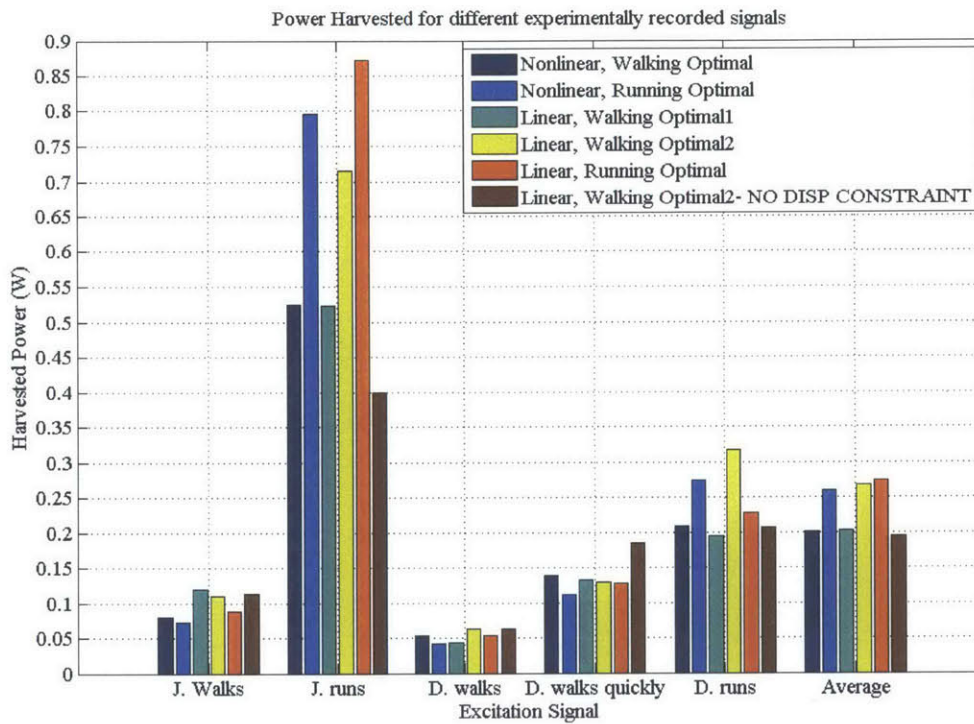


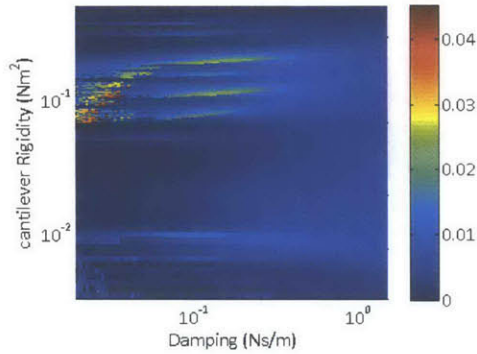
Figure 4-13: Power harvested by the optimal 1DOF springs when excited by different experimentally recorded foot motions. "J." stands for the foot motion of this author. "D." stands for the foot motion of another graduate student.

4.3 Comparison of 1DOF Systems Excited by Hip Motion

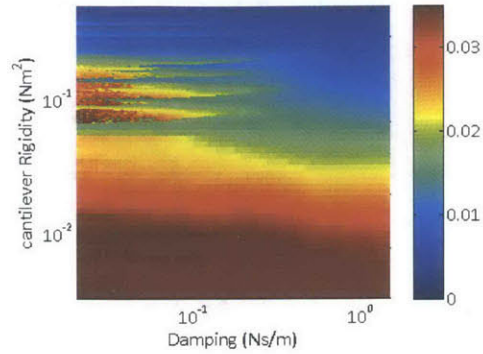
These energy harvesters have the same configuration as the 1DOF linear and nonlinear cantilever-surface springs described in Section 4.2 (see the EOM, Equation 4.2; and the harvester component schematic, Figure 4-4). Now, instead of the base being excited by the foot motion, it is excited by the hip motion shown in Figure 4-3. Section 4.3.1 shows the power and displacement amplitude for the linear and cantilever-surface harvesters when the base is excited by the hip while walking. Section 4.3.2 shows these results for the running hip motion.

The nonlinear harvester seems to show chaotic behavior for damping less than 0.06 Ns/m for walking. The linear system does not seem to show any chaotic behavior. The reason for this might be that the linear harvester resonates at low stiffnesses; so when its amplitude is large, its frequency is too slow for the rapid collisions with the boundaries that lead to chaotic behavior.

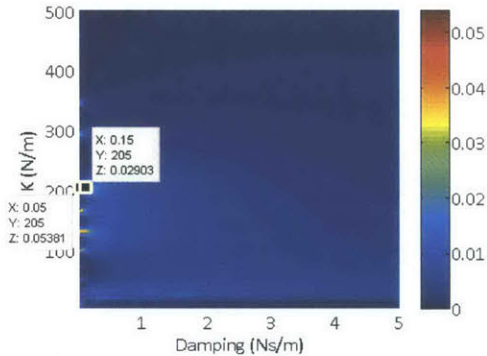
4.3.1 Walking



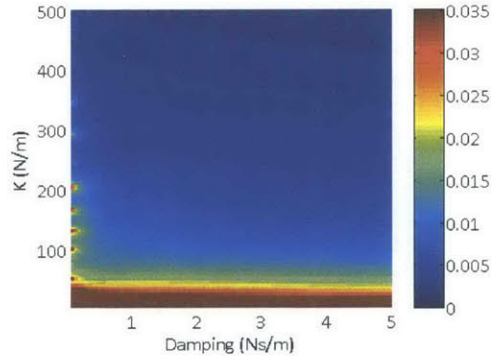
(a) Power, harvester with cantilever-surface spring (W)



(b) Steady state relative displacement amplitude, harvester with cantilever-surface spring (m)



(c) Power, linear harvester (W)



(d) Steady state relative displacement amplitude, linear harvester (m)

Figure 4-14: Power Harvested by 1DOF harvesters excited by hip while walking. Both systems have $mass = 60g$, and the displacement of the mass relative to the surfaces is constrained to $\pm 3.4cm$. The nonlinear harvester has parameters: cantilever length $L_{cant} = 15.7cm$ and surface length $L_{surf} = 15cm$, surface gap at surface end $D = 3cm$, and surface curve power $n = 3$. These simulations used simulated time steps of .0001 seconds, and calculated the power in between 15 and 30 seconds.

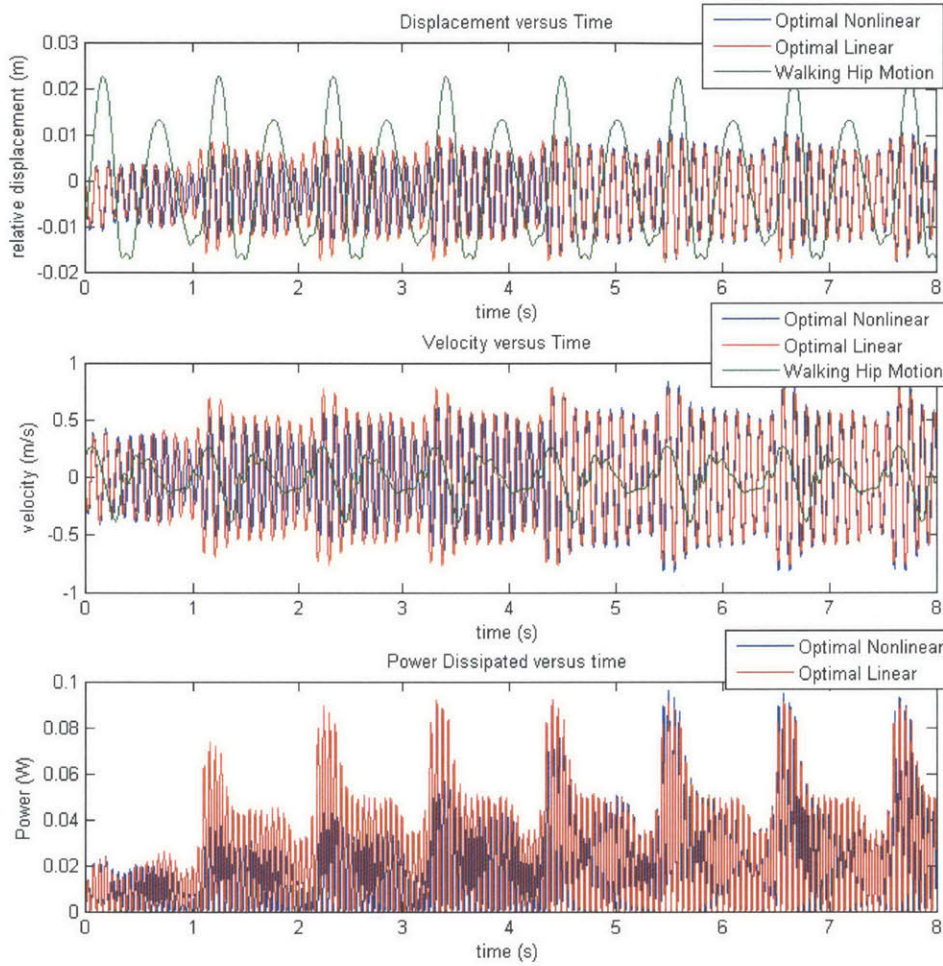
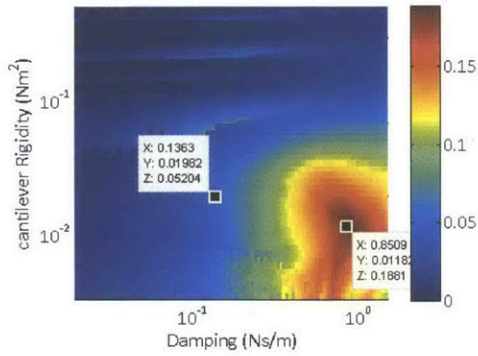
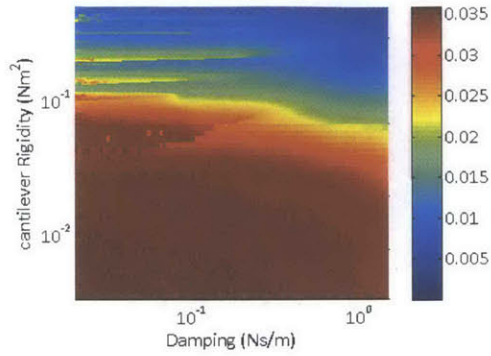


Figure 4-15: Dynamics of optimal linear and nonlinear 1DOF systems when excited by hip walking motion. Nonlinear system has parameters: $EI = 0.192Nm^2$, electromagnetic damping $\lambda = 0.1363Ns/m$, $mass = 60g$, $L_{cant} = 15cm$, surface length $L_{surf} = 15cm$, surface gap at surface end $D = 3cm$, and surface curve power $n = 3$. The linear system has parameters: $mass = 60g$, linear spring stiffness $K = 205N/m$, and damping coefficient $\lambda = 0.15Ns/m$. Both systems have a maximum displacement of the mass relative to the surface/base of $\pm 3.4cm$. Both the nonlinear and linear systems harvest 0.029 W.

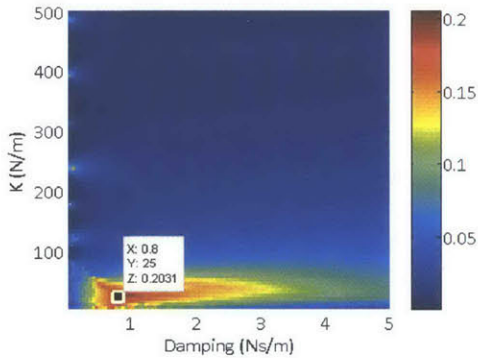
4.3.2 Running



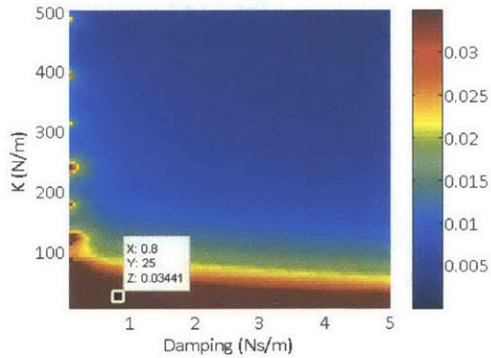
(a) Power, harvester with cantilever-surface spring (W)



(b) Steady state relative displacement amplitude, harvester with cantilever-surface spring (m)



(c) Power, linear harvester (W)



(d) Steady state relative displacement amplitude, linear harvester (m)

Figure 4-16: Power Harvested by 1DOF harvesters excited by hip while running. Both systems have $mass = 60g$, and the displacement of the mass relative to the surfaces is constrained to $\pm 3.4cm$. The nonlinear harvester has parameters: cantilever length $L_{cant} = 15.7cm$ and surface length $L_{surf} = 15cm$, surface gap at surface end $D = 3cm$, and surface curve power $n = 3$. These simulations used simulated time steps of .0001 seconds, and calculated the power in between 15 and 30 seconds.

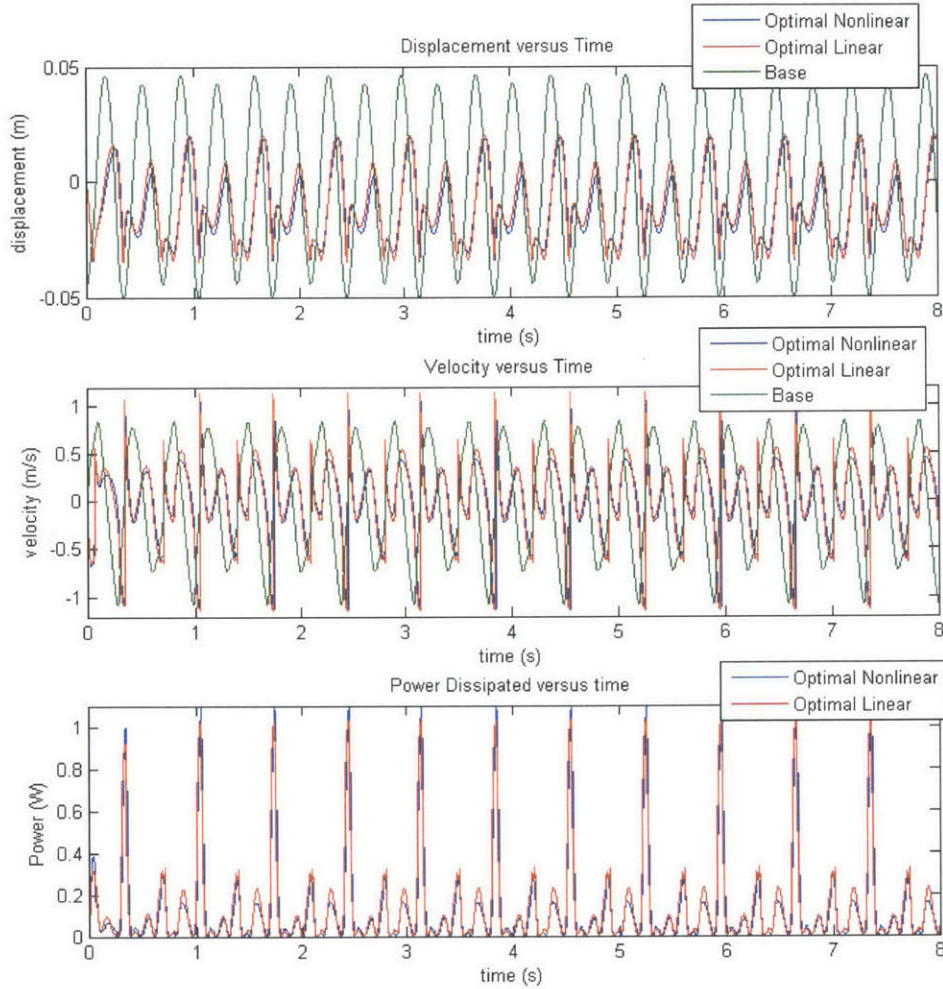


Figure 4-17: Dynamics of optimal 1DOF linear and nonlinear systems when excited by hip running motion. Nonlinear system has parameters: $EI = 0.01182Nm^2$, electromagnetic damping $\lambda = 0.85Ns/m$, $mass = 60g$, $L_{cant} = 15cm$, surface length $L_{surf} = 15cm$, surface gap at surface end $D = 3cm$, and surface curve power $n = 3$. The linear system has parameters: $mass = 60g$, linear spring stiffness $K = 25N/m$, and damping coefficient $\lambda = 0.8Ns/m$. Both systems have a maximum displacement of the mass relative to the surface/base of $\pm 3.4cm$. The nonlinear system harvests 0.19 W. The linear systems harvest 0.20 W.

4.3.3 Comparison of Robustness and Adaptivity

Sections 4.3.1 and 4.3.2 numerically determined the nonlinear cantilever-surface and linear systems that harvested the most power when excited by the hip motion while walking and running, respectively. In addition to the optimal walking linear harvester, which has small damping ($0.05Ns/m$), we are interested in the optimal linear harvester that has a minimum damping of $0.13Ns/m$ because harvesters with larger electromagnetic damping lose a smaller percent of harvested power when small parasitic damping is present. Here, the optimal systems of Sections 4.3.1 and 4.3.2 are compared for robustness and adaptivity.

Figures 4-18 and 4-19 show the harvesters' robustness to small changes in the excitation signal by showing the power harvested by each system when excited by a motion with a rescaled time signal. The rescaled time range of 0.5-2 represents the range of human walking frequencies described in [14]. Figure 4-20 shows the harvesters' adaptivity by showing the numerically simulated power harvested by each system when excited by different experimentally recorded hip accelerations.

Figure 4-18 shows that the linear systems are more robust for time scalings of 0.5-1, and the linear and nonlinear systems harvest roughly the same power for time scaling of 1-2, with the linear system harvesting slightly more power. Figure 4-19 shows that the linear and nonlinear systems optimized for running both harvest roughly the same power when the running excitation signal time scale is varied.

Since the 1DOF nonlinear harvester does not seem to perform better than the 1DOF linear harvester, Section 4.4 investigates the power harvested by 2DOF nonlinear oscillators, which [19] suggests should perform better than 1DOF harvesters.

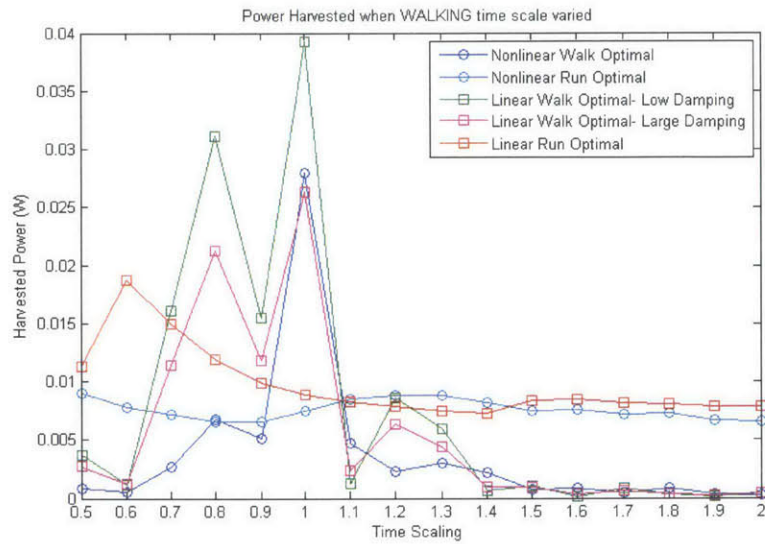


Figure 4-18: Power harvested by the optimal 1DOF harvesters when the time scale of the walking hip excitation signal is rescaled (e.g. when the "Time Scale" equals 2, the steps occur twice as fast).

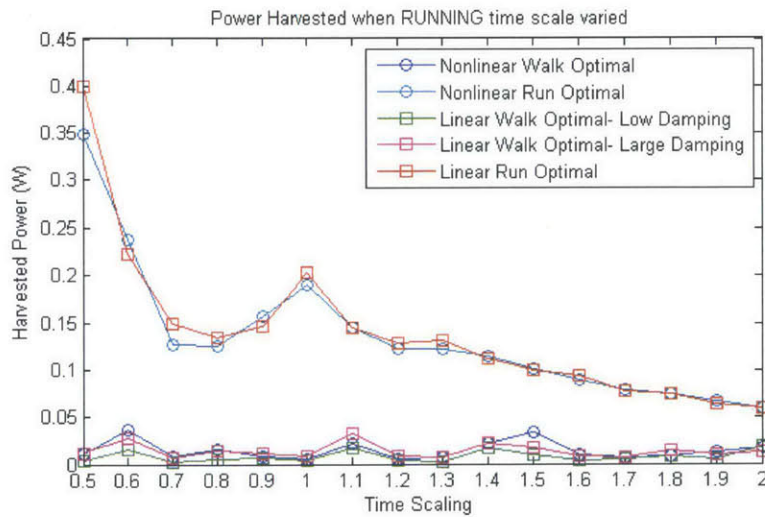


Figure 4-19: Power harvested by the optimal 1DOF harvesters when the time scale of the running hip excitation signal is rescaled (e.g. when the "Time Scale" equals 2, the steps occur twice as fast).

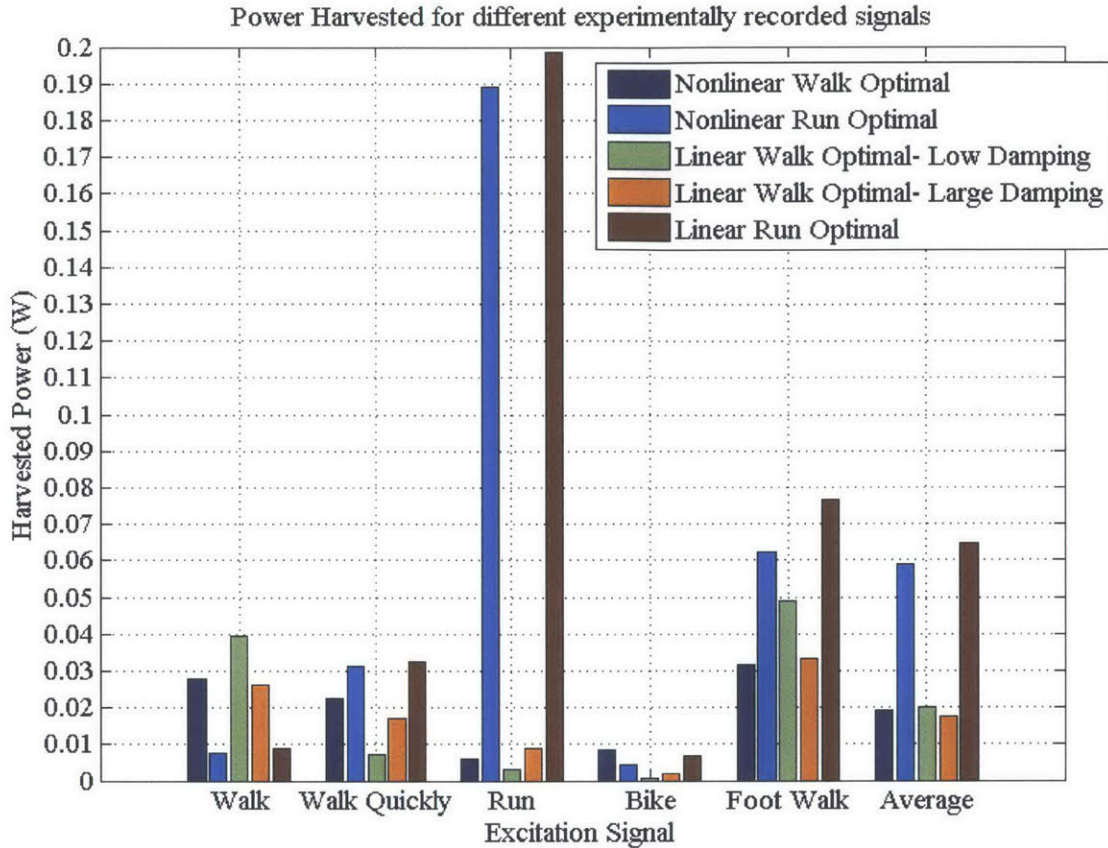


Figure 4-20: Power harvested by the optimal 1DOF harvesters when excited by different experimentally recorded hip motions.

4.4 Comparison of 2DOF Systems Excited by Hip Motion While Walking

This section studies the performance of different 2DOF energy harvesters with linear springs and cantilever-surface nonlinear springs. All of the 2DOF energy harvesters consist of two magnets with masses m_{Top} and m_{Bot} , where $m_{Top} + m_{Bot} = 60g$. The magnet motion is electromagnetically damped by coils. The motion of each mass relative to the base is restricted to $\pm 3.4cm$. The harvester's outer casing (i.e. "base") is excited by the human motion signal, h . A generalized component diagram of the 2DOF system is shown in Figure 4-

21. The equation of motion is:

$$\begin{aligned}
m_{Top}\ddot{X} &= -K_{Top}X - F_{S,Top}(X) - K_{Mid}(X - Z) - F_{S,Mid}(X - Z) \\
&\quad - \lambda_{Top}\dot{X} - \lambda_{Mid}(\dot{X} - \dot{Z}) - m_{Top}\ddot{h} - m_{Top}g \\
m_{Bot}\ddot{Z} &= K_{Mid}(X - Z) + F_{S,Mid}(X - Z) - K_{Bot}Z - F_{S,Bot}(Z) \\
&\quad - \lambda_{Bot}\dot{Z} + \lambda_{Mid}(\dot{X} - \dot{Z}) - m_{Bot}\ddot{h} - m_{Bot}g
\end{aligned} \tag{4.3}$$

where m_{top} is the top magnet mass, m_{Bot} is the bottom magnet mass, X is the top magnet displacement with respect to the base, Z is the bottom magnet displacement with respect to the base, K_i are the coefficients of the linear springs, λ_i are the coefficients of the electromagnetic damping, and g is the downwards acceleration due to gravity. The collisions of the masses with the base are simulated by large spring forces, as described in Equation 4.1. This simulation assumed that the masses were spaced far enough apart that they did not collide with each other.

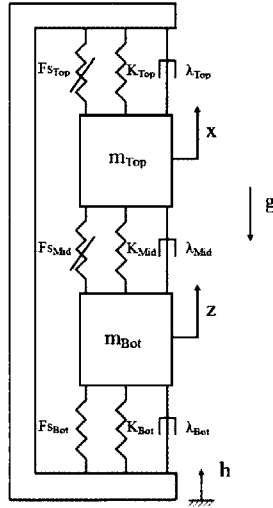


Figure 4-21: General 2DOF system component diagram. The various energy harvesters investigated in this section set some of these spring and damper components to zero. m_{Top} and m_{Bot} are the proof masses, λ_{Top} , λ_{Bot} , and λ_{Mid} are the electromagnetic damping coefficients, K_i indicate the linear spring stiffnesses, and F_{S_i} indicate the nonlinear springs forces. The position of the top mass is x . The position of the bottom mass is z . The position of the base is h . Gravity acts downwards.

Each of the 2DOF energy harvesters described in this section have only some of the spring components shown in Figure 4-21. The 2DOF energy harvesters examined are:

- The Nonlinear Type 1: Moderate EM damping harvester has only the top nonlinear spring, middle linear spring, and bottom linear spring. It has a middle damping coefficient of 0.4 Ns/m, while the top and bottom damping are negligible (0.001 Ns/m).
- The Nonlinear Type 2: Large EM damping harvester has only the top nonlinear spring, middle nonlinear spring, and bottom linear spring. It has a middle damping coefficient of 1.6 Ns/m, while the top and bottom damping is negligible (0.001 Ns/m).
- The Linear: Small damping harvester only has the top and bottom (identical) linear springs. It has top and bottom damping of 0.5 Ns/m, while the middle damping is negligible (simulated as 0 Ns/m).
- The Linear: Moderate damping harvester has the top, middle, and bottom linear springs. It has a middle damping coefficient of 0.4 Ns/m, while the top and bottom damping are negligible (0.001 Ns/m), which matches the damping of the Nonlinear Type 1: Moderate EM damping harvester.
- The Linear: Large damping harvester has the top, middle, and bottom linear springs. It has a middle damping coefficient of 1.6 Ns/m, while the top and bottom damping are negligible (0.001 Ns/m), which matches the damping of the Nonlinear Type 2: Large EM damping harvester.

For the linear systems, decreasing the electromagnetic damping to a value near 0 tended to increase the power harvested. The minimum acceptable damping for a harvester was set to $\lambda = 0.05Ns/m$ because decreasing the damping to a lower value would make parasitic damping losses (predicted to be on the order of $0.01Ns/m$ based on experiments) dissipate more than 20% of the dissipated mechanical power.

These numerical simulations used time steps of 0.0001 seconds, for which we found that the solution converged. The steady-state power was calculated between 2 and 8 simulated seconds. Each of the 3 sections below shows the 2DOF harvester image, component diagram, equation of motion, and sample optimization surfaces of the harvested power and relative mass displacements.

4.4.1 Nonlinear

Nonlinear Type 1: Moderate EM damping (0.4 Ns/m)

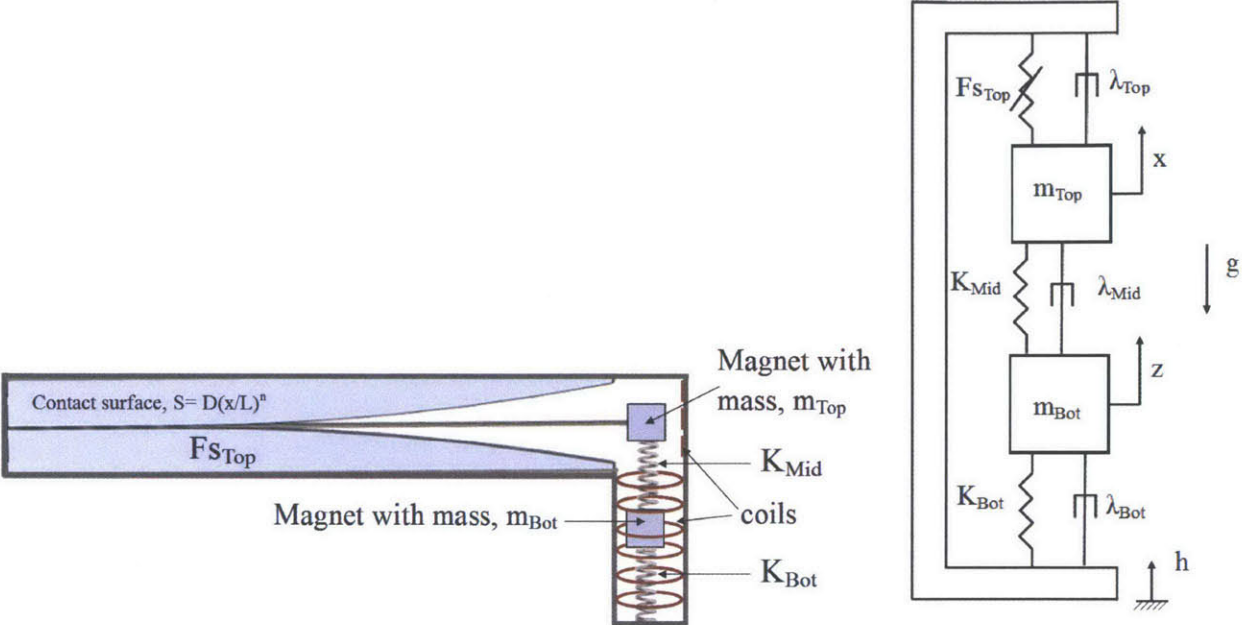
The first 2DOF nonlinear energy harvester examined has only the top nonlinear spring, middle linear spring, and bottom linear spring. It has a middle damping coefficient of 0.4 Ns/m, while the top and bottom damping is negligible (0.001 Ns/m). An illustration of the harvester and its component diagram are shown in Figure 4-22. The equation of motion for the system is:

$$\begin{aligned} m_{Top}\ddot{X} &= -F_{S,Top}(X) - K_{Mid}(X - Z) - \lambda_{Top}\dot{X} - \lambda_{Mid}(\dot{X} - \dot{Z}) - m_{Top}\ddot{h} - m_{Top}g \\ m_{Bot}\ddot{Z} &= K_{Mid}(X - Z) - K_{Bot}Z - \lambda_{Bot}\dot{Z} + \lambda_{Mid}(\dot{X} - \dot{Z}) - m_{Bot}\ddot{h} - m_{Bot}g \end{aligned} \quad (4.4)$$

where m_{top} is the top magnet mass, m_{Bot} is the bottom magnet mass, X is the top magnet displacement with respect to the base, Z is the bottom magnet displacement with respect to the base, K_i are the coefficients of the linear springs, λ_i are the coefficients of the electromagnetic damping, and g is the downwards acceleration due to gravity. The collisions of the masses with the base are simulated by large spring forces, as described in 4.1, whenever the relative displacement between the mass and the base exceeded $\pm 3.4\text{cm}$. This simulation assumed that the masses were spaced far enough apart that they did not collide with each other.

The strategy for determining the optimal 2DOF harvester was to stack the optimal 1DOF nonlinear "half system" on top of the optimal 1DOF linear "half system". "Half system" refers to a system for which the total displacement constraints and masses are halved (i.e. reduced to 3.4 cm pk-pk and 30 g). Figure 4-23 shows the optimization surfaces for the linear "half" system. Figure 4-24 shows the optimization surfaces for the nonlinear "half" system. Since the full 2DOF nonlinear system (60 g mass, 6.8 cm pk-pk displacement system) will have negligible top and bottom EM damping and large EM middle damping, the most critical performance measure of the 1DOF "half" systems is large displacement, rather than large dissipated power. Then, when the large middle damping is added to the "full" system, the relative mass displacements is still likely to be large. In addition to simply combining the two "half" systems into one full 2DOF nonlinear system (60 g mass, 6.8 cm pk-pk displacement

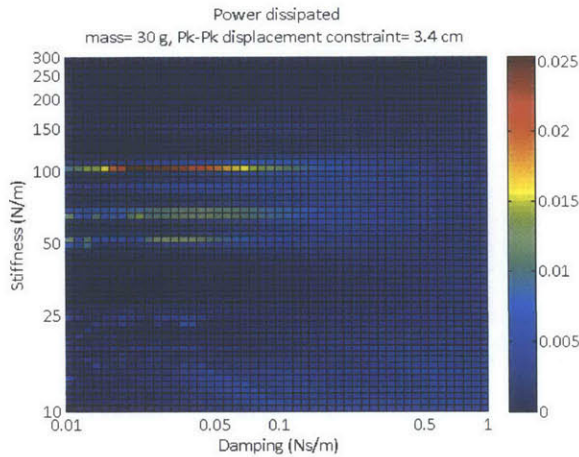
system), the middle and bottom linear springs are reoptimized in Figure 4-25. The time series for the motion of the system that harvests the most power is shown in Figure 4-26.



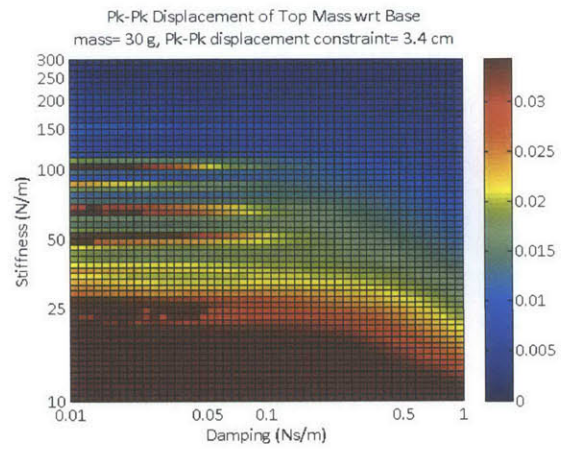
A) CAD rendering

B) component diagram

Figure 4-22: Nonlinear 2DOF Type1: Moderate EM damping system CAD rendering and component diagram. m_{Top} and m_{Bot} are the proof masses, λ_i are the electromagnetic damping coefficients, and F_s indicates the nonlinear spring force. K are the linear spring stiffnesses. The position of the top mass is x . The position of the bottom mass is z . The position of the base is h . Gravity acts downwards.

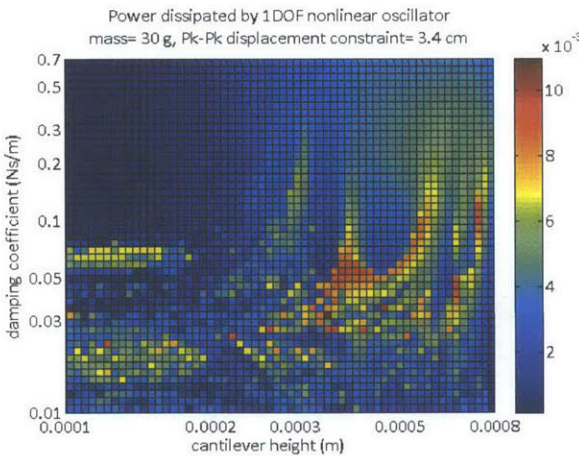


(a) Power

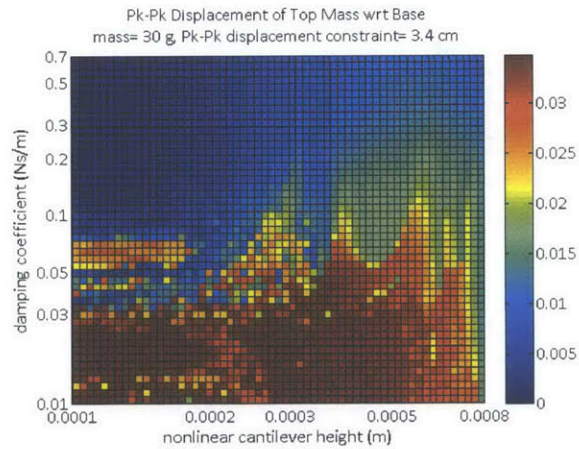


(b) Pk-Pk steady state displacement amplitude between mass and base

Figure 4-23: Power optimization for 1DOF linear "half" system ($\pm 1.7\text{cm}$ displacement constraints, 30g mass) excited by walking hip. Displacement plots are pk-pk displacement.

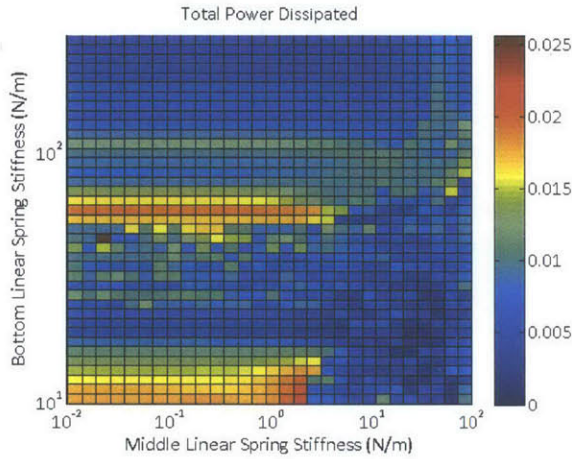


(a) Power

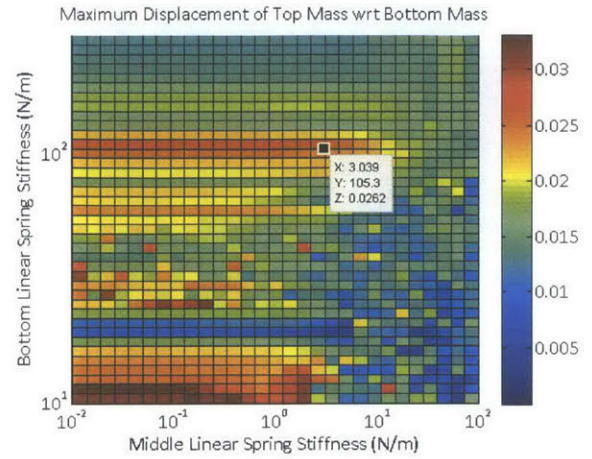


(b) Pk-Pk steady state displacement amplitude between mass and base

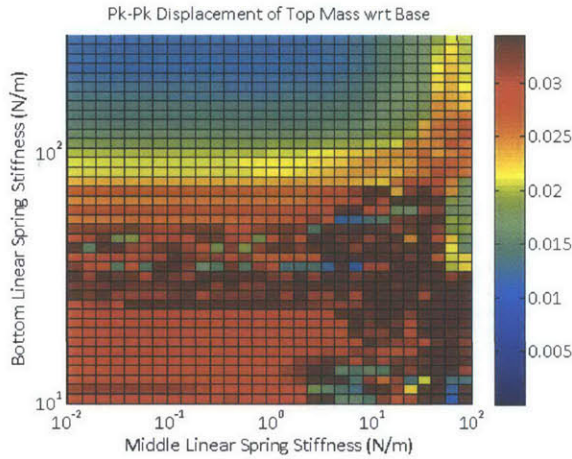
Figure 4-24: Power optimization for 1DOF nonlinear "half" system ($\pm 1.7\text{cm}$ displacement constraints, 30 g mass) excited by walking hip. Displacement plots are pk-pk displacement. $m = 30\text{g}$, cantilever height h and damping, λ are varied. The cantilever has a length of 10 cm, base dimension 4.76 mm, elastic modulus 160.6e9 Pa, surface length of 10 cm, surface maximum gap, $D = 1.5\text{cm}$, surface curve power $n = 3$. The mass overhangs the surface, so that the pk-pk displacement constraints are $\pm 1.7\text{cm}$.



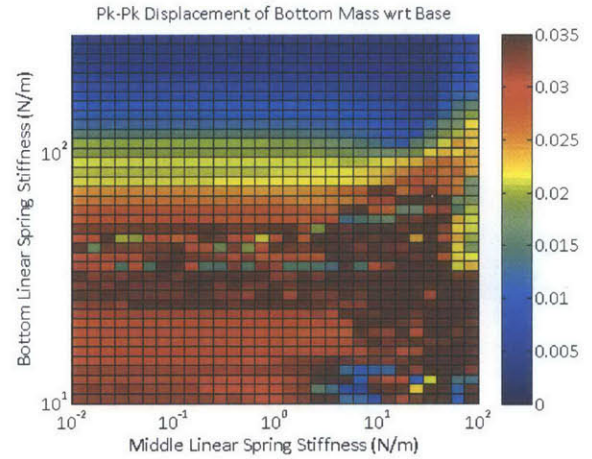
(a) Total Power



(b) Pk-Pk steady state displacement amplitude between top and bottom mass



(c) Pk-Pk steady state displacement amplitude between top mass and base



(d) Pk-Pk steady state displacement amplitude between bottom mass and base

Figure 4-25: Power Harvested by the 2DOF nonlinear type 1 system (moderate damping) when excited at hip while walking. Displacement plots are pk-pk displacement. $m_{Top} = M_{Bot} = 30g$, $K_{Top} = 100N/m$. The stiffnesses of a middle and bottom linear spring are varied. $\lambda_{Top} = \lambda_{bot} = 0.001Ns/m$, $\lambda_{Mid} = 0.4Ns/m$. Large values of linear spring stiffness result in chaotic dynamics, so those systems are ignored.

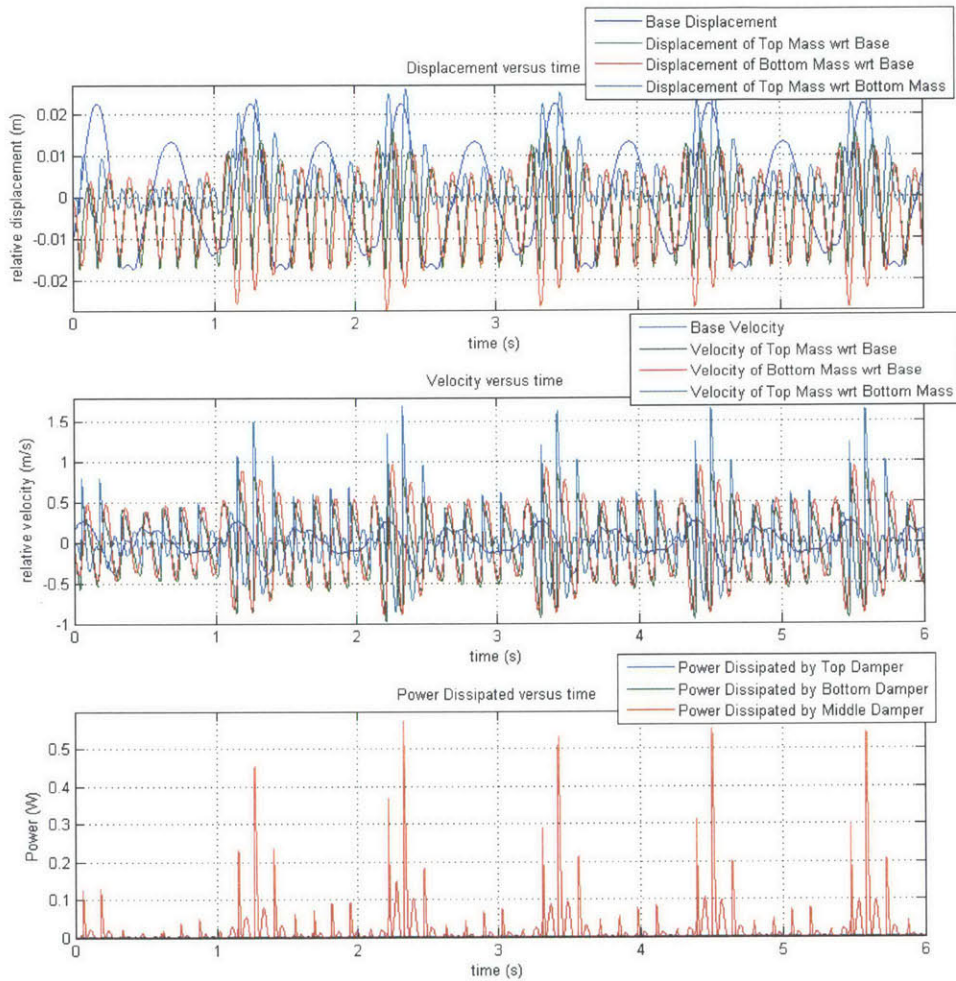


Figure 4-26: Time series of the second optimal 2DOF nonlinear energy harvester excited by hip walking motion. The parameters are: $m_{Top} = m_{Bot} = 30g$, $h_{Top} = 0.40mm$, $K_{bot} = 63N/m$, no middle spring, damping $\lambda_{Top} = \lambda_{bot} = 0.001Ns/m$, $\lambda_{Mid} = 0.4Ns/m$. Average dissipated power is 0.021 W.

Nonlinear Type 2: Large EM damping (1.6 Ns/m)

The second 2DOF nonlinear energy harvester examined has only the top nonlinear spring, middle nonlinear spring, and bottom linear spring. It has a middle damping coefficient of 1.6 Ns/m, while the top and bottom damping are negligible (0.001 Ns/m). An illustration of the harvester and its component diagram is shown in Figure 4-27. The equation of motion for the system is:

$$\begin{aligned} m_{Top}\ddot{X} &= -F_{S,Top}(X) - F_{S,Mid}(X - Z) - \lambda_{Top}\dot{X} - \lambda_{Mid}(\dot{X} - \dot{Z}) - m_{Top}\ddot{h} - m_{Top}g \\ m_{Bot}\ddot{Z} &= F_{S,Mid}(X - Z) - K_{Bot}Z - \lambda_{Bot}\dot{Z} + \lambda_{Mid}(\dot{X} - \dot{Z}) - m_{Bot}\ddot{h} - m_{Bot}g \end{aligned} \quad (4.5)$$

where m_{top} is the top magnet mass, m_{Bot} is the bottom magnet mass, X is the top magnet displacement with respect to the base, Z is the bottom magnet displacement with respect to the base, K_i are the coefficients of the linear springs, λ_i are the coefficients of the electromagnetic damping, and g is the downwards acceleration due to gravity. The collisions of the masses with the base are simulated by large spring forces, as described in Equations 4.1. This simulation assumed that the masses were spaced far enough apart that they did not collide with each other.

The strategy for determining the optimal 2DOF, Type 1 harvester was to modify the parameters of the optimal 1DOF linear harvester. The optimal 1DOF linear system had $mass = 60g$, linear spring stiffness $K = 205N/m$, electromagnetic damping coefficient $\lambda = 0.05Ns/m$, pk-pk mass amplitude constraint wrt the base of $6.8cm$. The starting point for this 2DOF nonlinear harvester was to set the bottom linear spring equal to the 1DOF optimal linear spring stiffness ($205N/m$), set the middle nonlinear spring to a very stiff value, and set the top nonlinear spring to a very weak value. The top and bottom damping coefficients were set to negligible values (0.001 Ns/m), and the middle damping coefficient was set to a large value. Then, the 2DOF dynamics nearly matched those of the 1DOF linear system. The 2DOF system's middle damping coefficient and middle nonlinear spring stiffness were then optimized in order to maximize the power dissipated by the middle electromagnetic damper (see Figure 4-28). The optimal system harvested 0.015 W. The time series of the system's motion is shown in Figure 4-30. Additionally, Figure 4-29 illustrates the nonlinear

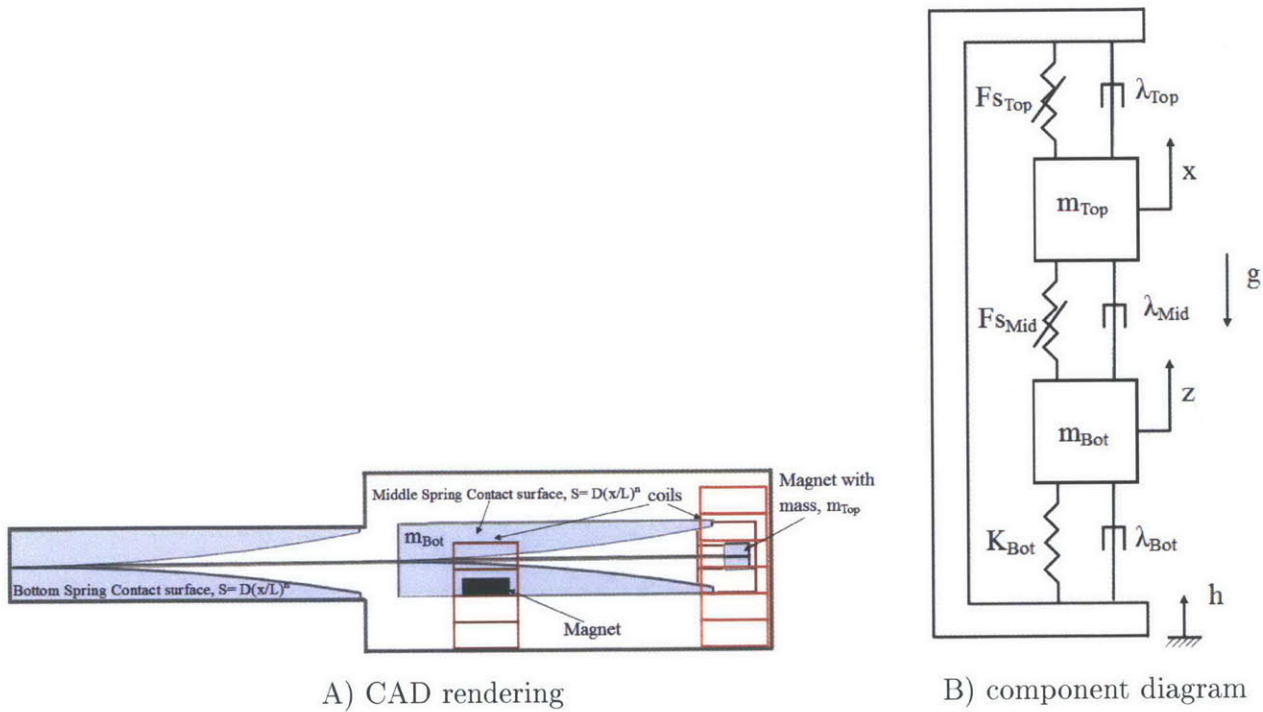
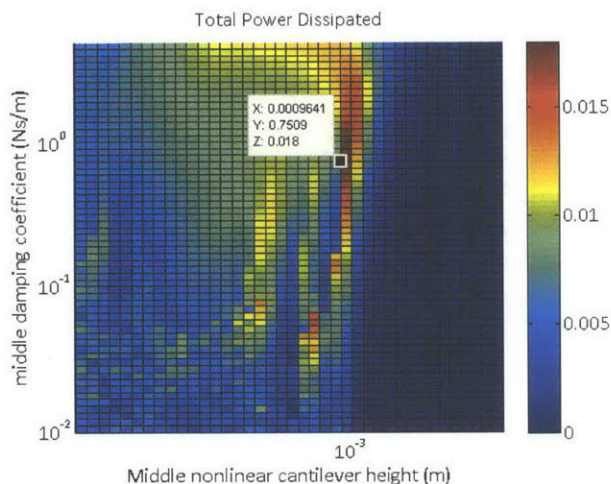
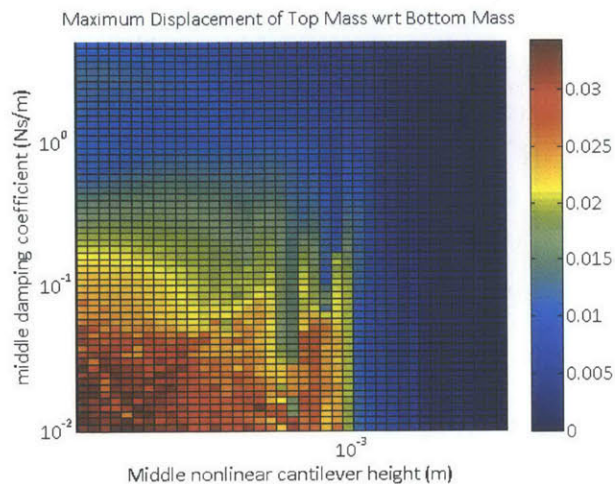


Figure 4-27: Nonlinear 2DOF Type1: Moderate EM damping system CAD rendering and component diagram. m_{Top} and m_{Bot} are the proof masses, λ_i are the electromagnetic damping coefficients, and F_s indicates the nonlinear spring force. K are the linear spring stiffnesses. The position of the top mass is x . The position of the bottom mass is z . The position of the base is h . Gravity acts downwards.

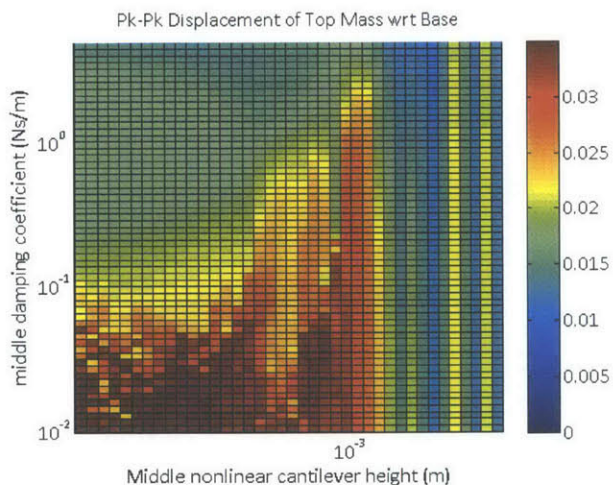
spring forces, modified to simulate collision at the deflections where the harvester casing is located.



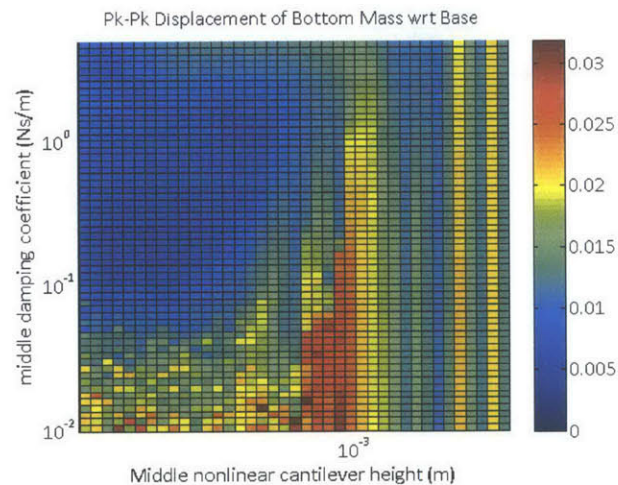
(a) Total Power



(b) Pk-Pk steady state displacement amplitude between top and bottom mass



(c) Pk-Pk steady state displacement amplitude between top mass and base



(d) Pk-Pk steady state displacement amplitude between bottom mass and base

Figure 4-28: Power Harvested by 2DOF nonlinear system excited at hip while walking. Displacement plots are pk-pk displacement. $m_{Top} = M_{Bot} = 30g$, $h_{Top} = 0.464mm$, $h_{mid} = 1mm$, (cantilever height ratios results in Top stiffness:bottom stiffness of 0.1), bottom linear spring stiffness $K = 205N/m$, damping $\lambda_{Top} = \lambda_{bot} = 0.001Ns/m$, $\lambda_{Mid} = 1.6Ns/m$. Average dissipated power is 0.0150 W.

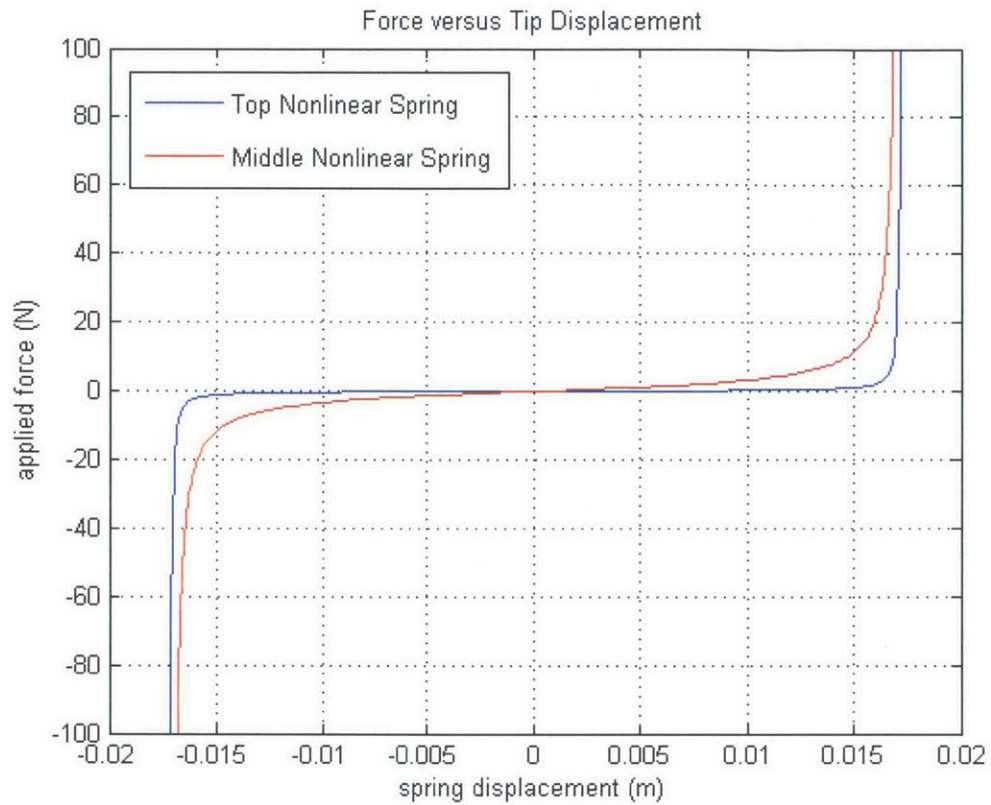


Figure 4-29: Modified force versus displacement curves for nonlinear springs in optimal nonlinear system 1. the curves are modified so that the force increases to very large values near and beyond the deflection values where an "elastic collision" occurs. These curves continue to displacements up to 0.25 m, where the force is on the order of $1e10$ N.

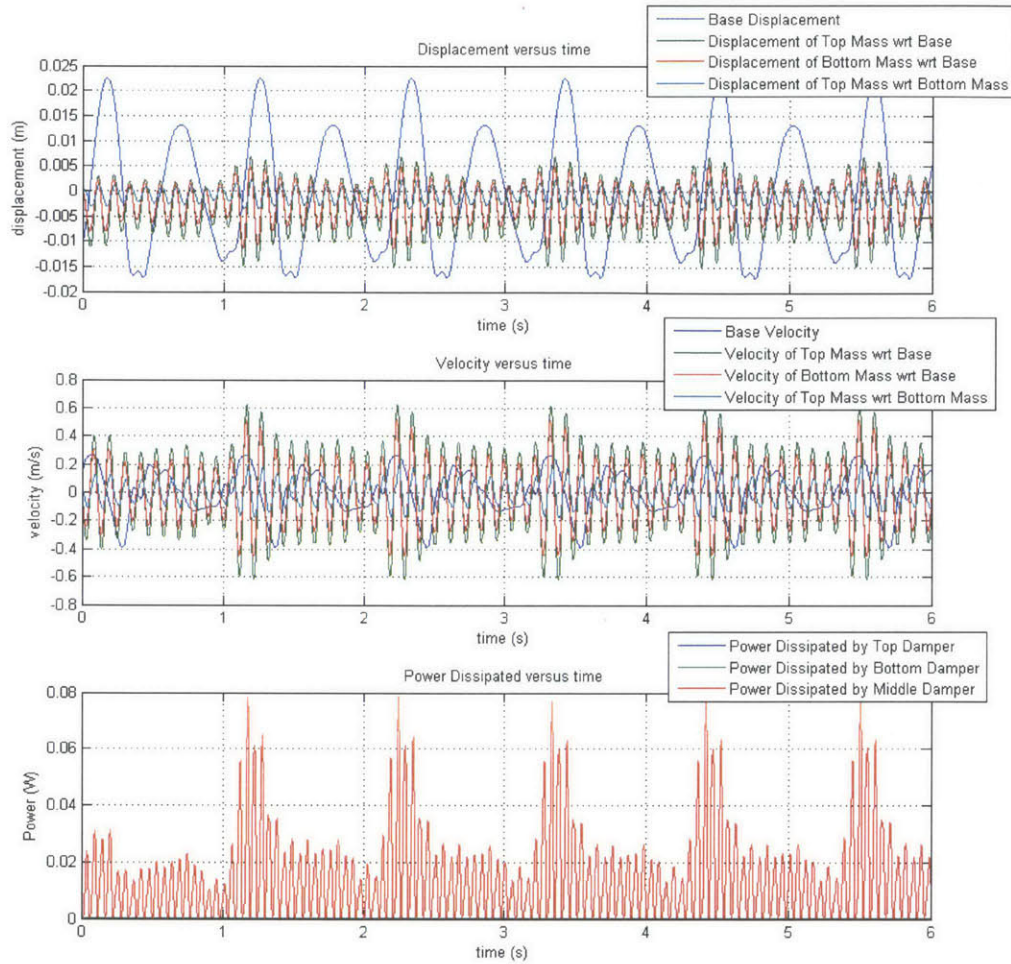


Figure 4-30: Time series of the first optimal 2DOF nonlinear energy harvester excited by hip walking motion. The parameters are: $m_{Top} = M_{Bot} = 30g$, $h_{Top} = 0.464mm$, $h_{mid} = 1mm$, (cantilever height ratios results in Top stiffness:bottom stiffness of 0.1), bottom linear spring stiffness $K = 205N/m$, damping $\lambda_{Top} = \lambda_{bot} = 0.001Ns/m$, $\lambda_{Mid} = 1.6Ns/m$. Average dissipated power is 0.0150 W.

4.4.2 Linear

The 2DOF linear systems consist of two 30g masses, three linear springs connecting the masses to the base in series, and three electromagnetic dampers in between the masses and base. An illustration and component diagram of the 2DOF linear system is shown in Figure 4-31. The equation of motion of this system is given by:

$$\begin{aligned}
m_{Top}\ddot{X} &= -K_{Top}X - K_{Mid}(X - Z) - \lambda_{Top}\dot{X} - \lambda_{Mid}(\dot{X} - \dot{Z}) - m_{Top}\ddot{h} - m_{Top}g \\
m_{Bot}\ddot{Z} &= -K_2Z + K_3(X - Z) - \lambda_{Bot}\dot{Z} + \lambda_{Mid}(\dot{X} - \dot{Z}) - m_2\ddot{h} - m_{Bot}g
\end{aligned} \tag{4.6}$$

where m_{top} is the top magnet mass, m_{Bot} is the bottom magnet mass, X is the top magnet displacement with respect to the base, Z is the bottom magnet displacement with respect to the base, K_i are the coefficients of the linear springs, λ_i are the coefficients of the electromagnetic damping, and g is the downwards acceleration due to gravity. The collisions of the masses with the base are simulated by large spring forces, as described in the introduction of this chapter. This simulation assumed that the masses were spaced far enough apart that they did not collide with each other.

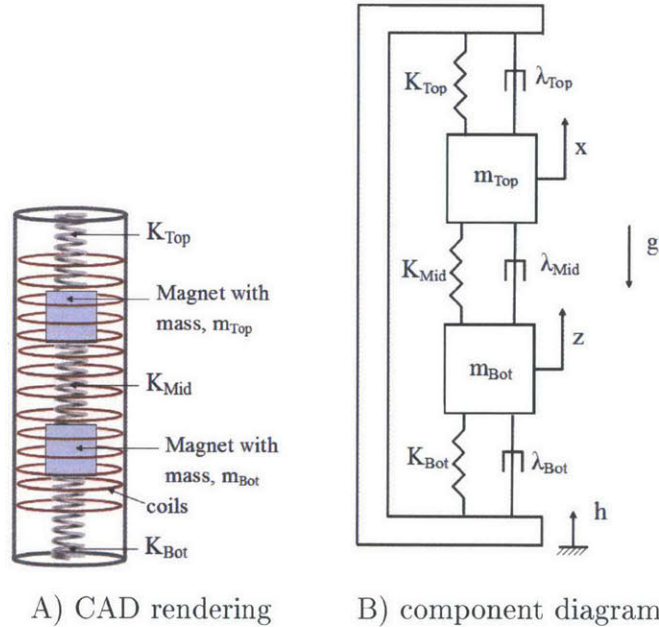


Figure 4-31: Linear 2DOF system component diagram. m_1 and m_2 are the proof masses, λ_1 , λ_2 , and λ_3 are the electromagnetic damping coefficients, and K_i indicate the linear spring stiffnesses. The position of the top mass is x . The position of the bottom mass is z . The position of the base is h . Gravity acts downwards.

Three different optimized 2DOF linear systems are included in this thesis. The first optimized 2DOF linear system was found by "stacking" two optimized "half" systems (systems

with half the total mass and displacement constraints) on top of each other. The 1DOF linear "half" system optimization surface is shown in Figure 4-23. This 2DOF system harvests more power than any other 2DOF system described in this thesis, but it also has the smallest damping, which makes it susceptible to large power losses when parasitic damping is present. Figure 4-32 shows the times series of this system's dynamics.

The second optimized 2DOF linear system was found by setting the top linear spring to the same value as the optimal 1DOF linear "half" system, setting the top and bottom damping coefficients to negligible values (0.001 Ns/m), setting the middle damping coefficient to the same value as that of the 2DOF nonlinear type 1 harvester (0.4 Ns/m), and varying the middle and bottom linear springs in order to maximize the harvested power. Figure 4-33 shows the optimization surface for the 2DOF linear harvester with 0.4 Ns/m electromagnetic damping, and Figure 4-34 shows the time series of the optimized system.

The third optimized 2DOF linear system was found in the same way, but the middle damping was set equal to the same value as the middle damping coefficient of the 2DOF nonlinear type 2 harvester (1.6 Ns/m). Figure 4-35 shows the optimization surface for the 2DOF linear harvester with 1.6 Ns/m electromagnetic damping, and Figure 4-36 shows the time series of the optimized system.

These methods were chosen in order to compare the power harvested by 2DOF linear systems with the same damping coefficients as the 2DOF nonlinear systems. We predicted that if the systems had the same amount of electromagnetically-induced damping, then they would have the similar robustness to added parasitic mechanical damping. This prediction is investigated in Figure 4-40 in Section 4.5.

System with small electromagnetic damping: 0.05 Ns/m

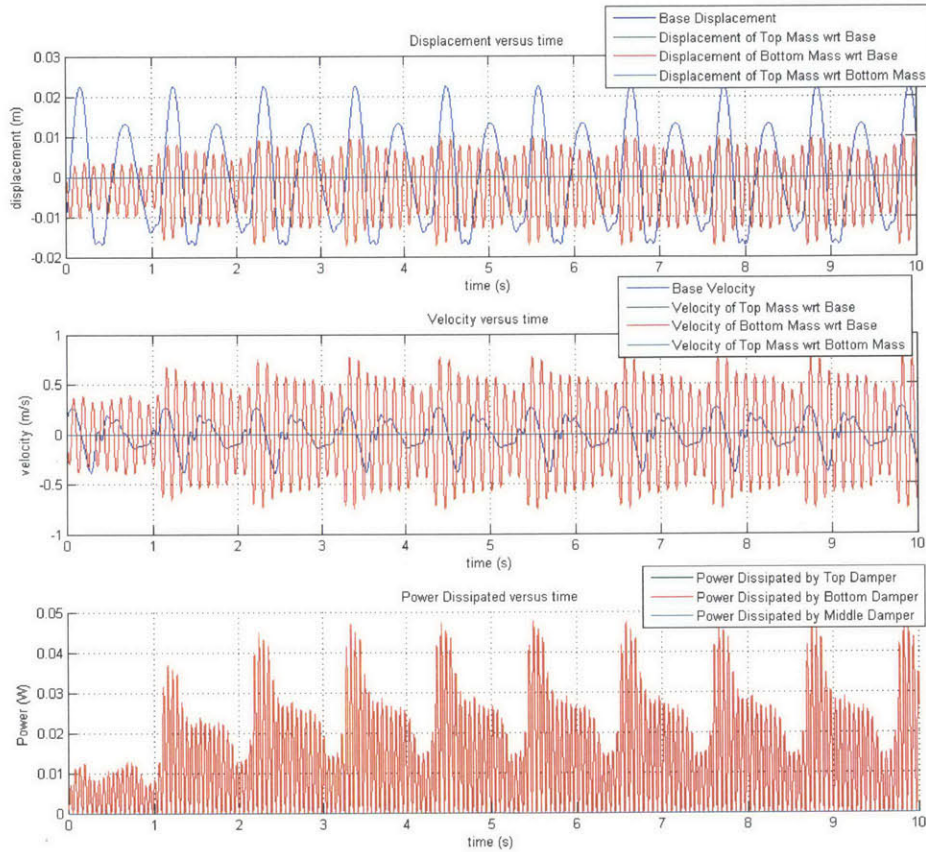
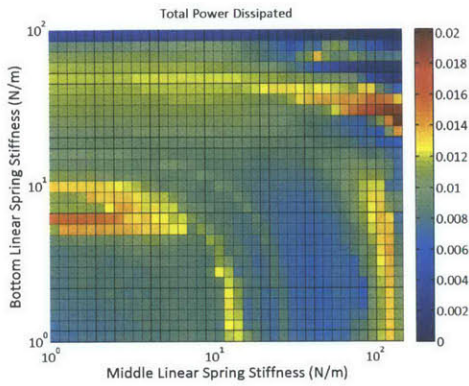
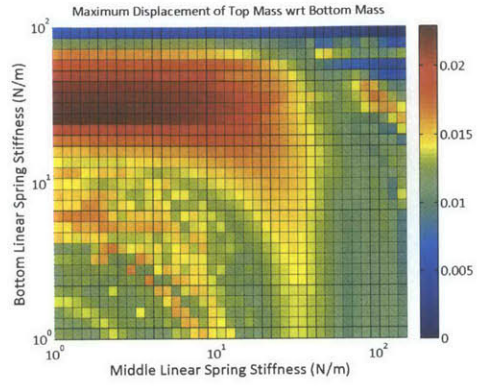


Figure 4-32: Time series of Optimal 2DOF linear energy harvester with low damping when excited by hip walking motion. The parameters are: $mass_{Top} = 30g$, $mass_{Bottom} = 30g$, $K_{Top} = 100N/m$, $K_{Bottom} = 100N/m$, $K_{Mid} = 0N/m$, $\lambda_{Top} = \lambda_{Bottom} = 0.05Ns/m$. $\lambda_{Mid} = 0Ns/m$. This configurations represents two "stacked" 1DOF linear half-systems, for which the optimization surface is shown in Figure 4-23. Allowable pk-pk relative displacement of masses to the base is 3.4 cm. The masses do not collide with each other. The harvested power is 0.031 W.

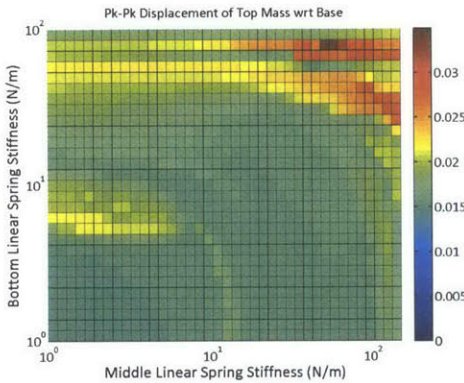
System with moderate electromagnetic damping: 0.4 Ns/m



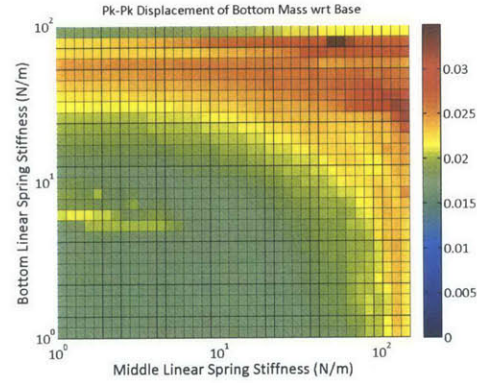
(a) Total Power



(b) Pk-Pk steady state displacement amplitude between top and bottom mass



(c) Pk-Pk steady state displacement amplitude between top mass and base



(d) Pk-Pk steady state displacement amplitude between bottom mass and base

Figure 4-33: Power Harvested by 2DOF linear system, with moderate electromagnetic damping when excited at hip while walking. $m_1 = m_2 = 30g$. Top spring, $K_{Top} = 100N/m$. The top and bottom dampers have $\lambda = 0.001Ns/m$. The middle damper has $\lambda = 0.4Ns/m$. Maximum allowable relative displacement between the masses and base: 1.7cm in each direction. Displacement plots are pk-pk displacement.

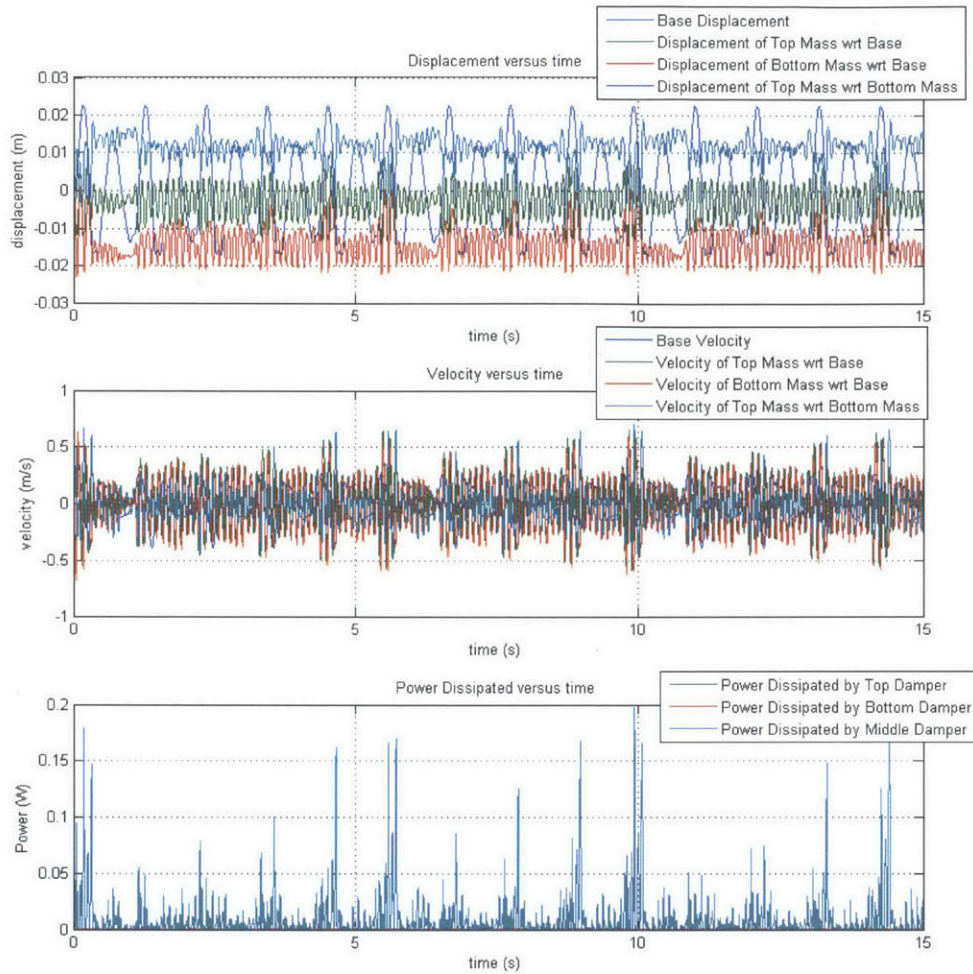
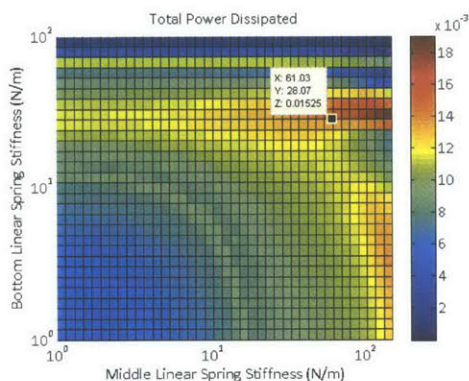
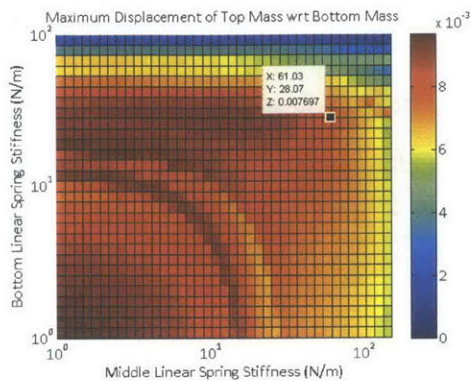


Figure 4-34: Time series of Optimal 2DOF linear energy harvester, with moderate damping, excited by hip walking motion. The parameters are: $m_1 = m_2 = 30g$. Top spring, $K_{Top} = 100N/m$, middle spring, $K_{Mid} = 0N/m$, bottom spring, $K_{Bot} = 5.7N/m$. The top and bottom dampers have $\lambda = 0.001Ns/m$. The middle damper has $\lambda = 0.4Ns/m$. Maximum allowable relative displacement between the masses and base: $1.7cm$ in each direction. Allowable pk-pk relative displacement of masses to the base is 3.4 cm . The masses do not collide with each other. The harvested power is 0.010 W .

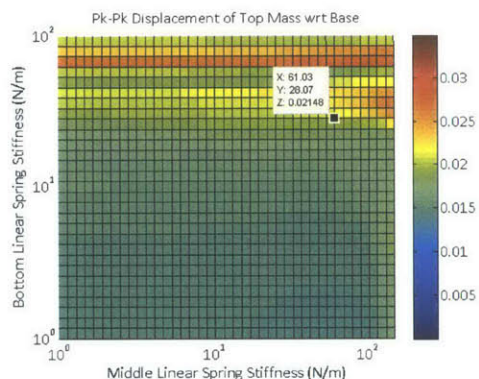
System with large electromagnetic damping: 1.6 Ns/m



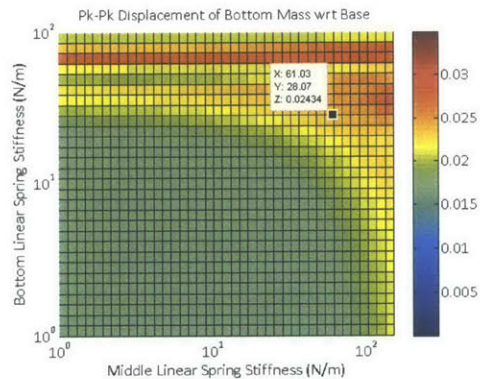
(a) Total Power



(b) Pk-Pk steady state displacement amplitude between top and bottom mass



(c) Pk-Pk steady state displacement amplitude between top mass and base



(d) Pk-Pk steady state displacement amplitude between bottom mass and base

Figure 4-35: Power Harvested by 2DOF linear system, with large electromagnetic damping when excited at hip while walking. $m_1 = m_2 = 30g$. Top spring, $K_{Top} = 100N/m$. The top and bottom dampers have $\lambda = 0.001Ns/m$. The middle damper has $\lambda = 1.6Ns/m$. Maximum allowable relative displacement between the masses and base: 1.7cm in each direction. Displacement plots are pk-pk displacement.

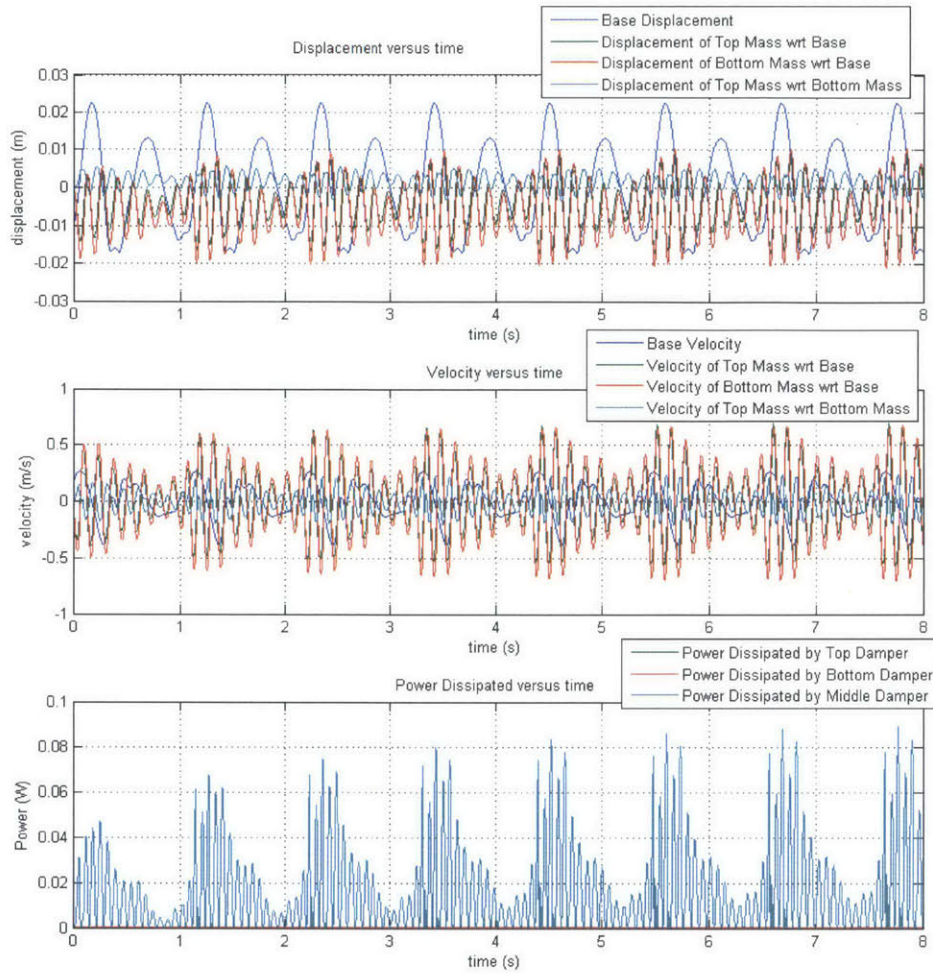


Figure 4-36: Time series of Optimal 2DOF linear energy harvester, with moderate damping, excited by hip walking motion. The parameters are: $m_1 = m_2 = 30g$. Top spring, $K_{Top} = 100N/m$, middle spring, $K_{Mid} = 61N/m$, bottom spring, $K_{Bot} = 28N/m$. The top and bottom dampers have $\lambda = 0.001Ns/m$. The middle damper has $\lambda = 1.6Ns/m$. Maximum allowable relative displacement between the masses and base: $1.7cm$ in each direction. Allowable pk-pk relative displacement of masses to the base is 3.4 cm. The masses do not collide with each other. The harvested power is 0.0176 W.

4.5 Energy Harvester Performance Summary

This section summarizes the optimal performance of all the different energy harvesters described in this chapter. The optimal energy harvester should maximize the power harvested

for a specific excitation signal (the hip walking signal, in this thesis). It should be adaptive to different people's different strides and robust to a person's slight changes in pace. Additionally, the harvested power should not significantly decrease when parasitic mechanical damping is present. This section also shows the progress that this thesis made toward demonstrating that a nonlinear system harvests more power than a linear system when the excitation signal has increasing amounts of noise.

The harvesters considered include: the 1DOF linear and nonlinear harvesters optimized for the walking foot, running foot, and walking hip excitations; and the 2DOF linear and nonlinear harvester types optimized for the walking hip.

Figure 4-37 shows the powers harvested by the 8 energy harvesters optimized for hip walking motions. Figure 4-37 also illustrates these harvesters' adaptivity to different walking motions. Figure 4-38 shows the power harvested by these systems when the walking hip motion frequency is rescaled. That is, Figure 4-38 illustrates the harvesters' robustness to slight variations in the walking signal. Figure 4-39 shows the power per system volume of each optimized system for the walking hip. Figure 4-40 shows how the power harvested is affected by parasitic damping. Finally, Figure 4-41 shows the optimized system power normalized by the excitation signal power versus signal noise for the 12 optimal harvester-signal pairs.

The conclusions regarding the five performance measures are as follows:

Adaptivity. Figure 4-37 shows that the 1DOF linear system with low damping harvests the most power when excited by the hip motion. However, when the excitation signal is varied to different types of motion (i.e. hip, running or foot walking), then the 2DOF nonlinear, type 2 system (top, middle springs nonlinear and $\lambda_{EM} = 1.6Ns/m$) is more adaptive than any other system considered.

Robustness. The results regarding the robustness of the harvesters to time-rescaled walking hip motion signals (figure 4-38) are mostly inconclusive, but the 2DOF nonlinear, type 1 harvester (top spring nonlinear and $\lambda_{EM} = 0.4Ns/m$) generally harvests more power than any other system for time rescalings of 1.3-2.

Power per Volume. Figure 4-39 shows that the nonlinear spring analyzed in this thesis is very space-inefficient. A linear oscillator requires only about one-fourth the volume.

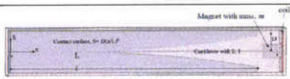
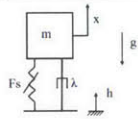
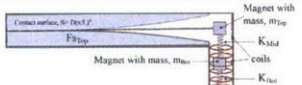
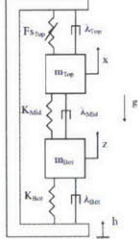
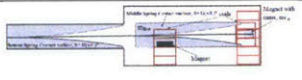
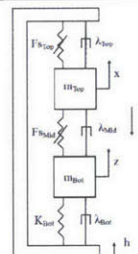
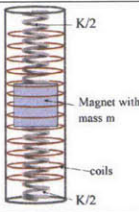
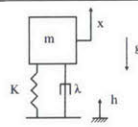
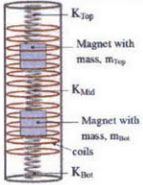
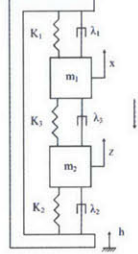
Power versus parasitic damping. Figure 4-40 shows that the power harvested by

the 2DOF nonlinear harvester, type 2 ($\lambda_{EM} = 1.6Ns/m$), and the 2DOF linear harvester with ($\lambda_{EM} = 0.13Ns/m$) decays the least when parasitic damping is present. Although this 2DOF linear harvester's power decays very little, it initially harvests the smallest amount of power out of all the harvesters optimized for the walking hip motion excitation signal.

Power versus signal noise. Figure 4-41 shows that the 1DOF linear harvester with low damping optimized for the human motions of this thesis always harvests more power than any other system. However, the difference in power harvested by the 1DOF linear and 1DOF nonlinear harvesters decreases as the signal noise increases from foot walking to foot running.

Based on these performance measures, the main advantages of the 2DOF nonlinear energy harvester over the 1DOF linear energy harvester are that it can be designed to be more adaptive to different excitation signals and resistant to power decay when parasitic damping is present (the 2DOF nonlinear harvester, type 2 ($\lambda_{EM} = 1.6Ns/m$)). These significant advantages are caused by the 2DOF nonlinear system harvesting its optimal power at large electromagnetic damping coefficients, whereas the optimal electromagnetic damping coefficient for the linear system occurs at low electromagnetic damping coefficient.

Table 4.3: Summary of human motion nonlinear energy harvesters studied in thesis. The first column lists the systems' optimal parameters for base excitation by the hip walking motion (the signal in Figure 4-3). For the 1DOF systems, the mass is 60 g. For the 2DOF systems, each mass is 30 g. For all of the nonlinear springs, the nonlinear spring's surface has the same length as the cantilever, and the surface's power curve is $n = 3$. For the 1DOF nonlinear system, the spring's maximum surface gap, D is 3 cm (mass overhang allows the mass to travel $\pm 6.8\text{cm}$ wrt the surface). For the 2DOF nonlinear systems, each nonlinear cantilever/surface spring has a maximum surface gap of 1.5 cm (mass overhang allows the mass to travel $\pm 3.4\text{cm}$ wrt the surface)

System	CAD rendering	Component diagram	Volume (cm^3)
1DOF Nonlinear: $\lambda = 0.136\text{Ns/m}$, cantilever length 15.7cm , cantilever rigidity $EI = 0.192\text{Nm}^2$			50.8
2DOF Nonlinear: Type 1, Moderate Damping: $\lambda_{Top} = \lambda_{Bot} = 0.001\text{Ns/m}$, $\lambda_{Mid} = 0.4\text{Ns/m}$, top spring cantilever length 10cm , $EI_{Top} = 4.08e - 4\text{Nm}^2$, $K_{Mid} = 0\text{N/m}$, $K_{Bot} = 63\text{N/m}$			22
2DOF Nonlinear: Type 2, Large Damping: $\lambda_{Top} = \lambda_{Bot} = 0.001\text{Ns/m}$, $\lambda_{Mid} = 1.6\text{Ns/m}$, top spring cantilever length 10cm , $EI_{Top} = 6.37e - 4\text{Nm}^2$, middle spring cantilever length 10cm , $EI_{Mid} = 6.26e - 3\text{Nm}^2$, $K_{Bot} = 205\text{N/m}$			49
1DOF Linear: Low Damping ($\lambda = 0.05\text{Ns/m}$. $K = 205\text{N/m}$). Moderate Damping ($\lambda = 0.15\text{Ns/m}$. $K = 205\text{N/m}$)			12
2DOF Linear: Low Damping ($\lambda_{Top} = \lambda_{Bot} = 0.05\text{Ns/m}$. $\lambda_{Mid} = 0\text{Ns/m}$. $K_{Top} = K_{Bot} = 100\text{N/m}$. $K_{Mid} = 0\text{N/m}$). Moderate Damping ($\lambda_{Top} = \lambda_{Bot} = 0.001\text{Ns/m}$. $\lambda_{Mid} = 0.4\text{Ns/m}$. $K_{Top} = 100\text{N/m}$, $K_{Mid} = 0\text{N/m}$, $K_{Bot} = 5.7\text{N/m}$). Large Damping ($\lambda_{Top} = \lambda_{Bot} = 0.001\text{Ns/m}$. $\lambda_{Mid} = 1.6\text{Ns/m}$. $K_{Top} = 100\text{N/m}$, $K_{Mid} = 61\text{N/m}$, $K_{Bot} = 28\text{N/m}$).			12

4.5.1 Adaptivity to different excitation signals

Figure 4-37 compares the harvesters' adaptivity by plotting the power harvested by each system when its base is excited by different human motion signals, in addition to the hip walking signal for which they were optimized.

Figure 4-37 shows that the 1DOF linear system with light damping harvests the most power when excited by the hip walking signal. The next system that harvests the most power is the 2DOF linear system with low damping. As described in Section 4.5.4, however, low damping makes the power harvested by the system significantly decrease when parasitic damping is present. Out of the systems with electromagnetic damping coefficients that are robust to parasitic damping ($\lambda > 0.05Ns/m$), the 1DOF nonlinear system harvests the most power; slightly more power than the 1DOF linear system with about the same damping.

Based on the average power harvested by these systems for the five different excitation signals, the 2DOF nonlinear type 2 oscillator (top and bottom nonlinear springs, large damping, $\lambda = 1.6Ns/m$) is the most adaptive system. While this system does not harvest the most power for the actual hip walking signal, it harvests significantly more power than the most powerful walking-hip-quickly linear system (15%) and most powerful hip-running system (76%) when it is excited by the hip walking quickly and running, respectively. When only the hip motions are considered (i.e. not considering the foot motion), then the 2DOF nonlinear type 2 oscillator harvests an average of 71% more power than the 1DOF harvesters.

When the foot motion is also considered, then the 2DOF nonlinear type 2 oscillator harvests an average of 11% more power than the most robust linear harvester. The linear harvester may be more robust than the nonlinear harvester for the foot motion because the large ratio in base displacement to mass constraints with respect to the base causes the system's vibro-impact behavior to dominate the linear spring behavior (this is discussed in more detail in 4.2.4).

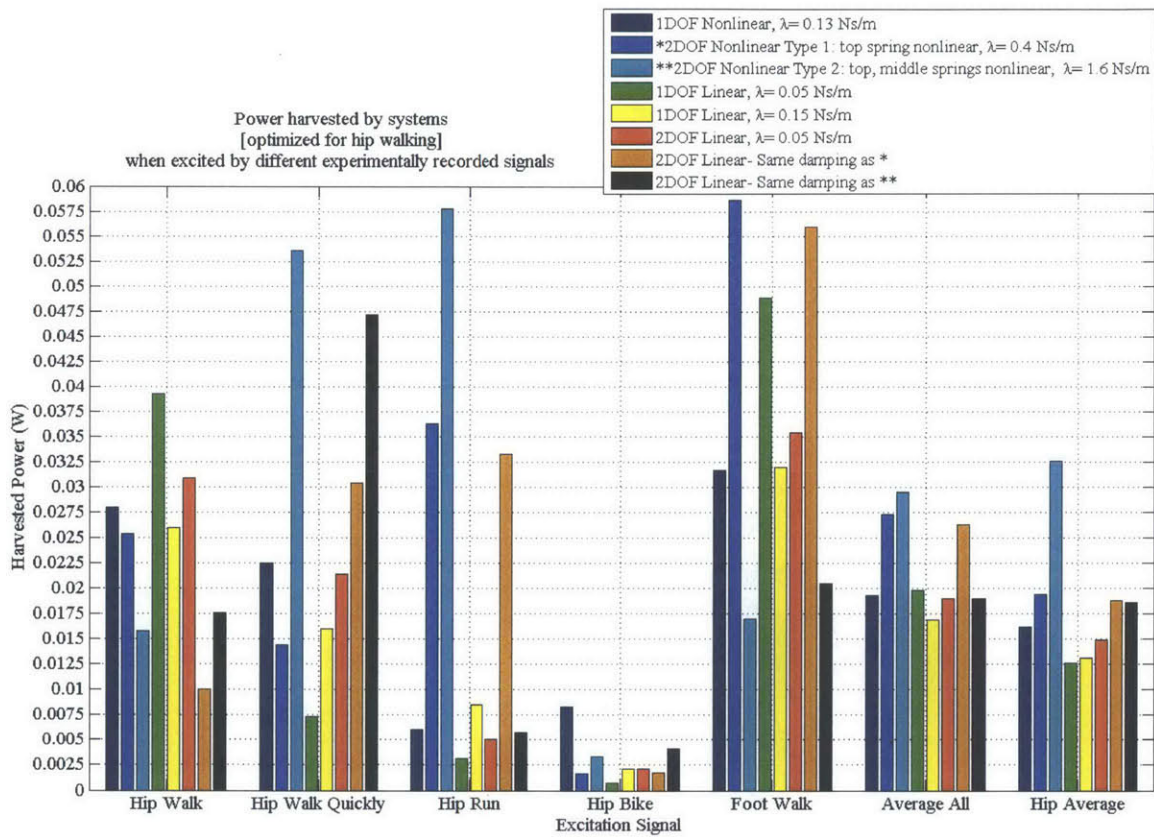


Figure 4-37: Power harvested by different systems optimized for hip walking when excited by different experimentally recorded motions.

4.5.2 Robustness to an excitation signal's small frequency variations

Figure 4-38 compares the harvesters' robustness to variations in the hip walking signal. Figure 4-38 rescales the frequencies of the hip motion to 0.5-2 times the experimentally recorded rate (roughly 0.5-2 steps per second per foot instead of 1 step/sec/foot), which [14] describes as typical human walking frequencies. Figure 4-38 does not show any linear or nonlinear system consistently harvesting significantly more power than the other systems over a range of frequencies. The plot does suggest that the 2DOF nonlinear, type 1 harvester (with a top and middle nonlinear spring, and damping $\lambda = 0.4Ns/m$) tends to harvest more power than any other system over rescalings of 1.3-2 times the walking frequency.

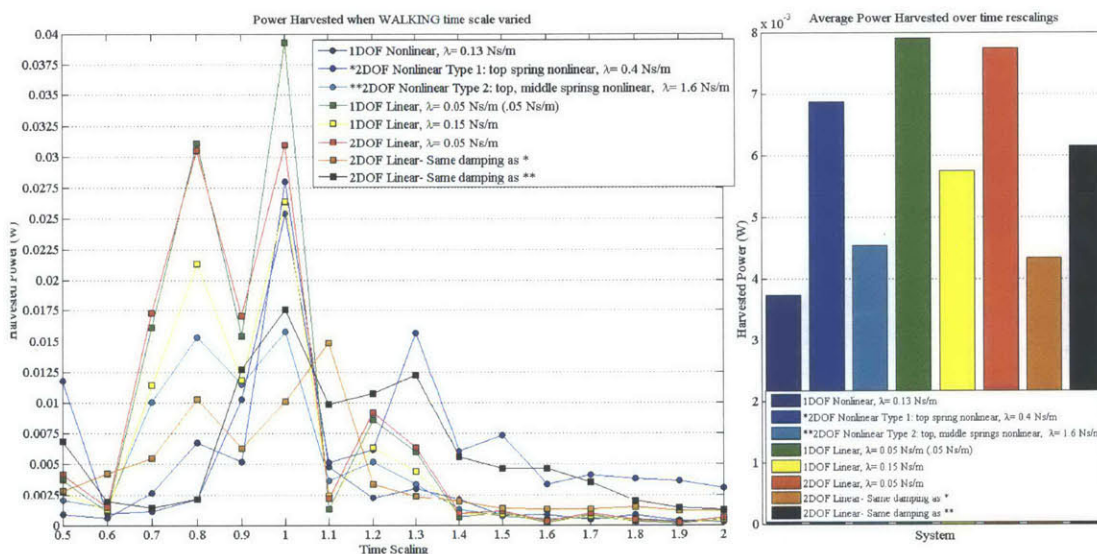


Figure 4-38: Power harvested by different 2DOF harvesters when the base is excited by a time-rescaled hip walking signal (e.g. time scale of 2 indicates the steps occur twice as fast). The left subfigure shows each system's average power for all of the time scales. The optimal 1DOF walking harvesters are included for reference.

4.5.3 Power per Volume

Figure 4-39 normalizes the power harvested by each system when excited by the walking hip signal versus rough estimates of the harvesters' volumes.

The volumes here are just rough estimates. For all of the linear systems, it is assumed that the harvesters use helical springs with outer diameters of 1.5 cm. Then the volume is estimated as the cross-sectional area of this spring x the pk-pk allowable mass displacement (6.8 cm). The 1DOF nonlinear harvester's volume is based on the cantilever's length x width x mass displacement amplitude. The volume of the 2DOF nonlinear, type 1 harvester (top spring is nonlinear, middle and bottom springs are linear) was estimated by adding the volume of the top nonlinear spring to the volume of the helical springs with 6.8 cm pk-pk displacement (Volume= cantilever length x width x top mass displacement (3.4 cm pk-pk) + helical spring cross section x 6.8cm mass displacement pk-pk). The volume of the 2DOF nonlinear, Type 2 harvester (top and middle springs nonlinear, bottom spring linear) was estimated by adding the volume of a nonlinear spring with a small magnet mass (Volume= cantilever length x cantilever width x mass pk-pk displacement constraints) and the volume of a nonlinear spring with a large-volume surface system as the mass (Volume= cantilever length x cantilever width x (mass pk-pk displacement constraints+3.4 cm mass height). Please refer to the 2DOF Nonlinear: Type 2 illustration in Table 4.3).

Since the helical springs require much less space than the nonlinear cantilever-surface springs, their power/volume is much higher. Figure 4-39 underlines the necessity for future work on this project to include redesigning the nonlinear spring to be more space efficient. For example, the contact surface stiffening effect could be employed with a helical spring.

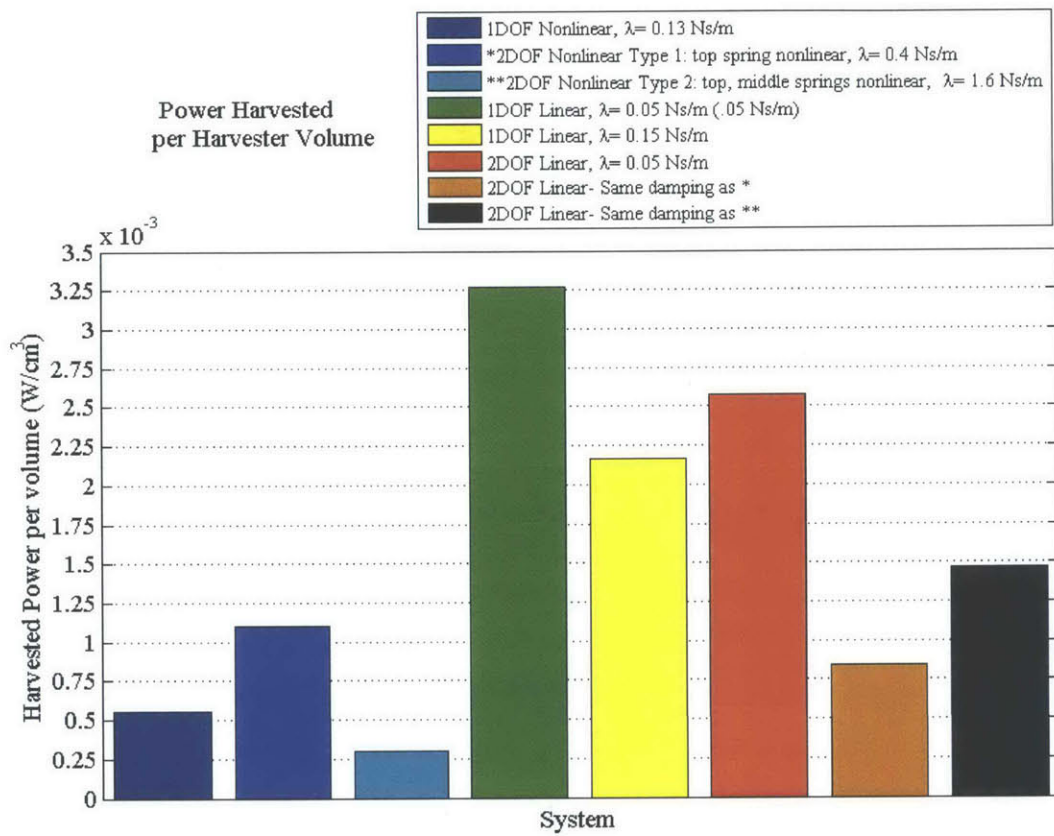


Figure 4-39: Power harvested per system volume when the base is excited by the hip walking signal (Figure 4-3 shows this excitation signal).

4.5.4 Power versus parasitic damping

Figure 4-40 shows the effect of mechanical damping on the power harvested by each system that was optimized for the hip walking signal. The experiments show that the mechanical damping for the 1DOF harvester can be on the order of 0.02 Ns/m.

For the 1DOF systems, the harvested power was calculated by multiplying the optimal harvested power by the fraction of electromagnetic damping to total damping ($\lambda_{Total} = \lambda_{EM} + \lambda_{Mech}$, where the total damping was left equal the optimal damping that was previously found to dissipate the most power from the system. That is, the systems were not resimulated, but the power converted to electricity was reduced.

For the 2DOF systems, the systems were resimulated with the half the added mechanical damping as additional damping in between each of the masses and the base (that is, the new damping coefficients were $\lambda_{Top} = \lambda_{Bot} = \lambda_{EM} + \frac{1}{2}\lambda_{Parasitic}$). For the 2DOF linear system with small damping, these $\lambda_{EM} = 0.05Ns/m$. For the other 2DOF systems, $\lambda_{EM} = 0.001Ns/m$. Then, the harvested power was the power harvested by the middle electromagnetic damping coefficient, $\lambda_{EM,Middle}$. $Power_{Harvested} = \lambda_{EM,Middle}(\dot{x} - \dot{z})^2$.

The left half of Figure 4-40 shows the power harvested by the systems when the parasitic damping on the masses is increased from 0 Ns/m to 0.06 Ns/m (0.03 Ns/m on each mass of the 2DOF systems). The right half of Figure 4-40 shows the fraction of theoretical power (0 Ns/m parasitic damping) that is actually harvested when 0.06 Ns/m parasitic damping is present.

Figure 4-40 shows that the 1DOF linear harvester power reduces to 0 W when 0.05 Ns/m parasitic damping is present. The 2DOF linear oscillator with $\lambda = 0.4Ns/m$ has the least power decay, but it harvests the least power for 0 Ns/m parasitic damping, and when 0.06 Ns/m damping is present, it harvests the least nonzero amount of power. After the 2DOF linear oscillator with electromagnetic damping $\lambda = 0.4Ns/m$, the harvester that has the least power decay at 0.06 Ns/m parasitic damping is the 2DOF nonlinear harvester with 1.6 Ns/m damping: with this large amount of parasitic damping, it still harvests 77% its optimized power. It makes sense that the 2DOF nonlinear harvester with large electromagnetic damping retains most of its power while the 1DOF linear harvester loses

most of its power when parasitic damping is present because 0.06 Ns/m parasitic damping is only 4% the 2DOF nonlinear harvester's electromagnetic damping while that is more than the 1DOF nonlinear harvester's electromagnetic damping.

The power harvested by the 2DOF linear harvester with 0.05 Ns/m damping does not decay as much as the 1DOF linear harvester with 0.05 Ns/m damping. This might be an effect of the significant vibro-impact behavior on the linear systems.

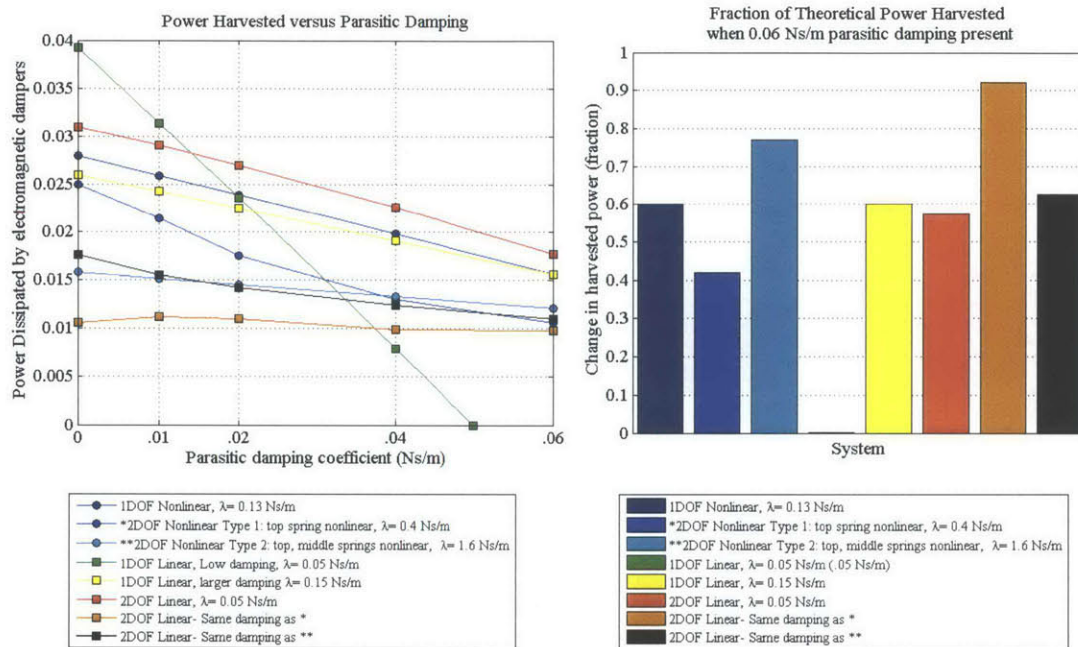


Figure 4-40: Effect of parasitic damping on optimal power harvested. Parasitic damping on the order of $0.05Ns/m$ greatly decreases the power harvested by the 1DOF linear system because this system requires total damping $\leq 0.05Ns/m$ for effective energy dissipation (as can be seen in Figure 4-14).

4.5.5 Power versus signal noise

Figure 4-41 shows the optimized system power normalized by the excitation signal power versus signal noise for the 12 optimal harvester-signal pairs of this thesis. The signal power is based on the root mean square (RMS) of the human motion velocity. The signal noise is based on the ratio of the dominant frequency signal's RMS velocity to the entire signal's RMS velocity. These RMS values are listed in Table 4.1 in Section 4.1.

For this plot, the 1DOF linear system represents the maximum power that can be harvested. The dip in normalized power for the foot motions might be related to the increase in base displacement for the same mass constraints with respect to the base. That is the regimes of base excitation are different between the hip and the foot. This difference is especially highlighted by the different normalized powers harvested for the walking hip and walking foot excitation, which have nearly the same noise. Also, even though the signals have nearly the same noise, the 1DOF linear system excited by the walking hip motion harvests 29% more power than the 1DOF nonlinear system, while the 1DOF linear system excited by the walking foot motion harvests 23% more power than the 1DOF nonlinear system.

Since the regimes are different, the plot is mostly inconclusive when comparing the nonlinear and linear harvester performances across the hip and foot excitation signals. However, the plot does show that as noise increases from the walking foot to the running foot, the additional power harvested by the 1DOF linear system over the nonlinear system decreases from 23%, to 9%.

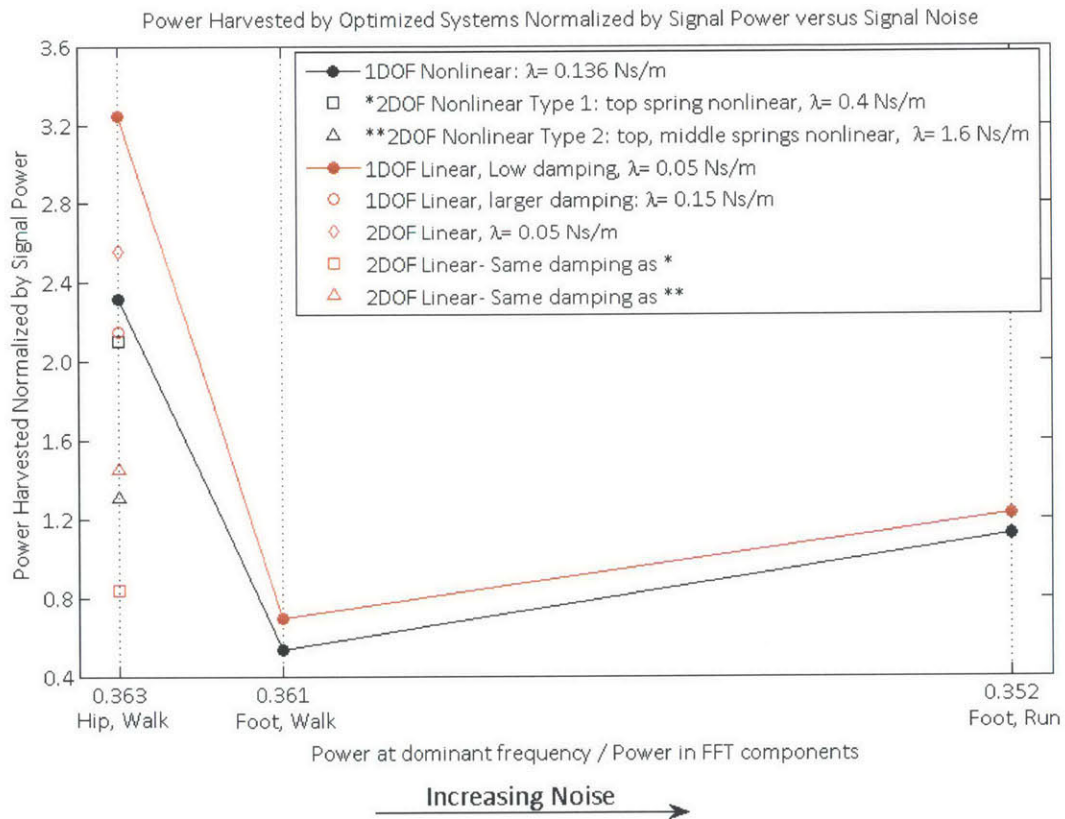


Figure 4-41: Optimized power (normalized by signal power) versus signal noise for the 12 optimized signal-system configuration pairs studied in this thesis. Future work on this project may include investigating other system configurations excited by the foot motions.

Chapter 5

Electromagnetic Theory

The energy harvester optimization in Chapter 4 simulated arbitrary electromagnetic damping coefficients without considering the electromagnetism theory. This chapter begins to examine the electromagnetic damping coefficients generated by different magnet and coil parameters. Future work for this project will include further theoretical investigation and actual fabrication of the electromagnetic systems; ultimately leading to the test of a complete energy harvester prototype.

This chapter describes the magnet-across-coil electromagnetic damping system with the schematic shown in Figure 5-1. First, it describes the equations used to simulate the electromagnetically-induced damping. Then, it describes the constraints on the electromagnetic system parameters. Thirdly, it shows several optimization surfaces of the electromagnetic damping produced by varied parameters satisfying the constraints.

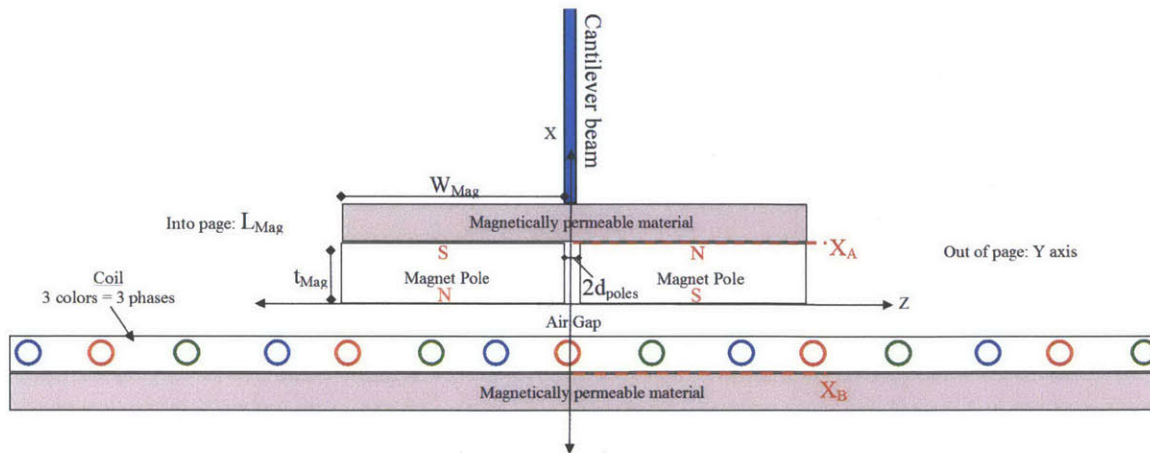


Figure 5-1: Magnet-Over-Coil System Diagram. The coil loops are in the Y-Z plane.

5.1 Theory

The theory is based on the Masters theses of Aparna Jonnalagadda [5] and Zach Trimble [23]. An overview of the calculations and Matlab code is given below.

5.1.1 Calculate the magnetic field

The magnetic flux density in the x-direction, B_x along z due to the magnet at the coil surface is calculated. The magnetic field generated by the coil current is ignored because the "magnetic potential created by the coil current is several orders of magnitude lower than that created by the magnets" (Jonnalagadda, 62). The Matlab code calculates B_x along z when the magnet is centered at $x = 0$.

The first step is to calculate the magnetic charge density, σ_M , at the interface between the magnets and air. The magnetic charge density depends on the magnet's # of poles, width, and length. This theory assumes a two-dimensional electromagnetic field in the X-Z plane, which is unaffected by L_{Mag} (L_{Mag} does affect the flux through the coil).

According to calculations in Aparna Jonnalagadda's masters thesis (page 32-36), the magnetic charge density at the interface between the magnets and air can be represented by Fourier coefficients. That is:

$$\sigma_M = a_{0(\sigma_M)} + \sum_{k=1}^{\infty} [a_{k(\sigma_M)} \cos(\frac{2\pi kz}{Z}) + b_{k(\sigma_M)} \sin(\frac{2\pi kz}{Z})] \quad (5.1)$$

where $Z = 2(2d_{poles} + W_{mag})$ is the spatial period of the magnetic charge density function and the Fourier coefficients are:

$$a_{0(\sigma_M)} = 0 \quad (5.2)$$

$$a_{k(\sigma_M)} = 0 \quad (5.3)$$

$$b_{k(\sigma_M)} = \begin{cases} \frac{4\sigma_{max}}{k\pi} \cos(\frac{\pi kd}{W_{mag}+2d}) & \text{for odd } k \\ 0 & \text{for even } k \end{cases}$$

where, $\sigma_{max} = Br$. Other parameter definitions are listed in Table 5.1 in Section 5.2 and depicted in Figure 5-1.

The magnetic charge density at the interface between the magnets and air (that is, where $x = 0$) is shown in Figure 5-2.

The magnetic field is calculated as the sum of the sinusoidal charge densities as given by Equation 5.1. For a sinusoidal charge density and a system with no current, Maxwell's equations state that:

$$\nabla \times H = 0 \quad (5.4)$$

$$\nabla \cdot B = 0 \quad (5.5)$$

Therefore, the magnetic field H is equal to the negative gradient of some scalar magnetic potential function ψ :

$$H = -\nabla\psi. \quad (5.6)$$

Using $B = \mu_0 H_m$ in air and combining the above three equations:

$$\nabla^2\psi = 0. \quad (5.7)$$

Jonnalagadda solves the boundary problem of Equation 5.7 as:

$$\psi_{air} = \sum_{k=1}^{\infty} \beta \sinh(\frac{2\pi k(x + x_B)}{2(W_{mag} + 2d_{poles})}) \sin(\frac{2\pi kz}{2(W_{mag} + 2d_{poles})}) \quad (5.8)$$

where

$$\beta = \frac{-b_{k_{\sigma M}} \sinh\left(\frac{2\pi k x_A}{Z}\right)}{\frac{2\pi k \mu_0}{Z} \left(\sinh\left(\frac{2\pi k x_A}{Z}\right) \cosh\left(\frac{2\pi k x_B}{Z}\right) + \sinh\left(\frac{2\pi k x_B}{Z}\right) \cosh\left(\frac{2\pi k x_A}{Z}\right) \right)}. \quad (5.9)$$

where x_A is the x-coordinate of the magnet-steel interface, $2d_{poles}$ is the gap between magnet poles, μ_0 is the magnetic permeability of air, Z is the spatial period of the magnetic charge function [$Z = 2(2d_{poles} + W_{mag})$].

x_B is the thickness of the x-coordinate of the coil-steel interface. As shown in Figure 5-1, $X_B = d_{air} + t_{coil}$, where t_{coil} is the coil thickness in the x direction. Zach Trimble's downhole vibration energy harvester used a 3-phase coil where the "coil was designed in two layers separated by insulation. By designing the coil in two layers, all the end turns can be made in the same direction on each layer and in the opposite direction on the other layer. This allows traces [a "trace"= a segment of coil turn on a layer] to travel in either direction" (Trimble, 72).

For a 2-layer coil, the coil thickness is defined as:

$$t_{coil} = 2t_{phase} + 3t_{ins}. \quad (5.10)$$

where t_{phase} equals the wire diameter and the insulation thickness, t_{ins} is set to 0.0028 inches, the value specified in Trimble's masters thesis.

A plot of the magnetic potential in the air gap is shown in Figure 5-3.

As stated above, the magnetic field, H is related to the magnetic potential function by $H = -\nabla\psi$. A plot of the magnetic field in the x-direction, H_x , at the coil ($x = x_B$) is shown in Figure 5-4.

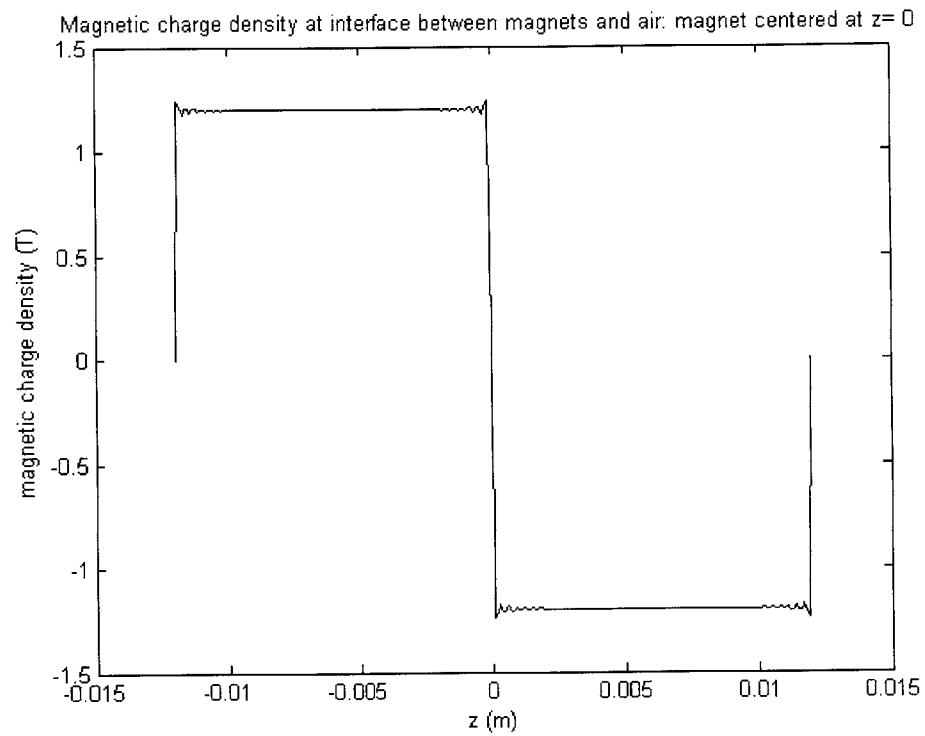


Figure 5-2: Magnetic charge density at the interface between the magnets and air, when the magnet is centered at $z=0$. This Fourier sum used $n = 200$, $Br = 1.2T$, $W_{mag} = 1.2cm$, $L_{mag} = 3cm$, $t_{mag} = 3cm$, $\#poles = 2$.

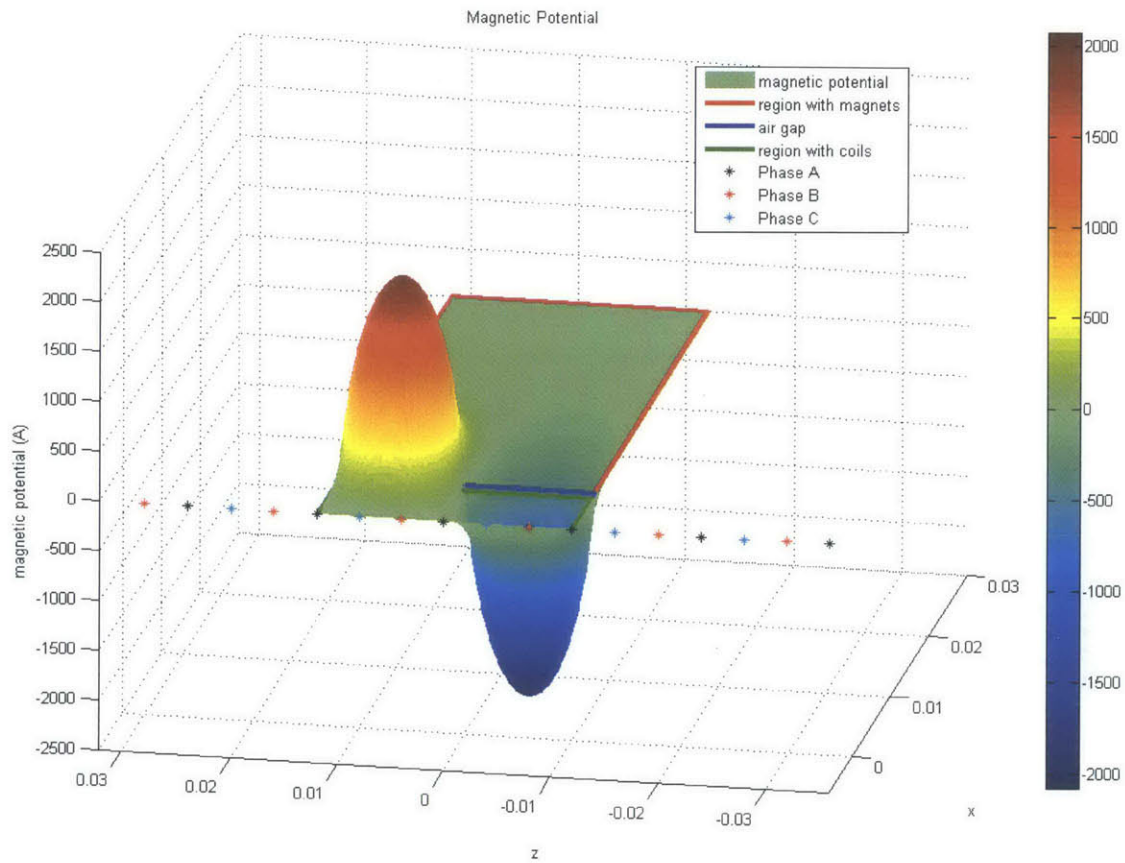


Figure 5-3: Magnetic potential (units: A). This potential plot is only accurate for $x < t_{Mag}/2$ because for $x > t_{Mag}/2$, the magnet polarity reverses. This plot shows the magnetic potential for the magnet with the magnetic charge density shown in Figure 5.1. This figure includes the location of the coil phases, which are in the Y-Z plane (the Y-axis is not shown in this plot) and stay stationary as the magnet moves in the z-direction.

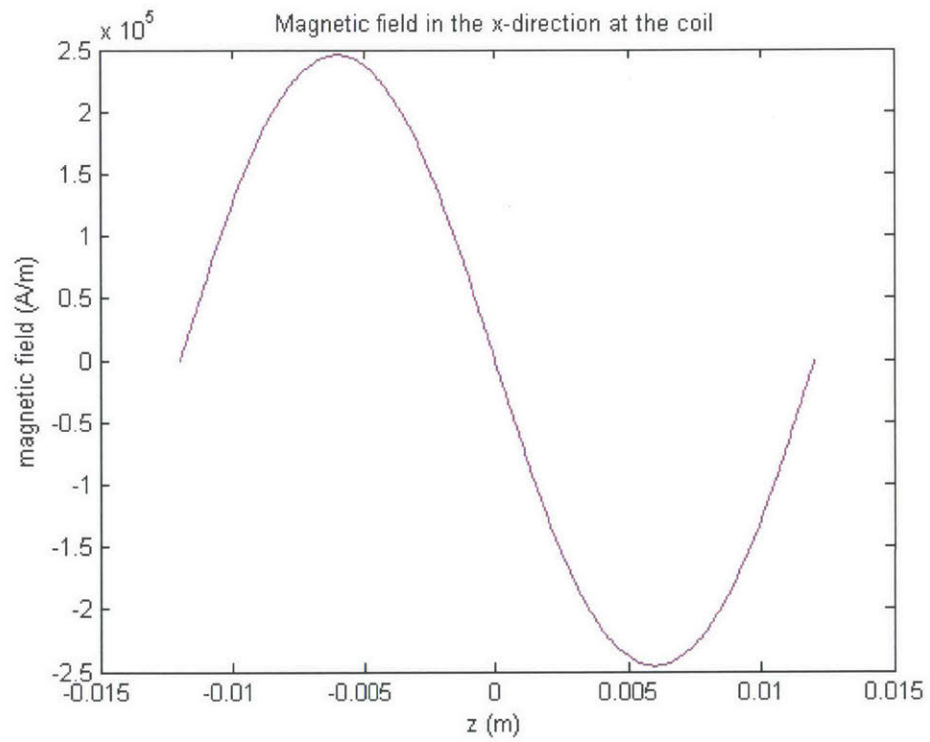


Figure 5-4: Magnetic field in the x-direction at the interface between the coil and magnetically permeable backing.

5.1.2 Calculate the flux through each coil

The magnetic flux λ through each coil phase as a function of magnet position is then calculated. The Matlab code stores the results as a table where each row is $[magPosition, Flux_A, Flux_B, Flux_C]$.

The flux through each coil phase is found according to:

$$\lambda_{phase} = B \cdot A_{phase} \quad (5.11)$$

where $B = \mu_0 I_{coils}$. The Matlab code numerically integrates small elements of $B \cdot dA$, where $dA = L_{mag} dz$.

5.1.3 Calculate the flux gradient through each coil

Next, the magnetic flux gradient with respect to magnet position z is calculated.

The magnetic flux gradient is:

$$\frac{d\lambda_{phase}}{dz} = \frac{dB}{dz} \cdot A_{phase}. \quad (5.12)$$

The Matlab code determines the flux gradient by using the built-in gradient function.

5.1.4 Calculate the electromagnetically-induced damping and Power to Load

Faraday's Law of Induction states:

$$\varepsilon = -u \frac{d\lambda}{dt} \quad (5.13)$$

where ε is the electromotive force, u is the number of wire loops, λ is the magnetic flux passing through the loops, and t is time. For our calculations, Faraday's Law can be rewritten as:

$$\varepsilon = -u \frac{d\lambda}{dz} \frac{dz}{dt} \quad (5.14)$$

where z is the magnet's position along the z -axis.

The electromotive force is a voltage source for the circuit attached to the coils. As stated in Trimble's masters thesis, "any device needing power will be connected in series and can be reduced to an equivalent load resistance" (Trimble, 38). According to Jonnalagadda, the inductive effects of a generator can be ignored when $R \gg \omega L$, where ω is the oscillation frequency of the system. The circuit used in this model is shown in Figure 5-5.

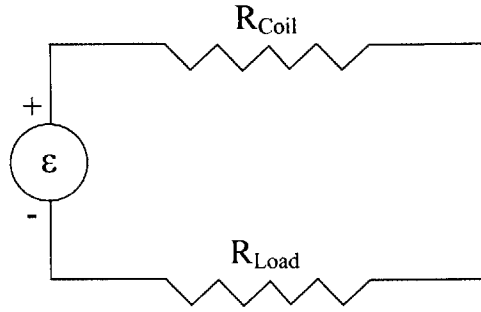


Figure 5-5: Equivalent circuit

The internal resistance of the coil, R_{Coil} is:

$$R_{Coil} = \frac{\rho_{wire} l_{wire}}{A_{wire}} \quad (5.15)$$

where ρ_{wire} is the resistivity of the wire, $l_{wire} = uN(2W_{Mag} + 2L_{Mag})$ is the wire length, and A_{wire} is the wire's cross-sectional area.

Combining the above equations, the power to the load is related to the flux gradient by:

$$Power_{Load} = u^2 \frac{R_{Load}}{(R_{Coil} + R_{Load})^2} \left(\frac{d\lambda_{total}}{dz} \right)^2 veloc^2. \quad (5.16)$$

where $veloc$ is the magnet's velocity.

The electromagnetically-induced damping coefficient, b_e , is related to the power converted to electricity by:

$$P_{elec} = P_{diss} = b_e veloc^2. \quad (5.17)$$

Using the above equations, the equivalent mechanical damping of the system is related to

the flux gradient by:

$$b_e = u^2 \frac{\left(\frac{d\lambda_{total}}{dz}\right)^2}{R_{coil} + R_{Load}}. \quad (5.18)$$

where u is the number of turns per phase and $\frac{d\lambda_{total}}{dz}$ is the summed magnitudes of the flux gradient in all three phases.

The results of these calculations are shown in Figure 5-6.

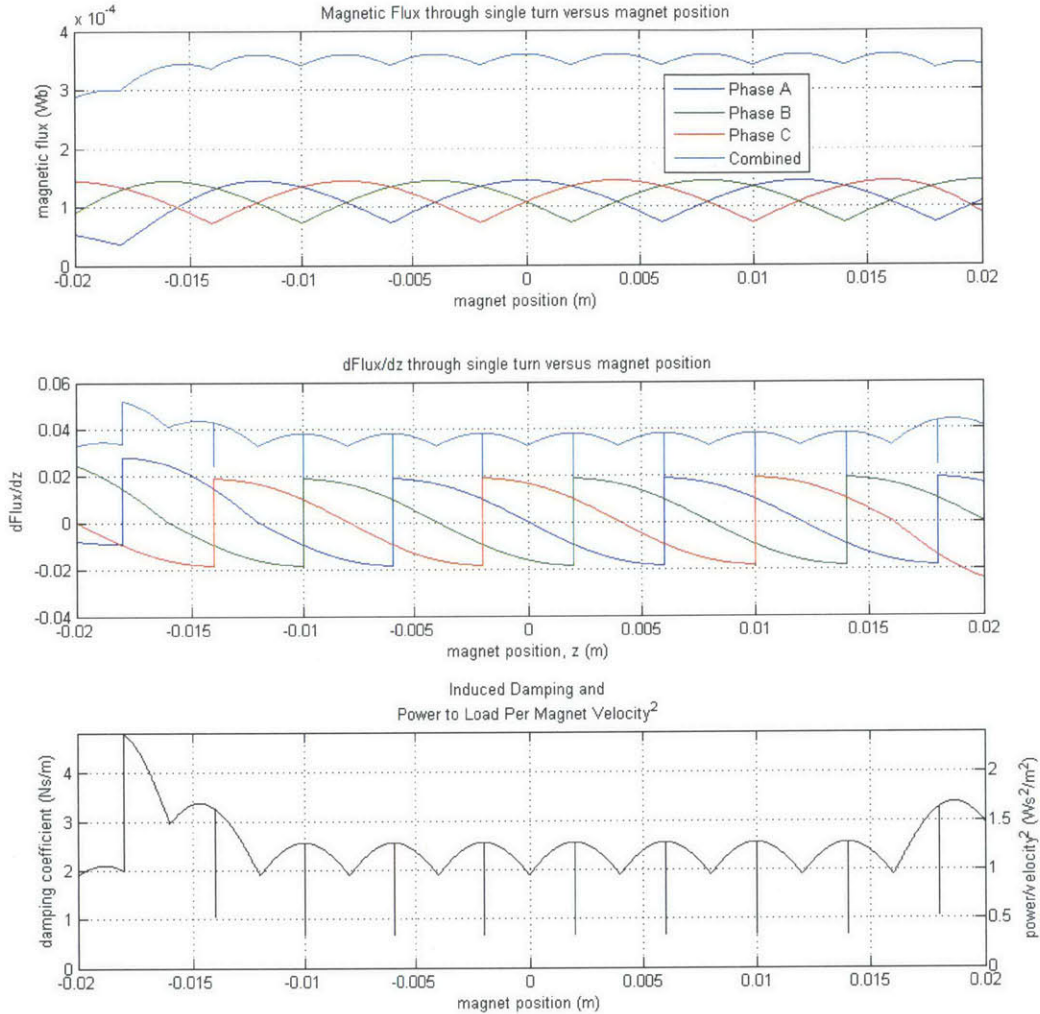


Figure 5-6: Numerically calculated magnetic flux, flux gradient, electromagnetically-induced damping, and power normalized by magnet velocity squared versus magnet position. The left y-axis of the bottom subfigure is the damping coefficient, while the right y-axis is the power delivered to the load normalized by the magnet velocity squared. This simulation used $L_{Mag} = 3cm$, $W_{Mag} = 1.2cm$, $t_{Mag} = 3cm$, wire diameter = 0.1 inches, number of turns per phase $u = 3$, number of coil loops [how many times coil repeats in the z-direction] = 5, air gap = .03 inches, insulation thickness = .0028 inches, $R_{Load} = R_{Coil} = 0.0025\Omega$.

5.2 Parameter Constraints

The system parameter values are constrained so that the device is easy for a person to carry (limit the mass and size), and machining tolerances are satisfied. These constraints on the electromagnetic system parameters are listed in Table 5.1. Additional constraints are that the number of magnetic poles is restricted to an even number in order to create full magnetic circuits (Trimble, 34). Also, the coils must be at the same pitch as the magnet width for maximum magnetic flux reversal (Trimble, 34). Finally, the theory assumes that the magnetically permeable backing does not saturate. If the backing does saturate, then B is no longer directly proportional to H . Trimble shows that the minimum backing thickness to prevent saturation is $t_{backing} = W_{Mag} \frac{Br_{Mag}}{Br_{backing}}$ (Trimble, 67).

Table 5.1: Electromagnetic System Parameters

Parameter	Value Range
L_{mag} , magnet length (cm)	0.5-5
W_{mag} , magnet pole width (cm)	0.5-5
t_{mag} , magnet pole thickness (cm)	0.5-5
d_{poles} , half the gap between magnet poles (cm)	0
m , magnet mass (Kg)	0.125
ρ_{mass} , mass material density (Kg/m^3)	7400
p , # magnetic poles	2,4
Br , magnetization flux density (T)	1.2
ρ_{wire} , wire material resistivity (Ωm)	1.68e-8
N , # coil phases	3
u , # turns in each phase	1-30
δ_{crit} , amplitude of magnet motion (cm)	2
d , wire diameter (mm)	0.15- 4
d_{air} , air gap between magnet and coil (mm)	0.25-5
R_{load} , load resistance (Ω)	

5.3 Optimization

The goal of the optimization is to determine parameters satisfying the constraints that produce a desired damping and maximize the power dissipated by the load resistor. Parameters that can be adjusted are: L_{mag} , W_{mag} , t_{mag} , # poles, # turns/phase, wire diameter d , d_{air} ,

and R_{Load} .

The mass dimensions were determined so that the total oscillating mass (magnet and required steel backing) equals 60 grams. The terms "width", "length", and "thickness" refer to the labeled dimensions in Figure 5-1. W_{mag} and L_{mag} were set to arbitrary constants. The steel backing length was set to $L_{steel} = L_{mag}$, and the steel backing width was set to $W_{steel} = W_{mag}$. The steel thickness, t_{steel} , was chosen to the minimum value that prevented the magnetic circuit from saturating (that is, $t_{backing} = W_{Mag} \frac{Br_{Mag}}{Br_{backing}}$). Then the magnet thickness t_{mag} was chosen so that the entire mass was 60g.

Unless stated otherwise, the simulations assume an airgap between the magnet and coil of 0.76 mm. This is the valued used by Trimble in his thesis.

The number of coil layers was determined by fitting as many turns per phase into the space allotted per phase on each layer. If more turns were required, then another layer was added behind the first layer:

$$\#layers = u/nWires \quad (5.19)$$

where u is the number of wire turns per phase, and $nWires$ is the number of wires that fit in the width available to each phase ($nWires = W_{Phase}/(d_{Wire} + W_{kerf})$). $\#layers$ is rounded to the larger whole number. W_{Kerf} is the spacing between wires on the same layer. The coil thickness was determined by:

$$t_{Coil} = 2(\#layers)(wireDiameter) + (2\#layers + 1)(insulationThickness) \quad (5.20)$$

The resistance of the load was set equal to the resistance of the coil.

This configuration matches those in the masters theses of Zach Trimble and Aparna Jonnalagada. The dimensions of the magnet were varied. All of the masses were kept at 60 g.

Figures 5-7 to 5-10 show sample optimization plots of the electromagnetic damping coefficient produced by varied parameters.

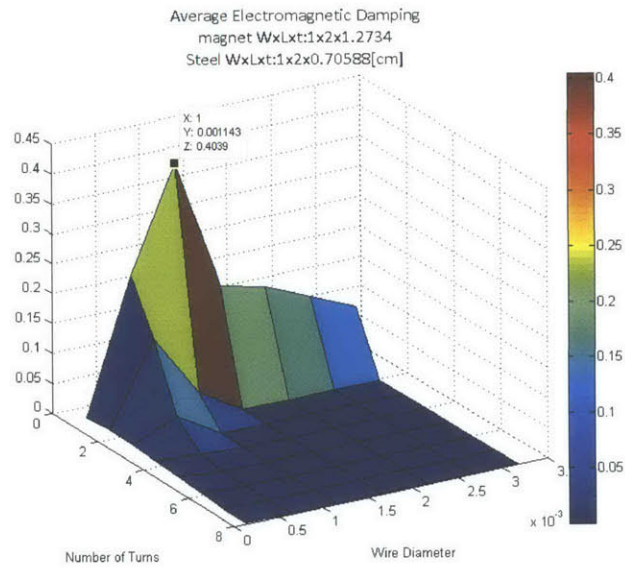


Figure 5-7: Electromagnetic Damping for varied coil turns per phase and wire diameter.

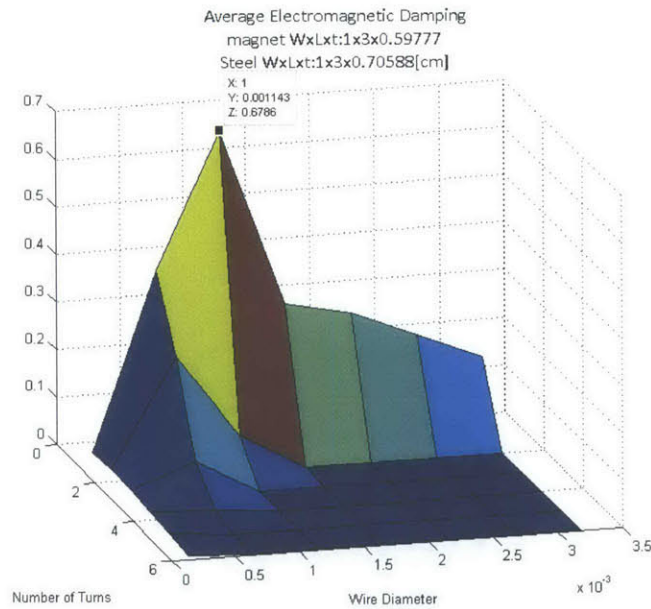


Figure 5-8: Electromagnetic Damping for varied coil turns per phase and wire diameter. Total steel and magnet mass: 60 g, air gap between magnet and coil: 0.02 inches.

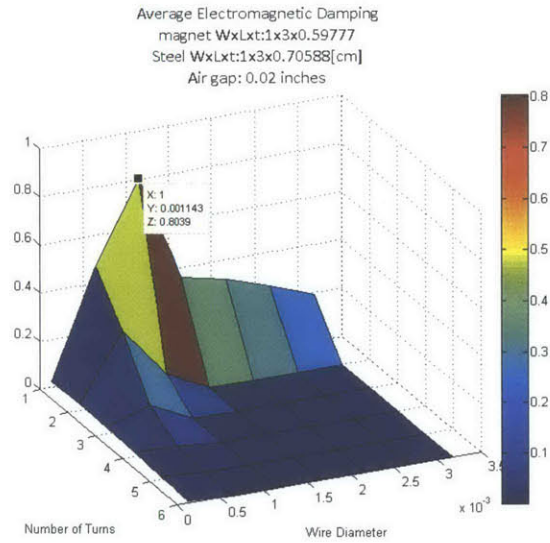


Figure 5-9: Electromagnetic Damping for varied coil turns per phase and wire diameter. This plot has the same mass dimensions as in Figure 5-8 (total steel and magnet mass of 60g) but with an air gap of 0.02 inches instead of 0.03 inches.

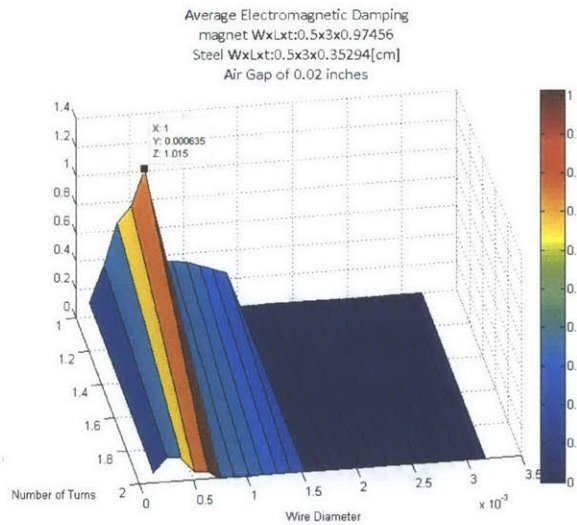


Figure 5-10: Electromagnetic Damping for varied coil turns per phase and wire diameter. This plot has the same mass dimensions as in Figure 5-8 (total steel and magnet mass of 60g) but with an air gap of 0.02 inches instead of 0.03 inches, and a magnet with 4 magnetic poles instead of 2 magnetic poles.

Chapter 6

Energy Harvester Conclusions

This thesis investigated a novel nonlinear spring for the application of charging personal electronics such as a cell phone from the energy of a person's walking vibrations. The goal of this thesis was to show that the nonlinear spring increased the power efficiency of the energy harvester when compared to current commercial energy harvesters. The results of this thesis (see Section 4.5.3) suggest that optimal nonlinear harvester (2DOF nonlinear harvester, type 2, $\lambda_{EM} = 1.6Ns/m$, which is adaptive to different walking signals and robust to parasitic damping) can harvest $0.017W$, which equates to $3.3e-3W/cm^3$, and $2.8e-1W/Kg$. The optimal linear harvester (based on the 1DOF linear harvester with $\lambda_{EM} = 0.15Ns/m$, which is not nearly as adaptive to different walking signals) can harvest $0.026W$, which equates to $2.2e-3W/cm^3$, and $4.3e-1W/Kg$. While these numbers emphasize that further optimization may be necessary for the nonlinear systems, they show that the harvesters studied in this thesis harvest one order of magnitude more power per volume than current commercial energy harvesters (the backpack harvests $3.1e-4W/cm^2$ and the nPEG harvests $6.1e-5W/cm^3$. See Table 1.2), and three orders of magnitude more power per mass than the commercial energy harvesters (the backpack harvests $1.9e-4W/Kg$ and the nPEG harvests $7.6e-5W/Kg$. See Table 1.2). Please note, however, that the simulated harvested power in this thesis does not account for electrical inefficiencies. The harvester masses and volumes do not account for the electrical components and casing.

Conclusions and future work for the different aspects of this project are described below.

For the nonlinear spring theory, this thesis described a spring that behaves similarly to

a cubic nonlinear spring but with two advantages. First, the spring is designed to have minimal frictional losses. Second, the force exerted by the nonlinear spring blows up for large displacements. This blow-up causes vibro-impact, which [25] describes as useful for energy harvesting.

This thesis experimentally verified the nonlinear spring theory by "initial displacement" tests for oscillators with several different parameters. The experiments showed that the theory is restricted to smaller end-mass:cantilever rigidity ratios and smaller end-mass volume:cantilever width ratios. The dynamics of oscillators for which these ratios are large do not agree with the theory because they have non-negligible energy in higher cantilever transverse and torsional modes. Future nonlinear spring experimental work may involve increasing the agreement of the base drop tests, which simulate foot motion.

This thesis compared the performance of nonlinear and linear energy harvesters in terms of optimal power output, adaptivity to different human motions, robustness to frequency variations, space efficiency, and robustness to parasitic damping. We sought to verify the theory that multi-DOF nonlinear energy harvesters outperform linear energy harvesters when the excitation signal has a lot of noise, especially when the nonlinear energy harvester's antisymmetric modes are excited.

Although optimization showed that the linear system always harvested more power than the nonlinear system when excited by the signal for which they were both optimized, Figure 4-41 shows that the difference in power between the linear and nonlinear systems decreases as the signal noise increases. Future optimization work could include optimizing the 2DOF nonlinear system for noisier excitation signals, such as the foot running, for which the nonlinear systems may harvest more power than the linear system.

For the excitation regimes investigated in this thesis, none of the systems seemed significantly more optimal over any other.

The main advantages of the 2DOF nonlinear energy harvester over the 1DOF linear energy harvester are that it can be designed to be more adaptive to different excitation signals and resistant to power decay when parasitic damping is present (the 2DOF nonlinear harvester, type 2 ($\lambda_{EM} = 1.6Ns/m$)). These significant advantages are caused by the 2DOF nonlinear system harvesting its optimal power at large electromagnetic damping coefficients,

whereas the optimal electromagnetic damping coefficient for the linear system occurs at low electromagnetic damping coefficient.

We note that the "linear" system described in this thesis is not a traditional linear system because of the displacement constraints.

As for volume efficiency, the nonlinear cantilever/surface spring is very inefficient compared to the helical spring. Future work will include converting the one-dimensional cantilever/surface design into a more volume-efficient two-dimensional design (such as a helical spring contacting a surface instead of a cantilever).

This thesis began to investigate the electromagnetic theory that could be used to design the energy harvester. Future work will include finalizing this theory and perhaps simplifying it for practical testing purposes. Other future work on the electromagnetic theory could include considering different magnet-coil configurations, such as a U-shaped magnet, O-shaped magnet, and magnet in between two coils to balance the forces between the magnets and coils. Then, a full energy harvester prototype could be fabricated and tested.

Some other future design directions for this project could include: investigating a different spring mechanism. In addition to looking at the two-dimensional equivalent of oscillating cantilever/surface springs, more human motion power might be available in a mechanism that bends at the knee or deforms in a shoe. Also, the project might investigate piezoelectric transducers instead of electromagnetic transducers. The optimized nonlinear energy harvesters of this thesis dissipate the energy in short bursts, and piezoelectric transducers are more efficient at converting short bursts of dissipated energy into electricity. Finally, future work of this project might consider applying this theory to different vibration applications, such as medical device implants (scale down the project volume) or harvesting ocean waves (scale up the project volume).

Chapter 7

Nonlinear Load Cell

7.1 Introduction

The nonlinear spring that was studied in Chapters 1-6 for the application of an energy harvester is also useful for measuring forces as a load cell. Load cells that use the nonlinear spring are shown in Figure 7-19.

Common types of load cells are hydraulic load cells, pneumatic load cells, and strain gauge load cells. For a hydraulic load cell, a load is applied to a piston that covers an elastic diaphragm filled with oil. When a load is applied to the piston, the piston moves and increases the pressure in the diaphragm. The pressure in the diaphragm is measured by a bourdon tube. For a pneumatic load cell, a pressure gauge measures the pressure inside a diaphragm filled with air. The most common load cell is the strain gauge load cell. The load cell is a solid object that deforms or displaces when it feels a force. When the load cell displaces, a strain gauge deforms. A typical strain gauge is flexible foil in a pattern. The strain gauge is adhered to the load cell, and it deforms as the load cell deforms. As the strain gauge is stretched, its electrical resistance increases. When it is compressed, its electrical resistance decreases. A Wheatstone bridge circuit measures the change in resistance. Thus the force applied to the load cell is converted to an electrical signal [8].

Commercially available strain gauge load cells come in many different shapes, such as bending beams (a cantilever), S-beams (an "S"-shaped configuration of beams), single point load cells (a double-clamped beam, for which the force measurement is insensitive to the

position of the load along the beam), shear beam load cells (an I-beam produces a uniform shear across its cross-section that can be measured by strain gauges), and "pancake" load cells (round, flat beams) [8].

A load cell can be designed for almost any force capacity. For example, [8] indicates that bending beam load cells can be used for force ranges of 50-25,000 ($5.0e1-2.5e4$) Newtons and pancake load cells can be used for force ranges up to $2.5e6$ N.

The load cell resolution- that is, the smallest force increment that it can measure- is constant for a given linear load cells. The Omega load cell manufacturer lists accuracies up to 0.03% full-scale load [8] . For example, if a load cell is designed to have a full scale capacity of $2.5e6$ N, then the smallest force increment it can measure is 75 N. (This analysis assumes that the load cell resolution is limited by the mechanical component and not the electrical instrument component).

Many of the load cells are designed to withstand a limited amount of force "overcapacity." For example, the Omega LCCE-100 S-Beam load cell can be safely overloaded to 500% its load capacity before breaking.

All of the commercial load cell discussed here have limitations on their force resolution, maximum force capacity, and overcapacity due to their reliance on linear springs. A load cell that uses the cantilever/surface nonlinear spring (see Figure 7-19) does not have these limitations. The proposed nonlinear load cell has a force resolution that increases with the force, which allows a high force accuracy over a large force range. Also, the geometry prevents it from breaking for forces well beyond its designed range.

More specifically, the proposed device consists of four cantilever/surface springs. The hardening nonlinearity of the springs in the load cell allow the surface pairs to displace a large distance for small forces and incrementally smaller distances for larger distances. For very large forces, the cantilevers effectively do not bend further because they are already in contact with the surfaces along the full cantilever length. The surfaces are significantly stiffer than the cantilever and can be designed to negligibly deform themselves in all desired applications. The top surface pair is connected to the object of interest while the bottom surface pair is connected to the tabletop (or visa-versa). The displacement measurements of this proposed load cell could be measured by an optical sensor that compares the displacement of the top

surface set to the bottom surface set.

If the optical sensor can detect changes as small as $0.1 \mu m$, then to achieve 1% accuracy in the force measurement, then we require a change in displacement per force: $dy/dF \geq 1e-7m/0.01F$. For $F=0.01$ N [1 gram], it is desirable to have a stiffness of $K = dF/dy \leq 1000N/m$. For $F=400$ N [40 Kg], it is desirable to have $K \leq 4e8N/m$.

This chapter describes the cantilever/surface nonlinear spring theory for the load cell and the experimental verification of this theory using aluminum load cells. Then, it simulates spring steel load cell performance (e.g. stiffness and safety factor against yield versus force). This chapter investigates a load cell for which the four nonlinear springs' cantilevers are rigidly connected in such a way that the cantilever tip is restricted to 0-slope. It also investigates a load cell for which the cantilevers are connected by rotational springs physically realized by 270° curved beams. The curved beams have the same base width (dimension into the page) and height as the cantilevers to which they are attached. The presence of the rotational springs reduces the stress on the cantilever beams caused by the first load cell's 0-slope requirement. The results of this investigation are summarized in Section 7.5.

7.2 Theory

The derivation of the force versus deflection of the load cell is similar to that of the oscillator described in Chapter 2. The load cell is a 2x2 grid of the nonlinear spring where the left and right elements are rigidly attached to each other as "surface pairs". The cantilever tips of the top and bottom elements are also rigidly attached. Load cell deflection occurs between the top and bottom surface pairs. The load cell theory differs from the oscillator theory in that: the full load cell's deflection is twice that of the single nonlinear spring, the full load cell's force is four times that of the single nonlinear spring (due to the 2x2 grid nonlinear spring configuration), and the cantilever tip connections must remain vertical (due to symmetry). When the cantilever tips are rigidly connected to these vertical connections (please refer to Figure 7-19), then the cantilever tips must remain at 0-slope. When the cantilever tips are connected to the vertical connections by rotational springs, then the 0-slope requirement is relaxed. This section uses Castigliano's Theorem to derive the force versus displacement

of the load cell with the rotational springs physically implemented by 270° curved beams. Setting the radii of the curved beams to 0 recovers the force versus deflection theory for the load cell with rigid cantilever tip connections.

The theory presented in this section is for one-fourth of an actual load cell. That is, the full load cell force would be the force derived in this section multiplied by 4, and the full deflection would be the deflection derived in this section multiplied by 2.

Set Up

This chapter examines the force versus displacement of a cantilever with a rotational spring attached to its end. As the cantilever bends, it wraps around a surface that has the shape:

$$S = D \left(\frac{z}{L} \right)^n \quad (7.1)$$

where $L = L_{Surf} = L_{Cant}$ is the cantilever and surface length, z measures the location along the length of the beam, and D is the gap between the surface and cantilever.

The deflection of the beam can be determined by solving the boundary value problem for the "free" part of the beam. for the free part of the beam, x measures the distance along the cantilever axis from the root. The free part of the beam is shown in Figure 7-1. The boundary conditions on the free part of the beam are: $w(x = 0) = S$, $dw/dX = S'$ at $x = 0$, downward force F applied at the top of the curved segment, and zero slope at the top of the curved segment; where w is the deflection of the beam in the z direction, and S and S' are the known deflection and slope respectively at the cantilever's contact point with the surface.

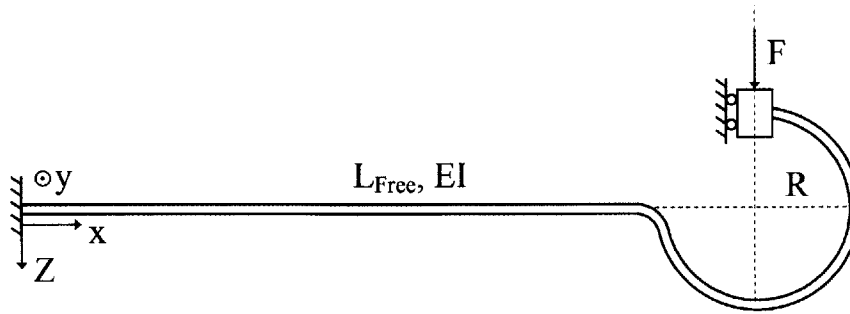


Figure 7-1: Problem Set-Up. The boundary conditions are: $w(0) = S$, $dw/dX = S'$ at $x=0$, downward force F applied at the top of the curved segment, and zero slope at the top of the curved segment.

Free Body Diagram and Reaction Forces

The free body diagram of the entire beam is shown in Figure 7-2. The forces at the left end of the beam are imposed by the contact surface and segment of the cantilever that is already in contact with the surface. At the right end of the beam, the top of the curved segment is attached to a rigid vertical bar. This vertical bar is allowed to move vertically and horizontally, but it does not allow the top of the curved segment to rotate. Thus, the top of the curved segment is subject to a reaction moment.

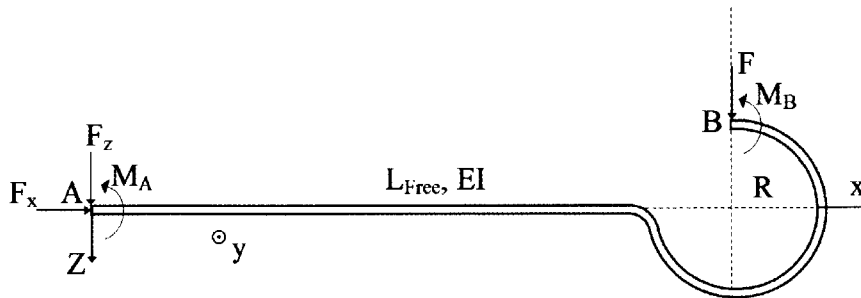


Figure 7-2: Free Body Diagram

Using the free body diagram in Figure 7-2, the reaction forces and moments can be

found:

$$\begin{aligned}
 \sum F_X &= F_x &= 0 &\longrightarrow F_x = 0 \\
 \sum F_Z &= F_z + F &= 0 &\longrightarrow F_z = -F \\
 \sum M_A &= -F(R + L_{Free}) + M_B + M_A = 0 &\longrightarrow M_B + M_A = F(R + L_{Free})
 \end{aligned}
 \tag{7.2}$$

The reaction moments are statically indeterminate. To determine the reaction moments, one can calculate the internal energy, U , in the "straight" segment and "curved" segment, differentiate the internal energies with respect to the interface tip moment (which equals the tip angle, according to Castigliano's Theorem: $\theta_{Tip} = \partial U / \partial M_{Tip}$), and solve the two equations for the unknown tip moment, M_{Tip} , and tip angle, θ_{Tip} . This procedure is given below.

The tip moment is defined in Figure 7-3.

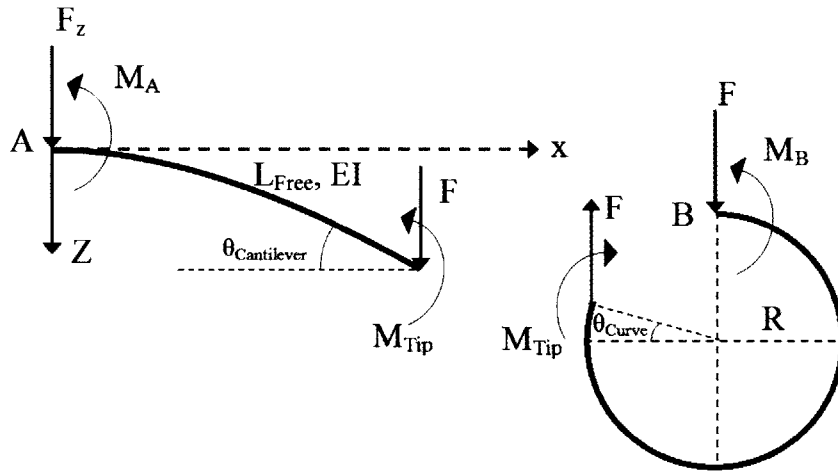


Figure 7-3: Free Body Diagram Segments.

The internal energy in the straight segment is calculated in Equation 7.3.

$$U_{Cantilever} = \int_0^L \frac{(Fx + M_{Tip} - F(L))^2}{2EI} dx
 \tag{7.3}$$

Since this is a slender beam, the internal energy due to the shear force and normal force is negligible compared to the internal energy due to bending. Integrating equation 7.3 with

respect to dx and differentiating with respect to M_{Tip} , the tip angle is:

$$\theta_{Cantilever} = \frac{FL_{Free}^2}{2EI} - \frac{M_{Tip}L_{Free}}{EI} + S' \quad (7.4)$$

The internal energy in the curved segment is calculated in Equation 7.5. Again, only the bending energy is considered.

$$U_{Curve} = \int_0^{3\pi/2} \frac{(-FR\sin(\theta) - FR - M_{Tip})^2}{2EI} R d\theta \quad (7.5)$$

Integrating equation 7.5 with respect to $d\theta$ and differentiating with respect to M_{Tip} , the end angle is:

$$\theta_{Curve} = \frac{(3\pi R^2 + 2R^2)F + 3\pi M_{Tip}R}{2EI} \quad (7.6)$$

Solving equations 7.4 and 7.6 for M_{Tip} (by setting $\theta_{Cantilever} = \theta_{Curve}$), the result is:

$$M_{Tip} = \frac{(-3\pi R^2 - 2R^2 + L_{Free}^2)F + 2S'EI}{3\pi R + 2L_{Free}} \quad (7.7)$$

The reaction moments M_A and M_B relate to M_{Tip} by:

$$M_A = FL_{Free} - M_{Tip} \quad (7.8)$$

$$M_B = FR + M_{Tip} \quad (7.9)$$

Deflection and Rotation of the Straight Segment

The displacement of the straight beam segment tip is found using the Euler-Bernoulli equation:

$$EI \frac{d^4 w}{dx^4} = -q(x) \quad (7.10)$$

where $q(x) = 0$ is the applied load along the free beam length, E is the beam's elastic modulus, and I is the beam's moment of inertia. Integrating equation 7.10 four times with

respect to x results in the beam deflection equation:

$$EIw = -\frac{q}{24}x^4 + \frac{c_1}{6}x^3 + \frac{c_2}{2}x^2 + c_3x + c_4 \quad (7.11)$$

where c_i are the constants of integration, q is the loading along the beam length ($q = 0$), and x is the distance measured from the contact point. The boundary conditions for this cantilever segment are:

$$\begin{aligned} w(x=0) &= S(z_c) && \text{[At root, beam deflection equals surface deflection]} \\ w'(x=0) &= S'(z_c) && \text{[At root, beam slope equals surface slope]} \\ w''(x=0) &= M_A/EI && \text{[internal bedding due to moment at cantilever root]} \\ w'''(x=L_{Free}) &= -F/EI && \text{[Point force applied at beam tip]} \end{aligned} \quad (7.12)$$

Substituting these boundary conditions into equation 7.11 results in the following values for the constants of integration:

$$\begin{aligned} c_1 &= -F \\ c_2 &= M_A \\ c_3 &= EIS'(z_c) \\ c_4 &= EIS(z_c) \end{aligned} \quad (7.13)$$

The resulting beam deflection is:

$$y = \frac{-F}{6EI}x^3 + \frac{3\pi FR^2 - 2FR^2 + 3\pi FLR + FL^2 - 2S'EI}{(6\pi R + 4L)EI}x^2 + \frac{dS}{dz} \Big|_{z=z_c} \cdot x + S(z_c) \quad (7.14)$$

where x is measured from the cantilever root. The free length is:

$$L_{free} = L - l(S(z_c)) \quad (7.15)$$

where z_c is the contact point of the cantilever with the surface, S is the spatial function of the surface curve, and s is the arc length of the surface from $z = 0$ to $z = z_c$.

Substituting in $x = L_{Free}$, the deflection at the tip of the straight segment is:

$$\delta_{Tip} = \frac{-FL^4 - 2FL^2R^2 - 2FL^3R - 2S'EIL^2}{6\pi EIR + 4EIL} + \frac{FL^2R}{2EI} + \frac{FL^3}{3EI} + S + S'L \quad (7.16)$$

where L is used in place of L_{Free} so that the equation fits on one line.

When $R = 0$, equation 7.16 simplifies to:

$$\delta_{Tip} = \frac{FL_{Free}^3}{12EI} + \frac{S'(x=0)L_{Free}}{2} + S(x=0) \quad (7.17)$$

Equation 7.17 is the cantilever tip deflection of the load cell for which the cantilever tips are rigidly connected to vertical bars.

When $R = 0$, $S' = 0$, and $S = 0$, equation 7.16 simplifies to:

$$\delta_{Tip} = \frac{FL^3}{12EI} \quad (7.18)$$

This result agrees with the deflection of a cantilever with a point load and 0-slope restriction at its tip.

The effective stiffness of the rotational spring (implemented by the 270° curved beam) acting on the straight segment tip is $K_{rot,eff} = M_{Tip}/\theta_{Tip}$. Substituting in the equations for M_{Tip} (Equation 7.7) and θ_{Tip} (Equation 7.4), $K_{rot,eff}$ is:

$$K_{rot,eff} = \frac{2EI(-3\pi FR^2 - 2FR^2 + FL_{Free}^2 + 2S'EI)}{R(6\pi FL_{Free}R + 4FL_{Free}R + 3\pi FL_{Free}^2 + 6\pi S'EI)} \quad (7.19)$$

where EI is the cantilever rigidity, F is the force acting down at the top of the curved segment, R is the radius of the curved segment, L_{Free} is the free cantilever length, and S' is the surface slope at the free cantilever root.

Deflection of the Curved Segment

Castigliano's Theorem can be used to find the displacement of the top of the curved segment with respect to the straight segment tip: $\delta = \partial U/\partial F$. Using equation 7.7 to define M_{Tip} and differentiating the internal energy, U with respect to F , the deflection is:

$$\delta = \frac{27\pi^3 FR^5 + 72\pi FR^5 + 36\pi^2 FLR^4 - 96\pi FLR^4 + 32FLR^4 - 12\pi FL^2 R^3 - 32FL^2 R^3}{4EI(3\pi R + 2L)^2} + \frac{-48\pi S'EIR^3 + 24\pi FL^3 R^2 - 16FL^3 R^2 + 24\pi S'EILR^2 - 16S'EILR^2 + 6\pi FL^4 R + 12\pi S'EIL^2 R}{4EI(3\pi R + 2L)^2} \quad (7.20)$$

7.2.1 Load Cell for Cantilevers With Rigid Connections

Below are the performance plots of an aluminum load cell with the following parameters: cantilever and surface lengths, $L = 10\text{cm}$; cantilever height, $h = 0.5\text{mm}$; cantilever base, $b = 9.5\text{mm}$; surface curve power $n = 3$; maximum surface gap, $D = 5\text{mm}$; elastic modulus, $E = 65e9\text{Pa}$; maximum allowable stress, $\sigma_{all} = 200e6\text{Pa}$. All plots correspond to a single cantilever/surface set (1/4 of an actual load cell). For a complete load cell, the displacement of a single cantilever tip is multiplied by 2 and the force is multiplied by 4.

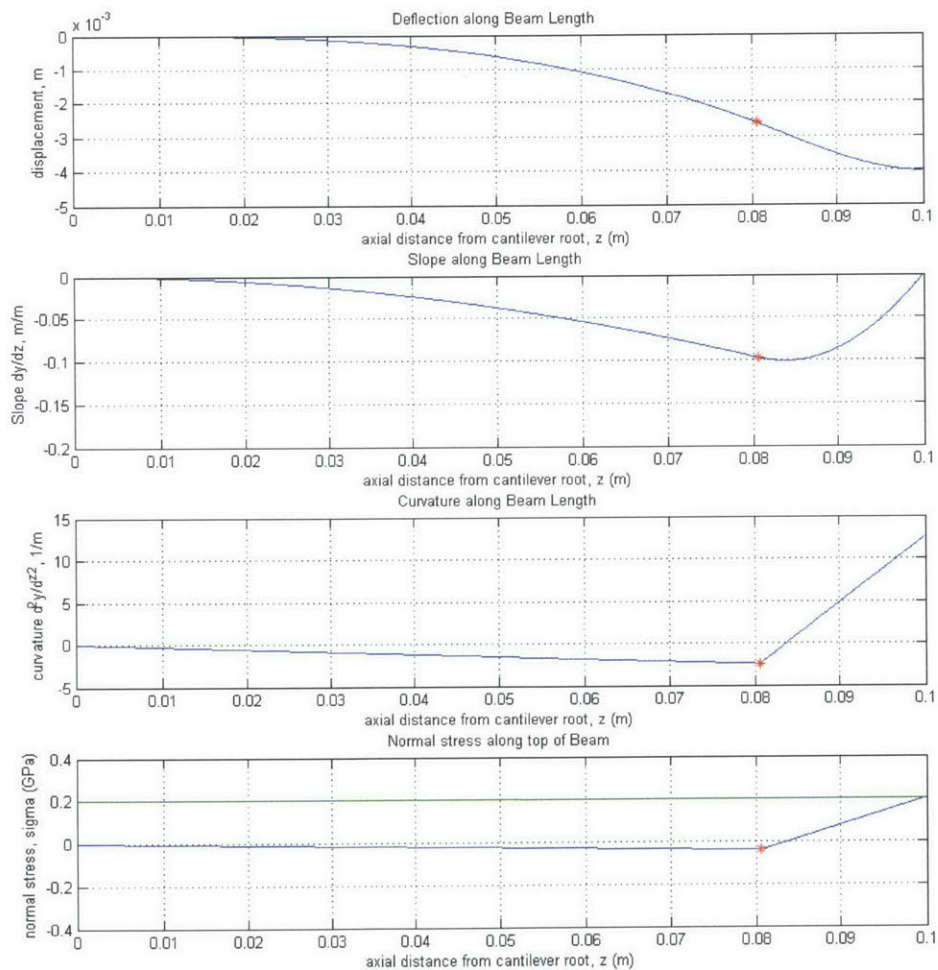


Figure 7-4: Deflection along length for a single cantilever, $F = 5\text{ N}$. Load cell parameters are $D = 5\text{ mm}$. $L = 10\text{ cm}$. $b = 9.5\text{ mm}$. $h = 0.5\text{ mm}$. $E = 69e9\text{ Pa}$.

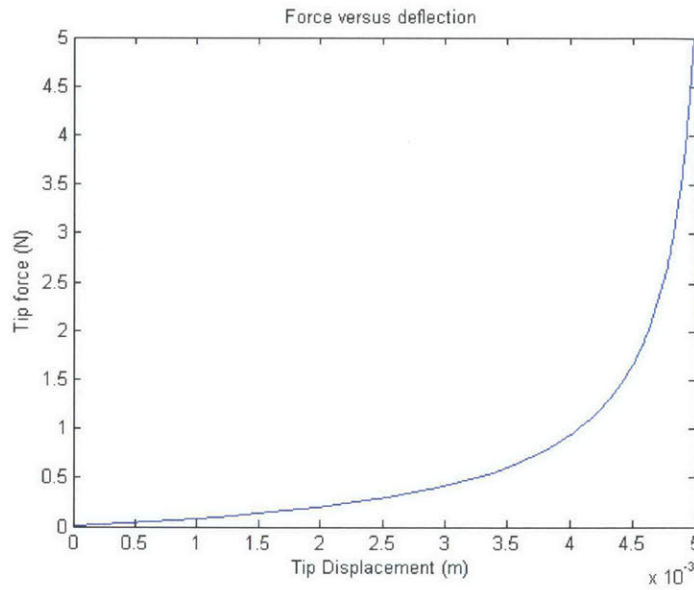


Figure 7-5: Force versus deflection for a single cantilever. Load cell parameters are $D=5$ mm. $L=10$ cm. $b=9.5$ mm. $h=0.5$ mm. $E=69e9$ Pa.

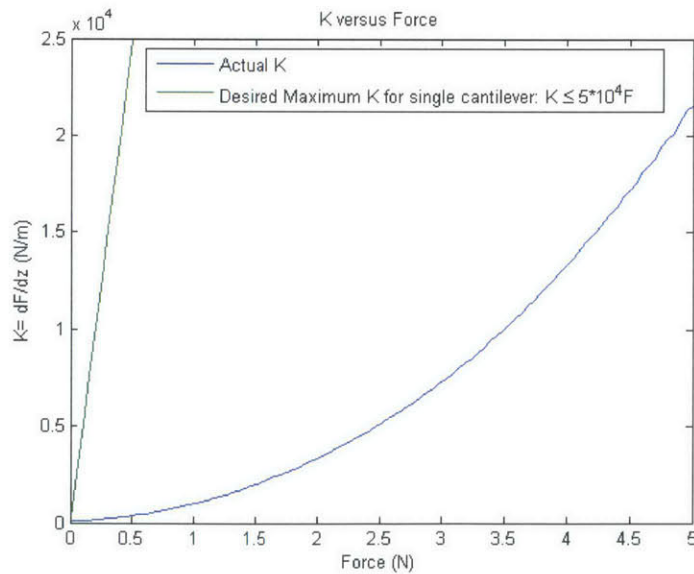


Figure 7-6: Stiffness versus force for a single cantilever. Load cell parameters are $D=5$ mm. $L=10$ cm. $b=9.5$ mm. $h=0.5$ mm. $E=69e9$ Pa. The green line indicates the maximum allowable stiffness such that an optical sensor that can detect deflection changes of $0.1 \mu\text{m}$ could detect changes within 1% of the given force value.

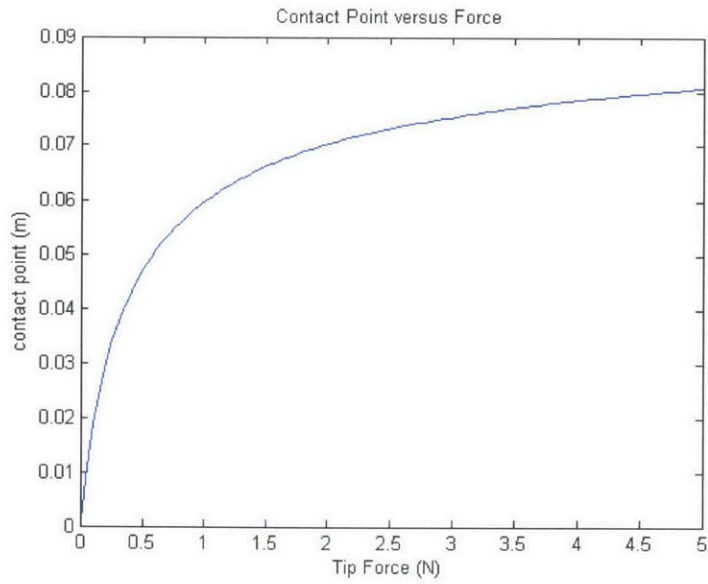


Figure 7-7: Contact Point versus force for a single cantilever. Load cell parameters are $D=5$ mm. $L=10$ cm. $b=9.5$ mm. $h=0.5$ mm. $E=69e9$ Pa.

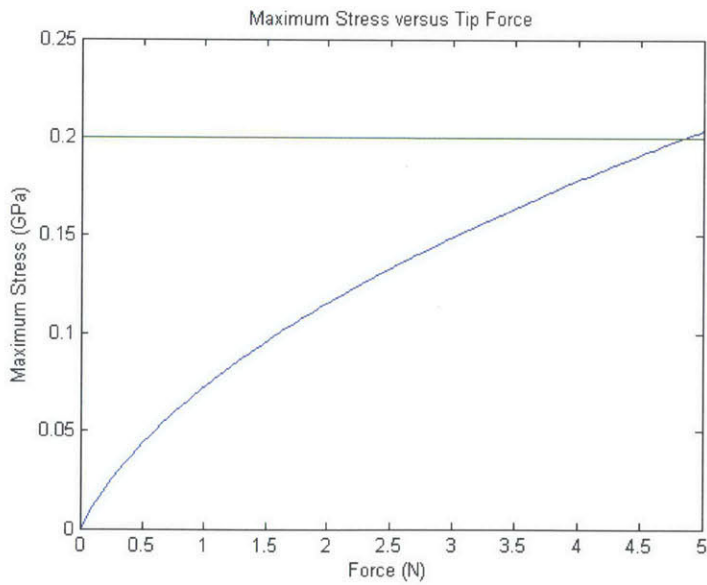


Figure 7-8: Stress versus force for a single cantilever. Load cell parameters are $D=5$ mm. $L=10$ cm. $b=9.5$ mm. $h=0.5$ mm. $E=69e9$ Pa. The green line indicates the maximum allowable stress for this aluminum load cell, $\sigma = 200$ MPa.

7.2.2 Load Cell for Cantilevers With Rotational Spring Connections

Below are the performance plots of an aluminum load cell with the following parameters: cantilever and surface lengths, $L = 10\text{cm}$; cantilever height, $h = 1\text{mm}$; cantilever base, $b = 9.5\text{mm}$; surface curve power, $n = 3$; maximum surface gap, $D = 5\text{mm}$; rotational spring radius, $R = .01\text{m}$; elastic modulus, $E = 65\text{e}9\text{Pa}$; maximum allowable stress $\sigma_{all} = 200\text{e}6\text{Pa}$. All plots correspond to a single cantilever/surface set (1/4 of an actual load cell). For a complete load cell, the displacement of a single cantilever tip is multiplied by 2 and the force is multiplied by 4. As shown in Figure 7-11, the theory has a slight error for the curved segment deflection. If you can fix this error, please contact this author at jociek@mit.edu.

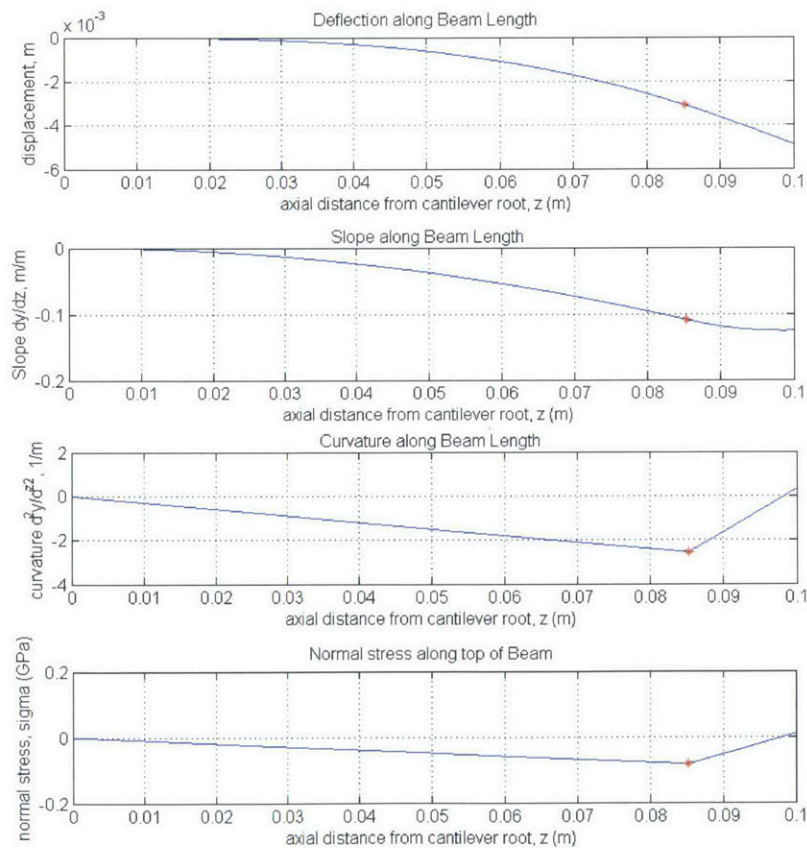


Figure 7-9: Deflection, slope, curvature, and stress along beam length when $F = 10\text{N}$. This force and deflection are for a single cantilever/surface. Load cell parameters are $D = 5\text{ mm}$. $L = 10\text{ cm}$. $b = 9.5\text{ mm}$. $h = 1\text{ mm}$. $E = 69\text{e}9\text{ Pa}$.

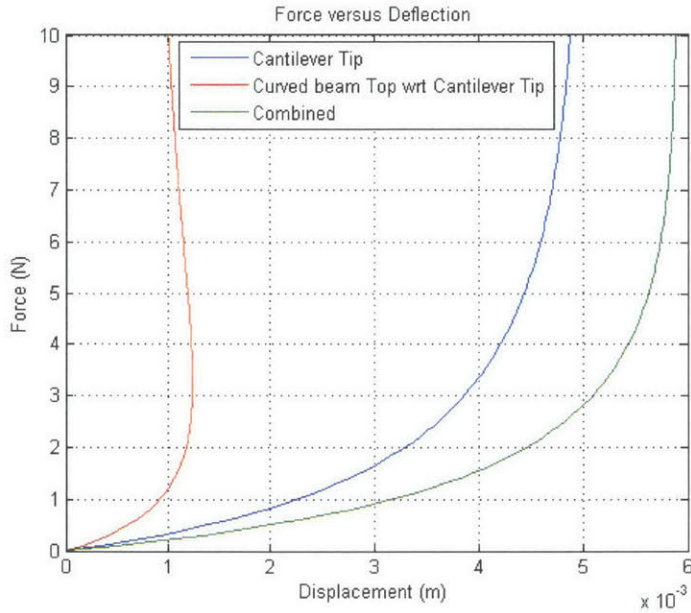


Figure 7-10: Force versus deflection of cantilever tip, top of curved beam (point B) with respect to the cantilever tip, and combined total structure deflection. This force and deflection are for a single cantilever/surface. Load cell parameters are $D= 5 \text{ mm}$. $L= 10 \text{ cm}$. $b= 9.5 \text{ mm}$. $h= 1 \text{ mm}$. $E= 69\text{e}9 \text{ Pa}$.

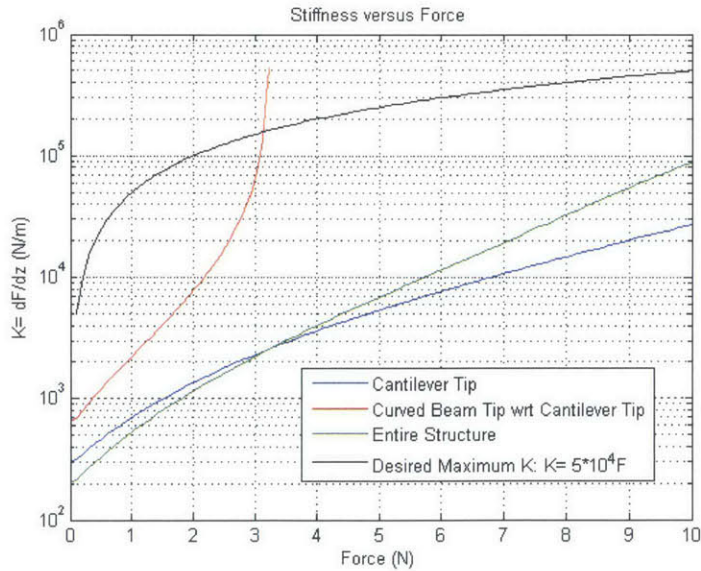


Figure 7-11: Stiffness versus force of cantilever tip, top of load cell (point B) with respect to the cantilever tip, and combined. This force and deflection are for a single cantilever/surface. Load cell parameters are $D= 5 \text{ mm}$. $L= 10 \text{ cm}$. $b= 9.5 \text{ mm}$. $h= 1 \text{ mm}$. $E= 69\text{e}9 \text{ Pa}$.

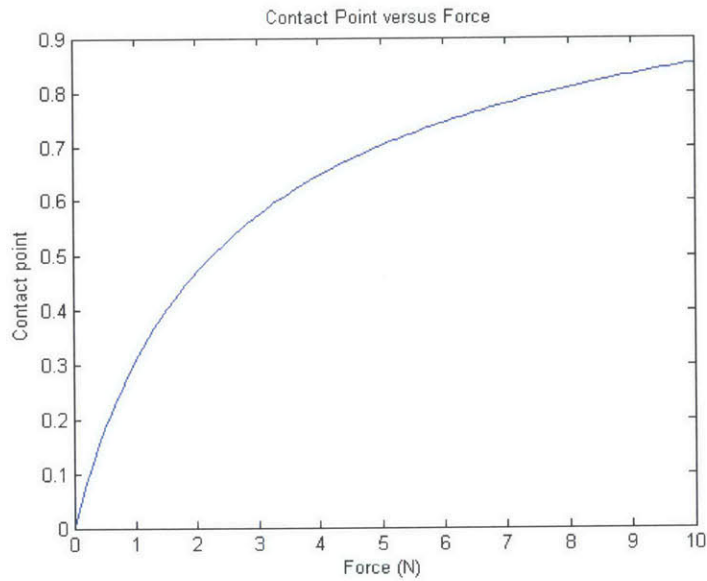


Figure 7-12: Contact point between surface and cantilever along surface axis versus force. The y-axis is normalized by the surface length, 10 cm. Force are for a single cantilever/surface. This force and deflection is for a single cantilever/surface. Load cell parameters are $D= 5$ mm. $L= 10$ cm. $b= 9.5$ mm. $h= 1$ mm. $E= 69e9$ Pa.

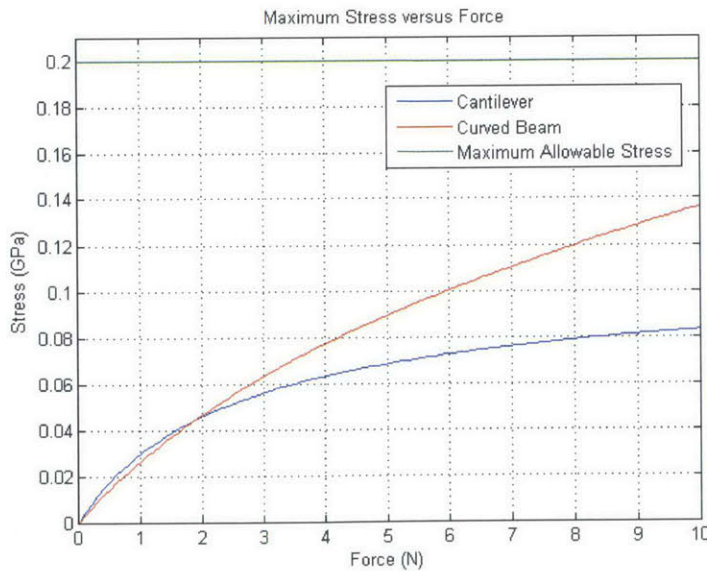


Figure 7-13: Maximum stress in the cantilever and curved beam segments versus force applied at the top of the curved beam. This force and deflection are for a single cantilever/surface. Load cell parameters are $D= 5$ mm. $L= 10$ cm. $b= 9.5$ mm. $h= 1$ mm. $E= 69e9$ Pa.

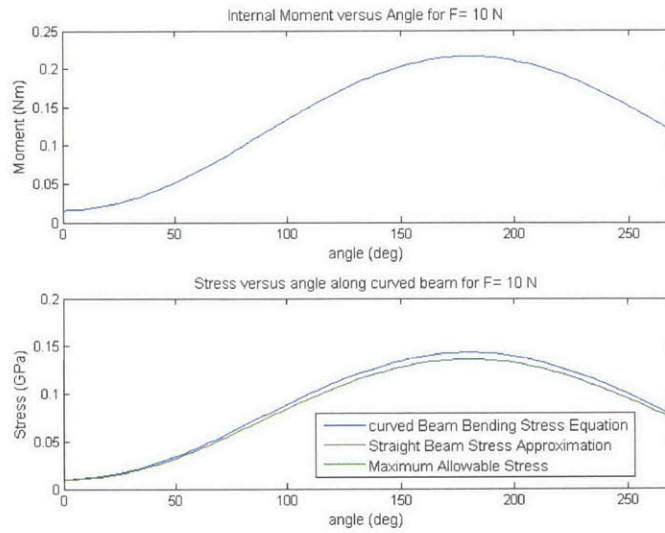


Figure 7-14: Bending moment and stress along curved segment when $F = 10\text{ N}$. θ corresponds to the angle below the horizontal between the curve center and the cantilever tip. This force and deflection are for a single cantilever/surface. Load cell parameters are $D = 5\text{ mm}$, $L = 10\text{ cm}$, $b = 9.5\text{ mm}$, $h = 1\text{ mm}$, $E = 69\text{e}9\text{ Pa}$.

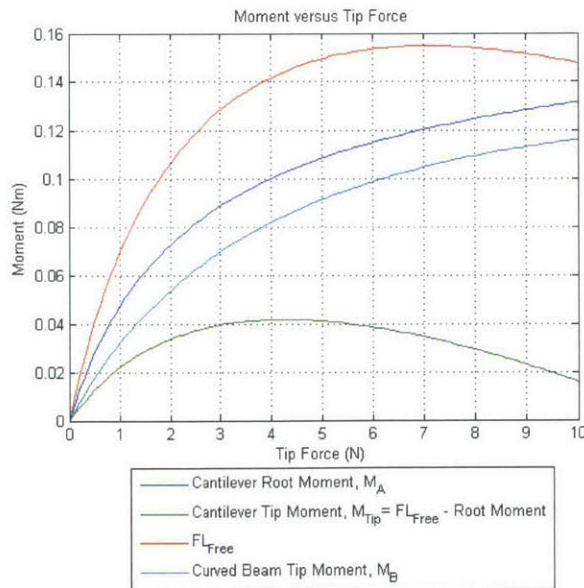


Figure 7-15: Bending moments versus force. θ corresponds to the angle below the horizontal between the curve center and the cantilever tip. This force and deflection are for a single cantilever/surface. Load cell parameters are $D = 5\text{ mm}$, $L = 10\text{ cm}$, $b = 9.5\text{ mm}$, $h = 1\text{ mm}$, $E = 69\text{e}9\text{ Pa}$.

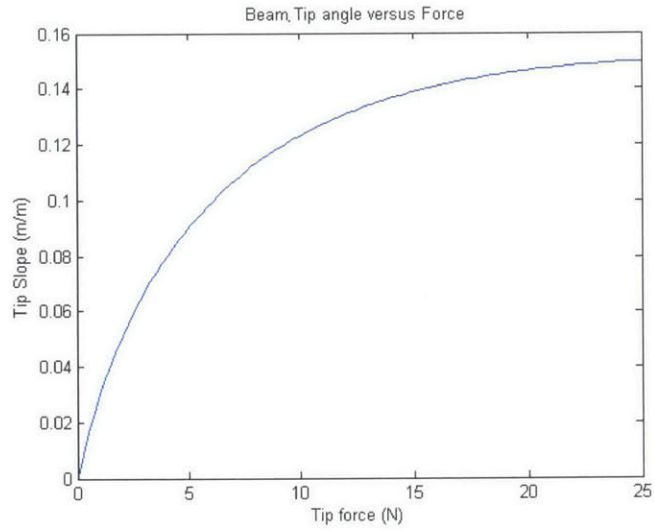


Figure 7-16: Cantilever tip angle versus force. θ corresponds to the angle below the horizontal between the curve center and the cantilever tip. This force and deflection are for a single cantilever/surface. Load cell parameters are $D= 5$ mm. $L= 10$ cm. $b= 9.5$ mm. $h= 1$ mm. $E= 69e9$ Pa.

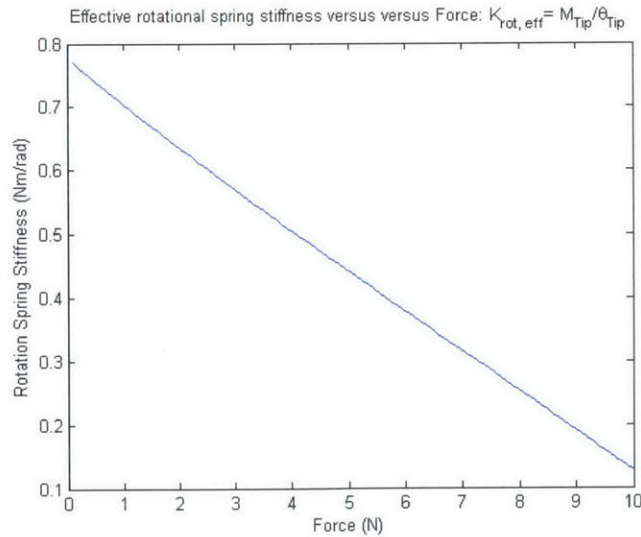


Figure 7-17: Effective rotational spring stiffness acting on cantilever tip versus force. $K_{Rot} = M_{Tip}/\theta$ corresponds to the M_{Tip} and θ shown in the two plots directly above. This force and deflection are for a single cantilever/surface. Load cell parameters are $D= 5$ mm. $L= 10$ cm. $b= 9.5$ mm. $h= 1$ mm. $E= 69e9$ Pa.

7.3 Experimental Verification

7.3.1 Fabrication

Two prototype aluminum load cells were fabricated using the tilted-head Omax waterjet machine in the Pappalardo Machine Shop. Both load cells had the following parameters: cantilever and surface lengths, $L = 10cm$; cantilever base, $b = 9.5mm$; surface curve power, $n = 3$; maximum surface gap, $D = 5mm$, elastic modulus, $E = 65e9Pa$; maximum allowable stress $\sigma_{all} = 200e6Pa$. The first load cell had rigid connections between the cantilever tips, and a cantilever height of 0.5 mm. The load cell geometry prevents the load cell from deflecting more than 8 mm in both tension and compression in order to keep the stress below $200e6Pa$. The second load cell had a cantilever height of 1 mm and rotational springs in between the cantilever tips that were physically realized by 270° curved beams with radii of $R = .01m$. The load cell geometry prevents the load cell from deflecting more than 8 mm in compression.

Although the theory assumes that the surfaces and cantilever roots meet at a point, the Omax machine is unable to cut such points. The solution was to cut away rectangular holes from the surfaces so that the minimum gaps required for the waterjet to cut inbetween the cantilever and surfaces was 1mm, as shown in Figure 7-18. "Plugs" for these holes were waterjetted with 0.1 mm clearance that could be adhered to the surface holes using epoxy. The fabricated load cells are shown in Figure 7-19.

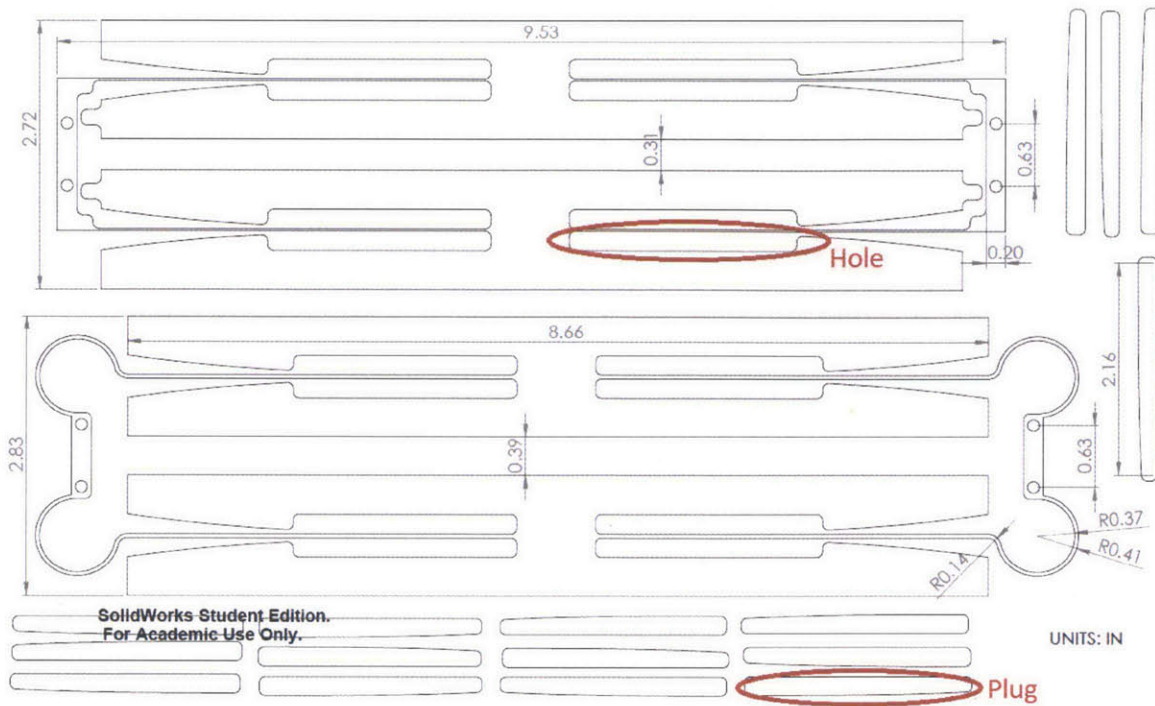


Figure 7-18: CAD of both aluminum load cells. Top: load cell without rotational springs. Bottom: Load cell with rotational springs. Included are 16 plugs to fill the rectangular holes. The rectangular holes (or "root gaps") are required so that the minimum gap required for the waterjet to cut is 1 mm.



Figure 7-19: Fabricated aluminum load cells. Top: load cell without rotational springs. Bottom: Load cell with rotational spring.

7.3.2 Experimental procedure

The force versus displacement test was performed using an Admet force tester machine with a 2.2 lbf load cell with the set-up shown in Figure 7-20. The tests were performed for the load cells with and without the "plugs", with compressive and tensile forces.



a) Load Cell with rigid connections, maximum compression



b) Load Cell with curved beam connections, maximum tension

Figure 7-20: Load cell force versus displacement experimental set-up

7.3.3 Results

Figure 7-21 shows the force versus displacement test results for the aluminum load cell without rotational springs. Figure 7-22 shows the force versus displacement test results for the aluminum load cell with rotational springs.

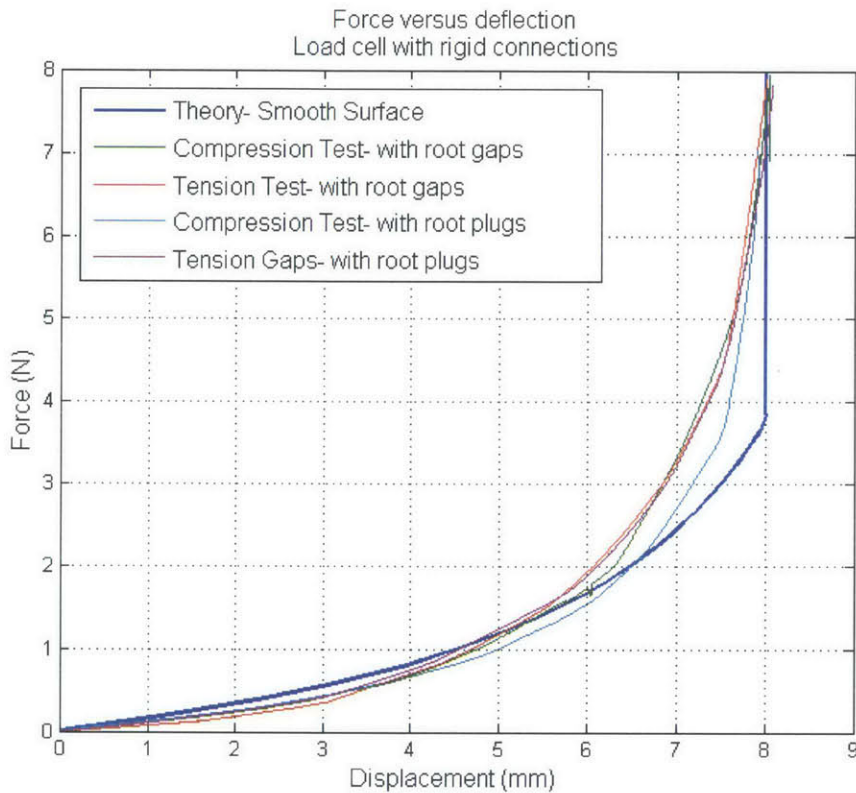


Figure 7-21: Force versus displacement test results for the aluminum load cell with rigid connections. The load cell parameters were: cantilever and surface lengths, $L = 10cm$; cantilever height, $h = 0.5mm$; cantilever base, $b = 9.5mm$; surface curve power $n = 3$; maximum surface gap, $D = 5mm$; elastic modulus, $E = 65e9Pa$; maximum allowable stress, $\sigma_{all} = 200e6Pa$. The terms "root gaps" (or "holes") and "plugs" are defined in Figure 7-18. Performance plots (e.g. deflection versus axis position and stress versus force) are shown in Section 7.2.1.

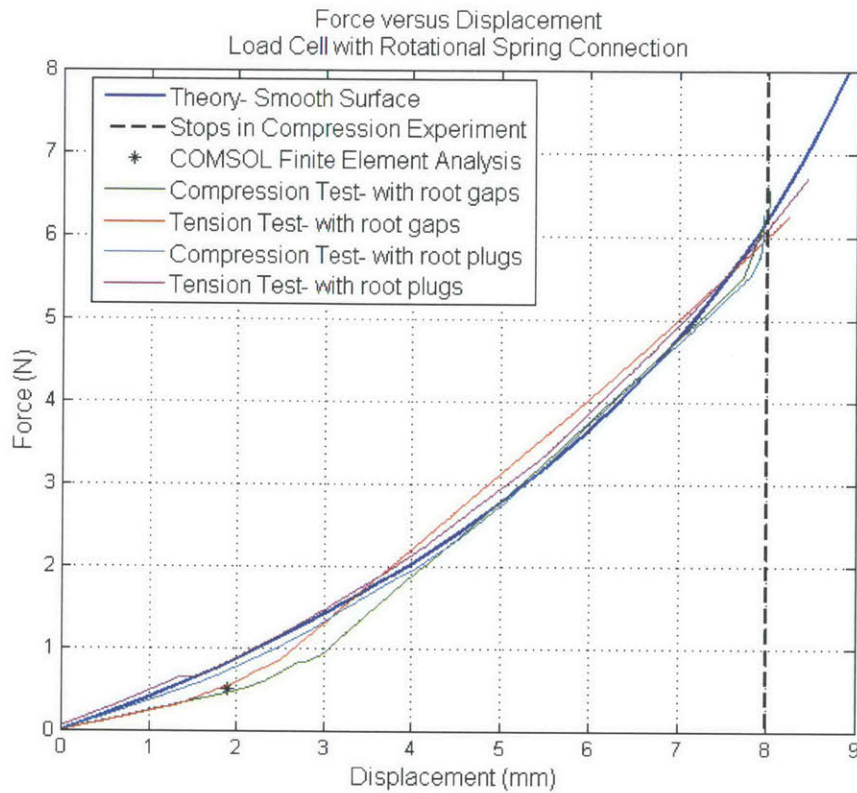


Figure 7-22: Force versus displacement test results for the aluminum load cell with rotational spring connections. The load cell parameters were: cantilever and surface lengths, $L = 10\text{cm}$; cantilever height, $h = 1\text{mm}$; cantilever base, $b = 9.5\text{mm}$; surface curve power $n = 3$; maximum surface gap, $D = 5\text{mm}$, rotational spring radius, $R = 1\text{cm}$; elastic modulus, $E = 65\text{e}9\text{Pa}$; maximum allowable stress, $\sigma_{all} = 200\text{e}6\text{Pa}$. The terms "root gaps" (or "holes") and "plugs" are defined in Figure 7-18. Performance plots (e.g. deflection versus axis position and stress versus force) are shown in Section 7.2.2.

7.4 Spring Steel Load Cells Simulated Performance

This section shows optimization curves for load cells made out of spring steel. Section 7.4.1 shows sample plots of load cell stiffness at $F = 0.01\text{N}$, at $F = 100\text{N}$, and maximum stress at $F = 100\text{N}$ for a varied cantilever width ("base") dimension and maximum surface gap, D , for the load cell with rigid connections. Section 7.4.1 then shows plots of displacement, stiffness, stress, and contact point versus applied force for varied maximum surface gaps, D . Section 7.4.2 repeats these plots for the load cell with rotational spring connections for

varied in rotational spring radii, R and constant D . For all of these plots, F refers to the total load cell force (4 nonlinear springs combined), and the displacement refers to the total load cell displacement (2 nonlinear springs combined).

7.4.1 Load Cell with Rigid Connections

These optimization plots are for spring steel load cells with the following constant parameters: cantilever and surface length, $L = 15\text{cm}$; cantilever height, $h = 0.8\text{mm}$; cantilever base dimension, $b = 9.5\text{mm}$ (unless otherwise specified); surface curve power, $n = 3$; cantilever elastic modulus, $E = 160.6\text{e}9\text{Pa}$; and yield stress, $\sigma_y = 1.2\text{e}9\text{Pa}$. In all of these plots, the force F refers to the total force applied to the load cell (4 nonlinear springs combined), and the displacement refers to the total load cell displacement (2 nonlinear springs' displacement combined).

Performance at $F = 0.17$ and $F = 100\text{N}$

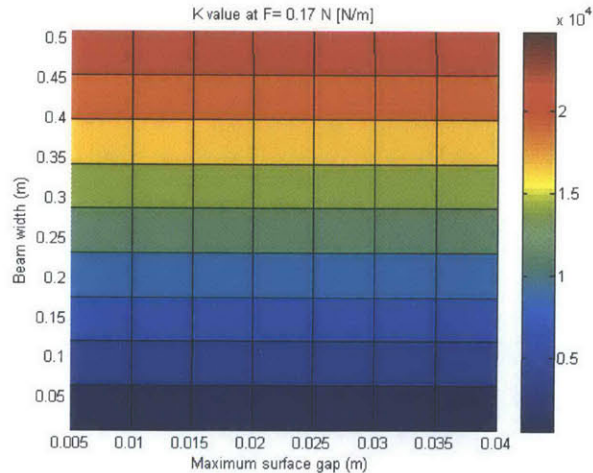


Figure 7-23: Load cell with rigid connections: stiffness at $F = 0.17\text{N}$, total load cell force and deflection. Load cell parameters are: cantilever and surface length, $L = 15\text{cm}$; cantilever height, $h = 0.8\text{mm}$; surface curve power, $n = 3$; cantilever elastic modulus, $E = 160.6\text{e}9\text{Pa}$; and yield stress, $\sigma_y = 1.2\text{e}9\text{Pa}$.

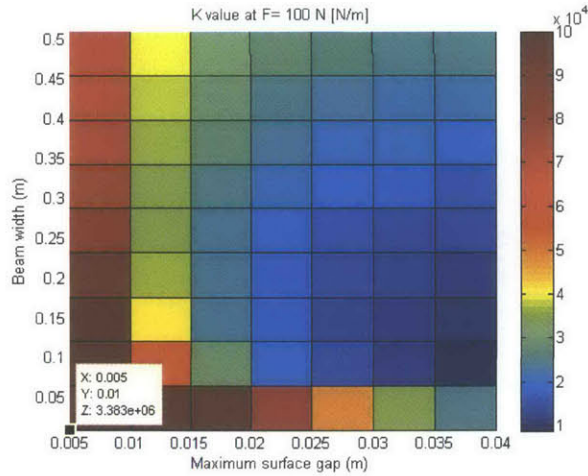


Figure 7-24: Load cell with rigid connections: stiffness at $F= 100\text{N}$, total load cell force and deflection. Load cell parameters are: cantilever and surface length, $L = 15\text{cm}$; cantilever height, $h = 0.8\text{mm}$; surface curve power, $n = 3$; cantilever elastic modulus, $E = 160.6e9\text{Pa}$; and yield stress, $\sigma_y = 1.2e9\text{Pa}$.

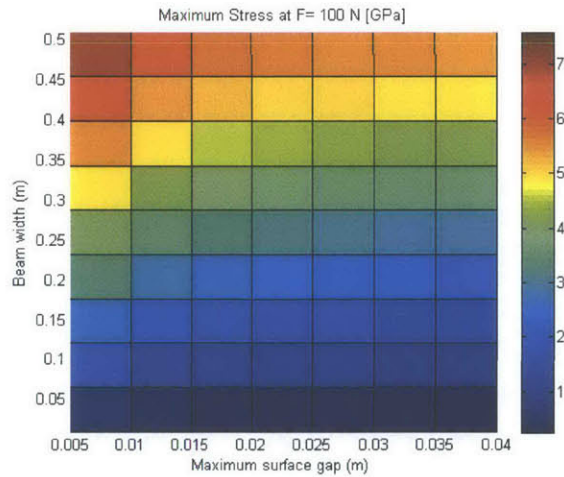


Figure 7-25: Load cell with rigid connections: maximum cantilever stress at $F= 100\text{N}$, total load cell force and deflection. Load cell parameters are: cantilever and surface length, $L = 15\text{cm}$; cantilever height, $h = 0.8\text{mm}$; surface curve power, $n = 3$; cantilever elastic modulus, $E = 160.6e9\text{Pa}$; and yield stress, $\sigma_y = 1.2e9\text{Pa}$.

Performance versus Force

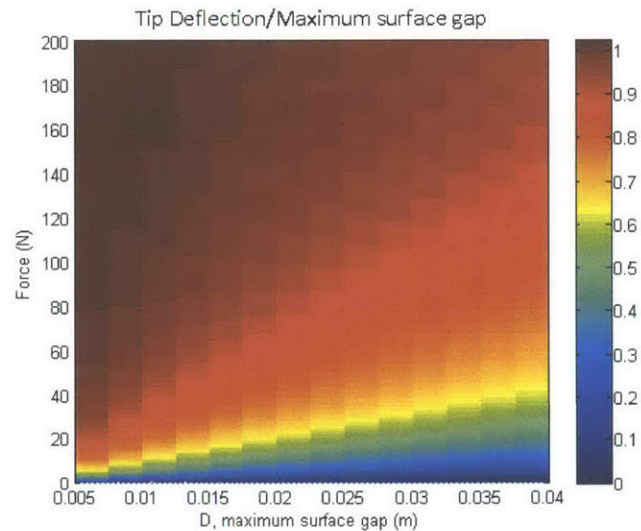


Figure 7-26: Spring steel load cell with rigid cantilever connections: deflection (normalized by maximum surface gap, D , for each nonlinear spring) versus force applied to load cell for varied surface gaps, D . The load cell has constant parameters: $L= 15$ cm, $h= 0.8$ mm, $b= 9.5$ mm, $n= 3$, $E= 160.6e9$ Pa, and yield stress is $1.2e9$ Pa.

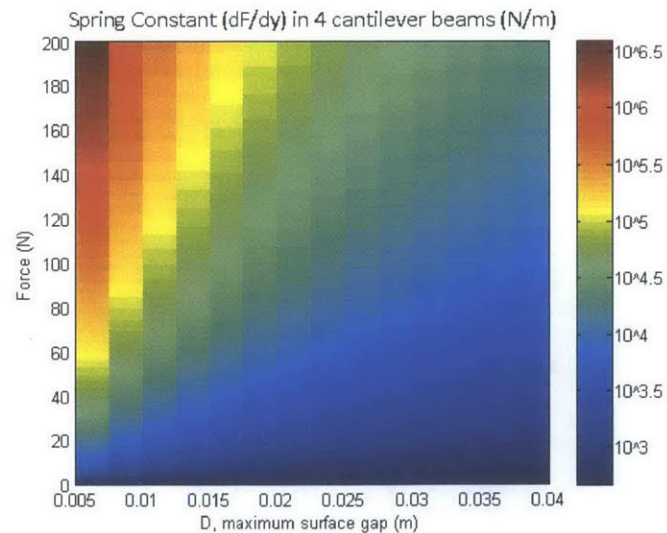


Figure 7-27: Spring steel load cell with rigid cantilever connections: stiffness versus force applied to load cell for varied surface gaps, D . The load cell has constant parameters: $L= 15$ cm, $h= 0.8$ mm, $b= 9.5$ mm, $n= 3$, $E= 160.6e9$ Pa, and yield stress is $1.2e9$ Pa.

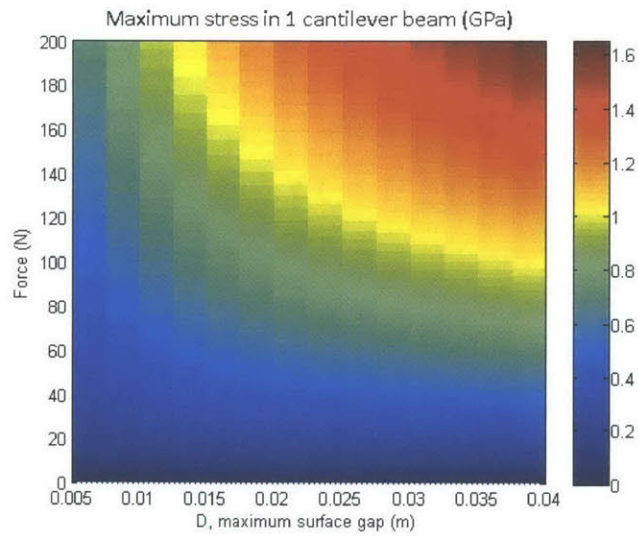


Figure 7-28: Spring steel load cell with rigid cantilever connections: maximum stress in the cantilevers versus force applied to load cell for varied surface gaps, D . The load cell has constant parameters: $L= 15$ cm, $h= 0.8$ mm, $b= 9.5$ mm, $n= 3$, $E= 160.6e9$ Pa, and yield stress is $1.2e9$ Pa.

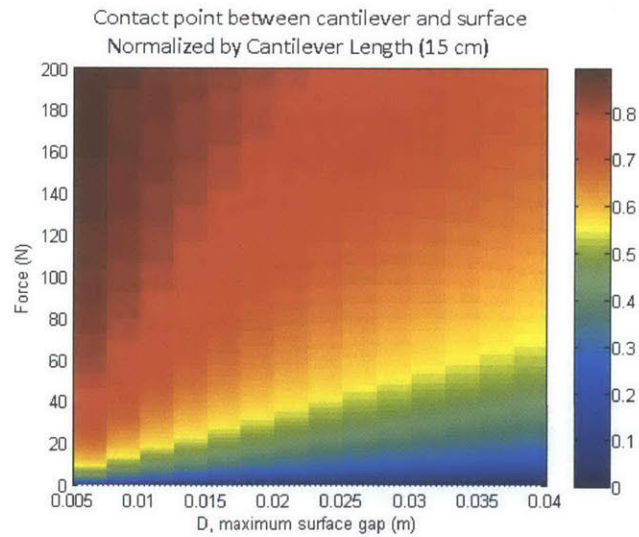


Figure 7-29: Spring steel load cell with rigid cantilever connections: contact point between each cantilever and contact surface versus force applied to load cell for varied surface gaps, D . The load cell has constant parameters: $L= 15$ cm, $h= 0.8$ mm, $b= 9.5$ mm, $n= 3$, $E= 160.6e9$ Pa, and yield stress is $1.2e9$ Pa.

7.4.2 Cantilevers with Rotational Spring Connection

These optimization plots are for spring steel load cells with the following constant parameters: cantilever and surface length, $L = 10\text{cm}$; cantilever height, $h = 0.8\text{mm}$; cantilever base dimension, $b = 9.5\text{mm}$ (unless otherwise specified); surface curve maximum gap, $D = 5\text{mm}$; surface curve power, $n = 3$; cantilever elastic modulus, $E = 160.6e9\text{Pa}$; and yield stress, $\sigma_y = 1.2e9\text{Pa}$. The rotational spring has a radius, R is varied in all of the plots. The rotational spring has the same base dimension and height dimension as the cantilever to which it is attached. In all of these plots, the force F refers to the total force applied to the load cell (4 nonlinear springs combined), and the displacement refers to the total load cell displacement (2 nonlinear springs' displacement combined).

Performance at $F = 0.01$ and $F = 800\text{N}$

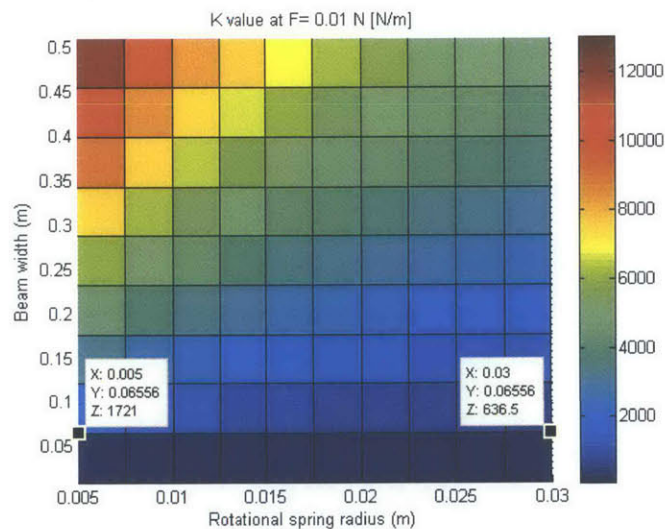


Figure 7-30: Load cell with rotational spring connections: stiffness at $F = 0\text{N}$, total load cell force and deflection. Load cell parameters are: cantilever and surface length, $L = 15\text{cm}$; cantilever height, $h = 0.8\text{mm}$; surface curve power, $n = 3$; surface curve maximum deflection, $D = 0.005\text{m}$; cantilever elastic modulus, $E = 160.6e9\text{Pa}$; and yield stress, $\sigma_y = 1.2e9\text{Pa}$.

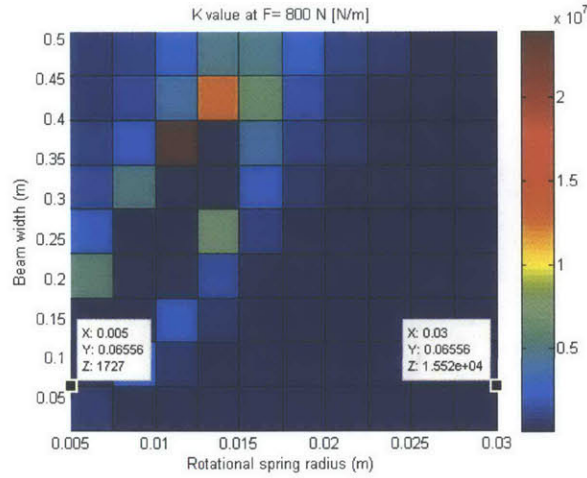


Figure 7-31: Load cell with rotational spring connections: stiffness at $F=800\text{N}$, total load cell force and deflection. Load cell parameters are: cantilever and surface length, $L = 15\text{cm}$; cantilever height, $h = 0.8\text{mm}$; surface curve power, $n = 3$; surface curve maximum deflection, $D = 0.005\text{m}$; cantilever elastic modulus, $E = 160.6e9\text{Pa}$; and yield stress, $\sigma_y = 1.2e9\text{Pa}$.

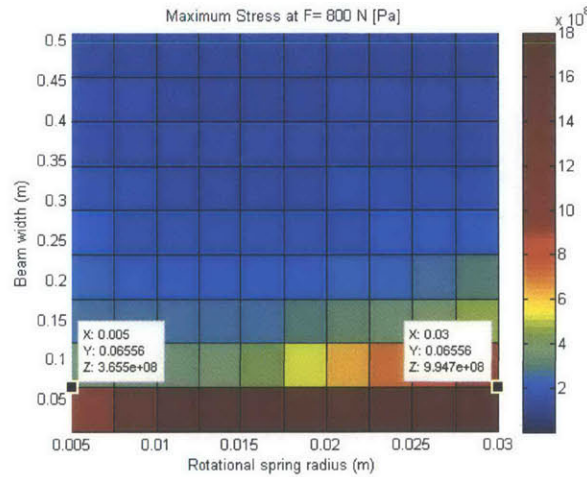


Figure 7-32: Load cell with rotational spring connections: maximum cantilever stress at $F=800\text{N}$, total load cell force and deflection. Load cell parameters are: cantilever and surface length, $L = 15\text{cm}$; cantilever height, $h = 0.8\text{mm}$; surface curve power, $n = 3$; surface curve maximum deflection, $D = 0.005\text{m}$; cantilever elastic modulus, $E = 160.6e9\text{Pa}$; and yield stress, $\sigma_y = 1.2e9\text{Pa}$.

Performance versus Force

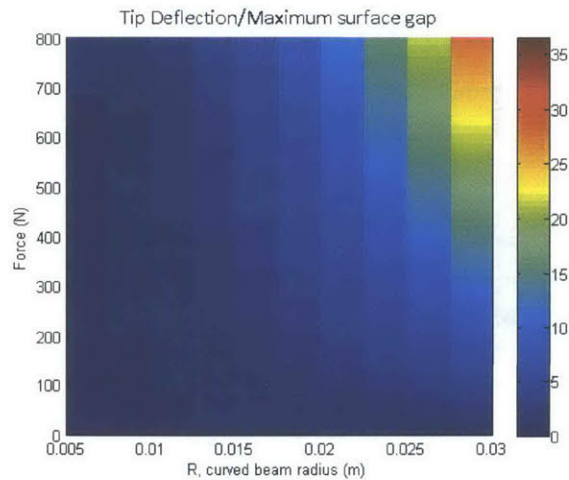


Figure 7-33: Spring steel load cell with rotational spring cantilever connections: deflection (normalized by maximum surface gap, D , for each nonlinear spring) versus force applied to load cell for varied curved beam radii, R . The ratio exceeds 1 because the curved beam deflects further than the cantilever tip. The load cell has constant parameters: $L = 15$ cm, $h = 0.8$ mm, $b = 9.5$ mm, $n = 3$, $D = 5$ mm, $E = 160.6 \times 10^9$ Pa, and yield stress is 1.2×10^9 Pa.

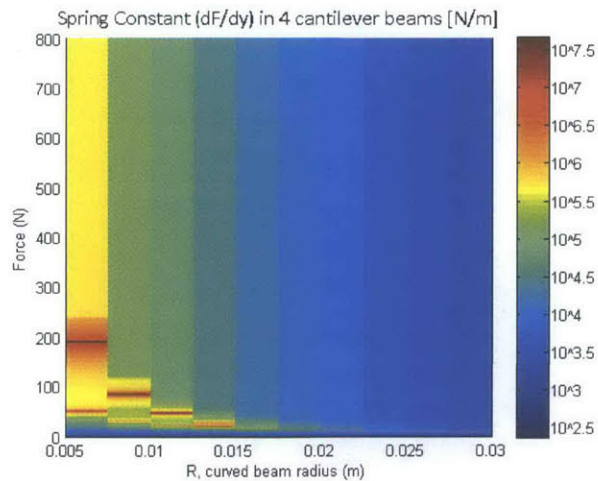


Figure 7-34: Spring steel load cell with rotational spring cantilever connections: stiffness versus force applied to load cell for varied curved beam radii, R . The load cell has constant parameters: $L = 15$ cm, $h = 0.8$ mm, $b = 9.5$ mm, $n = 3$, $D = 5$ mm, $E = 160.6 \times 10^9$ Pa, and yield stress is 1.2×10^9 Pa.

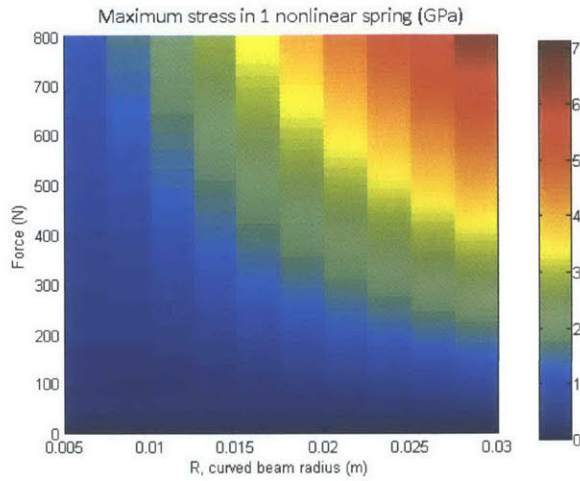


Figure 7-35: Spring steel load cell with rotational spring connections: maximum stress in the cantilevers versus force applied to load cell for varied curved beam radii, R . The load cell has constant parameters: $L = 15$ cm, $h = 0.8$ mm, $b = 9.5$ mm, $n = 3$, $D = 5$ mm, $E = 160.6 \times 10^9$ Pa, and yield stress is 1.2×10^9 Pa.

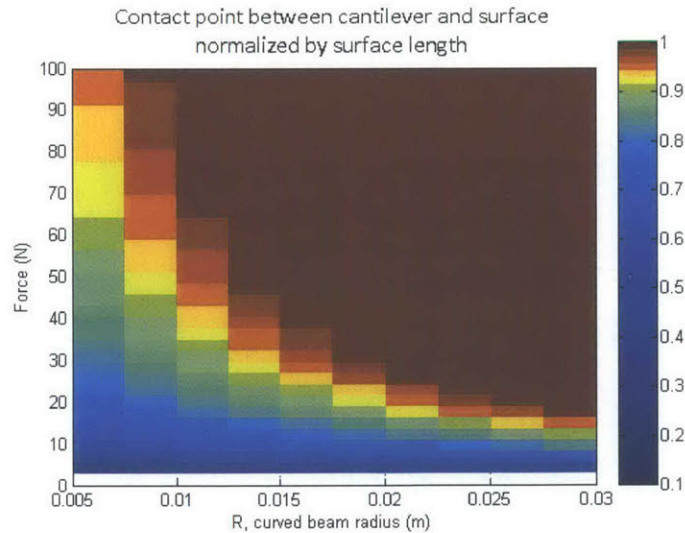


Figure 7-36: Spring steel load cell with rotational spring connections: contact point between each cantilever and contact surface versus force applied to load cell for varied curved beam radii, R . The load cell has constant parameters: $L = 15$ cm, $h = 0.8$ mm, $b = 9.5$ mm, $n = 3$, $E = 160.6 \times 10^9$ Pa, $D = 5$ mm, and yield stress is 1.2×10^9 Pa.

7.5 Conclusions and Future Work

This chapter presented a novel nonlinear load cell design that can measure forces with accuracies of 1% over nearly 5 orders of magnitude and will not break for forces several orders of magnitude beyond that. (see Section 7.4.2). The accuracy range is achieved by designing the stiffening spring's stiffness to remain below $10^5 F$, which allows an optical instrument to measure deflections equal to or greater than $0.1\mu m$ for a 1% change in force. Typical linear load cells that can accurately measure small forces break or reach their maximum capacity for large forces. Typical linear load cells that can accurately detect large forces cannot accurately measure small forces. The proposed nonlinear load cell can withstand forces well beyond its force measurement capacity because it can be designed so that beyond a certain force, the cantilevers do not bend further. Instead, the additional stress compresses solid blocks, which can be designed to withstand a desired large force.

The method of inserting "plugs" into the surface root holes so that the waterjet could make the parts worked well. It was noted that the fabricated load cells were delicate in the out-of-plane direction. The force versus displacement tests verified the theory for aluminum load cells and small forces. The simulations showed that load cells made out of spring steel can satisfy the maximum load cell stiffness ($K \leq 10^5 F$) required for high force measurement accuracy.

As for choosing the optimal parameters, there is a trade off between a low stiffness at $F=0$ N and a safety factor against yield at very large forces (see Sections 7.4.1 and 7.4.2), which limits the load cell performance (i.e. accuracy and ruggedness). For the load cell with rigid connections, this is because when most of the cantilever length is in contact with the surface, the slope of the free cantilever must change from the surface slope at its root to slope= 0 at its tip in a very small distance; causing a high curvature and stress at its right end. We tried to solve this problem by adding rotational springs at the end of the cantilever tips, implemented in the form of 270° arcs. This change does allow the cantilever to withstand much larger forces and fully wrap along the contact surface. The load cell maximum force is still limited by the maximum stress that can be withstood by the 270° arcs, which continue to deflect after the cantilevers have fully wrapped along the surfaces. When the maximum

allowable force is determined, the spring can easily be designed to stop deflecting due to touching of the top and bottom surface sets in compression and contact of surface stopper blocks with the vertical connections in tension (See Figure 7-19).

Future work will include:

- Fabricate and test spring steel load cells.

- Correct the theory for the load cell with the rotational spring curved beam. As shown in Figure 7-10, the derivation using Castigliano's theorem has a slight error for large force values where the curved beam deflection decreases before further increasing.

- Investigate a different type of rotational spring for which stress does not significantly increase for increasing forces.

- Investigate a variable pitch helical coil version of the nonlinear cantilever/surface spring load cell so that the load cell is more durable in the out-of-plane direction.

Appendix A

Matlab Codes

A.1 Nonlinear spring force versus displacement

```
1 function [XI, FI, SF, Yc]= cant_beam_force_AddSubD_Final_3cm_FINALforTHESIS
    (massA, E, h, EI, n, L, D, surfaceEndfraction, Pmax, numInt, XImax)
2
3 I= EI/E; %beam cross section moment of inertia
4
5 % massA= .0097; %length of end-mass that overhangs cantilever tip [m]
6 % E= 160.6e9; %beam elastic modlulus [Pa]
7 % h= .002*.0254; %cantilever height [m]
8 % b= .75*.0254; %cantilever base [m]
9 % I= b*h^3/12; %cantilever moment of inertia [m^4]
10 % EI= E*I; %cantilever rigidity
11 % n= 3; %surface curve power
12 % L= .1; %cantilever length [m]
13 % D= .015; %maximum surface end-gap (gap at surface tip) [m]
14 % surfaceEndfraction= .1/L; %fraction of surface length over cantilever
    length
15 % Pmax= .02; %maximum power value to calculate
16 % numInt= 100; %number of force values for which to calculate deflection
17 % Dt= Dtop;
18 % XImax= .017;
```

```

19
20 P= linspace(0,Pmax,numInt); %vector of force vlaues for which to calcualte
    cantilevr tip deflection
21
22 % definition of surface geometry
23 xx=linspace(0,1,100); %Normalized by surface length
24 SStop=xx.^n*D; % Surface geometry. given the constraints SS(0)=SS'(0)=SS
    ''(0)=0 amd SS(1)=D. Normalized by cantilever length [m]
25 SSg1top= D.*n.*xx.^(n-1); %surface slope [m/m]
26 SSg2top= D.*n.*(n-1).*xx.^(n-2); %surface radius of curvature [m/m^2]
27
28 y=0; %initial contact point along axis between cantilever and surface [m]
29 sigma_y= 1.8e9; %spring steel yield stress [Pa]
30 c= h/2; %distance from neutral axis
31
32 Lsurf= L*surfaceEndfraction; %surface length [m]
33
34 %for each force value, calculate the contact point along the axis between
    cantilever and surface
35 opts= optimset('TolFun',1e-10, 'TolX', 1e-10);
36 for i=1:length(P)
37     i
38     ff= @(y, opts) interp1(xx,SSg2top,y)./Lsurf.^2-P(i)/EI*(massA+L-L*y); %
        find value of SSg2 that corresponds to y, a distance along
        horizontal axis
39     y=fsolve(ff,y, opts);
40     yc(i)=y*Lsurf; %actual value of yc along axis.
41
42     %calculate maximum normal stress here
43     sigmaInContact= E.*c.*n.*(n-1).*D./Lsurf.^2.*(yc(i)./Lsurf).^(n-2);
44     sigmaFree= c./I.*P(i).*(L-y); %max stress for free segment
45     sigmaMax= max(abs([sigmaInContact sigmaFree]));
46     SF(i)= sigma_y/sigmaMax;
47
48 end
49

```



```

50 endFreeL= L - yc; %free L correponding to each P [m]
51
52 %cantilever tip deflection based on force and BC
53 d1=(P.*(endFreeL).^3)./(3*EI); %d1= [P(L-yc)^3] /3EI
54 d2=(endFreeL).*interp1(xx,SSg1top,yc/Lsurf)/Lsurf; %d2= surface slope at yc
    * (L-yc) <-- yc/L normalized in interp1 function
55 d3=interp1(xx,SStop,yc/Lsurf); %d3= height of surface at contact point
56 dd=d1+d2+d3; %this is the deflection at cantilever tip
57
58 %ACCOUNT FOR END MASS DEFLECTION
59 endSlope= interp1(xx,SSg1top,yc/Lsurf)/Lsurf + (P.*(endFreeL).^2)./(2*EI);
60 dd_mass= dd+ massA.*sin(atan(endSlope)); %this is the defleciton at the
    mass
61
62 %if mass bent so far that NaN values are created, remove them
63 P(isnan(dd_mass))= [];
64 SF(isnan(dd_mass))= [];
65 yc(isnan(dd_mass))= [];
66 dd_mass(isnan(dd_mass))= [];
67
68 %If extreme P values do not cause change in displacement, truncate XI
69 while dd_mass(length(dd_mass)) > XImax %== dd_mass(length(dd_mass)-1)
70     dd_mass(length(dd_mass))= [];
71     P(length(P))= [];
72     SF(length(SF))= [];
73 end
74
75 % figure(1)
76 % plot(dd_mass, P, 'b');%, dd_mass, .1.*dd_mass.^3, 'r');
77 % title('Force versus tip deflection');
78 % xlabel('Tip Displacement (m)')
79 % ylabel('Force (N)')
80 % %legend('Actual','Desired- Weak Spring');
81 % grid;
82
83

```

```

84 XI= dd_mass; %table of displacements [m]
85 FI= P; %table of forces [N]
86 Yc= yc; %table of contact points [m]
87 SF= SF; %table to safety factors against yield
88
89 end

```

A.2 Load cell force versus displacement

```

1 %This code outputs the total displacement versus force for 1/4 of a load
  cell.
2 %To get the total load cell force, multiply FI by 4.
3 %To get the total load cell displacement, multiply resultDisp by 2.
4 function [resultDisp, FI]= loadCellForce
5 %%%%%%%%%%%%%%%%%%%%%%%%%%%%%%%%%%%%%%%%%%%%%%%%%%%%%%%%%%%%%%%%%%%%%%%%%% INPUTS %%%%%%%%%%%%%%%%%%%%%%%%%%%%%%%%%%%%%%%%%%%%%%%%%%%%%%%%%%%%%%%%%%%%%%%%%%
6 plotIndividualP= 1; %set this equal to 1 if want to make plots of
  performance for individual force value
7 plotIndividualCase= 1; %set this equal to 1 if want to see plots of
  performance versus force
8
9 L= .1; % cantilever length [m]
10 h= 1e-3; % cantilever height [m]
11 b= .0095; % cantilever width [m]
12 R= .01; %radius of 270 degree curve at cantilever tip [m]
13
14 E= 160.6e9; %cantilever elastic modulus. Spring steel [Pa]
15 sigma_y= 1.8e9; %spring steel yield stress [Pa]
16
17 n= 3; %surface curve power
18 D= .005; %surface curve, maximum end gap [m]
19 surfaceEndfraction= 1; %ratio of surface length to cantilever length
20
21 Pmax= 10; %maximum force applied [N]

```

```

22 numInt= 100; %number of force intervals between 0 and Pmax to compute
23 %%%%%%%%%% END INPUTS %%%%%%%%%%
24
25 Lsurf= L*surfaceEndfraction; %surface length [m]
26
27 A= h*b; %cantilever cross section are [m]
28 I= b*(h^3)/12; %cantilever second moment of inertia [m^4]
29 EI= E*I; %cantilever rigidity [Nm^2]
30 c= h/2; %distance from neutral axis to top hheight for straight beam [m]
31
32 P= linspace(0, Pmax, numInt); %forces for computations [N]
33
34 % definition of surface geometry
35 xx=linspace(0,1,300); %intervals along surface axis. Normalized by surface
    length
36 SS=xx.^n*D; % Surface shape. given the constraints SS(0)=SS'(0)=SS''(0)=0
    amd SS(1)=D. Normalized by cantilever length [m]
37 SSg1= D.*n.*xx.^(n-1); %surface slope. Normalized by cantilever length [m]
38 SSg2= D.*n.*(n-1).*xx.^(n-2); %surface radius of curvature. Normalized by
    cantilever length [m]
39
40 y=0; %initial x-value point of contact between cantilever and surface. [
    unitless]
41 opts= optimset('TolFun',1e-10, 'TolX', 1e-10);
42
43 Yt= linspace(0,Lsurf, 200); %dimensionalized intervals along surface axis [
    m]
44 SSG1= D.*n.*(Yt./Lsurf).^(n-1)./Lsurf; %dimensionalized surface slope [m/m]
45 SSG2= D.*n.*(n-1).*(Yt./Lsurf).^(n-2)./Lsurf^2; %dimensionalized surface
    radius of curvature [m/m^2]
46
47 %calculate contact point between cantilever and surface for each force
48 for i=2:length(P)
49     i
50     %find value of SSG2 that corresponds to y, a distance along horizontal
        axis:

```

```

51     ff= @(y, opts) interp1(xx,SSg2,y)./Lsurf.^2- ((3.*pi.*R.^2 + 2.*R.^2 +3
        .*pi.*(L-L*y).*R +(L-L*y).^2 ).*P(i) -2.*(interp1(xx,SSg1,y)./Lsurf)
        *EI)./(3*pi*R +2*(L-L*y))/EI ;
52     y=fsolve(ff,y, opts);
53     yc(i)=y*Lsurf; %dimensionalized value of yc along axis [m]
54 end
55
56 S= interp1(xx, SS, yc./Lsurf); %deflection at free cantilever root for each
        applied force [m]
57 Sp= interp1(Yt,SSG1,yc); %slope at free cantilever root for each applied
        force [m/m]
58 Spp= (interp1(Yt, SSG2, yc)); %radius of curvature at free cantilever root
        for each applied force [m/m^2]
59
60 if (plotIndividualP== 1)
61     plotIndP(P, yc, L, Sp, R, E, n, D, Lsurf, EI, I, S, c, sigma_y);
62 end
63
64 %Straight Beam Deflection
65 c1= -P;
66 Lfree= L- yc;
67 Ma= ( (3.*pi.*R.^2 + 2.*R.^2 +3.*pi.*Lfree.*R +Lfree.^2 ).*P -2.*Sp.*E.*I).
        /(3.*pi.*R +2.*Lfree); %only include bending moment
68 c2= Ma;
69 c3= Sp*EI;
70 c4= S*EI;
71
72 dd= (c1./6.*Lfree.^3 + c2./2.*Lfree.^2 +c3.*Lfree + c4) ./EI;
73 angle= (c1./2.*Lfree.^2 + c2.*Lfree + c3)./EI;
74
75 %Straight Beam stress
76 sigmaFree_root= c/I.*(c2);
77 sigmaFree_tip= c/I*(c1.*Lfree + c2);
78 sigmaMax= max(abs([sigmaFree_root; sigmaFree_tip ]));
79
80 XI= dd; %table of cantilever tip displacements [m]

```

```

81 FI= P; %table of forces [N]
82 Yc= yc; %table of contact points [m]
83 SF= sigma_y./sigmaMax; %table of stress in cantilever [Pa]
84 Kinv= gradient(XI, FI(2)-FI(1)); %1/cantilever tip stiffness
85 K= 1./Kinv; %table of cantilever tip stiffness [N/m]
86 Mtip= -Ma +P.*Lfree; %moment applied at beam tip [Nm]
87
88 if (plotIndividualCase == 1)
89     figure(1)
90     hold off
91     plot(XI, FI);
92     title('Force versus Deflection');
93     xlabel('Displacement (m)');
94     ylabel('Force (N)');
95     grid;
96
97     figure(2)
98     hold off
99     KTemp= K;
100    bool= KTemp<0; %determine which elements are less than 0
101    ind= find(bool); %get index of first element less than 0
102    KTemp= KTemp(1:ind-1);
103    FITemp= FI(1:ind-1);
104    plot(FI, K, 'b');
105    title('Stiffness versus Force');
106    xlabel('Force (N)');
107    ylabel('K= dF/dz (N/m)');
108
109    %plot safety factor versus Force
110    figure(3);
111    hold off
112    plot(FI, sigmaMax./10^9, 'b');
113    hold on
114    xlabel('Force (N)');
115    ylabel('Stress (GPa)');
116    title('Maximum Stress versus Force');

```

```

117
118 %plot contact point versus Force
119 figure(4);
120 plot(FI, Yc./Lsurf);
121 xlabel('Force (N)');
122 ylabel('Contact point');
123 title('Contact Point versus Force');
124
125 %plot cantilever tip (+surface) angle versus force
126 figure(5)
127 plot(P, angle);
128 title('Beam Tip angle versus Force');
129 ylabel('Tip Slope (m/m)');
130 xlabel('Tip force (N)');
131
132 %plot Rotational spring stiffness versus force
133 figure(6)
134 plot(P, Mtip./angle);
135 title('Effective rotational spring stiffness versus Force:  $K_{\text{rot, eff}} = \frac{M_{\text{Tip}}}{\theta_{\text{Tip}}}$ ');
136 xlabel('Force (N)');
137 ylabel('Rotation Spring Stiffness (Nm/rad)');
138
139 figure(9)
140 Mb= P.*R + Mtip;
141 plot(P, Ma, P, Mtip, P, P.*Lfree, P, Mb);
142 xlabel('Tip Force (N)');
143 ylabel('Moment (Nm)');
144 title('Moment versus Tip Force');
145 legend('Cantilever Root Moment, M_A', 'Cantilever Tip Moment, M_{Tip}=
FL_{Free}-Root Moment', 'FL_{Free}', 'Curved Beam Tip Moment, M_B');
146 grid;
147
148 end
149
150 % OUTPUTS: Kmin, Kmax, maximum stress, SFmin, F80PContact

```

```

151     maxStress_beam= max(sigmaMax)
152     SFmin_beam= min(SF); %sigma_y/maxStress_beam
153     Kmin_beam= min(K)
154     Kmax_beam= max(K)
155     %F80PContact= interp1(FI,yc,.8*L); %force when 80% of cantilever length
        is in contact with surface
156
157 %deflection of top of curved segment- when Strain energy only includes
        bending
158 delta_Top= (R.*(27.*pi.^3.*P.*R.^4-24.*pi.*P.*R.^4+36.*pi.^2.*Lfree.*P.*R.
        ^3-32.*Lfree.*P.*R.^3+36.*pi.*Lfree.^2.*P.*R.^2+32.*Lfree.^2.*P.*R.^2+24
        .*pi.*Lfree.^3.*P.*R+...
159     16.*Lfree.^3.*P.*R+24.*pi.*Lfree.*Sp.*EI.*R+16.*Lfree.*Sp.*EI.*R+6.*pi.
        *Lfree.^4.*P+12.*pi.*Lfree.^2.*Sp.*EI))./(4.*EI.*(3.*pi.*R+2.*Lfree)
        .^2);
160
161 resultDisp= delta_Top+XI; %total structure displacement [m]
162
163 if plotIndividualCase== 1
164     figure(1);
165     hold on
166     plot(delta_Top, P, 'r', delta_Top+XI, P, 'g');%, delta_Top+XI, P, 'g');
167     legend('Cantilever Tip', 'Curved beam Top wrt Cantilever Tip', '
        Combined');
168     xlabel('Displacement (m)');
169     ylabel('Force (N)');
170
171     figure(2);
172     hold on
173     Kinv_curv= gradient(delta_Top, FI(2)-FI(1));
174     Kinv_Tot= gradient(delta_Top+XI, FI(2)-FI(1));
175     K_curv= 1./Kinv_curv;
176     K_Tot= 1./Kinv_Tot;
177     plot(FI, K_curv, 'r', FI, K_Tot, 'g');
178     plot(FI, FI.*5e4, 'k');

```

```

179     legend('Cantilever Tip', 'Curved Beam Tip wrt Cantilever Tip', 'Entire
        Structure', 'Desired K')
180     grid;
181 end
182
183 %stress versus angle
184 theta= linspace(0,3*pi/2, 100);
185 F= max(P);
186 MtipMax= Mtip(length(Mtip));
187 V= F.*cos(theta);
188 N= -F.*sin(theta);
189 Mb= -Ma(length(Ma)) +F*(R+L);
190 My= MtipMax +F*R.*(1-cos(theta));
191
192 R_n= h/log((2*R+h)/(2*R-h));%neutral radius: h/ln(rOut/rIn)
193 e= R- R_n; %e= R_centroid - R_neutral
194
195 sigma_bend_top= My.*(h/2)/(A*e*(R+h/2));
196 sigma_bend_bot= My.*(-h/2)/(A*e*(R-h/2));
197
198 sigma_bend_top_approx= My.*h/2./I;
199 sigma_bend_top_approx_vF= (Mtip+P.*R.*(2)).*h/2./I;
200
201 sigma_normal= N./A;
202
203 %Q= b*H^2/2; %H is distance from neutral axis
204 Q_top= b*(R+h/2- R_n)^2/2;
205 Q_bot= b*(R-h/2- R_n)^2/2;
206
207 %sigma_xy= V*Q/I/b;
208 sigma_xy_top= V.*Q_top./I./b;
209 sigma_xy_bot= V.*Q_bot./I./b;
210
211
212 % sigma_eff= (sigma_x.^2 +3.*sigma_xy.^2).^5;
213 sigma_eff_top=((sigma_bend_top + sigma_normal).^2 +3.*sigma_xy_top.^2).^5;

```



```

214 sigma_eff_bot=((sigma_bend_bot + sigma_normal).^2 +3.*sigma_xy_bot.^2).^5;
215 sigma_eff= max(sigma_eff_top, sigma_eff_bot);
216
217 if plotIndividualCase== 1
218     %plot normal stress versus theta.
219     %since R>>h, shear stress is negligible
220     figure(7)
221     subplot(2,1,1)
222     plot(theta.*180./pi, My)
223     xlabel('angle (deg)');
224     ylabel('Moment (Nm)');
225     title('Internal Moment versus Angle for F= 10 N');
226     xlim([0 270]);
227
228     subplot(2,1,2)
229     hold off
230     plot(theta.*180./pi, -sigma_bend_bot./10^9, theta.*180./pi,
          sigma_bend_top_approx./10^9)
231     hold on
232     plot([0 max(theta).*180./pi], [sigma_y sigma_y]./10^9./2, 'g');
233     xlabel('angle (deg)')
234     ylabel('Stress (GPa)');
235     title('Stress versus angle along curved beam for F= 10 N');
236     legend('curved Beam Bending Stress Equation', 'Straight Beam Stress
          Approximation', 'Maximum Allowable Stress');
237     xlim([0 270]);
238
239     %output location of maximum effective stress
240     [maxStress_curve, index]= max(sigma_eff);
241     maxStress_curve
242     maxStress_curve_theta= theta(index)
243
244     figure(3);
245     plot(FI, abs(sigma_bend_top_approx_vF)./10^9, 'r');
246     plot([FI(1) max(FI)], [.5 .5].*sigma_y./10^9, 'k');
247     legend('Cantilever', 'Curved Beam', 'Maximum Allowable Stress');

```

```

248     xlim([0 max(FI)]);% 0 10]); %axis([XMIN XMAX YMIN YMAX])
249     grid;
250 end
251 end
252
253
254 function plotIndP(P, yc, L, Sp, R, E, n, D, Lsurf, EI, I, S, c, sigma_y)
255
256     F= max(P);
257     y= max(yc);
258     Lfree= L- y;
259
260     zInContact= 0:.0001:y;
261     zFree= y:.0001:Lfree+y;
262     xFree= zFree- y;
263
264     SpMax= max(Sp);
265     c1= -F;
266     Ma= ( (3.*pi.*R.^2 + 2.*R.^2 +3.*pi.*Lfree.*R +Lfree.^2 ).*F -2.*SpMax.*
           *E.*I)./(3.*pi.*R +2.*Lfree); %only include bending moment
267     c2= Ma;
268     c3= SpMax*EI;
269     c4= max(S)*EI;
270
271     sigmaInContact= E.*c.*n.*(n-1).*D./Lsurf.^2.*(zInContact./L).^ (n-2); %
           Bottom of beam that is deflecting upwards, positive tip force
272     sigmaFree= c./I.* ( c1.*xFree +c2 ); %at end: -F*Lfree + F*Lfree/2 =
           F*Lfree/2
273
274     %subplots for maximum stress along beam length
275     figure(8);
276
277     Deflection_Free= (c1/6.*xFree.^3 + c2/2.*xFree.^2 +c3*xFree + c4) ./EI;
278     Slope_Free= (c1/2.*xFree.^2 + c2.*xFree +c3) ./EI;
279     Curvature_Free= (c1.*xFree + c2) ./EI;
280

```

```

281 Deflection_InContact= (zInContact./Lsurf).^n.*D;
282 Slope_InContact= n.*(zInContact./Lsurf).^(n-1).*D./Lsurf;
283 Curvature_InContact= n.*(n-1).*(zInContact./Lsurf).^(n-2).*D./Lsurf^2;
284
285 %Deflection
286 subplot(4,1,1)
287 hold off;
288 plot([zInContact zFree], -[Deflection_InContact Deflection_Free])
289 hold on;
290 plot(y, -max(Deflection_InContact), 'r*');
291 xlabel('axial distance from cantilever root, z (m)');
292 ylabel('displacement, m');
293 title('Deflection along Beam Length');
294 grid;
295
296 %Slope
297 subplot(4,1,2)
298 hold off;
299 plot([zInContact zFree], -[Slope_InContact Slope_Free])
300 hold on;
301 plot(y, -max(Slope_InContact), 'r*');
302 xlabel('axial distance from cantilever root, z (m)');
303 ylabel('Slope dy/dz, m/m');
304 title('Slope along Beam Length');
305 grid;
306
307 %Curvature
308 subplot(4,1,3)
309 hold off;
310 plot([zInContact zFree], -[Curvature_InContact Curvature_Free])
311 hold on;
312 plot(y, -max(Curvature_InContact), 'r*');
313 xlabel('axial distance from cantilever root, z (m)');
314 ylabel('curvature d^2y/d^z^2, 1/m');
315 title('Curvature along Beam Length');
316 grid;

```

```

317
318     %stress
319     subplot(4,1,4);
320     hold off;
321     plot([zInContact zFree], -[sigmaInContact sigmaFree]./10^9);
322     hold on;
323     plot([0 L], [sigma_y sigma_y]./10^9./2, 'g', [0 L], -[sigma_y sigma_y].
          /10^9, 'g');
324     plot(y, -max(sigmaInContact)./10^9, 'r*')
325     xlabel('axial distance from cantilever root, z (m)');
326     ylabel('normal stress, sigma (GPa)');
327     title('Normal stress along top of Beam');
328     grid;
329 end

```

A.3 Track objects in a video

```

1 function track_Red_and_Green_Object
2
3 redThresh = .35; % Threshold for red detection
4 greenThresh= .03; %Threshold for green detection
5
6
7 vidDevice = VideoReader('short_light_manyDrops_0904.mp4'); %load video file
8 numFrames= get(vidDevice, 'numberOfFrames'); %get number of video frames
9
10 FS= 1/480; %1 / Frame Rate (Hz)
11 startInd= 7300; %frame index at which to start tracking motion
12 endFrame= 9660; %frame index at which to stop tracking motion
13 PixelsPerCm= 7.3771; %conversion factor of pixel:cm for red object [pix/cm]
14 xPixelEq= 173; %x-pixel value at which red object has 0 displacement
    RELATIVE TO GREEN OBJECT

```

```

15 yPixelEq= -7.8824; %y-pixel value at which red object has 0 displacement
    RELATIVE TO GREEN OBJECT
16 PixelsPerCmBase= 6.508; %conversion factor of pixels:cm for green object [
    pixels/cm]
17 xPixelEqBase= 116; %x-pixel value at which green object has 0 displacement
18 yPixelEqBase= 101.409; %y-pixel value at which green object has 0
    displacement
19
20 %declare vectors that will store object locations
21 dataX= []; %red object x
22 dataY= []; %red object y
23 dataXBase= []; %green object x
24 dataYBase= []; %green object y
25
26 started= 0; %started= 1 if red object has been identified for first time
27
28 %Processing Loop
29 for nFrame= startInd:endFrame %numFrames
30     nFrame
31     rgbFrame= read(vidDevice,nFrame); %identify frame number
32     figure(1)
33     image(rgbFrame);
34
35     diffFrame = imsubtract(rgbFrame(:,:,1), rgb2gray(rgbFrame)); % Get red
        component of the image
36     diffFrameGreen = imsubtract(rgbFrame(:,:,2), rgb2gray(rgbFrame)); % Get
        red component of the image
37     diffFrame = medfilt2(diffFrame, [3 3]); % Filter out the noise by using
        median filter
38     diffFrameGreen = medfilt2(diffFrameGreen, [3 3]); % Filter out the
        noise by using median filter
39
40     binFrame = im2bw(diffFrame, redThresh); % Convert the image into binary
        image with the red objects as white
41     binFrameGreen = im2bw(diffFrameGreen, greenThresh); % Convert the image
        into binary image with the green objects as white

```

```

42
43 figure(2) %show the green "blob" identified as the green object. Adjust
      sensitivity of what is considered green by "greenThresh" value
44 image(binFrameGreen);
45 figure(3) %show the red "blob" identified as the green object. Adjust
      sensitivity of what is considered green by "greenThresh" value
46 image(binFrame);
47
48 s= regionprops(binFrame, 'centroid'); %find red object centroid [pix]
49 sGreen= regionprops(binFrameGreen, 'centroid'); %find green object
      centroid [pixels]
50 centroids= cat(1, s.Centroid);
51 centroidsGreen = cat(1, sGreen.Centroid);
52
53 blobArea= regionprops(binFrame, 'area');
54 blobAreaGreen= regionprops(binFrameGreen, 'area');
55 if isempty(blobArea)&& started== 0 %if blobArea is empty:
56     startInd= startInd+1; %add index number to startInd
57     started= 1;
58 elseif isempty(blobArea)
59     dataX(length(dataX)+1)= 0;
60     dataY(length(dataY)+1)= 0;
61 else
62     %determine the centroid of the larger blob, if there are multiple
        blobs
63     if length(blobArea)>1
64         centroidArea= [blobArea.Area]; %take bottom centroid because
            hand is on right
65         [value index]= max(centroidArea);
66         while (centroids(index,1)<170 || centroids(index,1)>208)%if
            centroid is too far to left
67             centroidArea(index)= 0; %delete element in centroidArea
68             [value index]= max(centroidArea); %determine next biggest red
                blob
69         end
70         centroids= [centroids(index,1) centroids(index, 2)];

```

```

71     end
72     if length(blobAreaGreen)>1
73         centroidAreaGreen= [blobAreaGreen.Area];
74         [valueG indexG]= max(centroidAreaGreen);
75         while (centroidsGreen(indexG,1)>150 || centroidsGreen(indexG,1)
76             <122)%if centroid is too far down, don't count it
77             centroidAreaGreen(indexG)= 0; %delete element in
78                 centroidArea
79             [valueG indexG]= max(centroidAreaGreen); %determine next
80                 biggest red blob
81         end
82         centroidsGreen= [centroidsGreen(indexG,1) centroidsGreen(indexG
83             , 2)];
84     end
85     figure(3) %show the red object centroid
86     hold on
87     plot(centroids(:,1), centroids(:,2), 'b*')
88     hold off
89     figure(2) %show the green object centroid
90     hold on
91     plot(centroidsGreen(:,1), centroidsGreen(:,2), 'b*')
92     hold off
93
94     %add the centroid locations to the vector that track location
95     dataX(length(dataX)+1)= centroids(:,1);
96     dataY(length(dataY)+1)= centroids(:,2);
97
98     dataXBase(length(dataXBase)+1)= centroidsGreen(:,1);
99     dataYBase(length(dataYBase)+1)= centroidsGreen(:,2);
100
101     end
102     nFrame = nFrame+1;
103
104     end
105     time= [0:FS:FS*(endFrame-startInd)]';

```

```

103 %Convert pixel data to displacement data. (Red object displacement relative
      to green object)
104 PixelsPerMeter= PixelsPerCm*100;
105 dataXm= (dataX-xPixelEq)./PixelsPerMeter;
106 dataY= dataY - dataYBase;
107 dataYm= -(dataY-yPixelEq)./PixelsPerMeter;
108
109 PixelsPerMeterBase= PixelsPerCmBase*100;
110 dataXmBase= (dataXBase-xPixelEqBase)./PixelsPerMeterBase;
111 dataYmBase= -(dataYBase-yPixelEqBase)./PixelsPerMeterBase;
112
113 figure(4);
114 subplot(3,1,1) %Base Displacement (green object)
115 hold on;
116 plot(time, dataYmBase, '-g'); %experimental base disp
117 title('Base Displacement versus Time');
118 ylabel('Displacement (m)');
119 xlabel('time (sec)');
120
121 subplot(3,1,2) %Base Velocity
122 hold on;
123 veloc= gradient(dataYmBase, time(2)-time(1)); %Base Drop- veloc- camera
124 plot(time, veloc, '-r'); %experimental base veloc
125 title('Base Velocity versus Time');
126 ylabel('velocity (m/s)');
127 xlabel('time (sec)');
128
129 subplot(3,1,3) %Base Acceleration
130 hold on;
131 acc= gradient(veloc, time(2)-time(1)); %Base drop- acc- camera
132 plot(time, acc, '-r'); %experimental base acc
133 title('Base Acceleration versus Time');
134 ylabel('acceleration (m/s^2)');
135 xlabel('time (sec)');
136
137

```



```

138 figure(5)
139 subplot(2,1,1) %Mass Relative Displacement (red object)
140 hold on;
141 % relDisp= dataYm- dataYmBase;
142 plot(time, dataYm, '-r'); %experimental relative mass disp
143 % plot(tspan(1:length(tspan)-1), xhist, '-b'); %simulation mass disp
144 title('Relative Displacement versus Time');
145 ylabel('displacement (m)');
146 xlabel('time (sec)');
147
148 subplot(2,1,2) %Mass Relative Velocity
149 veloc_m= gradient(dataYm, time(2)-time(1)); %Base Drop- veloc- camera (red
    object)
150 plot(time, veloc_m, '-r'); %experimental base veloc
151 title('Relative Velocity versus Time');
152 ylabel('velocity (m/s)');
153 xlabel('time (sec)');
154
155 end

```

A.4 Energy harvester simulation

```

1 % This code simulates the acceleration, velocity, displacement, and power
    harvested by a 1DOF or 2DOF energy harvester excited at the base by an
    input acceleration.
2 % Top to bottom system configuration is:
3 % Base
4 % nonlinear spring with htop, linear spring with K1, damper b1M
5 % m1
6 % nonlinear spring with hmid, linear spring with KM, damper b3M
7 % m2
8 % nonlinear spring with hbot, linear spring with K2, damper b2M
9 % Base

```

```

10 % Gravity acts downwards.
11 % The code outputs the time series or "optimization plots" of power and
    displacement versus two varied parameters.
12 function optimalPower= simulateEnergyHarvester
13 global n hDot h startPowerCalcTime FI XI optimalsurfaces plotTimeSeries m1
    m2 b1M b2M b3M KM K1 K2 htop hbot hmid FITopFactorM FIBotFactorM
    FIMidFactorM XImaxTop XImaxBot XImaxTopBot numCombos epsilon
14 %%%%%%%%%%%%%%%%%%%%%%%%%%%%%%%%%%%%%%%%%%%%%%%%%%%%%%%%%%%%%%%%%%%%%%%%%%% USER INPUT %%%%%%%%%%%%%%%%%%%%%%%%%%%%%%%%%%%%%%%%%%%%%%%%%%%%%%%%%%%%%%%%%%%%%%%%%%%
15 %NOTE: If want to vectorize two parameters and plot results, write the
    parameter here as a vector.
16 %The first vectorized paramters listed always becomes the xVector, and the
    second vectorized parameter always becomes the yVector in the plot.
17 %NOTE: colisions only occur if there is a nonlinear spring between the
    masses. If the user desires collisions, but no nonlinear spring, then
    set the cantilever height to a very small value (i.e. 1e-6 or 1e-4 m).
18
19 m1= .03; %top mass %UNITS: Kg
20 m2= .03; %bottom mass [Kg]
21
22 htop= .464e-3; %top nonlinear spring's cantilever height [m]
23 K1= 0; %top linear spring stiffness [N/m]
24
25 hmid= 1e-3; %middle nonlinear spring's cantilever height [m]
26 KM= 0; %middle linear spring stiffness spring [N/m]
27
28 hbot= 0; %.1e-4; %bottom nonlinear spring's cantilever height [m]
29 K2= 205; %28; %bottom linear spring coefficient [N/m]
30
31 b1M= .001; %top damper [Ns/m]
32 b3M= 1.6; %middle damper [Ns/m]
33 b2M= .001; %bottom damper [Ns/m]
34
35 %THE 8 COMMANDS BELOW ONLY APPLY IF optimal surfaces. Change to ratio. Note
    that one B ratio value must be 1 for calculations to not override each
    other
36 B2B1yes= 0;

```

```

37     B2B1ratio= 1; %b2M/b1M; %if b1 is vectorized, specify b2 as ratio to b1
38 B3B1yes= 0;
39     B3B1ratio= .5; %b3M/b1M; %if b1 is vectorized, specify b3 at ratio to
      b1
40 B3B2yes= 0; %these values are 1 if want to use the ratios
41     B3B2ratio= .5; %b3M/b2M; %if b2 is vectorized, specify b3 at ratio to
      b2
42 F1F3yes= 0; %keep F1 a ratio of F3
43     F1F3rat= .1;
44 %-----
45 %for parameters that want to vectorize and plot: specify here axes for surf
      command:
46 %NOTE: row must match first vectorized parameter. Column must match second
      vectorized parameter
47 paramRow= hmid;
48 RowLabel= 'Middle nonlinear cantilever height (m)'; %label for 3-D plots
49 paramCol= b3M;
50 ColLabel= 'middle damping coefficient (Ns/m)'; %label for 3-D plots
51
52 optimalsurfaces= 0; %optimalsurfaces= 1 if doing 2x2 minimum array --> show
      surfaces
53 plotTimeSeries= 1; %plotTimeSeries= 1 if want to plot time series (disp,
      veloc, acc, dissipated power)
54
55 endTime= 8;% sec
56 n= .0001; %time steps (sec)
57 numTimeSegments= 1; %NEED startPowerCalcTime to be an integer multiple of
      endTime/numTimeSegments. Also speeds up code
58 startPowerCalcTime= 0; %time in seconds to start power calculation. NEED
      startPowerCalcTime to be an integer multiple of endTime/numTimeSegments
59
60 fileName= 'a'; %name of data file of final outputs
61 powerFigName= 'b'; % name of the power surface
62 topDispFigName= 'c'; % name of the surface that shows top mass displacement
      wrt base versus 2 varied parameters

```

```

63 botDispFigName= 'd'; % name of the surface that shows the bottom mass
    displacement
64 topbotDispFigName= 'e'; % name of the surface that shows the top mass wrt
    bottom mass displacement
65
66 %If constraint does not apply, set the value to larger number (i.e. 5 m).
67 %CONSTRAINT MUST BE .017 IF NONLINEAR SPRING
68 XImaxTop= .017;%.017; %maximum displacement between top mass and base
69 XImaxTopBot= .017; %maximum displacement between top mass and bottom mass
70 XImaxBot= .017;%.017; %maximum displacement between bottom mass and base
71
72 D= .015; %surface curve end gap [m]
73 XImax= .0173; %maximum displacement value calculated for nonlinear spring
74
75 signal= 1; %indicate base acceleration signal (numbers are listed below)
76 timeScale= 1; %indicate multiple by which want to speed up acceleration
    signal time scale
77 %%%%%%%%%%%%%%%%%%%%%%%%%%%%%%%%%%%%%%%%%%%%%%%%%%%%%%%%%%%%%%%%%%%%%%%%%
78 base= .1875*.0254; %cantilever base dimension. [m]
79 q= 3; %surface curve: D*(x/L)^q
80
81 hBaseline= .032*.0254; %inches. All other spring stiffnesses are multiplied
    by their relation to this height.
82 FITopFactorM= htop.^3./hBaseline^3;
83 FIMidFactorM= hmid.^3./hBaseline^3;
84 FIBotFactorM= hbot.^3./hBaseline^3;
85
86 E= 160.6e9; %spring steel elastic modulus
87
88 L= .1; %Cantilever length. UNITS: m
89 l= L; %surface length. UNITS: m
90
91 massA= .0097; %end-mass length (overhang from cantilever) [m]
92 surfaceEndfraction= l/L;
93
94 Pmax= 60; %maximum force for calculating spring force/disp table

```

```

95 numInt= 600; %600; %number of intervals in table of spring force/disp table
96
97 %ACCELERATION DATA
98
99 % %SIGNALS
100 if (signal==1) %hip walk
101     load('run_forSimulation_Jocie_hip_walk_corrected_1114.mat');
102     %[tspanData, hDotDot, hDot, h]=
103         run_forSimulation_Jocie_hip_walk_corrected;
104 elseif (signal==3) %hip run
105     %[tspanData, hDotDot, hDot, h]=
106     %run_forSimulation_Jocie_hip_run_corrected; %
107     load('run_forSimulation_Jocie_hip_run_corrected_1118.mat');
108 elseif (signal==2) %hip walk quickly
109     [tspanData, hDotDot, hDot, h]=
110         run_forSimulation_Jocie_hip_walkFast_corrected;
111 elseif (signal==4) %hip bike
112     [tspanData, hDotDot, hDot, h]=
113         run_forSimulation_Jocie_hip_bike_corrected;
114 elseif (signal==5) %foot walk
115     [tspanData, hDotDot, hDot, h]= run_forSimulation_corrected;
116 elseif (signal== 6) %foot run
117     [tspanData, hDotDot, hDot, h]=
118         run_forSimulation_Heal_Running_Up_corrected;
119 else %Free fall of base drop experiment
120     [tspanData, hDotDot, hDot, h]= run_forSimulation_Drop_free_fall;
121 end
122
123 %select segment of data to use in simulation
124 tspanData= real(tspanData).*timeScale;
125
126 hDotDot= real(hDotDot);
127 hDot= real(hDot);
128 h= real(h);
129
130 tspan= 0:n:endTime; %horizontal array. Use smaller time steps than data

```

```

127 [minValue, startPowerCalcIndex]= min(abs(tspan-startPowerCalcTime));
128 numIntervalsinTimeSegment= floor(length(tspan)/numTimeSegments);
129
130 %create vectors that approximate the base acceleration, velocity,
      acceleration at each of the smaller time steps
131 hDotDot= (interp1(tspanData, hDotDot, tspan))'; %YI = INTERP1(X,Y,XI)
      interpolates to find YI
132 hDot= (interp1(tspanData, hDot, tspan))'; %these are horizontal arrays
133 h= (interp1(tspanData, h, tspan))';
134
135 %Vary the two chosen parameters, and specify number of combos
136 numCombos= length(paramRow)*length(paramCol);
137
138 % Determine the varied parameters
139 if optimalsurfaces==1
140     checkedVar= 0; %keep check of how many variables checked for as vectors
141     [m1, checkedVar]= createVectors(m1, checkedVar, paramCol, paramRow);
142     [m2, checkedVar]= createVectors(m2, checkedVar, paramCol, paramRow);
143     [FITopFactorM, checkedVar]= createVectors(FITopFactorM, checkedVar,
      paramCol, paramRow);
144     [K1, checkedVar]= createVectors(K1, checkedVar, paramCol, paramRow);
145     [FIMidFactorM, checkedVar]= createVectors(FIMidFactorM, checkedVar,
      paramCol, paramRow);
146     [KM, checkedVar]= createVectors(KM, checkedVar, paramCol, paramRow);
147     [FIBotFactorM, checkedVar]= createVectors(FIBotFactorM, checkedVar,
      paramCol, paramRow);
148     [K2, checkedVar]= createVectors(K2, checkedVar, paramCol, paramRow);
149     [b1M, checkedVar]= createVectors(b1M, checkedVar, paramCol, paramRow);
150     [b3M, checkedVar]= createVectors(b3M, checkedVar, paramCol, paramRow);
151     [b2M, checkedVar]= createVectors(b2M, checkedVar, paramCol, paramRow);
152
153     if B2Blyes== 1 % so that vector b2 is not affected
154         b2M= b1M.*B2B1ratio;
155     end
156     if B3Blyes== 1
157         b3M= b1M.*B3B1ratio;

```

```

158     end
159     if B3B2yes== 1
160         b3M= b2M.*B3B2ratio;
161     end
162     if FlF3yes==1 %keep Fl a ratio of F3
163         FITopFactorM= FIMidFactorM.*FlF3rat;
164     end
165 end
166
167 %Calcualte the baseline nonlinear spring force
168 [XI, FI, SF, Yc]= cant_beam_force (m1, massA, E, hBaseline, E*base*
    hBaseline^3/12, q, L, D, D, surfaceEndfraction, Pmax*base/.1875/.0254,
    numInt, XImax);
169 % load nonlinSpring_oneSided.mat XI
170 % load nonlinSpring_oneSided.mat FI
171
172 %append to XI and FI for x that exceeds XI
173 epsilon= 1e-5; %envelope parameter (bigger epsilon--> more XI values
    affected by envelope
174
175 XI(length(XI))= [];
176 FI(length(FI))= [];
177 FItemp= FI + epsilon./(XI-XImax).^2; %assume that if nonliear spring is
    used. XImax is the maximum value
178
179 %add additional large numbers
180 XItemp= linspace(1.01*max(XI), 1000*max(XI), 300);
181 FItemp2= FItemp(length(FItemp))+ 1e4.*(XItemp./XImax).^5;
182 XI= [XI XItemp];
183 FI= [FItemp FItemp2];
184 %create negative values
185 XI= [-fliplr(XI) XI(2:length(XI))]; %table of displacements
186 FI= [-fliplr(FI) FI(2:length(FI))]; %table of forces
187
188 %Declare arrays that will store each system's outputs
189 PharvestedBotAllSeg= [];

```

```

190 PharvestedTopAllSeg= [];
191 PharvestedMidAllSeg= [];
192 PinAllSeg= [];
193 maxDispTopAllSeg= [];
194 maxDispBotAllSeg= [];
195 maxDispTopBotAllSeg= [];
196
197 %initial state vector values
198 X0= zeros(1, numCombos); %X is displacement of top mass wrt base
199 XDot0= zeros(1, numCombos);
200 Z0= zeros(1, numCombos); %Z is displacement of bottom mass wrt base
201 ZDot0= zeros(1, numCombos);
202
203
204 for i= 1:numTimeSegments
205     i
206     tspanSeg= tspan(numIntervalsinTimeSegment*(i-1)+1:
                numIntervalsinTimeSegment*i);
207     hSeg= h(numIntervalsinTimeSegment*(i-1)+1:numIntervalsinTimeSegment*i
            -1);
208     hDotSeg= hDot(numIntervalsinTimeSegment*(i-1)+1:
                numIntervalsinTimeSegment*i-1);
209     HPrimePrimeMatrixSeg= hDotDot(numIntervalsinTimeSegment*(i-1)+1:
                numIntervalsinTimeSegment*i-1);%, :);
210
211     %ode45 settings
212     options = odeset('RelTol',1e-4,'AbsTol',(1e-5).*ones(4*numCombos,1));
213     Y0= [X0 XDot0 Z0 ZDot0]'; % initial conditions vector
214
215     [T,Y]= ode113 (@stateEqn, tspanSeg, Y0, options, tspan, hDotDot); %call
                differential equation solver
216
217     %extract displacements and velcoities from Y
218     X= Y(:,1:numCombos);
219     XDot= Y(:,numCombos+1:2*numCombos);
220     Z= Y(:,2*numCombos+1:3*numCombos);

```



```

221     ZDot= Y(:,3*numCombos+1:4*numCombos);
222
223     if (tspanSeg(length(tspanSeg))> startPowerCalcTime) %if time is
        greater than time to start calculating power:
224     [PharvestedTopSeg, PharvestedBotSeg, PharvestedMidSeg, PinSeg,
        maxDispTopSeg, maxDispBotSeg, maxDispTopBotSeg]=
        calculatePerformance (X, XDot, Z, ZDot, hDot, tspanSeg); %function
        to calculate power in, out, maximum displacement, etc.
225     %add the average time segment values to the vectors that track
        average values for entire simulated time
226     PharvestedTopAllSeg= [PharvestedTopAllSeg; PharvestedTopSeg];
227     PharvestedBotAllSeg= [PharvestedBotAllSeg; PharvestedBotSeg];
228     PharvestedMidAllSeg= [PharvestedMidAllSeg; PharvestedMidSeg];
229     PinAllSeg= [PinAllSeg; PinSeg];
230     maxDispTopAllSeg= [maxDispTopAllSeg; maxDispTopSeg];
231     maxDispBotAllSeg= [maxDispBotAllSeg; maxDispBotSeg];
232     maxDispTopBotAllSeg= [maxDispTopBotAllSeg; maxDispTopBotSeg];
233     end
234     %define initial values for new time segment
235     X0= X(length(X(:,1)),:);
236     XDot0= XDot(length(XDot(:,1)),:);
237     Z0= Z(length(Z(:,1)),:);
238     ZDot0= ZDot(length(ZDot(:,1)),:);
239     end
240     %average the average values of each time segment
241     if numTimeSegments>1 %only need to sum PharvestedAllSeg if
        numTimeSegments>1
242     PharvestedTop= mean(PharvestedTopAllSeg); %Pharvested= {P1*
        FirstTimeLength + [P2+...Pn]*timeSegLength } / (n-1)*
        timeSegLength + firstTimeLength
243     PharvestedBot= mean(PharvestedBotAllSeg);
244     PharvestedMid= mean(PharvestedMidAllSeg);
245     Pin= mean(PinAllSeg);
246     maxDispTop= max(maxDispTopAllSeg); %maximum of each column
247     maxDispBot= max(maxDispBotAllSeg);
248     maxDispTopBot= max(maxDispTopBotAllSeg);

```

```

249     else %there is only one time segment
250         PharvestedTop= PharvestedTopAllSeg;
251         PharvestedBot= PharvestedBotAllSeg;
252         PharvestedMid= PharvestedMidAllSeg;
253         Pin= PinAllSeg;
254         maxDispTop= maxDispTopAllSeg;
255         maxDispBot= maxDispBotAllSeg;
256         maxDispTopBot= maxDispTopBotAllSeg;
257     end
258
259
260 %convert row vectors into matrices where each row corresponds to a b-value.
    Each column to a C value
261 PoutTop= (reshape(PharvestedTop, length(paramCol), length(paramRow)))'
262 PoutBot= (reshape(PharvestedBot, length(paramCol), length(paramRow)))'
263 PoutMid= (reshape(PharvestedMid, length(paramCol), length(paramRow)))'
264 PoutAll= PoutTop + PoutBot + PoutMid
265 Pin= (reshape(Pin, length(paramCol), length(paramRow)))'
266 dispOutTop= (reshape(maxDispTop, length(paramCol), length(paramRow)))'
267 dispOutBot= (reshape(maxDispBot, length(paramCol), length(paramRow)))'
268 dispOutTopBot= (reshape(maxDispTopBot, length(paramCol), length(paramRow)))
    '
269
270
271 %%%%%%%%%%%%%%%%%%%%%%%%%%%%%%%%%%%%%%%%%%%%%%%%%%%%%%%%%%%%%%%%%%%%%%%%%Plots%%%%%%%%%%%%%%%%%%%%%%%%%%%%%%%%%%%%%%%%%%%%%%%%%%%%%%%%%%%%%%%%%%%%%%%%
272 if plotTimeSeries
273     %Plot 1: Force versus disp for spring
274     figure(3);
275     plot(XI, FI.*FITopFactorM(1), XI, FI.*FIBotFactorM(1), XI, FI.*
        FIMidFactorM(1));
276     grid;
277     xlabel('spring displacement (m)');
278     ylabel('applied force (N)');
279     title('Force versus Tip Displacement');
280     legend('Top Nonlinear Spring', 'Bottom Nonlinear Spring', 'Middle
        Nonlinear Spring');

```

```

281
282     %Plot 2: displacement versus time
283     figure(2);
284     subplot(3,1,1)
285     plot(tspanSeg(1:length(tspanSeg)-1), hSeg, tspanSeg, X(:,1), tspanSeg,
          Z(:,1), tspanSeg, X(:,1)-Z(:,1));
286     grid;
287     xlabel('time (s)');
288     ylabel('displacement (m)');
289     title('Displacement versus time');
290     legend('Base Displacement', 'Displacement of Top Mass wrt Base', '
          Displacement of Bottom Mass wrt Base', 'Displacement of Top Mass wrt
          Bottom Mass');
291
292     %Plot 3: velocity versus time
293     subplot(3,1,2)
294     plot(tspanSeg(1:length(tspanSeg)-1), hDotSeg, tspanSeg, XDot(:,1),
          tspanSeg, ZDot(:,1), tspanSeg, XDot(:,1)-ZDot(:,1));
295     grid;
296     xlabel('time (s)');
297     ylabel('velocity (m/s)');
298     title('Velocity versus time');
299     legend('Base Velocity', 'Velocity of Top Mass wrt Base', 'Velocity of
          Bottom Mass wrt Base', 'Velocity of Top Mass wrt Bottom Mass');
300
301 end
302
303
304 %output optimal power and displacement values
305 [optimalPower, colNum]= max(max(PoutAll));
306 optimalDispTop= max(max(dispenOutTop));
307 optimalDispBot= max(max(dispenOutBot));
308 optimalDispTopBot= max(max(dispenOutTopBot));
309
310 %reduce size of file about to save

```

```

311 clear tspanSeg tspanData tspan startPowerCalcInd plotTimeSeries
        numTimeSegments numIntervalsinTimeSegment nNondim minValue maxDispTopSeg
312 clear maxDispTopMatrix maxDispTopAllSeg maxDispBotSeg maxDispBotMatrix
        maxDispBotAllSeg i hDotSeg hDotDot hDot h figure1
313 clear dispTopFig dispBotFig b3M b2M b3 b2 b1 axes1 a ZDot0 ZDot Z0 Z XDot0
        XDot X0 X TMatrix T SFMatrixTemp
314 clear PinSeg PinMatrix PinAllSeg PharvestedTopSeg PharvestedTopAllSeg
        PharvestedTop PharvestedMidSeg PharvestedMidAllSeg
315 clear PharvestedMid PharvestedBotSeg PharvestedBotAllSeg PharvestedBot
        PdisstTopMatrix PdisstMidMatrix PdisstBotMatrix KMatrix K3 K2 K1
        HPrimePrimeMatrixSeg
316 clear FIBot FITop Pmax SF XI Yc ans maxDispBot maxDispTop powerLinFig
        powerTopfig safetyfig signal startPowerCalcInd
317 clear hMatrix HMatrix hDotMatrix HPrimeMatrix hDotDotMatrix
        HPrimePrimeMatrix
318 clear FITopFactorM FIBotFactorM maxDispTopBotAllSeg maxDispTopBotSeg
319 save(fileName);
320
321
322 if optimalsurfaces== 1 %create optimization surfaces
323
324     close all
325     figure1= figure(1);
326     axes1 = axes('Parent',figure1,'FontSize',12,'FontName','Calibri','CLim'
        , [0 max(max(PoutAll))]);
327     view(axes1,[-98 26]);
328     grid(axes1,'on');
329     hold(axes1,'all');
330     axis([paramRow(1) paramRow(length(paramRow)) paramCol(1) paramCol(
        length(paramCol))]); % axis([xmin xmax ymin ymax])
331     % Create surf
332     surf(paramRow, paramCol, PoutAll')
333     zlabel('Power (W)', 'FontSize',12,'FontName','Calibri');
334     title(['Total Power Dissipated'],'FontSize',12,'FontName','Calibri');
335     colorbar('peer', axes1, 'LineWidth',1, 'FontSize',12, 'FontName','Calibri',
        'CLim',[1 64]);

```

```

336 ylabel(ColLabel,'FontSize',14,'FontName','Calibri','HorizontalAlignment
      ', 'left');
337 xlabel(RowLabel,'HorizontalAlignment','right','FontSize',14,'FontName',
      'Calibri');
338 view(0, 90);
339 set(gca,'xscale','log')
340 set(gca,'yscale','log')
341 saveas(figure1,powerFigName,'fig');
342 saveas(figure1,powerFigName,'png');
343
344 close all
345 figure1= figure(1);
346 axes1 = axes('Parent',figure1,'FontSize',12,'FontName','Calibri','CLim'
      ', [0 max(max(dispNetTop))]');
347 view(axes1,[-98 26]);
348 grid(axes1,'on');
349 hold(axes1,'all');
350 axis([paramRow(1) paramRow(length(paramRow)) paramCol(1) paramCol(
      length(paramCol))]); % axis([xmin xmax ymin ymax])
351 % Create surf
352 surf(paramRow, paramCol, dispOutTop)
353 zlabel('Maximum Pk-Pk relative displacement (m)','FontSize',14,'
      FontName','Calibri');
354 title(['Pk-Pk Displacement of Top Mass wrt Base',],'FontSize',12, '
      FontName','Calibri');
355 colorbar('peer',axes1,'LineWidth',1,'FontSize',12,'FontName','Calibri',
      'CLim',[1 64]);
356 ylabel(ColLabel,'FontSize',14,'FontName','Calibri','HorizontalAlignment
      ', 'left');
357 xlabel(RowLabel,'HorizontalAlignment','right','FontSize',14,'FontName',
      'Calibri');
358 view(0, 90);
359 set(gca,'xscale','log')
360 set(gca,'yscale','log')
361 saveas(figure1,topDispFigName,'fig');
362 saveas(figure1,topDispFigName,'png');

```

```

363
364     close all
365     figure1= figure(1);
366     axes1 = axes('Parent',figure1,'FontSize',12,'FontName','Calibri','CLim'
        , [0 max(max(dispNetBot))] );
367     view(axes1,[-98 26]);
368     grid(axes1,'on');
369     hold(axes1,'all');
370     axis([paramRow(1) paramRow(length(paramRow)) paramCol(1) paramCol(
        length(paramCol))] ); % axis([xmin xmax ymin ymax])
371     % Create surf
372     surf(paramRow, paramCol, dispOutBot')
373     grid;
374     zlabel('Maximum Pk-Pk relative displacement (m)','FontSize',14,'
        FontName','Calibri');
375     title(['Pk-Pk Displacement of Bottom Mass wrt Base'],'FontSize',12,'
        FontName','Calibri');
376     colorbar('peer',axes1,'LineWidth',1,'FontSize',12,'FontName','Calibri',
        'CLim',[1 64]);
377     ylabel(ColLabel,'FontSize',14,'FontName','Calibri','HorizontalAlignment
        ','left');
378     xlabel(RowLabel,'HorizontalAlignment','right','FontSize',14,'FontName',
        'Calibri');
379     view(0, 90);
380     set(gca,'xscale','log')
381     set(gca,'yscale','log')
382     saveas(figure1,botDispFigName,'fig');
383     saveas(figure1,botDispFigName,'png');
384
385     close all
386     figure1= figure(1);
387     axes1 = axes('Parent',figure1,'FontSize',12,'FontName','Calibri','CLim'
        , [0 max(max(dispNetTopBot))] );
388     view(axes1,[-98 26]);
389     grid(axes1,'on');
390     hold(axes1,'all');

```

```

391 axis([paramRow(1) paramRow(length(paramRow)) paramCol(1) paramCol(
      length(paramCol))]); % axis([xmin xmax ymin ymax])
392 surf(paramRow, paramCol, dispOutTopBot')
393 grid;
394 zlabel('Maximum Pk-Pk relative displacement (m)', 'FontSize', 14, '
      FontName', 'Calibri');
395 title(['Maximum Displacement of Top Mass wrt Bottom Mass'], 'FontSize'
      , 12, 'FontName', 'Calibri');
396 colorbar('peer', axes1, 'LineWidth', 1, 'FontSize', 12, 'FontName', 'Calibri',
      'CLim', [1 64]);
397 ylabel(ColLabel, 'FontSize', 14, 'FontName', 'Calibri', 'HorizontalAlignment
      ', 'left');
398 xlabel(RowLabel, 'HorizontalAlignment', 'right', 'FontSize', 14, 'FontName',
      'Calibri');
399 view(0, 90);
400 set(gca, 'xscale', 'log')
401 set(gca, 'yscale', 'log')
402 saveas(figure1, topbotDispFigName, 'fig');
403 saveas(figure1, topbotDispFigName, 'png');
404 close all
405
406 end
407
408 end
409
410 %Calculate average power dissipated by each damper, maximum displacement of
      each mass wrt base, and maximum displacement of bases to each other
411 function [average_Dissipated_PowerTop_ss, average_Dissipated_PowerBot_ss,
      average_Dissipated_PowerMid_ss, average_Power_into_Base_ss,
      maximum_Relative_DisplacementTop, maximum_Relative_DisplacementBot,
      maximum_Relative_DisplacementTopBot]= calculatePerformance (x, xDot, z,
      zDot, hDotSeg, tspan)
412 global startPowerCalcTime plotTimeSeries b1M b2M b3M m1 m2
413
414 [minValue startPowerCalcIndex]= min(abs(tspan-startPowerCalcTime)); %
      startPowerCalcIndex will be a number ~=1 if this is the first interval

```

```

    and segment/startTime do not align. Otherwise, startPowerCalcIndex
    should be 1
415
416 %variables x, xDot, and tspan that are steady state
417 xss= x(startPowerCalcIndex:length(x(:,1))-1,:);
418 xDotss= xDot(startPowerCalcIndex:length(x(:,1))-1,:);
419 zss= z(startPowerCalcIndex:length(z(:,1))-1,:);
420 zDotss= zDot(startPowerCalcIndex:length(z(:,1))-1,:);
421
422 tspanss= tspan(startPowerCalcIndex:length(tspan)-1);
423
424 hDotss= hDotSeg(startPowerCalcIndex:length(x(:,1))-1); %Base velocity
425 hDotssMatrixSS= repmat(hDotss, 1, length(xss(1,:))); %matrix with as many
    elements are in xss
426
427 %create damping coefficient matrices with as many elements as are in the
    steady state variable matrices
428 if numel(b1M)>1
429 bMatrix1SS= repmat(b1M, length(xss(:,1)), 1); %matrix with as many elements
    are in tspanss
430 else
431     bMatrix1SS= b1M;
432 end
433 if numel(b2M)>1
434 bMatrix2SS= repmat(b2M, length(xss(:,1)), 1); %matrix with as many elements
    are in tspanss
435 else
436     bMatrix2SS= b2M;
437 end
438 if numel(b3M)>1
439     bMatrix3SS= repmat(b3M, length(xss(:,1)), 1); %matrix with as many
    elements are in tspanss
440 else
441     bMatrix3SS= b3M;
442 end
443 if numel(m2)>1

```



```

444 m2Matrix= repmat(m2, length(xss(:,1)), 1); %matrix with as many elements
      are in tspanss
445 else
446     m2Matrix= m2;
447 end
448
449
450 %calculate dissipated power- when steady state
451 dissipated_PowerTop_ss= bMatrix1SS.*(xDotss).^2; %when steady state
452 average_Dissipated_PowerTop_ss= sum(dissipated_PowerTop_ss)./length(
      dissipated_PowerTop_ss(:,1)); %ROW VECTOR
453
454 dissipated_PowerBot_ss= bMatrix2SS.*(zDotss).^2; %when steady state
455 average_Dissipated_PowerBot_ss= sum(dissipated_PowerBot_ss)./length(
      dissipated_PowerBot_ss(:,1)); %ROW VECTOR
456
457 dissipated_PowerMid_ss= bMatrix3SS.*(xDotss-zDotss).^2; %when steady state
458 average_Dissipated_PowerMid_ss= sum(dissipated_PowerMid_ss)./length(
      dissipated_PowerMid_ss(:,1)); %ROW VECTOR
459
460 power_into_Base_ss= -(m2Matrix.*zDotss).*hDotssMatrixSS;
461 average_Power_into_Base_ss= sum(power_into_Base_ss)./length(
      power_into_Base_ss(:,1)); %ROW VECTOR
462
463 % maximum_Relative_Displacement= max(abs(xhist)) %ROW VECTOR
464 maximum_Relative_DisplacementTop= max(xss)- min(xss); %ROW VECTOR
465 maximum_Relative_DisplacementBot= max(zss)-min(zss); %ROW VECTOR
466 maximum_Relative_DisplacementTopBot= max(xss-zss)-min(xss-zss); %ROW VECTOR
467
468 % Plot 4: power harvested versus time
469 if plotTimeSeries
470     figure(2);
471     subplot(3,1,3);
472     hold on
473     plot(tspanss', power_into_Base_ss, (tspanss)', dissipated_PowerTop_ss,
      (tspanss)', dissipated_PowerBot_ss, (tspanss)',

```

```

        dissipated_PowerMid_ss);
474 xlabel('time (s)');
475 ylabel('Power (W)');
476 title('Power Dissipated versus time');
477 legend('Power into Base', 'Power Dissipated by Top Damper', 'Power
        Dissipated by Bottom Damper', 'Power Dissipated by Middle Damper');
478 grid;
479 end
480
481 end
482
483 function [var, checkedVar]= createVectors(var, checkedVar, paramCol,
        paramRow)
484     if length(var)>1 %var is vectorized element
485         if checkedVar==0
486             var= repmat(var', 1, length(paramCol)); %ROW vector
487             var= reshape(var', 1, numel(var));
488         elseif checkedVar==1 %this is column element
489             var= repmat(var, 1, length(paramRow));
490         end
491         checkedVar= checkedVar+1;
492     end
493 end
494
495
496
497 function f= stateEqn(t, Y0, tspan, hDotDot) %all three nonlinear springs
        exist
498 global XI FI m1 m2 b1M b2M b3M KM K1 K2 FITopFactorM FIBotFactorM
        FIMidFactorM numCombos
499 X= Y0(1:numCombos);
500 XPrime= Y0(numCombos+1:2*numCombos);
501 Z= Y0(2*numCombos+1:3*numCombos);
502 ZPrime= Y0(3*numCombos+1:4*numCombos);
503
504 f= zeros(4*numCombos, 1);

```

```

505
506 f(1:numCombos)= XPrime; %return time derivative of X
507 f(2*numCombos+1:3*numCombos)= ZPrime; %return time rderivative of Z
508
509 W= X-Z;
510 f(numCombos+1:2*numCombos)= -K1'./m1'.*X - interp1(XI, FI, X).*
    FITopFactorM./m1' + KM'./m1'.*(Z-X) -interp1(XI, FI, W).*FIMidFactorM./
    m1' - b1M'./m1'.*XPrime - b3M'./m1'.*(XPrime-ZPrime) - interp1q(tspan',
    hDotDot,t) -9.81; %xDotDot (top mass). - SIGN CORRECT
511 f(3*numCombos+1:4*numCombos)= -K2'./m2'.*Z - interp1(XI, FI, Z).*
    FIBotFactorM./m2' - KM'./m2'.*(Z-X) + interp1(XI, FI, X-Z).*
    FIMidFactorM./m2' - b2M'./m2'.*ZPrime + b3M'./m2'.*(XPrime-ZPrime) -
    interp1q(tspan', hDotDot,t) -9.81; %zDotDot (bottom mass). - SIGN
    CORRECT
512
513 end

```

A.5 Electromagnetic Damping

```

1 %This function plots the electromagnetic damping and power [normalized by
    magnet velocity squared] versus position of a magnet moving over a coil.
    This code is based on the codes given by Zach Trimble and Aparna
    Jonnalagadda in their masters thesis (references listed in this thesis's
    appendix)
2 function ambulatoryElectromagneticDamping
3 wd= .1*.0254; %0017; %.07*.0254; %wire diameter. UNITS: m
4 u= 3; %number of turns in coil of each phase
5 m= .06; %0.125; %magnet mass. UNITS: Kg
6 % [Wmag, Lmag, tmag, Wst, Lst, tst]= magnetParameters(m);
7 Wmag= .012;
8 Lmag= .02;
9 tmag= .0127;
10

```

```

11 plotOneSystem= 1;
12 plotOptimization= 0;
13
14 %%%%%%%%%Constraints%%%%%%%%%
15 %Magnet mass= 0.125. UNITS: Kg
16 %Number of magnet poles: 2
17 %Number of phases: 3
18 %center the coil phase centered over magnet
19 %other coil phases are shifted +/- 0.5*magnet pole width
20 %magnet displacement restricted to +/- .03 m
21 %Assume airgap thickness of .03 inches
22
23 %%%%%%%%%Other Parameters%%%%%%%%%
24 %Rc= RL
25
26 %%%%%%%%%%%%%%%%%%%%%%%%%%%%%%%%%%%%%%%%%%%%%%%%%%%%%%%%%%%%%%%%%%%%%%%%%%
27 global nZ airgap
28
29 deltaCrit= .03; %maximum allowable displacement of center of magnet
30 nZ= 1e-4; % 1e-5; n is space step in pos and z.
31 pos= -deltaCrit:nZ:deltaCrit; %magnet range of motion. UNITS: m
32 W_device= 2*(deltaCrit+Wmag); %maximum width of device [coil]
33 n= 3; %number of coil phases
34 nLoops= ceil(W_device/Wmag - (n-1)/n); %number of loops
35
36 %constrained geometric parameters (could be changed)
37 rho= 7400; %density of neodymium. UNITS: Kg/m^3
38 airgap= 0.030*.0254; %air gap between magnets and front coils. UNITS: m
39 wresistivity= 1.68e-8; %copper resisitvity. UNITS: Ohms*m
40
41 %dependent geometric parameters
42 tphase= wd; %u*wd; %thickness of 1 coil phase
43
44 tins= .0028*.0254; %based on Trimble masters P. 95
45 WPhase= Wmag/3; %width available for each phase

```

```

46 Wkerf= .006*.0254; %[m], Minimum distance between traces (kerf). Trimble
    page 105
47 nWires= floor(WPhase/(wd + Wkerf)); %number of wires that fit in width
    available for each phase
48 nLayers= ceil(u/nWires); %number of layers required to get u turns per
    phase
49 tcoil= 2*nLayers*wd + (2*nLayers+1)*tins;
50
51 tgap= airgap + tcoil
52 A= Lmag*Wmag; %area of 1 phase. UNITS: m
53 lSingleTurn= 2*(Lmag+Wmag); %Assume wire is rectangle in shape of magnet (
    pitches align)
54 numTurns= n*u*nLoops; %number of coil phases * number of turns per phase
55 lwire=lSingleTurn*numTurns; %Assume wire is rectangle in shape of magnet
56 Awire= pi*wd^2/4; %wire cross sectional area. UNITS: m
57 Rcoil= wresistivity*lwire/Awire; %R= rho*l/A
58 Rload= Rcoil;
59
60 if ~isinf(nLayers)
61     %Calculate and plot for first layer
62     %%%%%%%%%Calculate dFlux through each phase%%%%%%%%
63     tLayer= airgap + wd + 1.5*tins; %FIRST LAYER- closest layer. positive
        number here
64     [z, B]= calculateField(tmag, tgap, Wmag, tLayer, plotOneSystem); %
        magnetic field in space when magnet is centered at z= 0
65                                     %inputs are (tmag, tgap, Wmag)= (x_A, x_B, l)
66     fluxTable= phaseFlux(z,B, Wmag, Lmag, pos, W_device, nLoops, tgap,
        plotOneSystem); %flux through each phase of coil as a function of
        magnet position
67                                     %fluxTable is a table where each row is [
        magPosition Flux_A Flux_B Flux_C]
68
69     dFluxTable= phaseDFlux(fluxTable, plotOneSystem);%dFlux through each
        phase as a function of magnet position
70
71     uLayer= min(nWires, u); %number of turns in each phase in this layer

```

```

72
73 fluxTot= uLayer.*sum(abs(fluxTable(:,2:4)'))';
74 dFluxTot= uLayer.*sum(abs(dFluxTable(:,2:4)'))';
75 dFluxSquared= dFluxTable.*dFluxTable;
76 dFluxSquaredTot= uLayer^2.*sum(dFluxSquared(:,2:4)')';
77 blah= 1
78 %%%%%%%%%%%%%%%%%%%%%%%%%%%%%%%%%%%%%%%%%%%%%%%%%%%%%%%%%%%%%%%%%%%%%%%%%
79
80 %Just calculate for remaining layers
81 if (nLayers>1)
82     uLayer= nWires;
83     for p=2:nLayers-1
84         %%%%%%%%%Calculate dFlux through each phase%%%%%%%%
85         tLayer= airgap + p*wd + 1.5*p*tins; %FIRST LAYER- closest layer.
            positive number here
86         [z, B]= calculateField(tmag, tgap, Wmag, tLayer, 0); %magnetic
            field in space when magnet is centered at z= 0
87         %inputs are (tmag, tgap, Wmag)= (x_A, x_B, l)
88         fluxTable= phaseFlux(z,B, Wmag, Lmag, pos, W_device, nLoops, tgap,
            0); %flux through each phase of coil as a function of magnet
            position
89         %fluxTable is a table where each row is [magPosition Flux_A Flux_B
            Flux_C]
90         dFluxTable= phaseDFlux(fluxTable, 0);%dFlux through each phase as a
            function of magnet position
91
92         fluxTot= fluxTot + uLayer.*sum(abs(fluxTable(:,2:4)'))';
93         dFluxTot= dFluxTot + uLayer.*sum(abs(dFluxTable(:,2:4)'))';
94         dFluxSquared= dFluxTable.*dFluxTable;
95         dFluxSquaredTot= dFluxSquaredTot + uLayer^2.*sum(dFluxSquared
            (:,2:4)')';
96
97         figure(1); subplot(3,1,1);
98         hold on;
99         plot(pos, fluxTot)
100        subplot(3,1,2); hold on;

```

```

101     plot(pos, dFluxTot);
102     subplot(3,1,3); hold on;
103     plot(pos, dFluxSquaredTot./ (Rcoil+Rload));
104     %%%%%%%%%%%%%%%%%%%%%%%%%%%%%%%%%%%%%%%%%%%%%%%%%%%%%%%%%%%%%%%%%%%%%%%%%
105 end
106 %Last layer [farthest away from magnet]
107 uLayer= u - (nLayers-1)*uLayer;
108
109     tLayer= airgap + nLayers*wd + 1.5*nLayers*tins; %FIRST LAYER-
        closest layer. positive number here
110     [z, B]= calculateField(tmag, tgap, Wmag, tLayer, 0); %magnetic
        field in space when magnet is centered at z= 0
111     %inputs are (tmag, tgap, Wmag)= (x_A, x_B, l)
112     fluxTable= phaseFlux(z,B, Wmag, Lmag, pos, W_device, nLoops, tgap,
        0); %flux through each phase of coil as a function of magnet
        position
113     %fluxTable is a table where each row is [magPosition Flux_A Flux_B
        Flux_C]
114     dFluxTable= phaseDFlux(fluxTable, 0);%dFlux through each phase as a
        function of magnet position
115
116     fluxTot= fluxTot + uLayer.*sum(abs(fluxTable(:,2:4)'))';
117     dFluxTot= dFluxTot + uLayer.*sum(abs(dFluxTable(:,2:4)'))';
118     dFluxSquared= dFluxTable.*dFluxTable;
119     dFluxSquaredTot= dFluxSquaredTot + uLayer^2.*sum(dFluxSquared
       (:,2:4)')';
120 end
121
122     %totalDFlux= abs(dFluxTable(:,2))+ abs(dFluxTable(:,3))+ abs(dFluxTable
       (:,4));
123
124     be= dFluxSquaredTot./ (Rcoil+Rload);
125     PpV2= Rload/(Rload+Rcoil)^2 .* dFluxSquaredTot;
126
127     if (plotOneSystem== 1)
128         figure(1);

```

```

129     subplot(3,1,3);
130     [AX,H1,H2] = plotyy(pos,be,pos,PpV2,'plot');
131     set(get(AX(1),'Ylabel'),'String','damping coefficient (Ns/m)');
132     set(get(AX(2),'Ylabel'),'String','power/velocity^2 (Ws^2/m^2)');
133     set(AX(1),'ycolor','k')
134     set(AX(2),'ycolor','k')
135     set(H1,'color','k')
136     set(H2,'color','k')
137     set(AX(1),'YLim',[0 max(be)])
138     set(AX(2),'YLim',[0 max(PpV2)])
139
140     % plot(pos, be);
141     title({'Induced Damping and';'Power to Load Per Magnet Velocity^2'
142           })
143     xlabel('magnet position (m)');
144     grid;
145 end
146
147 %print desired outputs
148 averageB= mean(be(floor(.25*length(be)):ceil(.75*length(be))))
149 rho_copper= 8960; %[Kg/m^3]
150 systemWeight= rho_copper*Awire*lwire + m
151 u
152 else
153     averageB= 0;
154     systemWeight= 0;
155     fprintf('WIRE DIAMETER EXCEEDS COIL PITCH');
156 end
157
158 function [z, B]= calculateField (x_A, x_B, l, xLayer, plotOneSystem) %tmag,
159     tgap, Wmag
160 %From Jonnalagadda SM thesis page 92
161 %Fourier sum parameters
162 global nZ airgap

```



```

163
164 %-----Inputs-----
165 N= 40; %number of terms added in the fourier sum. REDUCE SUM FOR LARGER MAG
      SIZES
166 res= 200; %number of points per coordinate array
167 %-----End inputs-----
168
169 Br= 1.2; %T (N/(Am) magnetization flux density
170 s_max= Br;
171 mu_0= pi*4e-7; %Wb/(Am) magnetic permeability of vacuum
172
173 %geometry parameters
174 % x_A= .005; %x_A is magnet thickness
175 % x_B= 4e-3; %x_B is airgap+coil thickness
176 np= 2; % number of magnets (poles)
177 d= 0; %1e-3; % half the gap between magnets [m]
178 % l= .01; %12.7e-3; %length of each magnet (pole) (in z-direction) [m]
179
180 %Coil Parameters
181 % t= .68e-3; %.08/3*.0254; %spacing between coils [m]
182 % g= (((1+2*d)/3)-t)/2; %half a coil length. { 1/2 phase length= (Wmag/3
      -   }
183 % wd= .8e-3; %.8128e-3; %diameter of wire [m]
184 % nc= 3; %number of coils (per phase). Should be same as # magnets
185 % nt= 8; %number of turns per coil
186 % R0= 16.78e-9; % resistivity of copper [ohm-m]
187
188 x_step= (x_A+x_B)/res; %number of steps in the x-direction of grid
189 z_step= nZ; %(np*(2*d+1))/res; %number of steps in the z-direction of grid
190
191 xVector= [-x_B:x_step:x_A]; %vector of x-values between rear of magnets and
      rear of coil
192 zVector= [0:z_step:np*(2*d+1)]; %vector of z-values between 0 and end of
      magnets
193 x= repmat(xVector, length(zVector), 1); %matrix of x-values. Repeated for z
      -values (each column- same #)

```

```

194 z= repmat(zVector, length(xVector), 1); z= z'; %matrix of z-values.
      Repeated for x-values (each row- same #)
195 %in matrices: z value changes in each row. x changes in each column
196
197 %Loop to calculate fourier coefficients and magnetic potential constants
198 for p= 1:N
199     k= 2*p-1; %even coefficients are 0, only calculate for odd values
200     w_m= pi*k/(2*d+1);
201     %     w_c= pi*k/(3*(2*g+t));
202     b_m(p)= (4*s_max/k/pi)*cos((k*pi*d)/(1+2*d)); % magnets' charge
      density in fourier coefficients [T]
203     %JK a_c(p)= (4*k/g/k/pi)*sin((k*pi*g)/(3*(2*g+t))); % coils' tangential
      magnetic field fourier coeff's [A/m]
204     A(p)= (b_m(p)*sinh(w_m*x_B))/(w_m*mu_0*sinh(w_m*(x_A+x_B))); %
      constants for psi_A calculation [A]
205     C(p)= (-b_m(p)*sinh(w_m*x_A))/(w_m*mu_0*sinh(w_m*(x_A+x_B))); %
      constants for psi_B calculation [A]
206     %JK D(p)= a_c(p)/(w_c*sinh(w_c*(x_A+x_B))); % constants for psi
      calculation [A]
207 end
208
209 sigma= 0*z; % magnets' charge density
210 psi_A= zeros(length(zVector), length(xVector)); %magnetic potential in
      region A due to magnets
211 psi_B= zeros(length(zVector), length(xVector)); %magnetic potential in
      region B due to magnets
212
213 for k= 1:N % loop to sum the fourier series terms
214     j= 2*k-1;
215     sigma= sigma + b_m(k).*sin(z.*(j*pi/(1+2*d))); % in T, magnet's charge
      density
216     psi_A=psi_A + A(k)*sinh(pi*j.*(x-x_A)/(1+2*d)).*sin(z.*(pi*j/(1+2*d)));
      %in A, magnetic potential in region A due to magnets
217     psi_B=psi_B + C(k)*sinh(pi*j.*(x+x_B)/(1+2*d)).*sin(z.*(pi*j/(1+2*d)));
      %in A, magnetic potential in region B due to magnets
218 end

```

```

219 if (plotOneSystem== 1)
220     figure(2);
221     plot(z(:,1)-l, sigma, 'k');
222     title('Magnetic charge density at interface between magnets and air:
           magnet centered at z= 0');
223     xlabel('z (m)')
224     ylabel('magnetic charge density (T)')
225 end
226
227     m1= ceil(length(xVector)*x_B/(x_A+x_B)); %m is fraction of z elements
           where divide region A(magnets) and B(air+coil)
228     m2= floor(length(xVector)*x_B/(x_A+x_B));
229     psi_A(:,1:m2)= 0; %zeroing out Region B where psi_A is invalid
230     psi_B(:,m1:length(xVector))= 0; %length(z))= 0; %zeroing out Region A where
           psi_B is invalid
231     psi_m= psi_A + psi_B;
232
233     %shift z-axis so that field is centered at z= 0.
234     %In above calculation: z= [0, 2*Wmag]. Desire z= [-Wmag, Wmag]
235     z= z-l;
236
237     [Hm_x, Hm_z]= gradient(-psi_m, x_step, z_step); %in A/m, H in x and z due
           to magnets
238     %H is the magnetic field
239
240 if (plotOneSystem== 1)
241     figure(4);
242     surf(x(1,:), z(:,1), psi_m, 'LineStyle','none');
243     hold on;
244     %draw box indicating magnets (region A)
245     plot([0 x_A x_A 0], [-l -l l l], '-r', 'LineWidth', 3);
246     %draw box indicating air gap (part of region B)
247     plot([-airgap 0 0 -airgap], [-l -l l l], '-b', 'LineWidth', 3);
248     %draw box indicating coils
249     plot([-x_B -airgap -airgap -x_B], [-l -l l l], '-g', 'LineWidth', 3);
250     axis([-x_B x_A -l l])

```

```

251
252     xlabel('x');
253     ylabel('z');
254     zlabel('magnetic potential (A)');
255     title('Magnetic Potential');
256 end
257
258 %determine column of xVector that corresponds to xLayer
259 [value, index]= min(abs(xVector + xLayer));
260
261 Hm_x_surf= Hm_x(:,index); %Values of Hm_x at the coils surface. (First
    column is at x= -x_B?)
262
263 if (plotOneSystem== 1)
264     figure(3);
265     plot(z, Hm_x_surf);
266
267     xlabel('z (m)');
268     ylabel('magnetic field (A/m)');
269     title('Magnetic field in the x-direction at the coil');
270 end
271
272 %FUNCTION OUTPUTS
273 B= mu_0*Hm_x_surf;
274 z= (z(:,index))'; % originally: z= (z(:,1))';
275 end
276
277 function fluxTable= phaseFlux (z, B, Wmag, Lmag, pos, W_device, nLoops, x_B
    , plotOneSystem)
278 %Inputs: z, B is Table of flux at coils along z-direction.
279 %z is horizontal position in space along the magnet, centered at magnet
    center.
280 %Outputs: fluxTable is a table where each row is [magPosition Flux_A
    Flux_B Flux_C]
281
282 %endpoints of A, B, and C phases

```

```

283
284 %Acoil endpoints are [-5/6*Wmag, 1/6*Wmag]
285 %Bcoil endpoints are [-3/6*Wmag, 3/6*Wmag]
286 %Ccoil endpoints are [-1/6*Wmag, 5/6*Wmag]
287
288 %Calculate phase flux when magnet is centered at 0
289 %sum the flux inbetween the start and end points
290 %shift position of magnet
291 %sum the flux inbetween the start and end points
292
293 dS= Lmag*(z(2)-z(1));%incremental area: Lmag[dim into page] * dZ
294
295 %pos is magnet position
296 Aflux= zeros(length(pos), 1);
297 Bflux= zeros(length(pos), 1);
298 Cflux= zeros(length(pos), 1);
299 for i= 1:length(pos)
300     newZ= z-pos(i); %magnet moves right = same as coil moves left
301
302     Loopmin= floor(nLoops/2)+1; %leftmost loop number
303
304     %determine endpoints for A phase. Put these in a column vector where
305     %each element is loop start/end point
306     Aphase= []; Bphase=[]; Cphase= [];
307     for j= 1:nLoops+1
308         Aphase(j)= Wmag*(-Loopmin + j-1);
309         Bphase(j)= Wmag*(-Loopmin + j-2/3); %add 1/3
310         Cphase(j)= Wmag*(-Loopmin + j-1/3); %add 2/3
311     end
312
313     for j= 1:nLoops%-1
314         [value AstartIndex]= min(abs(newZ - Aphase(j)));
315         [value AendIndex]= min(abs(newZ - Aphase(j+1)));
316         [value BstartIndex]= min(abs(newZ - Bphase(j)));
317         [value BendIndex]= min(abs(newZ - Bphase(j+1)));
318         [value CstartIndex]= min(abs(newZ - Cphase(j)));

```

```

319     [value CendIndex]= min(abs(newZ - Cphase(j+1)));
320
321     Aflux(i)= Aflux(i) + abs(sum(B(AstartIndex:AendIndex)))*dS;
322     Bflux(i)= Bflux(i) + abs(sum(B(BstartIndex:BendIndex)))*dS;
323     Cflux(i)= Cflux(i) + abs(sum(B(CstartIndex:CendIndex)))*dS;
324     end
325 end
326
327 fluxTable= [pos' Aflux Bflux Cflux];
328
329     if (plotOneSystem== 1)
330         figure(1)
331         subplot(3,1,1)
332         plot(pos, Aflux, pos, Bflux, pos, Cflux, pos, abs(Aflux)+abs(Bflux)
333             +abs(Cflux))
334         title('Magnetic Flux through single turn versus magnet position');
335         xlabel('magnet position (m)');
336         ylabel('magnetic flux (Wb)');
337         grid;
338         legend('Phase A', 'Phase B', 'Phase C', 'Combined')
339
340     %add coil positions to figure 4 3D plot
341     figure (4)
342     hold on
343     %for first iteration: add to legend.
344     plot([-x_B -x_B], [Aphase(1) Aphase(2)], 'k*') %plot lines
345     of phase
346     plot([-x_B -x_B], [Bphase(1) Bphase(2)], 'r*') %plot lines
347     of phase
348     plot([-x_B -x_B], [Cphase(1) Cphase(2)], 'c*') %plot lines
349     of phase
350     legend('magnetic potential', 'region with magnets', 'air gap',
351         'region with coils', 'Phase A', 'Phase B', 'Phase C')
352     for j=2:nLoops %for each of the loops
353         plot([-x_B -x_B], [Aphase(j) Aphase(j+1)], 'k*') %plot
354         lines of phase

```

```

349         plot([-x_B -x_B], [Bphase(j) Bphase(j+1)], 'r*') %plot
           lines of phase
350         plot([-x_B -x_B], [Cphase(j) Cphase(j+1)], 'c*') %plot
           lines of phase
351     end
352     %adjust plot limits
353     ylim([min(Aphase) max(Cphase)]);
354 end
355 end
356
357 function dfluxTable= phaseDFlux(fluxTable, plotOneSystem)
358 %fluxTable is a table where each row is [magPosition Flux_A Flux_B Flux_C]
359
360 % F is a vector, DF = GRADIENT(F, H). H is spacing between points
361 H= fluxTable(2,1) - fluxTable(1,1); %steps in z-direction
362
363 dFluxA= gradient(fluxTable(:,2), H);
364 dFluxB= gradient(fluxTable(:,3), H);
365 dFluxC= gradient(fluxTable(:,4), H);
366
367 dfluxTable= [fluxTable(:,1) dFluxA dFluxB dFluxC];
368
369     if (plotOneSystem== 1)
370         figure(1);
371         subplot(3,1,2)
372         plot(dfluxTable(:,1), dFluxA, dfluxTable(:,1), dFluxB, dfluxTable
           (:,1), dFluxC, dfluxTable(:,1), abs(dFluxA)+abs(dFluxB)+abs(
           dFluxC));
373         title('dFlux/dz through single turn versus magnet position')
374         xlabel('magnet position, z (m)');
375         ylabel('dFlux/dz');
376         grid;
377     end
378 end

```

Bibliography

- [1] Aaron Carroll and Gernot Heiser. An analysis of power consumption in a smartphone. In *USENIX Annual Technical Conference*, 2010.
- [2] F. Cottone, H. Vocca, and L. Gammaitoni. Nonlinear energy harvesting. *Physical Review Letters*, 102, February 2009.
- [3] D.C. Freeman. *Nonlinear springs with applications to flow regulation valves and mechanisms*. PhD thesis, Massachusetts Institute of Technology, 2008.
- [4] A. Hajati, S. P. Bathurst, H. J. Lee, and S. G Kim. Design and fabrication of a nonlinear resonator for ultra wide-bandwidth energy harvesting applications. In *Proceedings of the Ieee International Conference on Micro Electro Mechanical Systems (mems)*, pages 1301–1304, April 2011.
- [5] Aparna S. Jonnalagadda. Magnetic induction systems to harvest energy from mechanical vibrations. Master’s thesis, Massachusetts Institute of Technology, 2007.
- [6] Han Kyul Joo and Themistoklis P. Sapsis. Performance measures for single-degree-of-freedom energy harvesters under stochastic excitation. *J. Sound and Vibrations*, Submitted 2013.
- [7] Y.S. Lee, A.F. Vakakis, L.A. Bergman, D.M. McFarland, and G. Kersche. Suppressing aeroelastic instability using broadband passive targeted energy transfers, part 1:theory. *AIAA Journal*, 45(3):693–711, 2007.
- [8] Omega Engineering Limited. An introduction to load cells, history, theory & operating principles, 2014.
- [9] L.I. Manevitch, A.I. Musienko, and C. Lamarque. New analytical approach to energy pumping problem in strongly nonhomogeneous 2dof systems. *Meccanica*, pages 77–83, February 2007.
- [10] B.P. Mann and N.D. Sims. Energy harvesting from the nonlinear oscillations of magnetic levitation. *Journal of Sound and Vibration*, 319:515–530, 2009.
- [11] D.M. McFarland, L.A. Bergman, and A.F. Vakakis. Experimental study of non-linear energy pumping occurring at a single fast frequency. *International Journal of Non-Linear Mechanics*, 40:891–899, 2005.

- [12] P.D. Mitcheson, T.C. Green, E.M. Yeatman, and A.S. Holmes. Architectures for vibration-driven micropower generators. *Journal of Microelectromechanical Systems*, 2004.
- [13] H.J. Ralston M.Y. Zarrugh, F.N. Todd. Optimization of energy expenditure during level walking. *European Journal of Applied Physiology*, 1974.
- [14] Penglin Niu, Patrick Chapman, Raziell Reimer, and Xudong Zhang. Evaluation of motions and actuation methods for biomechanical energy harvesting. In *Annual IEEE Power Electronics Specialists Conference*, 2004.
- [15] J.A. Paradiso and T. Starner. *Low Power Electronics Design*, chapter Human Generated Power for Mobile Electronics. CRC Press, 2004.
- [16] J.A. Paradiso and T. Starner. Energy scavenging for mobile and wireless electronics. *IEEE Pervasive Computing*, 4(1):18–27, 2005.
- [17] Tara Parker-Pope. The pedometer test: Americans take fewer steps. *The New York Times*, 2010. <http://well.blogs.nytimes.com/2010/10/19/the-pedometer-test-americans-take-fewer-steps/>.
- [18] T.P. Sapsis, D.D. Quinn, A.F. Vakakis, and L.A. Bergman. Effective stiffening and damping enhancement of structures with strongly nonlinear local attachments. *Journal of Vibration and Acoustics*, 134(1), 2012.
- [19] T.P. Sapsis, A. Vakakis, O. Gendelman, L. Bergman, G. Kerschen, and D. Quinn. Efficiency of targeted energy transfers in coupled nonlinear oscillators associated with 1:1 resonance captures: Part ii, analytical study. *Journal of Sound and Vibration*, 325(1):297–320, 2009.
- [20] S. C. Stanton, C. C. McGehee, and B. P. Mann. Nonlinear dynamics for broadband energy harvesting: Investigation of a bistable piezoelectric inertial generator. *Physica D*, 239:640–653, 2010.
- [21] X. Tang and L. Zuo. Simulation and experiment validation of simultaneous vibration control and energy harvesting from buildings using tuned mass dampers. In *Proceedings of the American Control Conference*, pages 3134–3139, 2011.
- [22] S. Timoshenko. *Strength of materials*. 1955.
- [23] A. Zachary Trimble. Downhole vibration sensing by vibration energy harvesting. Master’s thesis, Massachusetts Institute of Technology, 2007.
- [24] A. Zachary Trimble. *Energy harvesting of random wide-band vibrations with applications to an electro-magnetic rotational energy harvester*. PhD thesis, Massachusetts Institute of Technology, 2011.
- [25] A.F. Vakakis, O.V. Gendelman, L.A. Bergman, D.M. McFarland, G. Kerschen, and Y. S. Lee. *Nonlinear Targeted Energy Transfer in Mechanical and Structural Systems*, volume 156. Springer, 2009.

- [26] B. Vaurigaud, L.I. Manevitch, and C.-H. Lamarque. Suppressing aeroelastic instability in a suspension bridge using a nonlinear absorber. In *IUTAM Symposium on Nonlinear Dynamics for Advanced Technologies and Engineering Design*, volume 32, pages 263–277, 2013.
- [27] T. von Büren, P.D. Mitcheson, T.C. Green, E.M. Yeatman, A.S. Holmes, and Gerhard Tröster. Optimization of inertial micropower generators for human walking motion. *IEEE Sensors Journal*, 6(1):28–38, 2006.
- [28] Onnik Yaglioglu. Modeling and design considerations for a micro-hydraulic piezoelectric power generator. Master’s thesis, Massachusetts Institute of Technology, 2002.